TAMPEREEN TEKNILLINEN YLIOPISTO
TAMPERE UNIVERSITY OF TECHNOLOGY

Ahmad Mardoukhi

Effects of microstructural features, thermal shocks and strain rate on the mechanical response of granitic rocks

Julkaisu 1493 • Publication 1493

Tampere 2017

Tampereen teknillinen yliopisto. Julkaisu 1493
Tampere University of Technology. Publication 1493

Ahmad Mardoukhi

Effects of microstructural features, thermal shocks and strain rate on the mechanical response of granitic rocks

Thesis for the degree of Doctor of Science in Technology to be presented with due permission for public examination and criticism in Konetalo Building, Auditorium K1702, at Tampere University of Technology, on the 6th of October 2017, at 12 noon.

Tampereen teknillinen yliopisto - Tampere University of Technology
Tampere 2017

Doctoral candidate: Ahmad Mardoukhi
Laboratory of Materials Science
Tampere University of Technology
Finland

Supervisor: Professor Veli-Tapani Kuokkala
Laboratory of Materials Science
Tampere University of Technology
Finland

Instructor: Dr. Mikko Hokka
Laboratory of Materials Science
Tampere University of Technology
Finland

Pre-examiners: Professor Leopold Kruszka
Military University of Technology
Poland

Assistant Professor Xue Nie
Department of Mechanical Engineering
Southern Methodist University, Lyle School of Engineering
The United States of America

Opponents: Professor Leopold Kruszka
Military University of Technology
Poland

Professor Ezio Cadoni
University of Applied Science and Arts of Southern Switzerland
Switzerland

ISBN 978-952-15-4003-5 (printed)
ISBN 978-952-15-4015-8 (PDF)
ISSN 1459-2045

Abstract

Percussive drilling is regarded as the most effective method for excavation, tunneling, and shallow well boring in the hard rock such as granite. However, its efficiency has been questioned in some specific environments and applications such as drilling for geothermal energy, where bores as deep as 5000 m are needed to reach the desired temperature zone. It is therefore understandable that attempts to drill bores that deep can face significant difficulties, and even though these difficulties have already been overcome by developing new techniques for deep drilling, there still are no replacement for the percussive drilling technique. The reason for this situation can be found in the shortage of technological readiness and in the nature of the rock and its behavior itself. However, in the previous attempts to find a replacement for percussive drilling, not enough of attention has been paid to altering the rock's properties before drilling for example by using a thermal shock.

In this work, the mechanical behavior of the rocks before and after applying heat shocks was studied in quasi-static and dynamic loading conditions. Two different heat shocks were applied on the two studied rocks, one using a flame torch and one using a plasma gun. The heat shocks using the flame torch were applied on the Brazilian disc samples with durations of 10, 30, or 60 seconds. The thermal shocks using the plasma gun were applied on the Brazilian disc samples and on the bulk of the rock for dynamic indentation tests. Three different plasma gun heat shocks were applied on Brazilian disc samples with durations of 0.40, 0.55, or 0.80 second. The heat shocks applied on the bulk of the rock had a duration of 3, 4, and 6 seconds.

A methodology was developed to analyze and characterize the damage caused by the heat shocks on the surface of the specimens. In this method, a liquid penetrant was applied on the surface of the samples before and after applying the heat shocks with images taken from the specimens' surface under an ultraviolet light. Later on, the fractal dimension of the surface crack patterns was calculated using the box counting method. The results indicate that the fractal dimension of the samples increases by increasing the duration of the thermal shock and there is a relationship between the relative increase of the fractal dimension and the mechanical response of the rock material. Even though the fractal dimension analysis is limited to the surface of the samples, the computed tomography results suggest that the effects of the heat shocks are also limited to the very surface of the specimens. Therefore, the fractal dimension analysis provides a fast and accurate enough estimation of the mechanical response of the rock.

The mechanical behavior of rock was studied at low and high strain rates using the Brazilian disc samples. The results indicate that by increasing the duration of the thermal shock, increasing the fractal dimension, the strength of the rock decreases in the studied strain rate range. Nonetheless, there are some differences in the rock mechanical behavior at low and high strain rates. The dynamic strength of the rock decreases considerably faster with increase of the fractal dimensions than the quasi-static strength. Therefore, the strain rate sensitivity of the rock decreases with the increasing fractal dimension.

The dynamic indentation tests were performed to study the effects of heat shocks in situations similar to percussive drilling. The tests were performed using both single and triple button indenters. Even though the direct measurements of the bit-rock interactions obtained from the stress waves are useful, they do not provide any information about the side chipping and

chipping between the indenters. Therefore, optical profilometry was used to study the craters formed during the impacts, and the concept of destruction work was used to characterize the effects of the heat shocks on the material removal during dynamic indentation. The results imply that after applying the heat shock, the extent of material removal increases even though the force levels are not affected much. This means that the efficiency of the indentation processes cannot be evaluated only by using the force-displacement curves but additional analysis such as the ones used in this work are needed.

Preface

The work presented in this thesis was carried out at the Laboratory of Materials Science of Tampere University of Technology during the years of 2014-2017. This work was founded by Suomen Luonnonvarain Tutkimussäätiö and Finnish Cultural Foundation. Scientific Foundation of the City of Tampere is greatly acknowledged for covering a part of printing costs of this work. The work was done under the supervision of Professor Veli-Tapani Kuokkala, to whom I wish to express my deepest gratitude for the guidance and encouragement.

I would also like to express my sincere appreciation to Dr. Mikko Hokka for providing this great opportunity for me to carry out such an interesting project. None of this would have been possible without his continuing support, encouragement, and valuable advices during the course of this project.

All the staff and colleagues working at the Laboratory of Materials Science, especially in the High Strain Rate Research Group are acknowledged for creating such a pleasant working environment. Specially M.Sc. Naiara Vazquez for the joyful office conversations. Mr. Ari Varttila deserves my special thanks for helping with designing, building, and fixing all the parts and apparatuses, which were used during this project. Special thanks to Dr. Timo Saksala for great effort in modeling and simulation of the results. Mr. Mikko Kylmälahti is greatly acknowledged for his help to carry out the heat treatments processes.

To my best friends, Daniele and Francesco, who were there any time that I needed them even though they were far away. I would also to thank my other friends, Georg, Alessia, Siavash, and the ones who I did not mention theirs names because the list will go forever.

Finally, for my loved ones, my parents Masoud and Mitra. None of this would have been possible without your support and encouragement. My lovely brother, Yousof, who was there not only as my brother, but also as a colleague during these years.

Tampere, Finland

October 2017 Ahmad Mardoukhi

LIST OF PUBLICATIONS

This thesis is based on the work reported and discussed in the following publications:

I Effects of surface cracks and strain rate on the tensile behavior of Balmoral Red granite, A. Mardoukhi, M. Hokka, V.T. Kuokkala, *EDP Sciences*, Vol. 94, 2015

II Effects of strain rate and surface cracks on mechanical behavior of Balmoral Red, A. Mardoukhi, Y. Mardoukhi, M. Hokka, V.T. Kuokkala, *Philosophical Transactions of Royal Society A*, Vol. 375 (2085), 2016

III Effects of heat shock on the dynamic tensile behavior of granitic rocks, A. Mardoukhi, Y. Mardoukhi, M. Hokka, V.T. Kuokkala, *Rock Mechanics and Rock Engineering*, Vol. 50 (5), 2017

IV A numerical and experimental study on the tensile behavior of plasma shocked granite under dynamic loading, A. Mardoukhi, T. Saksala, M. Hokka, V.T. Kuokkala, *Rakenteiden Mekaniikka*, Vol. 5(2), 2017

Unpublished manuscript

I Experimental study of the dynamic indentation damage in thermally shocked granite. A. Mardoukhi, M. Hokka, V.T. Kuokkala.

Author's contribution

Ahmad Mardoukhi planned and performed the experiments and analyses presented in this thesis with the following exceptions:

-M.Sc. Yousof Mardoukhi performed the calculations of the fractal dimension at the Institute of Physics and Astronomy of the University of Potsdam.

-The plasma heat treatments were carried out by Mr. Mikko Kylmälahti at the Laboratory of Materials Science of Tampere University of Technology.

-The X-ray Computed Tomography images were obtained by Dr. John Walmsley at SINTEF Materials and Chemistry.

-Dr. Timo Saksala carried out the modeling and simulation part in Publication IV and wrote the corresponding part of the manuscript.

In all the publications, Professor Veli-Tapani Kuokkala and Dr. Mikko Hokka gave advice and commented the manuscripts. All manuscripts were commented also by all the co-authors.

List of symbols and abbreviations

Greek symbols:

α	Constant factor which includes Poisson's ratio of the ellipsoid
β	Numerical constant of the order of unity (Eqn. 1)
β	Constant factor which includes the axial ratio of the ellipsoid (Eqn. 9)
γ	Specific surface energy
ε_i	Measured and dispersion corrected incident strain as a function of time
ε_r	Measured and dispersion corrected reflected strain as a function of time
ν	Poisson's ratio
ρ	Density of the bar material
σ	Stress
σ_i	First principal stress
σ_{ii}	Second principal stress
σ_{iii}	Third principal stress
σ_m	Mean stress on σ_I and σ_{III} plane
σ_n	Normal compressive stress
σ_T	Interatomic cohesive strength
σ_y	Principal tensile stress along the vertical diameter
τ	Shear stress
μ	Coefficient of internal friction

Latin symbols:

a	Interatomic spacing
A_b	Cross sectional area of the drill rod (incident bar)
C	Sound speed of the bar material
C	Half-length of a crack
C_0	Uniaxial compressive strength
E	Young's modulus
E_b	Young's modulus of the bar material
F	Force
L	Length of the Brazilian disc

m	Dimensionless empirical constant in the original non-linear Hoek-Brown criterion for intact rock
M_{abs}	Absolute strain rate sensitivity
m_b	Dimensionless empirical constant for fractured rock in the Hoek-Brown criterion
n	Constant which describes the time dependency of the rock behavior
P	Concentrated compressive forces
r	Radius of curvature at the tip of the crack
R_1	Radius of the Brazilian disc
s	Dimensionless empirical constant in the original non-linear Hoek-Brown criterion for intact rock
S_0	Finite shear stress
S_0	Cohesion in Coulomb failure criterion
t	Time
T_0	Uniaxial tensile strength
V_s	Speed of impact

Abbreviations:

BD	Brazilian disc
BSE	Back-scattered electron
CCD	Charge-Coupled Device
CT	Computed Tomography
DIC	Digital Image Correlation
FD	Fractal Dimension
GTE	Geothermal Energy
LP	Liquid Penetrant
NDT	Non-Destructive Testing
RGB	Red Green Blue
RT	Room Temperature
SCB	Semi-Circular Bending
SE	Secondary electron
SEM	Scanning Electron Microcopy
SHPB	Split Hopkinson Pressure Bar
UV	Ultraviolet

Table of Contents

1. Introduction

Geothermal energy (GTE) is a rapidly growing business worldwide, and a possible solution for the energy demands for our future society. Geothermal energy, however, has its downsides as well. The biggest disadvantage is that the enormous energy deposits lie deep under the Earth's surface, and with the current technologies, reaching the geothermal energy is an extremely challenging task. To produce electricity from the geothermal energy, the temperature of the bedrock needs to be around 200 ^{0}C, which can usually only be reached at depths of around 5 km in areas away from the tectonic plate boundaries. Therefore, widespread utilization of the geothermal energy requires faster and more economical drilling and well-construction technologies. The most important problems in deep-hole drilling for GTE are the low rate of penetration and the rapid wear of drilling tools, which are mainly caused by the high strength and hardness of the bedrock, especially when drilling through hard igneous rock. Drilling in these conditions results in high temperatures and high hydrostatic pressures. Because of these problems, drilling holes up to the depth of 5 km, especially in Nordic bedrock, can be regarded as one of the most challenging engineering tasks we currently face.

Percussive drilling is considered to be an effective process for excavation, tunneling, and shallow-well boring in hard igneous rock such as granite. The efficiency of this method is closely related to the brittleness of the rock material. The more brittle the rock is, the longer the radial cracks that are formed by each impact of the drill. These cracks, in turn, facilitate the chipping that occurs between the drill buttons. Even though percussive drilling is recognized as one of the most effective drilling techniques, it still lacks some efficiency in certain specific environments.

Many attempts have been made to improve the drilling technology to overcome the deficiencies in percussive and rotary drilling. Examples of these attempts include microwave-assisted hard rock cutting [1], laser assisted drilling [2], water-jet assisted drilling [3], abrasive-jet drilling [4], diamond drilling [5], and ultra-high-pressure jet drilling [6, 7]. Although considerable research and development efforts have been put in developing these new techniques, none of them has yet become commercially viable. The reason for this may well be due to the lack of technological readiness, but it may also be due to the nature of the rock itself and our inability to understand how to break the rock efficiently without causing excess wear and damage to the tools.

The current drilling technologies are based on rotary and impact drilling. To design more efficient drill tools and systems, engineers need to know the rock strength and other properties of the drilling conditions, which involve high hydrostatic pressures and elevated temperatures. However, since experimental testing under these conditions is complicated for both scientific and practical reasons, various numerical simulations and constitutive models are currently being used to better understand the rock-tool interactions. The construction of these models, as well as validation of the simulation results, rely both on a good scientific understanding of the material behavior and on the gathering of experimental data to calibrate the parameters of the material used in the model. Among engineering materials, rocks have not attracted much scientific attention and our understanding of their behavior is poorer than it is for the other materials, such as steels or other metals. Because of this, there are still various scientific

problems in our understanding of the rock behavior, especially in the conditions deep below the Earth's surface, such as those encountered when drilling for geothermal energy. Consequently, we are still trying to design and construct better drill tools and systems with an incomplete understanding of the drilling conditions and with a poor overall understanding of the drill tool–rock interactions. Therefore, *there is a strong scientific and practical need* to understand better the behavior of rock under these challenging conditions.

In recent years, some work has been done to develop thermally assisted drilling techniques, where the rock is weakened by a powerful thermal shock before the impact of the drill tool. Preliminary studies indicate that these methods can significantly increase the rate of penetration and reduce the wear of the drilling tools by weakening the rock while increasing its abrasiveness prior to the impact of the drill hammer. Currently, there are some patents for assisted drilling, but there are no commercial products available and the technologies are still very immature. The reason for this is that the true scientific and technological potential of these methods is still not well known because the effects of the thermal shock on the rock structure and its properties have not yet been properly investigated. With this in mind, the research questions of this thesis are the following:

1. What are the effects of heat shocks on the microstructural features and mechanical behavior of rock, and what are the effects of the testing condition on the rock's mechanical behavior?
2. How can one generate the desired cracks and crack patterns in the rock structure, and how can these crack patterns be characterized in an accurate, quantifiable, and efficient way?
3. Is there any correlation between the information obtained from the cracks and their patterns and the mechanical behavior of the rock?
4. How can sufficient, reliable, and reproducible data for numerical simulations and modeling purposes be generated?

To find answers to these questions, a broad literature survey and a considerable amount of experimental work involving thermal shocks must be conducted. The objective is to characterize the material before and after the thermal shocks using optical microscopy, electron microscopy, optical profilometry, and various mechanical tests. Chapter 3 explains the mechanical behavior of the rock and the affecting parameters, while Chapters 4 and 5 describe the fracture behavior of the rock on the macro and micro scales. Chapter 6 summarizes the experimental procedures. Chapter 7 contains the results and discussion of the data obtained by different testing methods, and Chapter 8 finally summarizes the findings of this research and presents the author's conclusions.

2. Rock as a material

Rock is the material that makes up the solid part of the ground beneath our feet. Rocks themselves comprise minerals, which are categorized as inorganic solids, and all the different rock types have a specific chemical composition [8]. Rocks are usually classified according to their mineral composition and by the conditions under which they were formed. Based on this categorization, rocks can be divided into three groups:

- **Igneous rocks** are formed from the solidification of molten material (magma). The most common magma is the result of a partial melting of the Earth's mantle. The magma moves towards the Earth's surface, as it is less dense than the surrounding mantle material. Once the magma reaches the surface of the earth, it is called lava. In most cases, lava reaches the surface due to a volcanic eruption. In addition to lava, volcanic eruptions can produce ash and other fragmentary rocks. There are two ways, in which rocks are formed from lava. In the first way, lava reaches the surface and due to the rapid cooling, fine-grained igneous rocks are formed. It is possible to observe some large crystals in the structure of these kind of rocks, but the matrix is always fine-grained. In some cases, the crystals do not have time to nucleate due to the rapid cooling rate, and rocks with a glassy (amorphous) structure are formed. In the second way, the magma may not reach the Earth's surface. When magma gets trapped beneath the surface, it cools down slowly, resulting in a completely crystalline igneous rock with coarse grains [8, 9].
- **Sedimentary rocks** are formed by the solidification of material deposited by wind, water, or chemical precipitation. These processes are called *weathering*. The rock fragments altered by weathering can form sediments. During weathering, minerals can break down to form clay minerals. Burying the clay of minerals leads to the consolidation and formation of compact rock. Sedimentary rocks can be produced also by the precipitation of minerals from water, such as rock salt.
- **Metamorphic rocks** are formed by the modification of pre-existing rocks under natural circumstances, such as heat or pressure [10]. If the rock, igneous or sedimentary, becomes subjected to heat, the rock may change its original mineralogy and structure to form a metamorphic rock. If the rock, in addition to heat, becomes subjected to deformation, regionally metamorphosed rock may be formed. This type of rock usually develops a new layered structure (foliation). The most well-known examples of metamorphic rocks are schists and gneisses.

3. Mechanical properties of rocks

The mechanical properties of rocks are highly dependent on the scale and degree of the details at which they are studied. However, each property has a different degree of importance in different situations. In general, rocks are made of aggregates of crystals and amorphous particles, which are attached to each other by cementing materials. In some rocks, such as limestone, the chemical composition of the crystals is almost homogenous, whereas the chemical composition of granites is highly heterogeneous [11]. The crystals are usually the smallest scale at which the mechanical properties are studied. The reason for this is that the crystal boundaries are the weak points in the rock structure, as they are the smallest discontinuities in the structure. In addition, the crystals themselves provide useful information about the deformation that the rock has been subjected to [11, 12].

The rock specimens used in the laboratory experiments are usually no more than a few centimeters in size. In most cases, these specimens contain enough particles to be considered homogeneous. Even though the crystals themselves are often anisotropic and the behavior of one crystal can be completely different from another crystal in the same specimen, it is accepted that the crystals and the grain boundaries between them interact in an adequately random manner. Therefore, the laboratory specimens provide average homogenous properties [11]. However, the laboratory samples are not necessarily isotropic. This is due to the processes, which affect the rock during its formation or alteration. These processes often align the crystals in the rock structure in a manner in which their interaction is random according to the size, composition, and distribution but not to their anisotropy. The strength of rock type materials is highly affected by the size of the sample, as the peak stresses decrease by the increase of the sample size [13, 14]. This phenomenon is related to the statistical effects caused by the random strength and defect distributions [11] and the energy allocation and dissipation around the cracks [15, 16]. Scale effects however, are stronger in very brittle materials, however, tending to decrease when going from brittle to semi-brittle materials and disappear in ductile (fully plastic) materials [17]. In rock materials, it is generally observed that the uniaxial compressive strength decreases with increasing the size of samples [13, 14]. The mechanical properties of granites do not depend only on the above-mentioned factors but also on many external factors such as the testing conditions, temperature, confining pressure, strain rate, etc.

3.1 Mineral composition

The mechanical properties of the rocks are defined by the strength, stiffness, and deformation capability of the components of the minerals and the cohesion and frictional resistance between them. The effects of the chemical composition on the mechanical properties of rocks have been investigated before. However, most of these studies are based on the amount of quartz [18, 19, 20]. The reason for this is that the chemical composition of rocks cannot be modified, as it can be for example for metallic materials. Rocks have a fixed chemical composition, which is set during their formation, and it is not possible to modify this chemical composition. The mineral's mechanical properties are also affected by other features, such as discontinuities, porosity, orientation, etc. However, one should note that each mineral has different mechanical properties compared to the other ones. For instance, the strength of quartz, which consists of SiO_2, is higher compared to potassium feldspar, which is composed

of $K_2O,Al_2O_3,6SiO_2$ [21]. Hogan et al. [22] reported that the amount of quartz has a strong impact on the fragmentation of rock. When the amount of quartz increases, the particles that are formed are larger, and therefore less fractured rock masses are produced for example during drop tower impact tests.

3.2 Texture

Unlike in metallic materials, the preferred orientation (texture) in rocks cannot be altered by thermal or chemical modifications of the rock's structure. In granites, the texture usually starts to develop when they are plastically deformed. The development of texture is the result of intercrystalline slip and mechanical twinning. However, these processes usually vary from one case to another. The texture is important especially when studying the geological history of the rocks. For example, pole figures showing orthorhombic symmetry can point to prior coaxial deformation, while monoclinic or triclinic pole figures imply a component of non-coaxial deformation. However, the actual deformation mechanism cannot be identified based on the symmetry of the pole figures [23]. In addition, texture does not only reveal the previous deformation of the granite but it also has effects on the future mechanical response of the rock. It is evident that loading the rock in the direction parallel to the textured orientation will result in a different mechanical response compared to the case when the rock is loaded in the direction perpendicular to the textured orientation [23].

3.3 Grain size

The effect of the rock grain size has been studied quite much over the years. Wong et al. [24] reported that the peak strength decreases with the inverse square root of the mean grain size. This observation is accordance with the previous studies conducted by Olsson [25] and Brace [26]. Tugrul and Zarif [27] showed that the size and shape of the grains have a strong impact on the mechanical properties of granites. Brace [26] has shown that the strength of the rock is greater for finer grains. Onodera and Asoka [28] reported the same observation also for igneous rocks and proposed a linear relationship between the rock strength and its grain size. In a similar work, Prikryl [29] proposed a more accurate relationship between the strength of the rock and its grain size, and reported that the average grain size seems to be the most important factor affecting the strength of the rock with very similar mineralogy. In the more recent work, Mardoukhi et al. [30] reported that the rocks with smaller grain size exhibit more brittle behavior compared to the rock with a bigger grain size. This is simply because of the fact that when the grain size gets smaller, there will be more grain boundaries. These boundaries act as barriers to crack propagation during the loading of the rock. Therefore, the strain prior to the fracture is limited and more brittle behavior is observed.

3.4 Structure and porosity

Prikryl [31] studied the effects of the rock structure on its geomechanical quality. Quantifiable rock fabric parameters, such as the area and perimeter of the grains, were obtained using image analysis. Using these parameters, Prikryl concluded that the texture coefficient [32] and the degree of interlocking and the grain size homogeneity [33] do not have any major correlation with the rock's measured mechanical properties. Haney and Shakoor [34] reported that the density of the rock has an effect on the rock strength and deformation properties. The

same hypothesis was presented by Goodman [30]. However, in the study conducted by Prikryl [31], this hypothesis was not completely confirmed.

The effect of porosity on the mechanical response of the rock has been studied by several researchers [36, 37]. Zhu et al. [38] obtained an analytical approximation for the uniaxial compressive strength, which indicates that the compressive strength scales with the square root of the pore radius. Baud et al. [39] concluded that for a rock with pore spaces, which are dominated by equant pores, the compressive strength is controlled only by the porosity and pore radius. They also stated that in limestones, tuffs, and sandstones the ultimate compressive strength decreases with increasing amount of porosity.

3.5 Temperature and heat treatments

The effects of temperature on the mechanical behavior of rock has been studied extensively. The main effect of temperature on the rock behavior is that increasing temperature leads to a decrease in the rock's strength [40, 41]. Dwivedi et al. [40] reported a 27% drop in the tensile strength of the studied rock when increasing the temperature from RT to 150˚C, while the corresponding decrease in the compressive strength was only about 11%. Liu and Xu [41] concluded that increasing the temperature not only reduces the rock's strength but also affects the strain rate sensitivity of the rock as well. Bauer and Johnson [42] showed that the thermal expansion of quartz and feldspar have an important role in the development of thermal cracks, which are the main reason for the weakening of the rock at higher temperatures. In addition, Roy and Singh [43] studied the effect of heat treatment and layer orientation on the tensile properties of granitic gneiss under confined stress using the Brazilian disc geometry. They also reported a decrease in the tensile strength of the rock when increasing the temperature of the heat treatment. Sengun [44] studied the influence of thermal damage on the physical and mechanical properties of carbonate rocks. He reported that up to 300°C no significant changes were observed in the properties of carbonate, but increasing the temperature from 300°C to 600°C caused the tensile strength of the rock to decrease from 28% to 75%. Mahanta et al. [45] studied the effect of heat treatment on the mode I fracture toughness of three different Indian rocks. The study was carried out at temperatures ranging from RT up to 600˚C. The results indicated that when increasing the temperature from RT to 100˚C, the fracture toughness of all studied rock types increased significantly. From that on, the fracture toughness decreased with increasing temperature up to 600˚C. Additionally, Verma et al. [46] reported that by increasing the temperature the amount of porosity increased by 2.3% in Ganurgrah shales. As mentioned before, the main reason for the change in the characteristics of rock during heating is the mineral's thermal expansion, which changes the amount of porosity and microfracturing, and alters the rock's mechanical behavior. However, there is a critical temperature zone for each rock, above which the decrease in the strength becomes more drastic [47, 48, 49]. An example of this temperature zone is 200-250˚C for sandstone [50].

3.6 Strain rate

The effect of strain rate on the mechanical behavior of rock has been studied extensively in tension [51, 52, 53], compression [54, 55], and bending [56, 57]. Cho et al. [51] reported that an increase in the strain rate leads to the generation of larger number of microcracks. In addition, the cracks are arrested from further propagation by the stress released from the

adjacent microcracks interfering with the formation of a fracture plane. This leads to an increased stress in the rock without the formation of fracture and results in a higher dynamic tensile strength. However, at lower strain rates the number of microcracks and the crack arresting effect caused by the stress release from adjacent microcracks are less compared to the high strain rates, and consequently the number of longer microcracks increases. In general, this means that increasing of the strain rate in the quasi-static region leads to the fracturing of the rock into smaller particles, as shown for example by Liang et al. [58]. In addition, microscopy studies indicate that the fracture mechanism changes from intergranular to transgranular when the strain rate increases. At low strain rates, axial splitting has been observed and reported as the main fracture mechanism, but with increasing strain rate the fracture mode changes slowly to shear fracture. Overall, previous research indicates a significant difference between the behavior of the rock material at low strain rates compared to the high strain rates [59, 60, 61, 62, 63]. As an example, the peak strength of the rock is highly dependent on the strain rate [64]. Brace and Jones [60] and Sano et al. [65] reported that the peak strength of the rock is proportional to $\frac{1}{n+1}\mathrm{Log}\,\dot{\varepsilon}$, where *n* is a constant, which describes the time dependency of the rock behavior. It has been reported that this relationship can be used in triaxial compression [66], shear, estimation of the loading-rate dependency of fracture toughness [67], stress dependency of creep life [69], and the relation between the crack growth rate and the stress intensity factor [64, 70].

3.7 Confining pressure

Especially the compressive strength of the rock is affected by the hydrostatic or confining pressure, the role of which is significant in some engineering applications such as percussive drilling. In the case of geothermal energy, very deep holes, up to 5 km, are needed, and at this depth the confining pressure can rise up to 100-200 MPa [63]. Kawakata et al. [71, 72] performed triaxial compression tests on Westerly granite under the confining pressure of up to 100 MPa. The tests were interrupted when the samples were reaching their peak stress, and the samples were unloaded and recovered before complete fracture. Based on the results gathered from the tests, the crack patterns formed without a confining pressure were more complex compared to the crack patterns formed under a confining pressure. In addition, Kawakata et al. [71, 72] reported that the shear cracks propagated inwards into the sample at a higher angle when the confining pressure was increased. Li et al. [73] reported that when the confining pressure increases, the strain rate sensitivity of the rock decreases. Hokka et al. [63] showed that at confining pressures below 20 MPa, the strength of the Kuru Grey granite increases faster at a higher strain rate. However, at confinements higher than this, the effect of confinement pressure is higher at the lower strain rate. The authors also concluded that the rate sensitivity increases even when a small confining pressure is applied. Additionally, the fracture behavior of the rock is highly dependent on the strain rate and confining pressure. At a high loading rate without the presence of confining pressure, pulverization of the sample is observed but by applying confining pressure, the fracture behavior changes to shear fracture.

4. Fracture behavior of rocks

There are two different approaches to characterize the brittle fracture of rocks. The first approach relies on empirical attempts to describe the fracture criteria. The second approach to describe the brittle fracture is based on constructing a physical model of the process that is adaptable to theoretical treatment, although also some empiricism can be included in the approach. The empirical approaches take into account the observed failure conditions, such as the testing conditions and the type of experiments. However, these approaches only provide a basis for calculating the failure conditions in specific situations and the more general states of the stress. Even though these theories may be presented in physical terms (strain energy or stress limit on certain planes), usually they include only little information about the physical mechanisms of failure [74]. The most well known of these failure criteria is the Mohr-Coulomb criterion [75]. This criterion is described in terms of stress, but it does not include nor depend on the intermediate principal stress σ_2, which has been shown to have an effect on the failure [76]. In addition to the stress state, also the strain state has been used to describe the failure criteria. For example, in the simplest version the failure occurs if the strain reaches the critical value of the maximum tensile strain [77].

The second approach tries to create an actual representation of the physical mechanisms of the fracture and provide a firmer basis for establishing the criteria of failure, rather than just using the general states of stress. These approaches are based on the optimized Griffith's theory of brittle fracture [78] in conjunction with different applications. Griffith originally proposed that the strength of brittle materials is controlled by the initial presence of small cracks. There is no argument over the fact that the brittle materials generally have crack-like flaws in their microstructure, and rocks are no different from the other brittle materials in this respect. Microcracks, in particular, are found both inside the grains and in and across the grain boundaries. Accordingly, as the Griffith's theory is physically applicable, a great amount of effort has been put into the development and derivation of macroscopic failure criteria in combined stresses conditions [79, 80, 81, 82].

The basis of the Griffith's theory in a biaxial state [84] indicates that the failure occurs when the weakest crack in a larger population of randomly oriented cracks begins to spread under the applied stress. The extension of the crack is assumed to occur when the level of the stress reaches the value at which it overcomes the interatomic cohesion of the material. To simplify the calculation of the stress distribution, Griffith assumed that the cracks are cylindrical and have a flattened elliptical cross-section, using the classical theory of linear elasticity to calculate the stress distribution around the crack. The Griffith's theory has been used to describe the failure criteria in different situations. Some of the most common conditions will be discussed in the following chapters.

4.1 Uniaxial Tension

Griffith [78] introduced an energy argument to discuss the crack propagation in order to calculate the brittle tensile strength. The principle of this approach is based on the surface energy as a function of local cohesive strength of the material. Therefore, the criteria for the failure of the material is based on the potential energy of the system when it tends to have a

minimum value. The crack will propagate if the result of this propagation leads to a situation where the sum of the following three terms is negative or zero:

- The surface energy of the newly created crack surface
- The change in the elastic energy of the rigid body
- The change in the potential energy of the system

Any other factor that changes the energy of the system is assumed to change the Gibbs potential. Thus, the Gibbs potential should be minimized as well. This assumption is usually referred to as the thermodynamic criterion of the failure [81, 85, 86]. In the case of applied uniaxial loading, the energy criterion predicts the failure at the stress level as:

$$\sigma = \sqrt{\beta \frac{E\gamma}{c}} \tag{1}$$

where E is the Young's modulus, γ is the specific surface energy, and 2c is the length of the crack. β is a numerical constant of the order of unity. However, the exact value of β depends on the assumption that is made during the calculation of the elastic stress distribution around the crack. In the case of plane strain, we can write:

$$\beta = \frac{2}{\pi(1-v^2)} \tag{2}$$

where v is the Poisson's ratio.

The value of β in the Griffith formula (Equation 1) is not very sensitive to the shape of the crack. In addition, the Griffith's energy approach to the derivation of Equation 1 does not consider the local stresses at the crack tip. Instead, Griffith stated that the maximum stress at the tip of the crack is approximately $2\sigma\sqrt{\frac{c}{r}}$, where r is the radius of curvature at the tip of the crack and σ is the applied macroscopic tensile stress normal to the crack [74]. This means that at some values of *r*, local stresses at a high level of magnitude (probably of an order corresponding to the interatomic force) are generated. Orowan [87] used an argument similar to the Griffith's energy argument but applied it only to the vicinity of the crack tip. This argument led to the relationship to calculate the interatomic cohesive strength, σ_T. According to the Orowan's relationship, σ_T is equal to $2\sqrt{\frac{E\gamma}{a}}$. In this relationship, *a* is the interatomic spacing. Also more complex attempts have been made to explain the local stresses at the tips of the cracks [88, 89, 90, 91, 92].

The importance of the surface energy term is worth discussing. The specific surface energy, γ, of a solid can be estimated based on the elastic constant of the solid [93], or on the specific energy of evaporation [89]. The estimated values for the specific surface energy of most materials are in the range of 0.1 to 1 Jm^{-2} [74]. In the simple cases such as local plastic deformation or multiple fracturing at the crack tip, especially in single crystals, the measured values of γ match well with the estimated values and therefore support the Griffith's theory [95, 96]. However, when the studied case is a polycrystalline material, the measured values of γ are much higher than the predicted ones, usually by an order of magnitude or even more. In the case of ceramic materials, values of γ in the order of 10 Jm^{-2} have been measured [97, 98]. These observed differences have shown that there are other important energy absorption processes associated with the propagating cracks. These processes include plastic

deformation at the vicinity of the crack [87], proliferation of microcracking (rapid spread of microcracking) and relaxation of internal stresses [99], and other processes such as acoustic [100] and thermal losses [101]. Therefore, when using Equation 1, γ should be considered only as a general energy absorption factor at the crack tip and its vicinity, since the value of γ is usually obtained empirically [74]. Finally, the Griffith's equation only considers a stationary crack. Therefore, in the case of a moving crack, the absorbed kinetic energy should be considered as well [102, 103]. Consideration of the kinetic energy term of absorption sets an upper limit to the crack propagation velocity [104]. In addition, according to Peterson and Wong [69], the stress field around the crack is modified as the velocity increases.

4.2 Uniaxial compression and biaxial stresses

Equation 1 describes the Griffith's energy argument for the tensile loading condition. In this argument, the assumption is that the crack will spread on its own plane. However, in more complex loading conditions it can no longer be assumed that the crack will spread on its own plane. [105, 106] . Additionally, if the crack has a negligible width, it tends to close under a compressive loading condition. Consequently, it is not possible to assume that the crack faces are not loaded and no elastic stress relaxation takes place.

Griffith [84] solved the first problem by changing the critical local tensile strength criterion of failure and the second problem by just considering open cracks. Although he argued about the value of the maximum stress at the crack tip in uniaxial tensile loading, he did not give any explanation for the change of the failure criterion in the general case. However, it is commonly accepted that the critical local tensile stress criterion is equivalent to the critical energy release rate [74].

In the case of biaxial loading with randomly distributed cracks of given length, the Griffith criterion includes the biaxial principal stresses σ_1, σ_2, and the magnitude of the uniaxial tensile strength T_0, *i.e.*:

$$(\sigma_1 - \sigma_2)^2 - 8T_0(\sigma_1 - \sigma_2) = 0 \qquad \text{if } \sigma_1 > -3\sigma_2 \tag{3}$$

$$\sigma_2 = T_0 \qquad \text{if } \sigma_1 < -3\sigma_2 \tag{4}$$

In the above equations, the compressive stress is considered positive. The expression $\sigma_1 > -3\sigma_2$ describes the situation with a predominantly compressive stress state. By describing Equations 3 and 4 in terms of shear stress and the normal compressive stress acting on the plane of the axis of an elliptical cavity, we obtain:

$$\tau^2 - 4T_0\sigma_n = 4T_0^2 \tag{5}$$

where τ is the shear stress and σ_n is the normal compressive stress. Equation 5 is then the Mohr envelope corresponding to failure [107]. This indicates that the uniaxial compressive strength is eight times higher than the uniaxial tensile strength. However, this ratio is even bigger for rocks [108].

4.3 Triaxial stresses

According to Orowan [87], the Griffith's theory can be used in the general state of stresses. The reason for this is that the normal or shear stresses on the plane perpendicular to the edge of the crack do not have considerable influence on the failure condition. Therefore, the Griffith criterion for the biaxial loading condition has been used for triaxial loading tests in the form of:

$$(\sigma_1 - \sigma_3)^2 - 8T_0(\sigma_1 + \sigma_3) = 0 \quad \text{if } \sigma_1 > -3\sigma_3 \tag{6}$$

$$\sigma_3 = -T_0 \tag{7}$$

where σ_1 and σ_3 are the biggest and smallest principal stresses and T_0 is the uniaxial tensile strength.

Murrell [109, 110] introduced the dependence of the tensile strength on σ_2 to generalize the biaxial criterion for the triaxial loading condition:

$$(\sigma_2 - \sigma_3)^2 + (\sigma_3 - \sigma_1)^2 + (\sigma_1 - \sigma_2)^2 - 24T_0(\sigma_1 + \sigma_2 + \sigma_3) = 0 \tag{8}$$

To complete the solution for the triaxial loading condition, Murrell and Digby [111, 112] concluded a general triaxial failure criterion in a predominantly compressive condition:

$$(\sigma_1 - \sigma_3)^2 - \alpha T_0(\sigma_1 + \sigma_3) = \beta T_0^2 \tag{9}$$

where α and β are constants that include the Poisson's ratio and the axial ratio of the ellipsoid.

4.4 Mohr-Coulomb failure criterion

Even though the Griffith's failure criterion explains the rock fracture behavior quite well, the Coulomb failure criterion is the simplest and most widely used failure criterion [11]. Based on the work of Coulomb [113] , failure in the rock occurs along the planes due to the shear stress (τ) acting on the plane. The movement is assumed to be restricted by a friction force with the magnitude of the normal stress (σ) acting along the plane multiplied by a constant factor μ. In the absence of a normal stress, a finite shear stress (S_0) is needed to initiate the failure, and therefore:

$$|\tau| = S_0 + \mu\sigma \tag{10}$$

According to Equation 10, failure will take place in any plane where $|\tau| < S_0 + \mu\sigma$. The parameter μ is known as the coefficient of internal friction and S_0 represents cohesion. The representation of Equation 10 in the Mohr's diagram is a straight line at an angle Φ with the σ-axis (see Figure 1). An alternative expression for Equation 10 can be obtained by constructing the Mohr circle tangent to this line. In terms of principal stresses, the alternative Equation is:

$$(\sigma_I - \sigma_{III}) = (\sigma_I + \sigma_{III})\mathrm{Sin}\Phi + 2S_0 Cos\Phi \tag{11}$$

One form of the Mohr's failure criterion is:

$$\tau_m = F(\sigma_m) \tag{12}$$

where

$$\tau_m = {}^{(\sigma_I - \sigma_{III})}/_{2} \tag{13}$$

and

$$\sigma_m = {}^{(\sigma_I + \sigma_{III})}/_{2} \tag{14}$$

Considering Equation 14, the Mohr envelope can be constructed on the σ-τ plane. A circle with a diameter of (σ_I-σ_{III}) is tangent to the failure envelope. Therefore, by considering Equation 13, the Coulomb's criterion is equivalent to the assumption of a linear Mohr envelope.

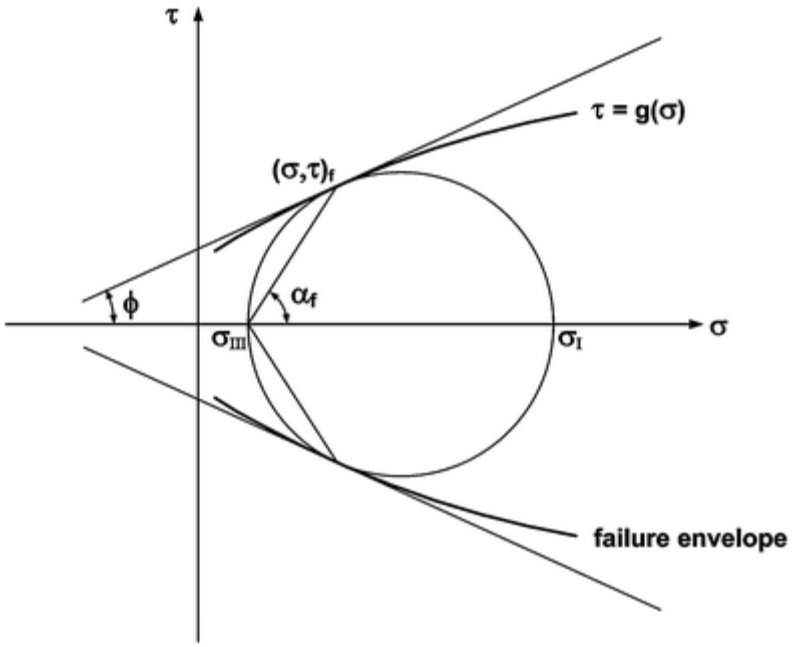

Figure 1 Mohr diagram and failure envelopes [109].

An important point in the Coulomb's and Mohr's criteria is the effect of σ_m, which is the mean stress on the σ_I and σ_{III} plane. The importance of σ_m becomes more significant in materials such as rocks, as τ_m at failure increases by the increase of σ_m. Additionally, the Mohr's criterion considers the curved shape of the failure envelope, and this non-linear behavior is observed in many rock types [11, 115].

4.5 Hoek-Brown failure criterion

Hoek and Brown [13, 116] designed their failure criterion to provide input data for underground excavation. This criterion is empirically derived to describe the non-linear increase of the peak

strength of isotropic rocks with increasing confining pressure [117]. The original non-linear Hoek-Brown criterion for intact rock is:

$$\sigma_I = \sigma_{III} + \sqrt{mC_0\sigma_{III} + sC_0^2} \quad (15)$$

where σ_I and σ_{III} are the principal stresses at failure, C_0 is the uniaxial compressive strength of the intact rock, and *m* and *s* are dimensionless empirical constants. The criterion is linear on the biaxial plane. As it is evident, the Hoek-Brown criterion does not include σ_{II} except for the condition of a conventional triaxial compression test.

The Hoek-Brown criterion has been updated several times over the years [118, 119, 120, 121]. These updates include adjustments to improve the estimation of the rock strength. However, one important update was the generalized form of the criterion [120]:

$$\sigma_I' = \sigma_{III}' + C_0(m_b \frac{\sigma_{III}'}{C_0} + s)^a \quad (16)$$

where the term m_b was introduced for the fractured rock. The dependency of the parameter m (in the original form of the equation) on mineralogy, composition, and grain size was shown in ref. [119]. The exponential term *a* describes the system's bias towards hard rock and is used to take better into account the poorer quality rock masses, especially under very low normal stresses [119].

5. Deformation microstructures and mechanisms

Deformation microstructures are the microscopic features created during deformation. Deformation mechanisms, in turn, refer to the processes that accommodate the deformation on a larger scale. This section deals with the microstructures and mechanisms commonly found in rock materials.

Generally, microcracks are classified into three different categories; intergranular (within a grain), transgranular (across two or more grains), and circumgranular or grain boundary cracks. Depending on the deformation mechanism(s) and the microstructure of the rock, different kinds of microcracks may be visible in the rock structure [123]. Intergranular microcracks are often seen in porous and poorly cemented rocks. On the other hand, transgranular cracks are more often found in the structure of well-cemented and low porosity rocks.

Several microcrack mechanisms can be identified in the rocks. This identification is commonly based on experiments, where axial microcracks form from about half of the peak strength until post failure [124]. Compared to the fundamentals of cracking physics, these mechanisms are regarded as secondary mechanisms [125, 126]. Several of these mechanisms will be discussed in the following.

Flaw-induced microcracks are associated with the existing flaws in the structure, such as other microcracks, pores, and grain boundaries. The reason for the appearance of these microcracks is due to the stress field developed on the flaw surface when an external stress is applied. These microcracks propagate along curved trajectories from both ends of the flaw and produce a wing-crack geometry [127, 128, 129]. Usually the flaw-induced microcracks are transgranular or circumgranular [123]. Examples of flaw-induced microcracks are shown in Figure 2.

Cleavage microcracking is an important mechanism for the fracture of minerals that have a basal plane. For instance, microcracking in biotite is controlled by the (001) basal plane cleavage [130]. Cleavage microcracking of feldspars has a great importance in the deformation of granitic rocks. Cleavage microcracking is easily recognizable as it happens in crystallographically controlled sets parallel to a known cleavage plane in a single grain [123].

When minerals with different elastic moduli come into contact within the rock structure, elastic mismatch microcracks start to appear. Examples of this kind of microcracks can be observed when feldspar or mica comes into contact with quartz [130, 124]. These microcracks can be recognized from the localization of intergranular microcracks around the contact area of two grains with a different mineralogy. However, distinguishing elastic mismatch microcracks from thermally induced microcracks can be challenging, as will be discussed later on.

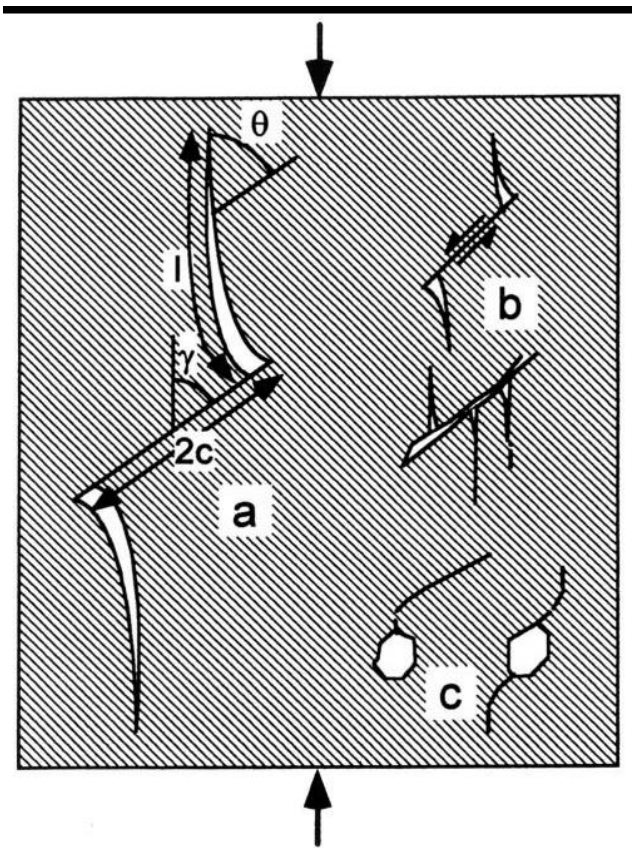

Figure 2 Flaw induced microcracks a) the geometry of analytical solution for the propagation of flaw induced microcracks b) two examples of flaw induced microcracks c) two examples of microcrack/pore interaction [123].

Plastic mismatch microcracks (Figure 3) are observed when there is a strain incompatibility between the plastically deformed area and the neighboring undeformed area [130, 131]. An example of this case is when feldspar is surrounded by deformed quartz grains [132]. Plastic mismatch microcracks can also be observed within a single grain or phase due to the stress concentration caused by intercrystalline plasticity, as will be discussed later on.

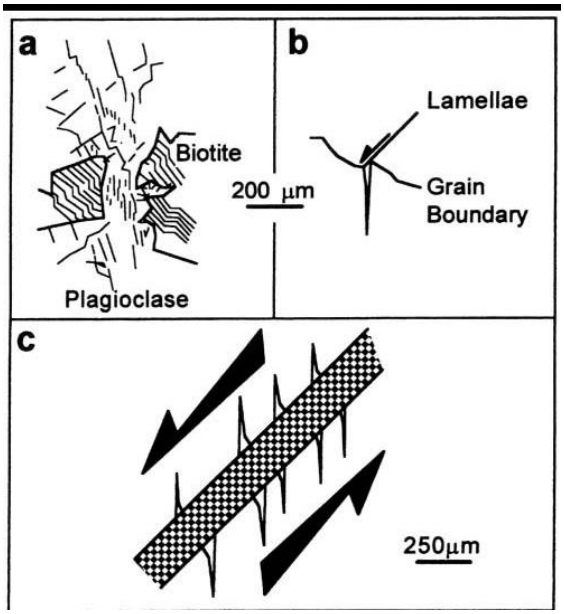

Figure 3 Plastic mismatch microcracks a) Intense microcracking in plagioclase developed between kinked biotite grains b) a microcrack developed at the end of a lamella displaces a grain boundary, and c) microfault-induced microcracks [123].

Microcracking is one of the mechanisms to relieve the stress caused by the differences in thermal expansion, i.e., the contraction coefficient of two adjacent minerals. Thermally induced microcracks start to form within a grain of a mineral surrounded by another mineral during heating or cooling. In the presence of a pressure change, the elastic microcracks can form as well during heating or cooling. These two different types of microcracks can be distinguished from one another if the pressure-temperature path is known [133]. Considering granite as a composite material consisting of feldspar and quartz, in the case of cooling, microcracks can appear in the quartz structure because of its greater thermal contraction. Thermally induced microcracks can be recognized by intergranular microcracks concentrated in quartz surrounded by feldspar [123].

The strain caused by a solid-state phase transformation can also lead to the appearance of microcracks in the rock structure. For instance, the transformation from coesite to quartz involves a volume increase by 11%. This expansion leads to the formation of a microstructure where quartz inclusions are surrounded by radial extension microcracks [134, 135]. A distinctive feature of the phase transformation induced microcracks is the existence of intergranular microcracks alongside the evidence of phase transformation. In the case of the transformation of coesite to quartz, radial microcracks around the inclusion of quartz can be visible in the coesite surroundings [123].

6 Materials and methods

Samples for the mechanical testing were prepared from two different granites: Balmoral Red and Kuru Grey. A detailed description of the tested materials is given in section 6.1. Brazilian disc samples were used for the quasi-static and dynamic testing. The samples of Balmoral Red were cut from the rock plate with the thickness of 21 mm. The diameter of the samples was 40.5 mm. Kuru Grey samples were core drilled with the diameter of 41 mm and thickness of 16 mm. Figure 4 shows the samples used in this study.

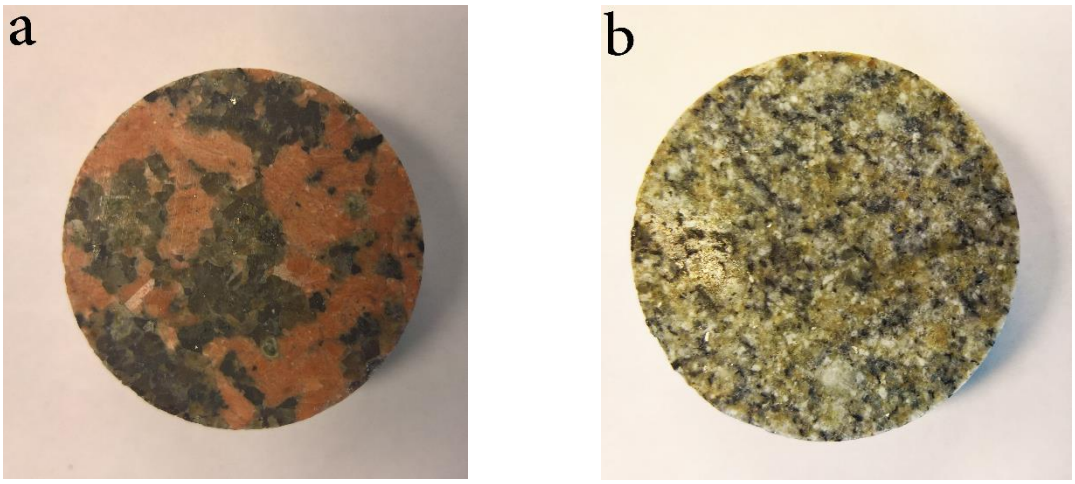

Figure 4 Brazilian disc samples of a) Balmoral Red and b) Kuru Grey

The BD test is not the only method to measure the tensile strength of the rock. The other methods are the dynamic direct tension method, semi-circular bending (SCB) method, and the spalling method. However, because of the following reasons, the BD method was chosen for this study. Normally, the direct tensile test is the best option to measure the tensile strength of a material, as the stress state in the test is (more or less) one-dimensional. However, when considering the requirement of sample alignment and the difficulty of machining rock samples of complex shapes (such as a dog bone), the direct tensile test is not a viable alternative for testing this type of materials [136]. The SCB method appears to be simpler than the direct tension method, although the result obtained from the SCB test defines the flexural strength of the rock, which is different from the tensile strength obtained from the BD method [137]. The spalling method has its own limitations as well; first, achieving a one-dimensional stress state is difficult, second, the compressive wave can influence the sample before the tensile wave arrives, and third, the stress wave is attenuated in the rocks [136]. It is also worth mentioning that applying a heat shock on a sample with a complex geometry is not an easy task to perform. The samples can become damaged and there is always the possibility of the formation of asymmetric crack patterns. The BD test was originally designed to overcome the known difficulties of the other methods, especially the problems of the direct tension method. Therefore, the BD test seemed to be the most convenient method to choose for the purpose of this study. Nonetheless, the BD method has its own limitations as well. For instance, in order to perform a valid BD test, the sample has to break first along the loading direction close to the center of the disc [138, 139]. Additionally, the tensile strength is not measured directly but calculated from the axial loading with the assumption of sample remaining elastic and not experiencing any plastic deformation. It should also be mentioned that the stress state in the

BD test is two-dimensional. Carneiro and Barcellos [140] used the Hertz analysis [141] to calculate the principal tensile stress along the vertical diameter as

$$\sigma_y = \frac{P}{\pi R_1 L} \quad (17)$$

where P is the concentrated compressive forces, R_1 is the radius of the Brazilian disc, and L is the length of the disc. According to the analytical model, the principal tensile stresses (σ_y) are uniformly distributed along the vertical diameter [142].

6.1 Tested materials

The materials used in this study were two slightly different types of granite, Balmoral Red and Kuru Grey. The microstructure of neither of the rocks shows significant texture, and the minerals are distributed homogenously in the structure. Therefore, the mechanical properties of the sample materials are considered essentially isotropic. The only significant physical difference between these two granites is that Kuru Grey has a smaller grain size compared to Balmoral Red. Additionally, the mean values of open porosity were 0.38% for Balmoral Red and 0.44% for Kuru Grey. The quasi-static compression strength of the rocks is 180 MPa and 220 MPa for Balmoral Red and Kuru Grey, respectively. The corresponding values in the tensile loading condition were 8 ±2 MPa for Balmoral Red and 11 ± 2 for Kuru Grey. Tables 1 and 2 show the chemical compositions of the studied rocks.

Table 1 Mineral composition of Balmoral Red granite [143]

Mineral	Wt.%
Potash feldspar	40
Quartz	33
Plagioclase	19
Biotite & Hornblende	8

Table 2 Mineral composition of Kuru Grey granite [144]

Mineral	Wt.%
Quartz	35
Albite	31
Microcline maxi	28
Biotite	3
Diopside	2
Chlorite IIb	1

6.2 Thermal shock procedure

Two different types of thermal shocks were applied on the BD samples: one using the acetylene-oxygen flame torch and one using a plasma gun. The flame torch was used for the samples of both quasi-static and dynamic tests, while the plasma gun was used only for the samples used in the dynamic Brazilian disc and indentation tests.

The samples to be thermally shocked by the flame torch were place at the fixed distance of 6 cm from the tip of the torch. Three different heat shocks were applied on the samples according to the duration of the heat shock. The durations of the heat shocks were 10, 30, and 60 seconds.

In the case of the heat shock done by the plasma gun, the gun was moved over the surface of the BD samples at the speeds of 50, 75, or 100 mm/s. These movements provided the durations of 0.80, 0.55, and 0.40 seconds for the heat shocks. The power of the gun was set at 50kW, and the distance of the samples from the tip of the gun was 6.5 cm.

In the dynamic indentation tests, the same characteristics of the plasma gun were used. However, the difference in the dimensions of the samples (30 cm × 30 cm × 30 cm) led to the heat shock durations of 6, 4, and 3 seconds.

After the heat shocks, the samples were let to cool down to room temperature in air. As both rocks are mostly composed of quartz, feldspar and plagioclase, it is highly unlikely that the heat shocks alter the nature of the rocks. The reason for this is that the temperature required for quartz to go through a phase transformation is about 600˚C, and for feldspar this temperature is about 1000˚C [145, 146]. However, one should note that even though the rocks do not go through a phase transformation during the heat shocks, some mechanical damage such as thermally induced cracking and grain refinement will or might occur during the thermal shocks.

6.3 Liquid penetrant non-destructive testing

The liquid penetrant technique and optical microscopy were used to analyze the patterns of the surface cracks before applying the heat shock. After the heat shock, the liquid penetrant (BYCOTEST PB50) was re-applied on the samples to observe the changes in the surface crack patterns caused by the thermal shock. The images were obtained with a LEICA CLS 150 XE stereomicroscope. The source of natural light in the microscope was replaced by an ultraviolet (UV) light source to take the images under UV light.

6.4 Scanning electron microscopy

The Brazilian disc samples before applying the heat shocks were studied using Philips XL30 scanning electron microscope (SEM). The samples were cleaned using an ultrasonic cleaner. Before the SEM examination, the samples were coated with gold to ensure their electrical conductivity. The same principle was applied on the samples after applying the heat shock, and the changes in the microstructure caused by the heat shock were studied and analyzed.

6.5 Fractal dimension analysis

The concept of fractal dimension arises from the need to describe the geometry of different objects in the nature in a simple manner. For instance, clouds are not spheres, mountains are not cones, and coastlines are not circles. The important feature shared between these examples is the fact that these objects have a repetitive shape; when zoomed in or out, these objects look self-similar for example for a cloud, if one concentrates on a portion of it, that portion possesses essentially the same shape as a bigger zoomed out cloud. The concept of fractal dimensions was first introduced by Hausdorff in 1918 [147]. In the period between 1875 and 1925, the mathematicians realized that it is not possible to assign a dimension as a number of coordinates to some irregularities and fragments. Euclidian objects are limited to sets for which all the useful dimensions coincide. However, the dimensions of sets that are needed to describe the shape of irregularities and fragments (fractals) fail to coincide [148]. Fractals are mathematically defined as sets of spatial co-ordinations on a plane or volume, which once drawn, are repetitive and self-similar at every scale. That means if one looks at a small fragment of the whole object, he or she recovers the same shape as if the object was observed as a whole. Among the famous fractal sets, the Cantor set and the Sierpinski gasket are the standard representatives of such sets. The Cantor set is constructed "iteratively" by removing one third of given line and repeating this process infinitely (Figure 5). By this procedure, one observes that at each iteration, every remaining segments of the line is one third (S) of the previous line, and the number of segments remained after the removal is 2 (M). Defining the fractal dimension as D = -log M/log S, one finds the fractal dimension for the Cantor set to be log2/log3 = 0.631.

Figure 5 Example of the Cantor set [147].

For the Sierpinski gasket, by considering an equilateral triangle (Figure 6), and connecting the midpoints of each edge of the triangle and removing the new central equilateral triangle, one observes that the mass scales by the factor of 3, and the length of each edge by the factor of 1/2 thus, the fractal dimension for the Sierpinski gasket will be log3/log2 = 1.585. These are examples of "iterative fractals", which are deterministic in the sense that the procedures to produce such sets are definite.

Figure 6 Example of the Sierpinski gasket [147].

Nevertheless, most of the fractals in the nature are randomly formed, thus belonging to the class of “random fractals”. Clouds are members of such class. Alternatively, the trace of a particle performing a Brownian motion is another example (Figure 7).

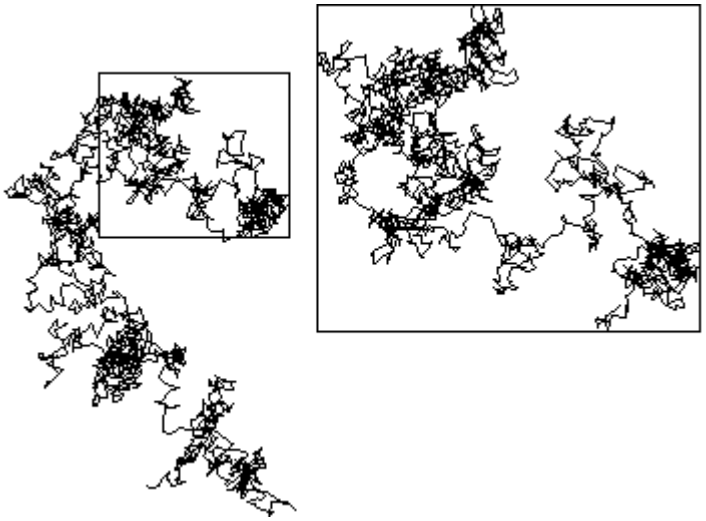

Figure 7 Example of Brownian motion [147].

As the pattern of the surface cracks cannot be fit in the normal dimension sets, the concept of fractal dimension was used to characterize the surface cracks and their patterns. The fractal dimension of the surface crack patterns was calculated from the images obtained with a stereo microscope using a box counting method in Matlab. The box counting method is a common tool to estimate the fractal dimension of an object with a complicated structure.

The box counting method is used when the fractal dimension of an object cannot be achieved by numerical or analytical methods. Good examples of such cases are the cloud patterns or ocean waves, and in this particular case, the crack patterns on the surface of a rock specimens. The accuracy of the box counting method is highly restricted by the image resolution, as the pixels are the grids used in this method. Therefore, background noise or blurred pixels can alter the accuracy of the method. A detailed description of the box counting method with a discussion of its possibilities and limitations can be found in ref. [149].

The images taken from the surface of the samples under UV light were imported as RGB images to Matlab. In these images, the color of each pixel is represented by three numbers, i.e., Red, Green, and Blue. The threshold is set on color “Red” as it is the dominant color in liquid penetrant images. A pixel that has the “Red” color higher than the threshold is regarded a crack pixel, and therefore it is represented by the digit “1” instead of “0” for the rest of the image. The leads to the formation of a binary matrix, which constitutes a map of the identified cracks. The resolution of the image and the threshold value affect strongly the value of the obtained fractal dimension. The resolution of the image defines also the spatial resolution of the crack detection method. The background noise is another important factor since it contributes to the RGB combination of the pixels. Therefore, once the matrix is created, the crack pattern has to be checked by naked eye to decide whether it represents surface cracks in the original image or not.

6.6 X-ray tomography

Tomography refers to the cross-sectional imaging of an object using either transmitted or reflected data obtained by illuminating the specimen with a suitable form of electromagnetic radiation [150]. The basic principle of tomography is based on the use of x-ray radiation in the creation of images. By using X-rays, it is possible to form images of phases based on their different attenuation coefficients. The resolution of the computed tomographic images depends on the number of parallel beam projections and the number of data points in each projection. In both conventional 3D computed tomography (CT) and micro-computed tomography, hundreds of 2D projection radiographs of the sample are taken at different angles. Each radiograph contains information about the absorption density distribution of the sample along the X-ray beam onto the plane perpendicular to the direction of the X-ray beam propagation. By imaging the sample at different angles, information about the whole volume of the sample structure is obtained by using a proper computer algorithm [151]. In this work, the tomography samples were core drilled from the original BD samples with diameters of 7 mm and 15 mm. The CT scans were carried out using a Nikon/XTec XT H225 ST device.

6.7 Dynamic testing

The high strain rate tests were carried out using a compression Split Hopkinson Pressure Bar (SHPB) device. The flat-ended pressure bars were made of AISI 4340 steel with a diameter of 22 mm and the length of 1200 mm. The striker bar with a length of 300 mm was made of the same material. The bars are resting on bearings mounted on adjustable stanchions, which makes the accurate alignment of the bars in the z- and y-directions possible. The striker bar is impacted on the incident bar end using an air gun, and three optical IR sender-receiver pairs are used to measure the impact velocity of the striker. These sensors also provide the trigger signal for the oscilloscope. There are two active strain gages attached to the center of the incident and transmitted bars. The strain gages signal are amplified by a Kyowa CDV 700A series signal conditioner and recorded on a 12-bit 10MSample Yokogawa digital oscilloscope. All functions of this device, including loading of the striker, pressurizing, shooting of the striker bar, and reading of the data from the oscilloscope are controlled by a computer. More details of the instrument are given in ref. [152]. A numerical dispersion correction method adopted from the work of Gorham and Wu [153] is used to correct for any changes in the signals due to the dispersion of the waves as they travel in the pressure bars. A disc of soft and deformable copper with a thickness of 0.5 mm was used between the striker and the incident bar to increase the rise time of the incident stress pulse and to improve the dynamic equilibrium in the specimen. Use of the pulse shaper is of great importance in the BD tests, as the stress state in the disc sample is two-dimensional and the force balance at the bar/sample boundaries does not necessarily ensure the dynamic equilibrium in the whole volume of the sample. For example Dai et al. [154] have shown that the dynamic force balance can be achieved by using the pulse shaper. Figure 8 shows a schematic picture of the high strain rate testing setup used in this study.

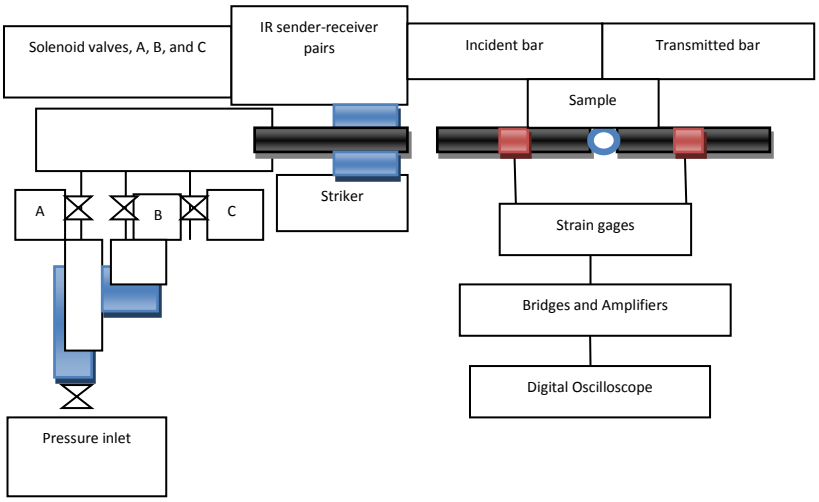

Figure 8 Schematic picture of the Split Hopkinson Pressure Bar device at Tampere University of Technology.

6.8 Digital image correlation

Digital image correlation (DIC) is a non-contacting method, which takes images of an object, stores the images in a digital form, and performs analysis to obtain full-field shape, deformation, and/or motion of the object [155]. DIC works by comparing digital photographs taken from the specimen or component at different stages of deformation. The system can measure the surface displacements and create full-field 2D and 3D deformation vector fields and strain maps. This is done by tracking blocks of pixels. However, there are limitations for DIC to work accurately. For instance, the blocks of pixels should be random and unique. In addition, the blocks should have an adequate range of contrast and intensity levels. The DIC system usually does not need any special lighting condition, and in many cases the natural surface of the specimen provides enough texture for the system to work. The sources of images for DIC can be conventional CCD or consumer digital cameras, high-speed videos, or microscopes, including electron and atomic force microscopes. Additionally, the correlation process is not restricted to optical images but can also be applied on datasheets such as surface roughness maps and 2D surfaces of structures [156].

The basic principle of DIC is based on the displacement of the pixels from one image to another. In 2D DIC, the displacement is directly detected from the digital images of the surface of the specimen. Usually the deformation on the surface of the specimen is recorded and stored as digital images (one before and one after the deformation). Later on, these images are compared to quantify the displacement by searching for match points between the images. As it is almost impossible to determine the deformation by comparing one pixel to another, a block of pixels is used to carry out the matching process. This area of the pixels is called a subset. An assumption is made when comparing the subset before and after deformation is that the gray level intensity of a physical point in the reference image does not change in the deformed image [157]. Once the location of the deformed subset is found in the second image, the displacement of this subset can be determined. To determine the deformation of the

subset, the surface has to have some features that allows the matching process. If the surface does not have any features of its own, an artificial random pattern must be applied on the surface of the specimen. Figure 9 shows how the matching process is carried out for a subset [158].

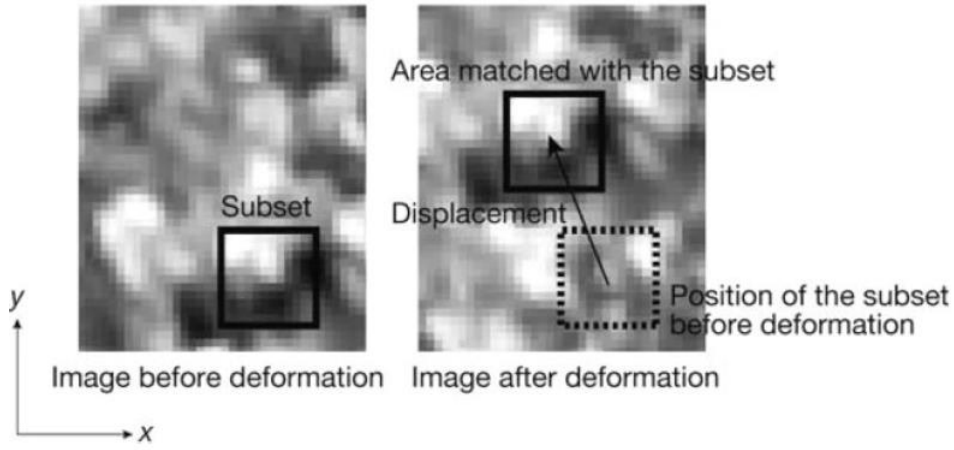

Figure 9 Matching of the subset before and after deformation [158]

In this work, two Photron SA-X2 high speed cameras were used to record images for DIC, and to study the fracture of the samples during the high strain rate tests. As the rock surface itself does not have a very strong contrast for the correlation algorithms, the surfaces of the samples were first painted with a white base coat, after which black speckles were applied on the surface using a permanent marker, as shown in Figure 10. For the samples heat shocked with the flame torch, images of 256 *176 pixels in size were recorded at 160 kfps. For the samples heat shocked with the plasma gun, the images were recorded at 25 kfps with the size of 1024*812 pixels. Two Decocool lights were used for illuminating the samples. The recorded images were analyzed with LaVision StrainMaster (DaVis) 3D-DIC software using a subset size of 25 pixels and a step size of 9 pixels.

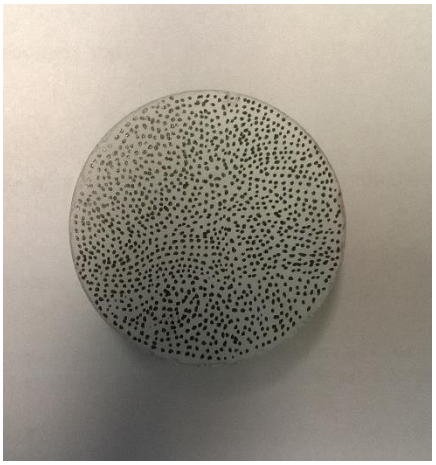

Figure 10 Brazilian disc sample with a speckle pattern for DIC.

6.9 Dynamic indentation tests

The indentation test used is a simplified version of the percussive drilling act carried out in the laboratory scale. The indentation tests were carried out using single-button and triple-button indenters with the hemispherical geometry shown in Figure 11. The experimental setup was basically a Split Hopkinson Pressure Bar (SHPB) without the transmitted bar. The drill buttons were embedded in the impact end of the incident bar. The experimental setup is shown in Figure 12. The reader is referred to refs. [30, 149, 156] for more technical details and examples of tests carried out at different speeds and other testing parameters.

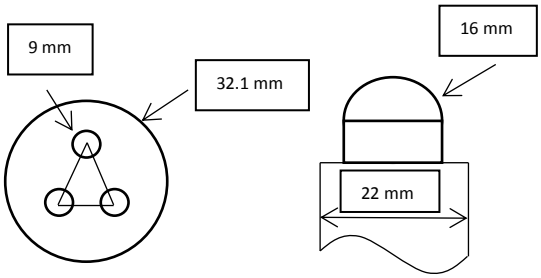

*Figure **11** Triple-button and single-button indenters used in the dynamic indentation tests.*

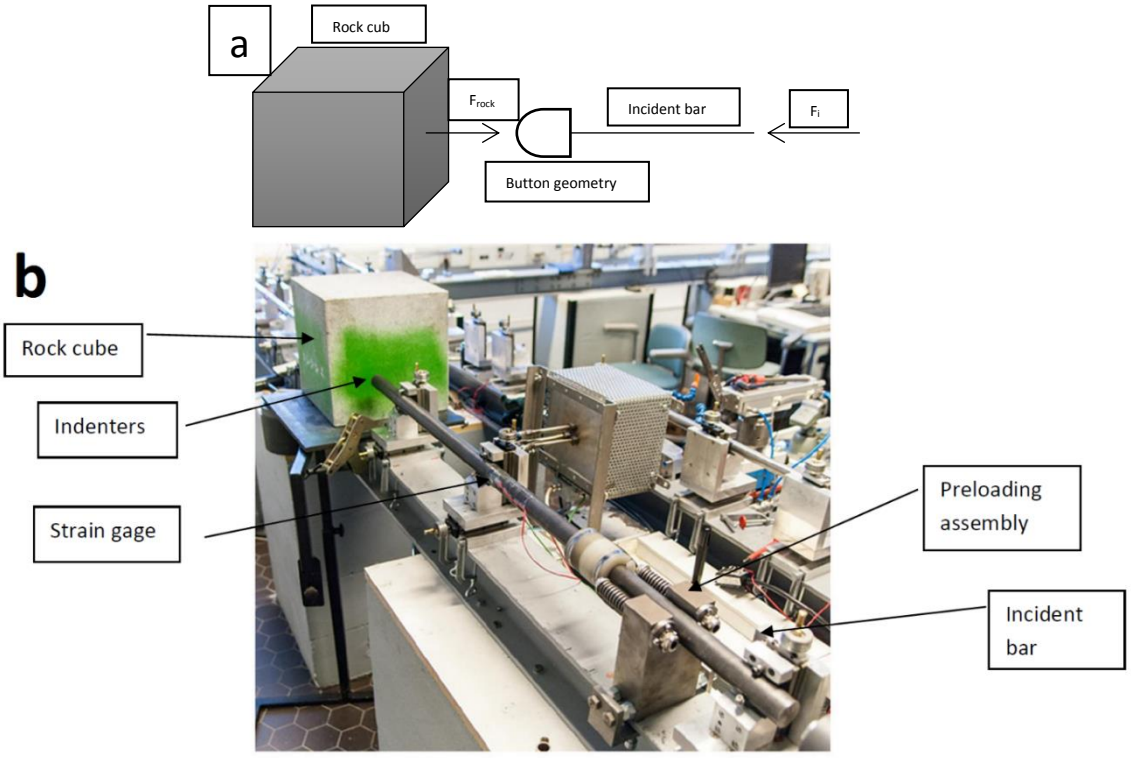

Figure 12 a) Schematic picture of the dynamic indentation test and b) the experimental setup.

The setup includes an air gun, a striker bar with the length of 20 cm, and an incident bar with the length of 120 cm and a diameter of 22mm made of AISI 4340 steel for the single-button tests. In the triple-button tests, the incident bar had a diameter of 32.5 mm. The stress pulses were measured using two strain gages bonded on the surface of the incident bar at the center of the bar. The force on the bar-rock interface was calculated using the following Equation:

$$F = A_b E_b(\varepsilon_i + \varepsilon_r) \tag{20}$$

where A_b is the cross sectional area of the drill rod (incident bar), E_b is the bar material's Young's modulus, and ε_i and ε_r are the measured and dispersion corrected incident and reflected strain pulses. To secure a sufficient initial contact between the buttons and the rock cube, a feed force of negligible magnitude compared to the rock fracture load was applied to the incident bar by two springs. In addition, the quality of the contact was checked before every test by using a white sheet of paper and a carbon copy paper between the rock and the indenters. The diameter of the marks on the paper caused by the feed pressure was measured and compared to the diameter of the buttons.

The single-button tests were conducted at the impact speed of 19 m/s. To generate the same stress also in the triple-button tests, the impact speed has to be higher due to the larger diameter of the incident bar. This speed can be calculated using the following equation:

$$\sigma_{striker} = \sigma_{bar} = \frac{\rho C V_s}{2} \tag{21}$$

where ρ is the density of the bar material, C is the speed of the stress wave inside the bar material, and V_s is the speed of the impact. According to Equation 21, the impact speed for the triple-button test should be 41 m/s. Unfortunately, due to the limitation of the device, this speed could not be reached. Instead, the triple-button tests were carried out at the impact speed of 35 m/s.

It should be noted that unlike with the single-button bit, equal contact between three buttons and the rock surface cannot be fully guaranteed during the interaction. This is partly due to the rock heterogeneity, which can affect the distribution of the contacting forces. Additionally, during the impact, bending stresses may be introduced in the incident bar, which can lead to a non-uniaxial stress condition in the drill bit and the buttons. In such a case, Equation 20 might not be fully valid for calculating the force acting on the sample. Considering all possible errors, however, careful alignment of the incident bar largely minimize such errors and the data obtained from the experiments can be expected to be representative for the bit-rock interactions.

6.10 Optical profilometry

Optical profilometry was used to study the formation of craters on the sample surface during the dynamic indentation tests. To prepare samples for profilometry, the craters were replicated using a commercial NDT quality resin. The replicas were then analyzed using Alicona Infinite Focus G5 optical profilometer. The 3D images obtained from the profilometry were processed using the IF-MeasureSuite software.

7. Results and discussion

The results obtained from the tests and investigations described in Chapter 6 are presented and discussed in the following sub-chapters. Each sub-chapter contains the main results and observations obtained with the different techniques in a concise form, and more detailed data and discussions can be found in the attached articles published in various journals and proceedings.

7.1 Fractal dimension measurement analysis

The fractal dimension analysis was carried out based on the optical images obtained from the sample surfaces after applying the liquid penetrant. The fractal dimensions were obtained from the center of the samples' surface as the maximum tensile stress during BD tests is limited to the area in the middle of the sample. The analysis was carried out on as-received (intact) and flame torch shocked BD samples of both Balmoral Red and Kuru Grey, and on intact and plasma shocked BD samples of Kuru Grey. Figure 13 shows the results for the Balmoral Red and Kuru Grey in the intact and flame torch heat-shocked conditions. The surface crack patterns of Balmoral Red before applying the heat shock consist of small cracks, which are mainly located at the grain boundaries. However, after applying the heat shock, new cracks are introduced to the surface and the existing cracks have grown in length, leading to a more complex network of surface cracks. On the other hand, the surface pattern of intact Kuru Grey (Figure 14) contains pores in addition to the surface cracks, which can be located at the grain boundaries. After the heat shock, both the number of the surface cracks and the pores increases. This difference in the reaction to the heat shock between Balmoral Red and Kuru Grey is important in view of their mechanical response, as it will be discussed later on in Chapter 7.6.1.

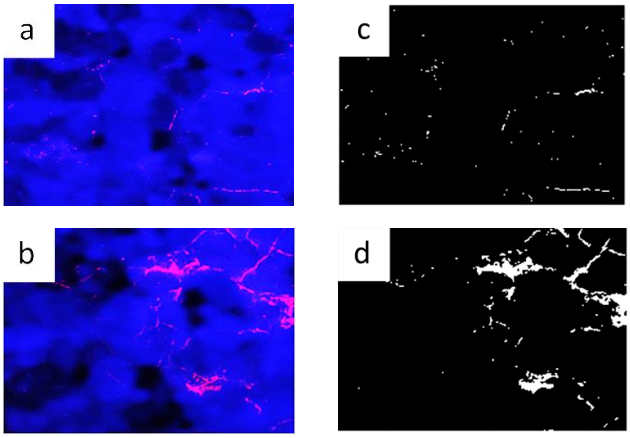

Figure 13 Optical images a) before and b) after a 30 s flame torch thermal shock, and the identified cracks c) before and d) after the thermal shock for the Balmoral Red.

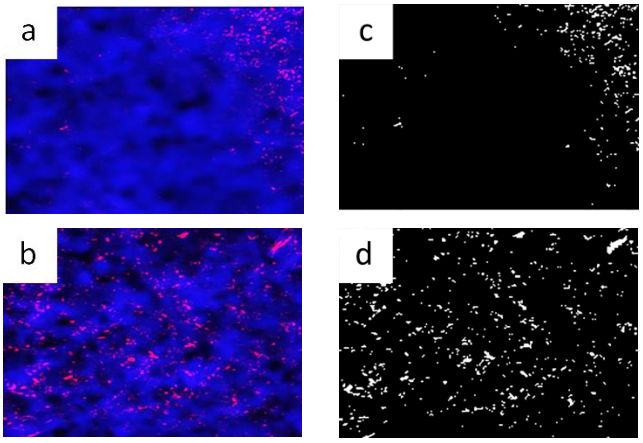

Figure 14 Optical images a) before and b) after a 30 s flame torch thermal shock and the identified cracks c) before and d) after the thermal shock for the Kuru Grey.

The fractal dimension was calculated for all the samples used in this study. The results of the calculations for the flame heat shocked samples are summarized in Tables 3 and 4. The average fractal dimension for intact Balmoral Red is 1.07 ± 0.14, and for intact Kuru Grey 1.22 ± 0.22. After a 10 second heat shock, the average fractal dimension increases by 14% for Balmoral Red and by 15% for Kuru Grey. As the duration of the heat shock increases, the fractal dimension increases by 18% and 21 % for the 30 second and 60 second heat shocks for Balmoral Red. The corresponding values for Kuru Grey are 16% and 22%.

Table 3 Fractal dimension of the intact and flame torch heat shocked Balmoral Red samples.

	10 seconds		***30 seconds***		***60 seconds***	
	Before	**After**	**Before**	**After**	**Before**	**After**
	1.19	1.47	1.05	1.45	1.21	1.48
	0.66	0.99	1.06	1.22	1.013	1.39
	1.08	1.17	1.07	1.35	1.11	1.33
	1.33	1.41	1.08	1.14	1.01	1.32
	1.01	1.12	1.07	1.33	1.13	1.45
Average	**1.05**	**1.23**	**1.06**	**1.30**	**1.09**	**1.40**
STDEV	**0.25**	**0.20**	**0.01**	**0.11**	**0.08**	**0.07**
Normalized		**1.17**		**1.22**		**1.27**

Table 4 Fractal dimension of the intact and flame torch heat shocked Kuru Grey samples.

	10 seconds		***30 seconds***		***60 seconds***	
	Before	**After**	**Before**	**After**	**Before**	**After**
	1.38	1.76	1.17	1.16	1.16	1.29
	1.31	1.77	1.22	1.40	0.79	1.40
	1.46	1.57	1.21	1.48	0.99	1.38
	1.37	1.64	1.17	1.39	0.91	1.44
	1.71	1.72	1.27	1.37	1.11	1.21
Average	**1.44**	**1.69**	**1.21**	**1.43**	**0.99**	**1.34**
STDEV	**0.16**	**0.08**	**0.04**	**0.05**	**0.15**	**0.09**
Normalized		**1.17**		**1.19**		**1.35**

Figure 15 shows images obtained from the Kuru Grey samples before and after applying the heat shock using the plasma gun. It is evident from the images that the heat shock damage caused by the plasma gun is considerably more severe than that done by the flame torch (see figure 14). After the heat shock by the plasma gun, the surface suffers also from material removal. Therefore, the cracks and pores are not visible in these images like the images taken from the surface of the heat-shocked sample by flame torch. It is apparent that by increasing the duration of the plasma heat shock, the amount of damage on the surface increases as well.

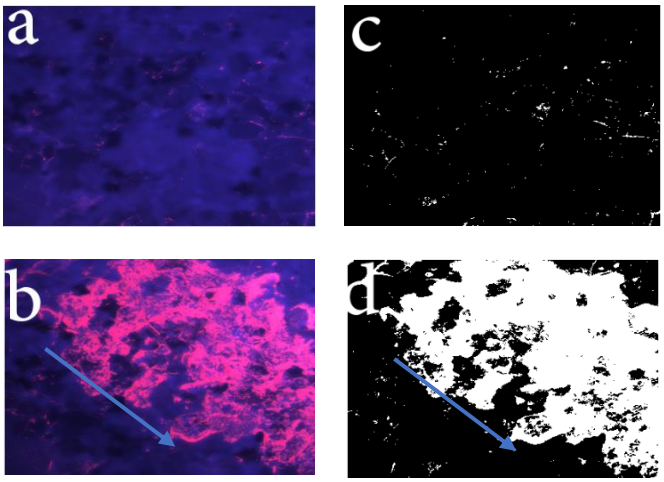

Figure 15 Microscope images a) before and b) after a 0.8 second plasma heat shock, and the damaged surface and identified cracks c) before and d) after the plasma shock. The arrow indicates the direction of the movement of the plasma gun.

The fractal dimension values for the intact (non-heat shocked) and plasma shocked samples of Kuru Grey are presented in Table 5, showing that the average value of the fractal dimension increase from the intact samples value of 1.04 ± 0.08 to 1.39 ± 0.17, 1.60 ± 0.08, and 1.74 ± 0.05 for the samples heat shocked for 0.4, 0.55, and 0.8.

Table 5 Fractal dimension of Kuru Grey samples before and after applying a plasma shock

	0.4 second		***0.55 second***		***0.8 second***	
	Before	**After**	**Before**	**After**	**Before**	**After**
	1.11	1.40	1.03	1.53	1.14	1.69
	1.05	1.40	1.03	1.58	0.78	1.82
	1.05	1.52	1.10	1.68	1.06	1.70
	1.09	1.55	1.02	1.55	1.08	1.73
	1.02	1.12	1.02	1.71	1.01	1.81
Average	**1.07**	**1.39**	**1.04**	**1.61**	**1.01**	**1.75**
STDEV	**0.04**	**0.17**	**0.03**	**0.08**	**0.14**	**0.06**
Normalized		**1.31**		**1.54**		**1.72**

7.2 Scanning electron microscopy

Figure 16 shows the scanning electron microscope images obtained from the surface of a Balmoral Red sample with a 10-second heat shock. The back-scattered electron (BSE) image (Figure 16a) shows the existence of intergranular cracks. These cracks are not well visible in the secondary electron (SE) image (Figure 16b) due to the roughness of the surface structure

of the rock. The appearance of this kind of cracks is due to the weak bonding of different grains. However, the images obtained from a sample of Balmoral Red with a 60-second heat shock (Figure 17) shows the existence of transgranular cracks as well. The reason to observe the transgranular cracks can be found in the stress induced by the adjacent grains. It is well known the rock structure is full of cracks. The surrounding grains can expand at a faster rate compared to the surrounded grain due to the different thermal expansion coefficient as the duration of the heat shock increases. Therefore, adjacent grains induce stress to the surrounded grain and this stress causes the expansion of the existing cracks within the surrounded grain.

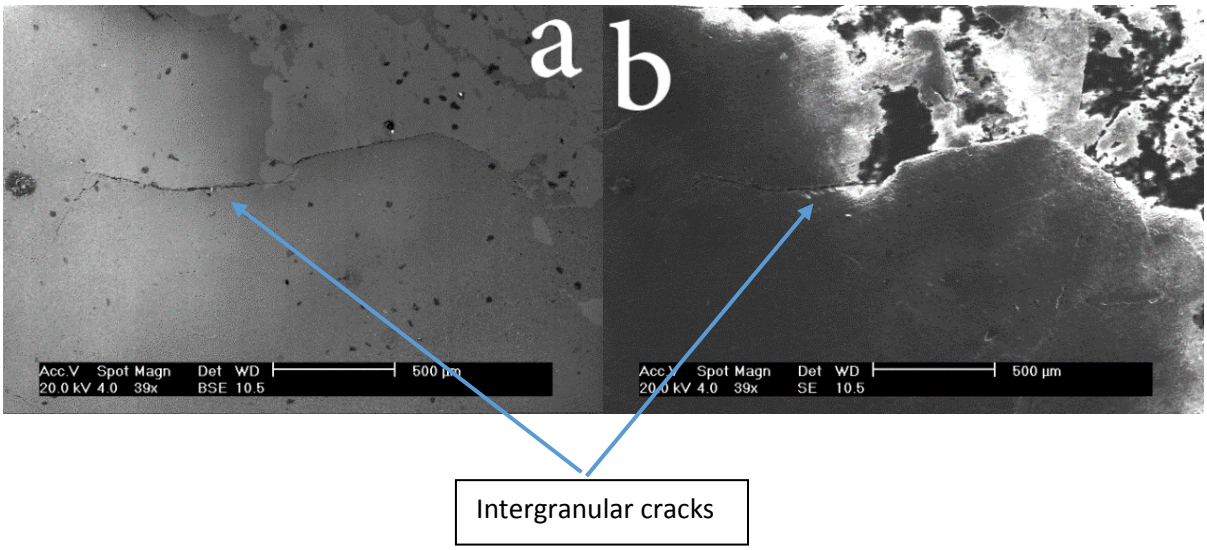

Figure 16 SEM images of the surface of a 10-second heat shocked Balmoral Red sample a) BSE image and b) SE image.

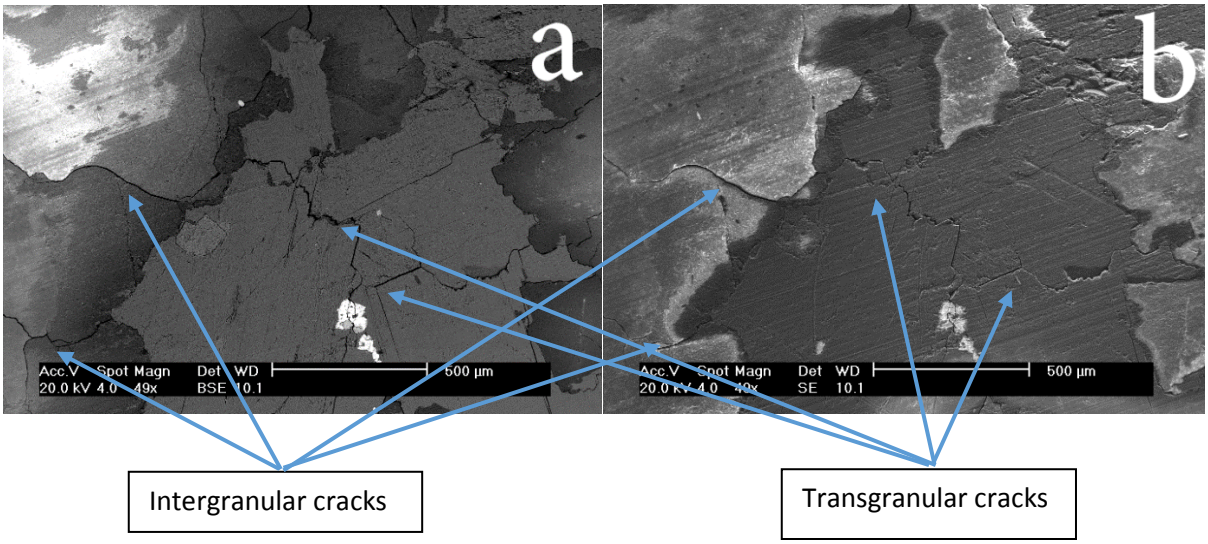

Figure 17 SEM images of the surface of a 60-second heat shocked Balmoral Red sample a) BSE image and b) SE image.

Figure 18 shows the BSE and SE images obtained from a 10-second heat-shocked Kuru Grey sample. The difference between the images obtained from Kuru Grey compared to Balmoral Red is the existence of pores in the structure, which was visible also in the fractal dimension analysis results of the rocks.

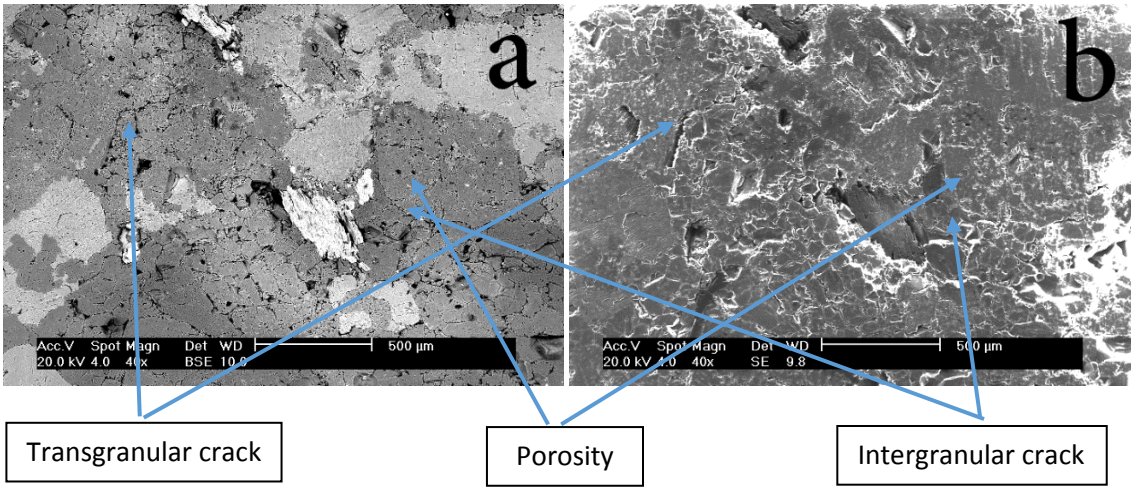

Figure 18 SEM images of the surface of a 10-second heat shocked Kuru Gray sample a) BSE image and b) SE image.

By increasing the duration of the shock to 60 seconds, the intergranular and transgranular cracks become longer and more porosity becomes visible in the structure (Figure 19). The increase in the length and number of intergranular and transgranular cracks can be readily explained be the thermally induced microcracking.

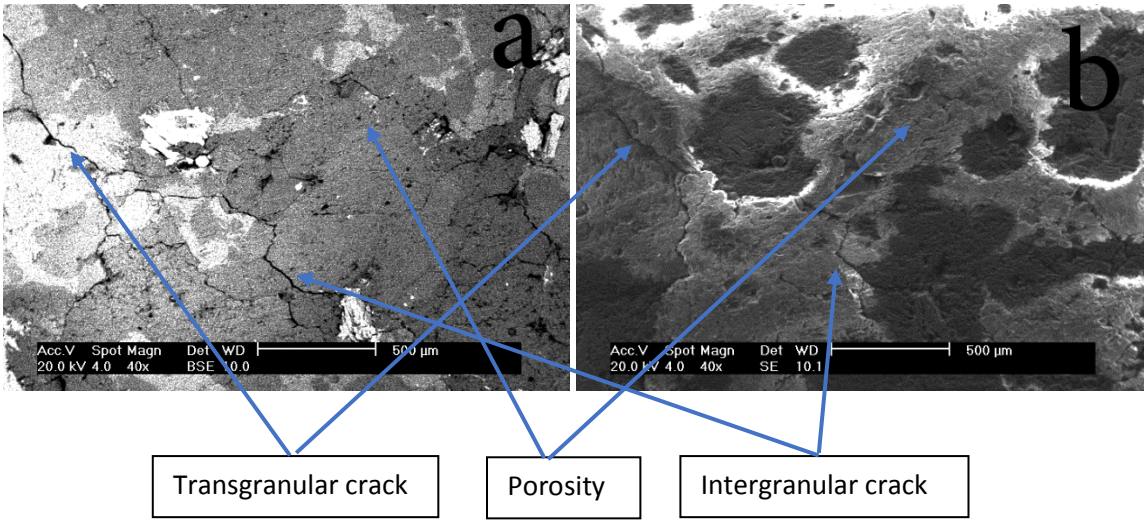

Figure 19 SEM images of the surface of a 60-second heat shocked Kuru Grey sample a) BSE image and b) SE image.

7.3 X-ray tomography results

Figure 20 shows the CT scan results for a 10 second heat shocked Balmoral Red sample. From the figure it is evident that the cracks induced by the heat shock do not penetrate deep into the sample, and even in the cross section images very close to the surface no evident cracks can be observed. Therefore, it is possible to say that most, if not all, of the induced cracks reside on the surface of the sample and that the volume of the specimen is not affected by the heat shock. Figure 21 shows similar results for a 10 second heat shocked sample of

Kuru Grey, i.e., there are no cracks visible in the images. Therefore, it can be concluded that in both studied types of rock, the cracks induced by 10 second thermal shocks are either too small to be observed with the used instrument or they remain at the very surface or, at best, in the depth of just a few tens of microns from the surface of the samples.

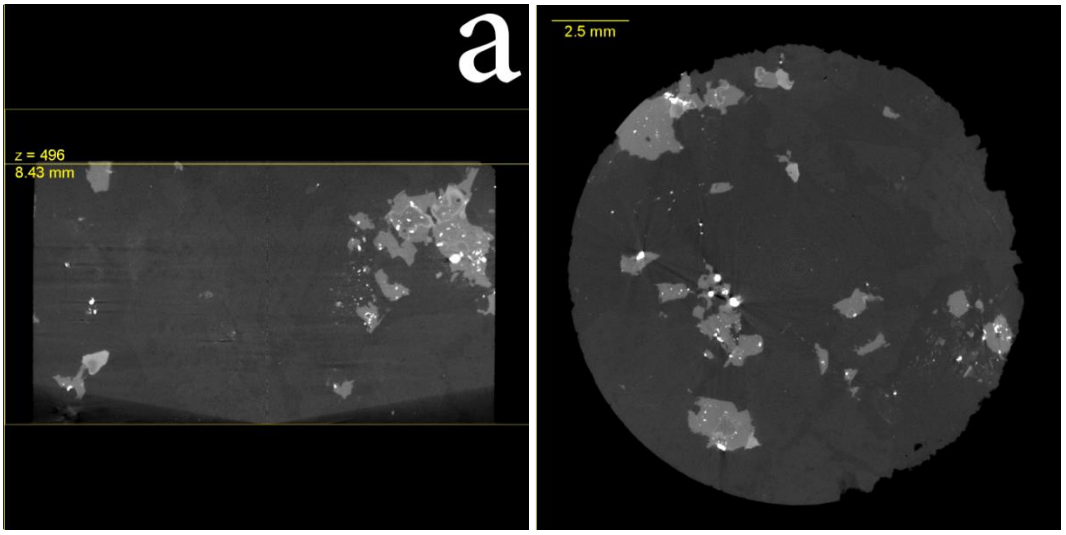

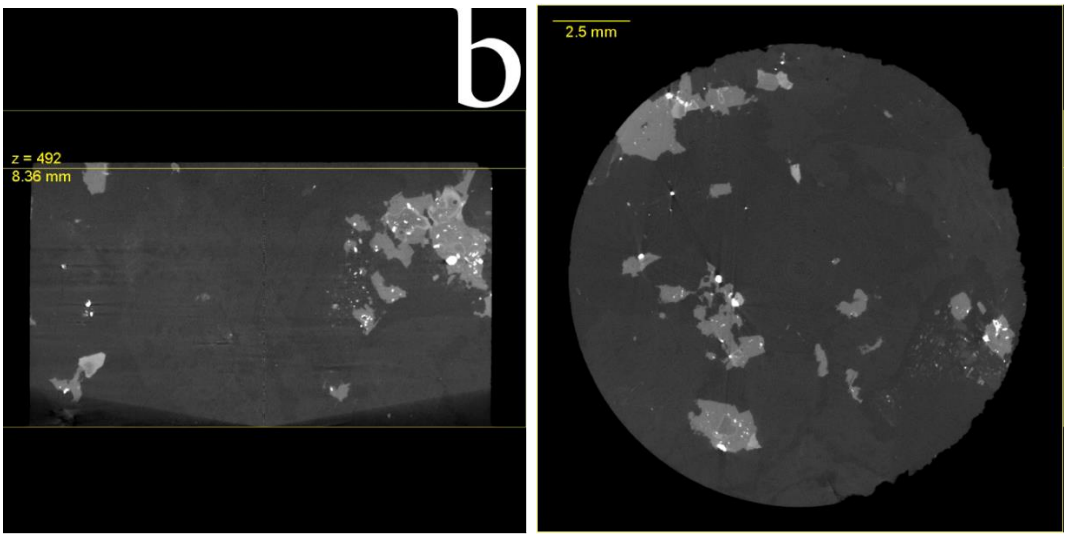

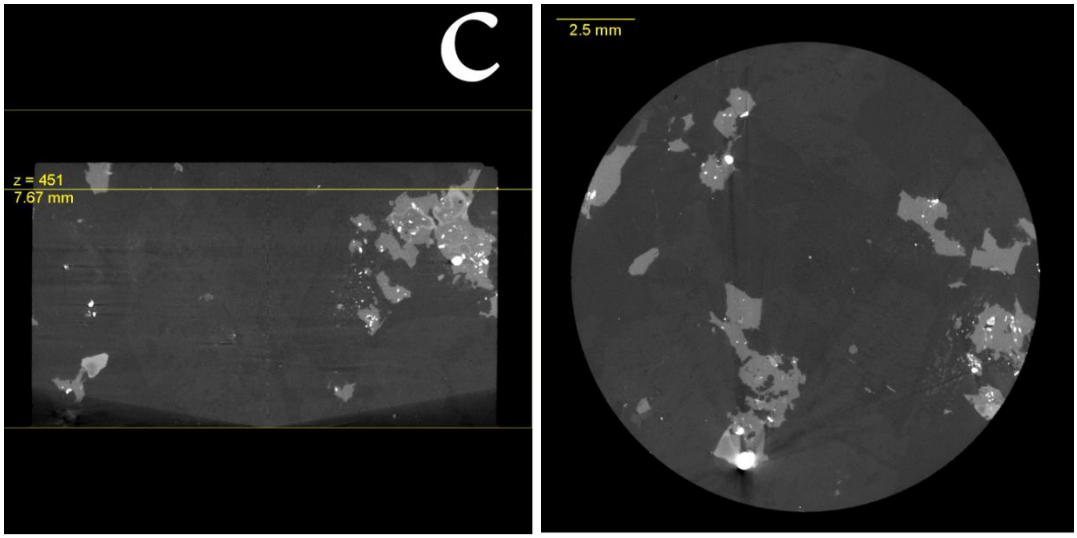

Figure 20 CT scan images of the cross sections of a Balmoral Red sample with a 10 second heat shock.

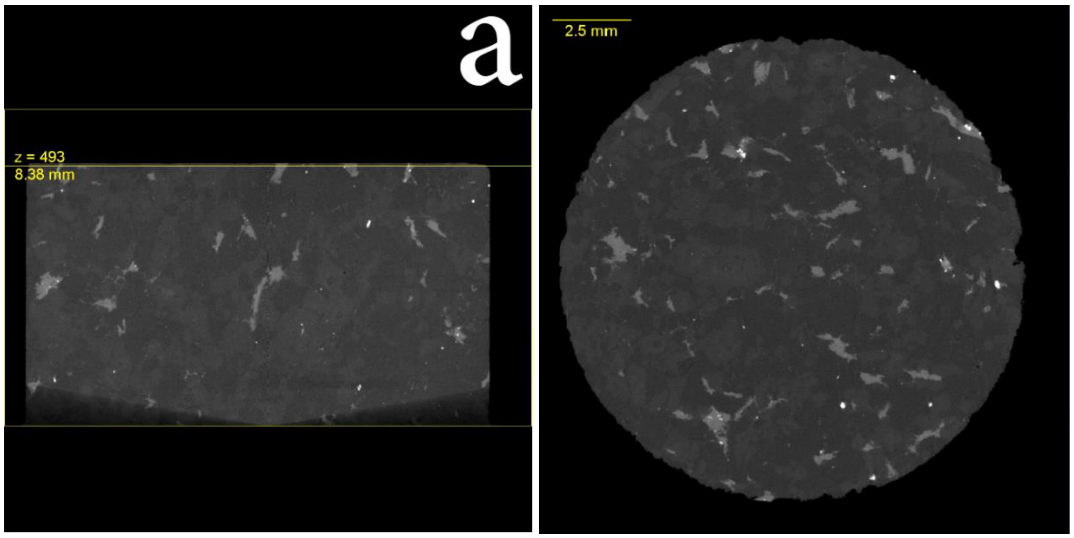

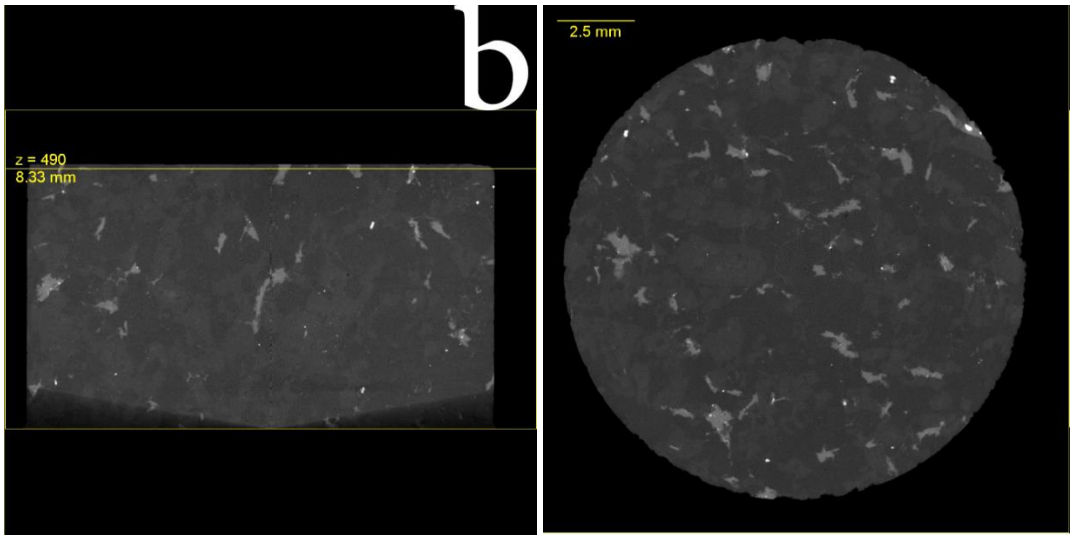

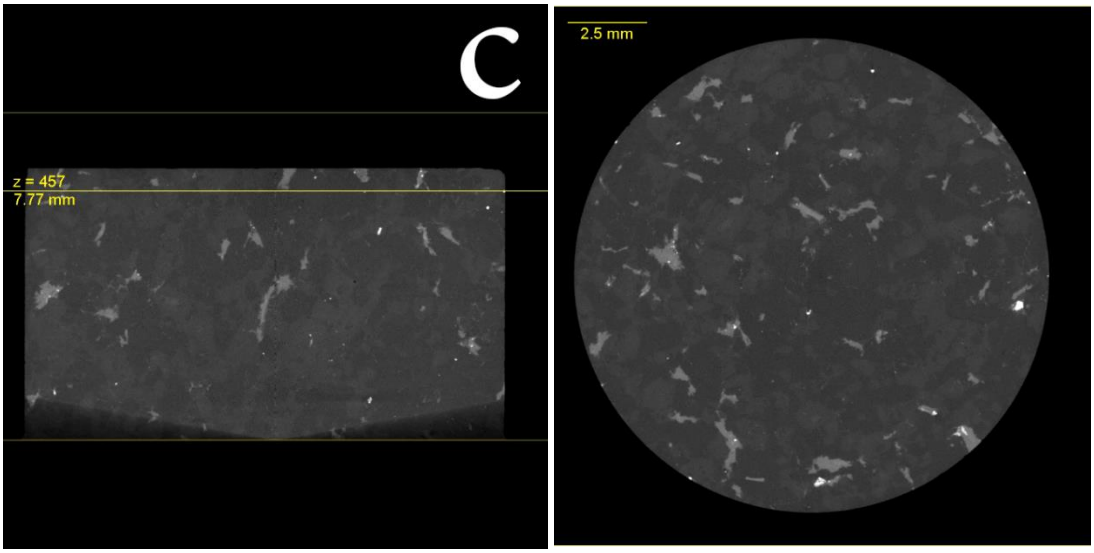

Figure 21 CT scan images of the cross sections of a Kuru Grey sample with a 10 second heat shock.

When the duration of the heat shock is extended to 60 seconds, the situation, changes. Figure 22 shows cross section CT scan images of a Balmoral Red sample, where the cracks are visible also deep below the surface of the sample. However, it should be considered that the samples used for the CT scans were core drilled from the original BD specimens, and therefore the sample preparation also might have caused damage on the sample. Therefore, it remains somewhat uncertain whether the cracks seen in the 60 second heat shocked Balmoral Red sample are (entirely) due to the heat shock, or if the sample preparation is at least a partial reason for their appearance. In any case, there seems to be a difference in the CT scan results of the Balmoral Red samples heat shocked for 10 and 60 seconds presented in Figures 20 and 22.

In the case of a Kuru Grey sample with a 60-second heat shock (Figure 23), the situation remains the same as after a 10-second heat shock and there are no cracks visible in the bulk of the sample. Therefore, one can conclude that for Kuru grey the effects of the heat shock are limited to depth of a few microns from the surface of the sample.

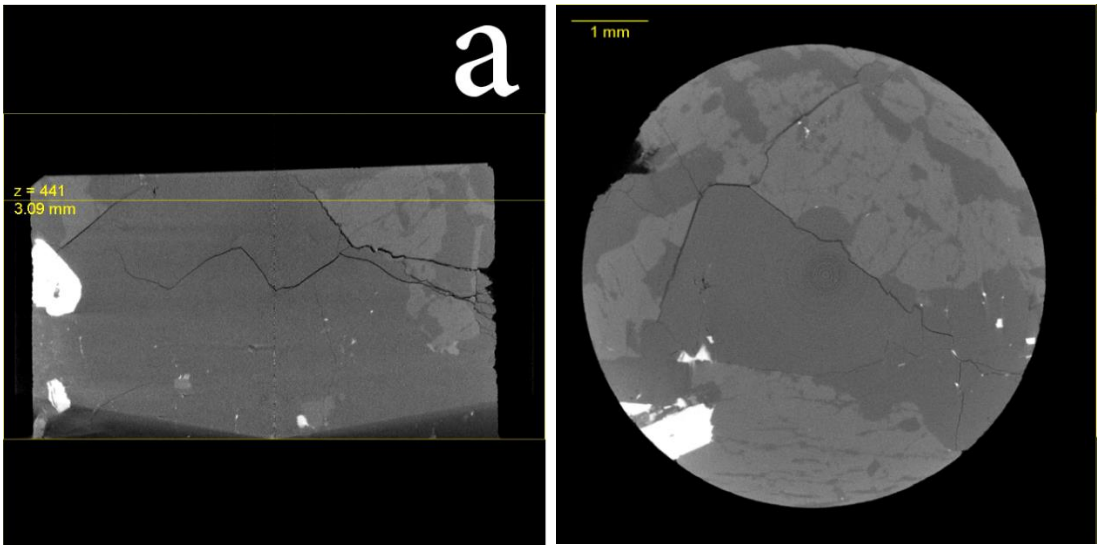

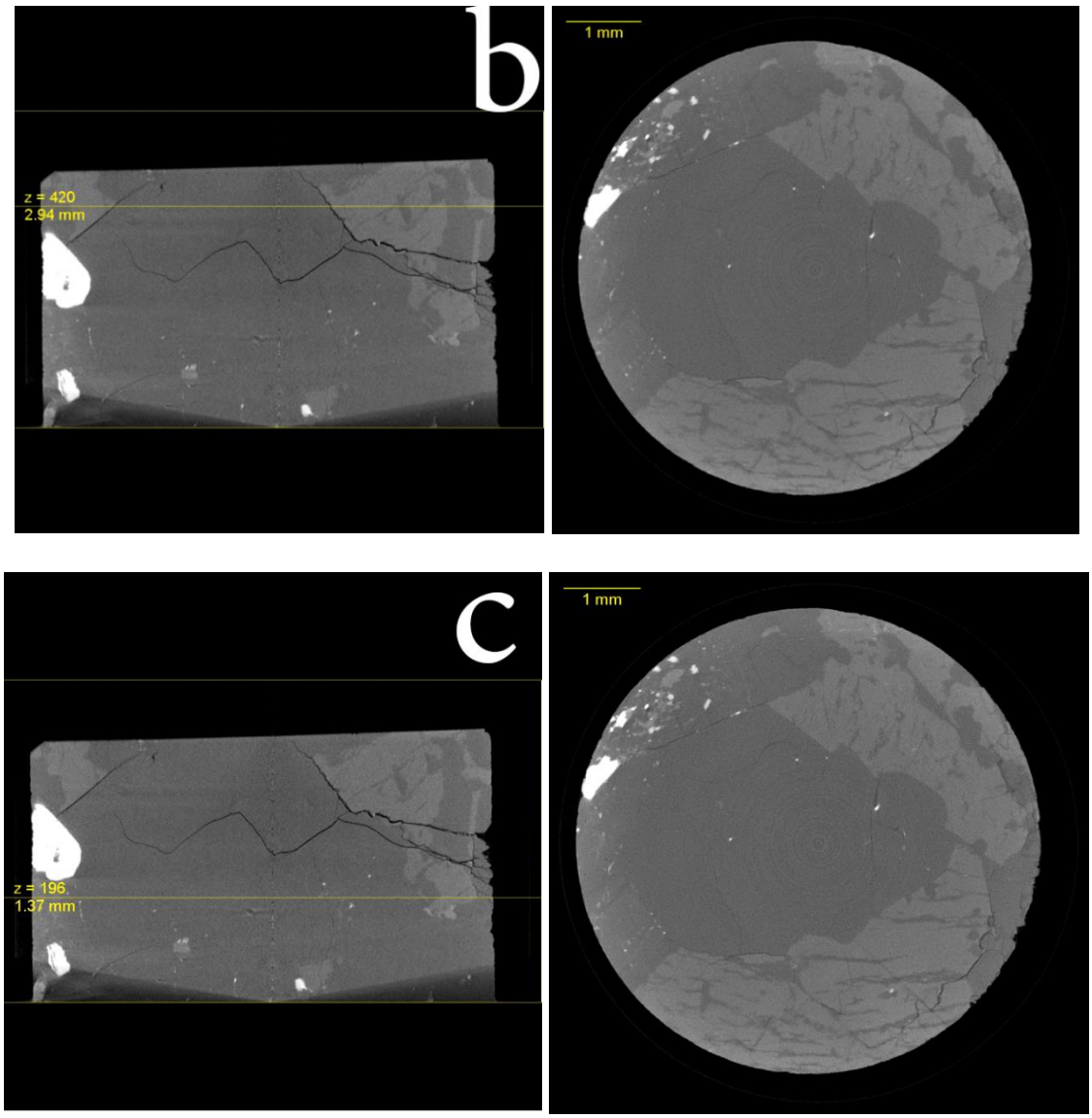

Figure 22 CT scan images of the cross section of a Balmoral Red sample with a 60 second heat shock.

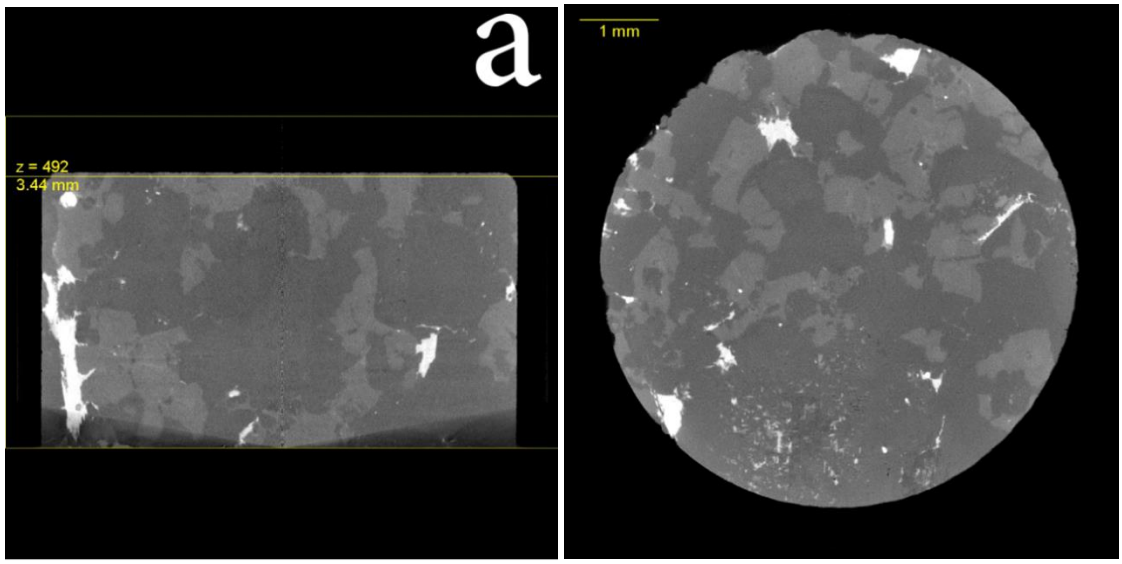

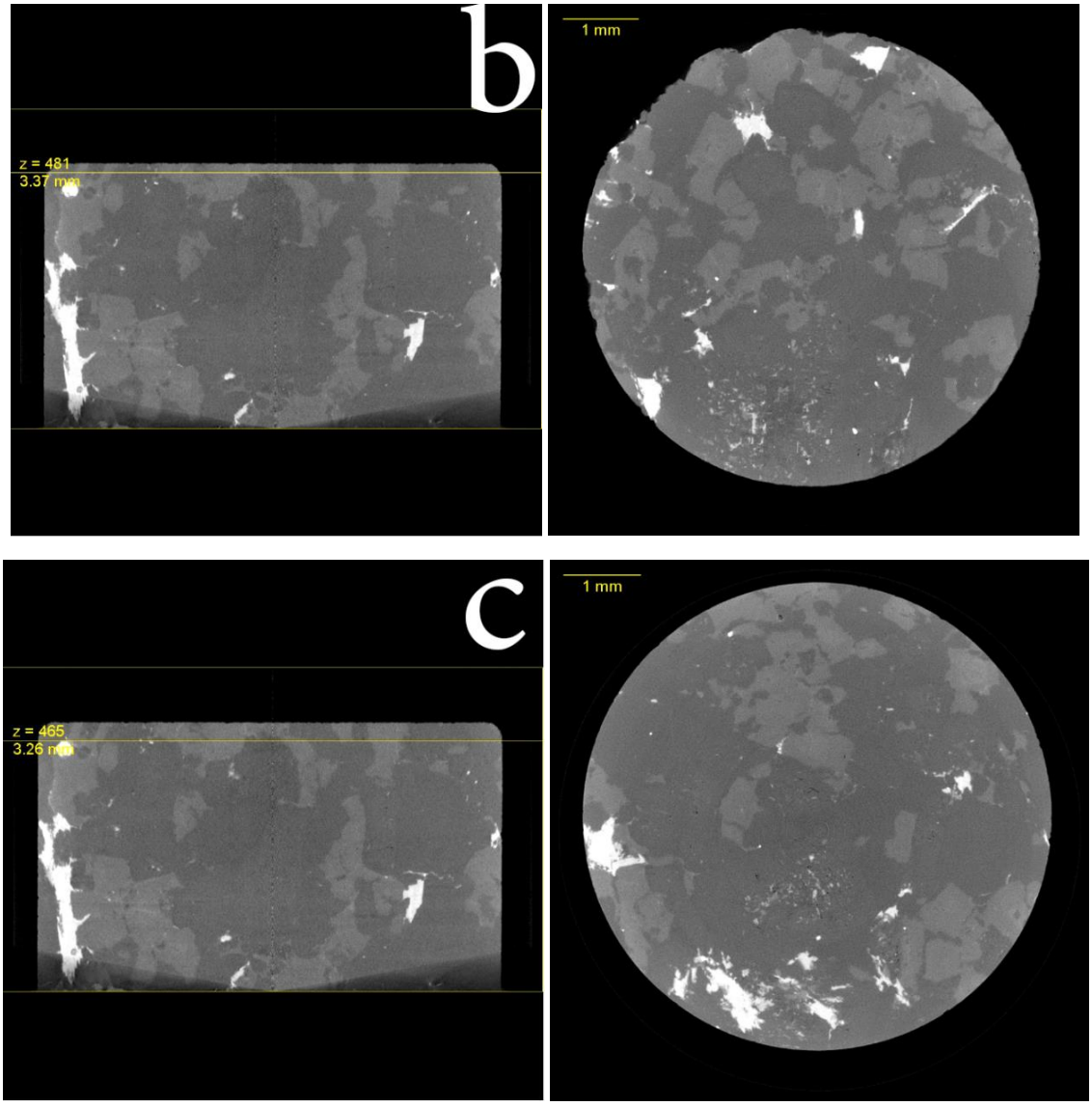

Figure 23 CT scan images of the cross section of a Kuru Grey sample with a 60-second heat shock.

7.4 Quasi-static test results

The low strain rate tests were carried out using an Intron 8800 servohydraulic materials testing machine with the displacement rate of 1 mm/min. The quasi-static tests were carried out on Balmoral Red granite. Figure 24 shows the results of these tests. The average tensile strength of the rock before the heat shock is 8.2 ± 2.2 MPa. After applying the heat shocks, the strength of the rock drops to 5.8 ± 0.7 MPa, 4.3 ± 0.5 MPa, and 3.8 ± 1.1 MPa for 10, 30, and 60 second heat shocks, respectively. Before the heat shocks, the behavior of the rock is quite consistent and stable: after reaching the maximum tensile strength, the stress drops sharply and the samples are divided into two pieces. The behavior of the rock becomes different after applying the thermal shocks as the sharp drop after the maximum strength becomes less pronounced. In addition, in some cases several maxima are observed instead of one clear maximum point. This behavior becomes even more pronounced for the samples with a 60 second heat shock. As the heat shock time of the samples becomes longer, cracking also in directions other than

the loading direction increases. Therefore, the macroscopic fracture does not take place only by one dominant crack. When the force applied on the heat shocked samples increases, the crack first propagates through the sample in a similar manner as in a non-heat shocked sample, but in this case the crack stops at some point and other cracks start to propagate. This behavior continues to the point where the main macrocrack parallel to the loading direction propagates through the whole sample. As these processes during quasi-static loading are rather slow, this phenomenon can be observed even by naked eye during the tests. This observation also explains the appearance of several maxima in the stress-time curves of thermally shocked samples.

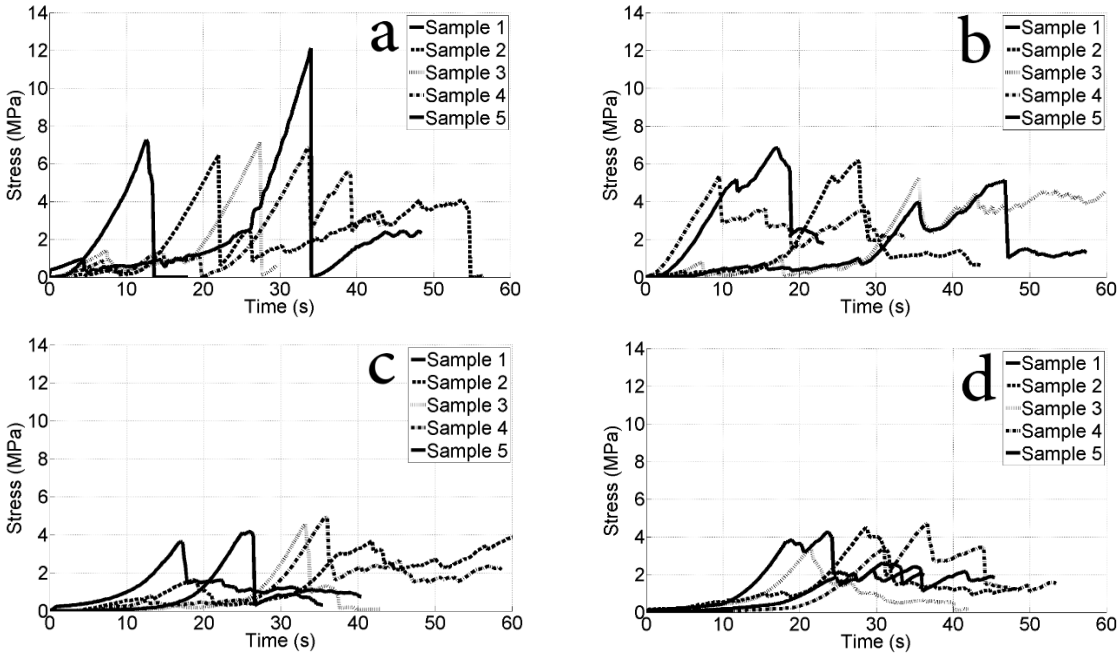

Figure 24 Low strain rate tensile stress as a function of time for a) samples without a heat shock, b) with a 10 s heat shock, c) with a 30 s heat shock, and d) with a 60 s heat shock.

7.5 Dynamic test results

The behavior of the Balmoral Red granite is different in the dynamic loading conditions compared to the quasi-static loading conditions. Figure 25 shows the response of the Balmoral Red without any heat shock and after applying a 10, 30 and 60 second heat shock. The strength of the rock before applying the heat shock is 29 ± 3 MPa. As the duration of the thermal shock increases, the strength deceases to 23 ± 4 MPa, 16 ± 2 MPa, and 12 ± 2 MPa for 10, 30 and 60 second thermal shocks, respectively. After the heat shock, the strong peak in the stress-time curves again partly disappears, and the stress drops at a slower rate after the peak stress. When compared to the low rate tests, the scatter at the higher rate is reduced and the rock shows more consistent behavior.

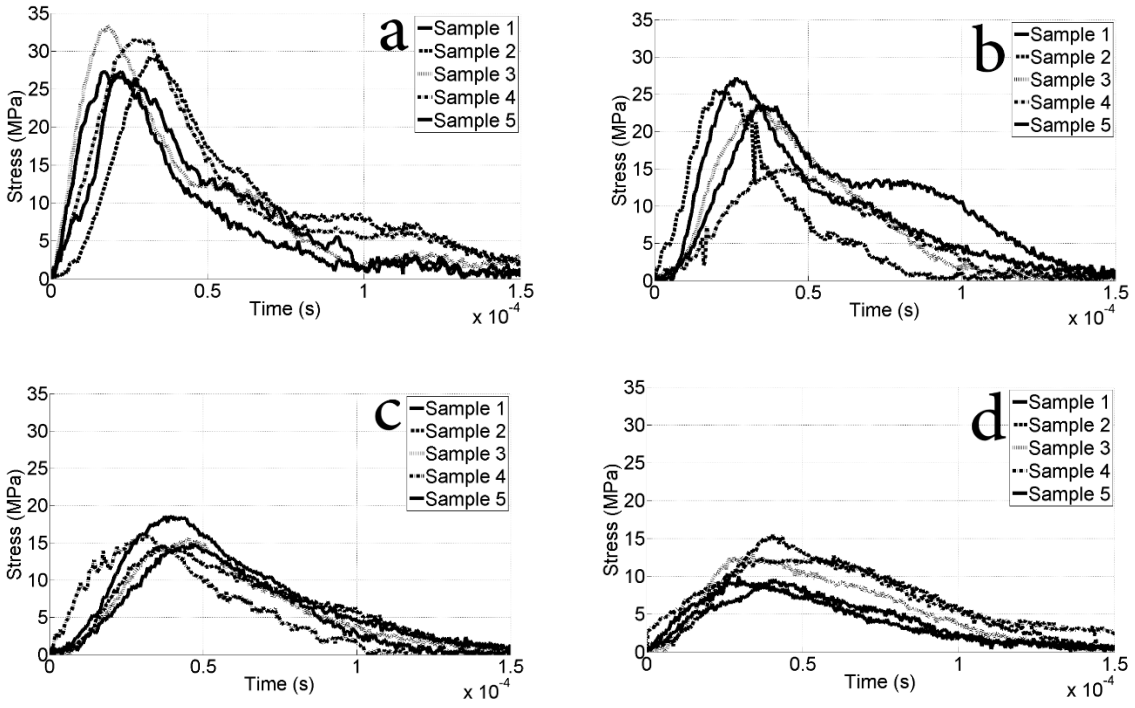

Figure 25 High strain rate tensile stress as a function of time for samples of Balmoral Red a) without a heat shock, b) with a 10 s heat shock, c) with a 30 s heat shock, and d) with a 60 s heat shock.

The behavior of Kuru Grey is quite similar to that of Balmoral Red at the dynamic loading conditions. Figure 26 shows the response of Kuru Grey when subjected to dynamic loading before and after being thermally shocked. The average dynamic tensile strength for the non-heat shocked specimens is 27 ± 3 MPa, while the strengths of the heat-shocked samples are 21 MPa, 16 MPa and 15 MPa for the 10, 30 and 60 second heat shocks, respectively. After applying the thermal shocks, the strong peak in the stress vs. time curves observed for the non-heat treated samples fades away. Both the reduction in the maximum stress and the change in the shape of the curve can be explained by the increasing number, length, and interconnectivity of the cracks due to the heat shocks.

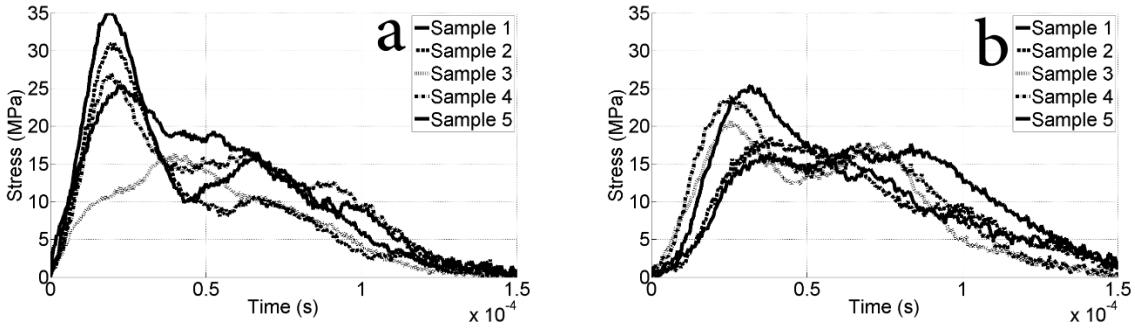

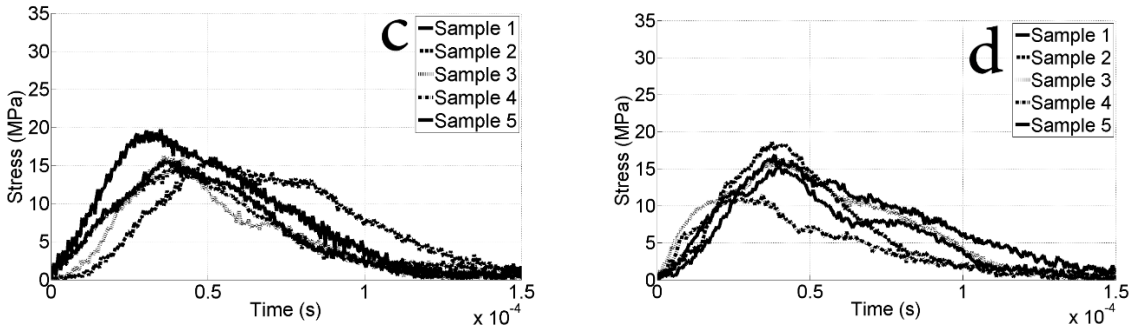

Figure 26 High strain rate tensile stress as a function of time for samples of Kuru Grey a) without a heat shock, b) with a 10 s heat shock, c) with a 30 s heat shock, and d) with a 60 s heat shock.

Figure 27 shows the mechanical behavior of plasma-shocked Kuru Grey under the dynamic loading condition. The average tensile strength of five non-shocked BD samples is 29 ± 3 MPa. The values of the tensile strength for 0.4 s, 0.55 s, and 0.8 s heat shocked samples are 29 ± 3 MPa, 25 ± 4 MPa, and 23 ± 3 MPa, respectively. As can be seen, even though the plasma gun is powerful (50kW) and the plasma shock itself can provide a great amount of energy in a very short time, there is still a minimum amount of time needed for this energy to affect a reasonable thickness of the rock material and decrease the strength of the rock.

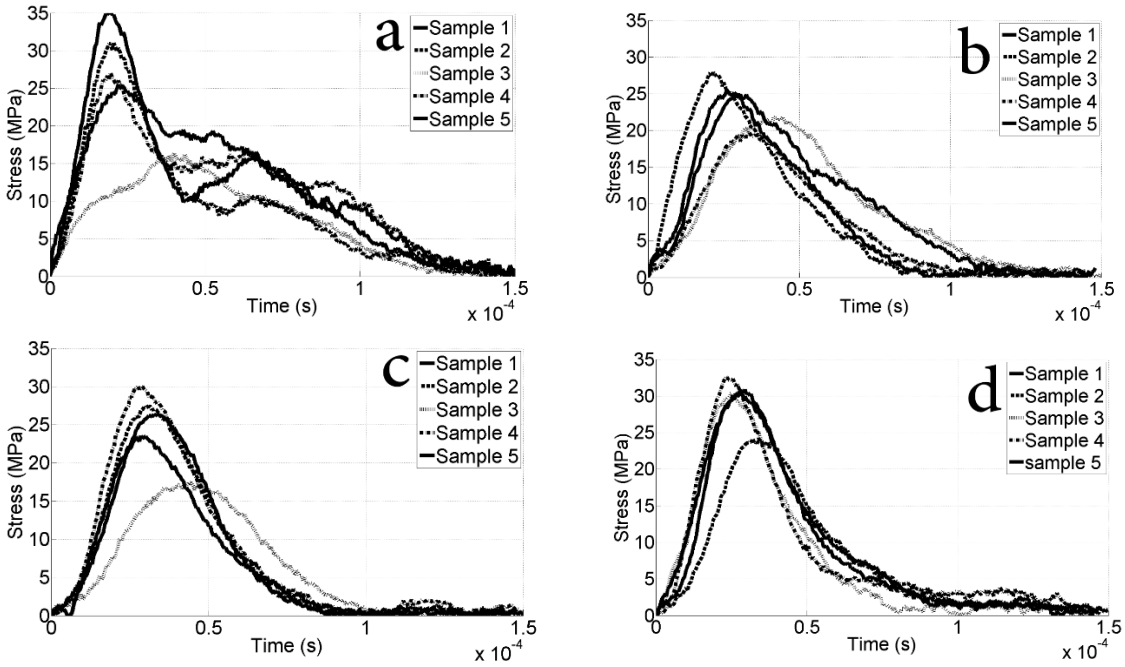

Figure 27 High strain rate test results for Kuru Grey showing the tensile stress as a function of time for a) samples without a heat shock, b) samples with a 0.4 s plasma heat shock, c) samples with a 0.55 plasma heat shock, and d) samples with a 0.8 s plasma heat shock.

7.6 Characterization of the rock behavior based on fractal dimension

As mentioned before, there appears to be a correlation between the normalized fractal dimension and the mechanical behavior of the rock. This correlation will be discussed in the following sub-chapters.

7.6.1 Comparison of the mechanical behavior of flame-shocked Balmoral Red and Kuru Grey

Figure 28 shows the behavior of the flame-shocked rocks as a function of the normalized fractal dimension revealing that when the normalized fractal dimension increases to 1.1, the tensile strength of both rocks decreases rapidly. After this point, the strength of Balmoral Red shows a continuously decreasing trend, while Kuru Grey seems to show a little bit different kind of behavior by saturating on a certain level. As pointed out in section 7.1, the amount of porosity in Kuru Grey increases with an increase in the duration of the heat shock, and these pores can act as barriers to the propagating cracks [160]. Consequently, it appears that after a certain point the increasing fractal dimension (due to the microstructural changes) does not anymore weaken nor promote the fracturing of Kuru Grey. On the other hand, Balmoral Red shows a different response to the heat shock: the number of cracks both in the volume and the surface increases and the existing cracks become longer. All these events promote the fracturing Balmoral Red. Therefore, even though the fractal dimension of both rocks shows almost the same values with increasing the duration of the heat shock, the responses of the rocks to external loading are different because of the differences in their microstructural response to the heat shocks.

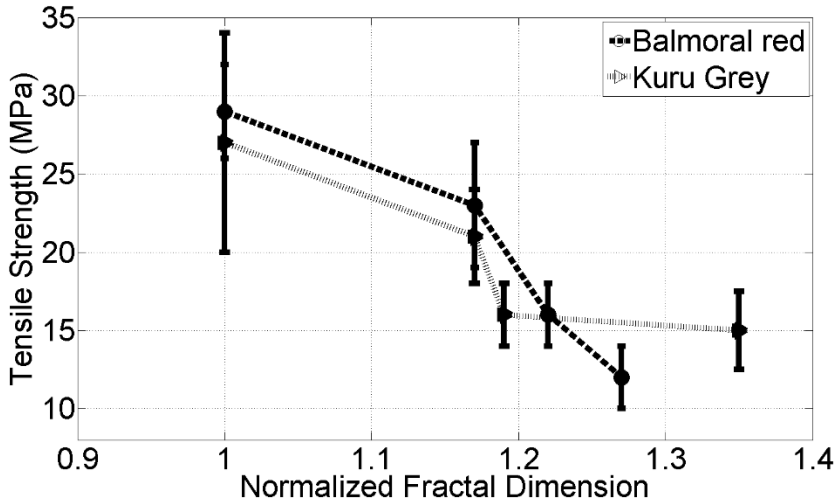

Figure 28 Tensile strength of the flame-shocked rocks as a function of the normalized fractal dimension.

7.6.2 Characterization of the plasma-shocked Kuru Grey based on fractal dimension

Figure 29 demonstrates the strength of the plasma-shocked Kuru Grey as a function of the normalized fractal dimension. The strength of the rock shows no change up to the normalized fractal dimension value of 1.3. As discussed before, the plasma heat shock of 0.40 s was not powerful (or long) enough to penetrate into the volume of the sample to affect the microstructure. It should also be reminded that the behavior of Kuru Grey is different depending whether it is shocked by a plasma gun or a flame torch. The heat shock generated by the flame torch creates a considerable amount of porosity in the sample structure, which slows down the decreasing trend in the rock's strength with increasing the duration of the heat shock. The situation is different when the samples are thermally shocked with a plasma gun, which does not introduce pores into the rock's microstructure but only damages the sample surface. Therefore, increasing the duration of the heat shock leads only to a continuing decrease in the rock's strength.

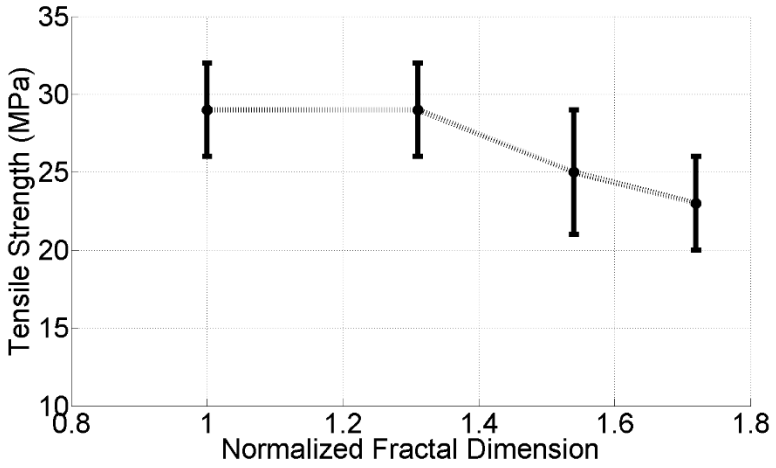

Figure 29 Tensile strength of the plasma-shocked Kuru Grey as a function of the normalized fractal dimension.

7.6.3 Strain rate sensitivity of Balmoral Red granite as a function of the fractal dimension

Figure 30 shows the tensile strength of Balmoral Red in the quasi-static and dynamic loading conditions as a function of the normalized fractal dimension. When the loading rate increases, the strength of the rock is higher but decreases at a much faster rate with increasing fractal dimension. The rate of the strength reduction $(\Delta\sigma/\Delta FD)$ is in the quasi-static condition -13.78 MPa for the 10 second heat shock, -52.57 MPa for the 30 second heat shock, and -5.34 MPa for the 60 second heat shock. The corresponding values in the dynamic loading condition are -38.52 MPa for the 10 second heat shock, -141.32 MPa for the 30 heat shock, and -78.32 MPa for the 60 second heat shock.

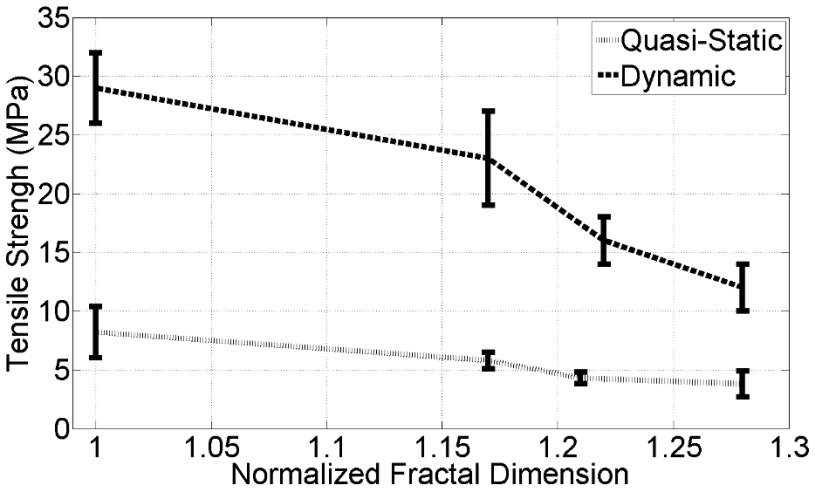

Figure 30 Tensile strength of Balmoral Red as a function of the normalized fractal dimension in different loading condition.

With the following Equation and the data obtained from the stress-time curves, we can calculate the strain rate sensitivity of the tested rock materials:

$$M_{abs} = \frac{\Delta\sigma}{\Delta Log(\dot{\varepsilon})} \quad (18)$$

Where

$$\dot{\varepsilon} = \Delta\sigma / E\Delta t \quad (19)$$

and $\Delta\sigma/\Delta t$ is obtained from the stress-time curves. Figure 31 shows the strain rate sensitivity of Balmoral Red as a function of the normalized fractal dimension.

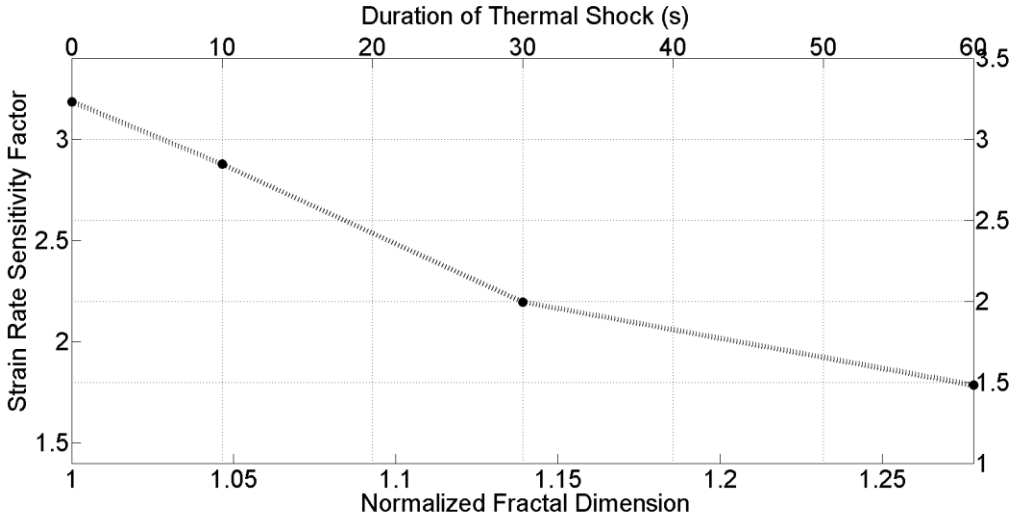

Figure 31 Strain rate sensitivity of Balmoral Red as a function of the normalized fractal dimension.

As Figure 31 shows, the strain rate sensitivity factor decreases with increasing normalized fractal dimension. The main reason for this is the faster decrease of the dynamic tensile strength of the rock compared to the quasi-static strength, which again can be explained by the different rock fracture behavior at these conditions. The fracture energy is largely consumed in creating new surfaces (see section 4.1). In addition to this, some amount of energy is consumed on the kinetic energy of the fragments, acoustic emission, and heating due to friction. In the quasi-static tests, the sample fractures into a few large fragments only. Therefore, the specific area of the fragments is rather low and the decrease in the strength of the rock due to the heat shock can be readily explained by the existing larger cracks in the structure. On the other hand, the situation is quite different in the dynamic condition, and the fracturing of the sample consumes a considerably greater amount of energy when the sample is partly pulverized and the fragments are ejected at high velocities. In this case, too, some energy is again consumed by acoustic emission and frictional heat. Among the rock fracturing processes that consume energy, pulverization is the most affected by the heat shock. Considering a non-heat shocked sample in the dynamic loading condition, the external stress (loading) reaches the tensile strength of the rock at several places simultaneously. This leads to the initiation and propagation of thousands of cracks, which pulverize the sample, or large parts of it, quite effectively. However, after the thermal shock, the local strength of the rock decreases especially in the center of the heat-shocked surface of the sample, where the maximum tensile load will be applied during the BD test. As the stress increases in a thermally shocked BD sample, the dynamic strength of the rock is exceeded locally in the center of the sample, while the rest of the sample still remains in the elastic region. Therefore, fewer microcracks are formed, the degree of pulverization stays lower, and larger fragments are produced as the fractal dimension increases. Consequently, the macroscopic dynamic tensile strength of the rock decreases due to the existence of larger cracks and smaller amount of new surface that is created. Because of this, the dynamic strength of the rock also drops faster as a function of fractal dimension compared to the quasi-static strength. However, to fully confirm this hypothesis requires more testing and careful analysis of the size distribution of the fragments formed during the dynamic loading of samples with different heat shocks.

7.7 Digital image correlation studies

Digital image correlation provides useful information about the fracture behavior of the rock at the dynamic loading condition. Figure 32 shows the tensile stress as a function of time for a 10 second heat shocked Balmoral Red BD sample. Point (a) corresponds to the start of the loading and point (b) refers to the moment just before reaching the peak stress. The high speed images taken at the different stages of loading are shown in Figure 33. The strain maps perpendicular to the loading direction (Y-direction) are overlaid on the original captured images. It is evident from Figures 33a and 33b that no strain localization takes place until the rock strength starts to decrease. Even Figure 33c, which corresponds to the point where the strength of the rock has already dropped, shows no clear signs of strain localization. This observation indicates that the fracture starts inside the rock sample and reaches the surface of the sample only after some microseconds after the peak stress has been passed. Later on, the crack propagates very fast through the whole sample (Figures 33d and 33e). This process is continued by crushing of the sample surfaces at the contact points with the stress bars. Due to the speckle pattern and base coat (white paint) applied on the surface of the samples, it

unfortunately is not possible to use the obtained high speed images to study the mechanism(s) of crack propagation (*e.g.*, intergranular *vs.* transgranular) in the samples in more detail.

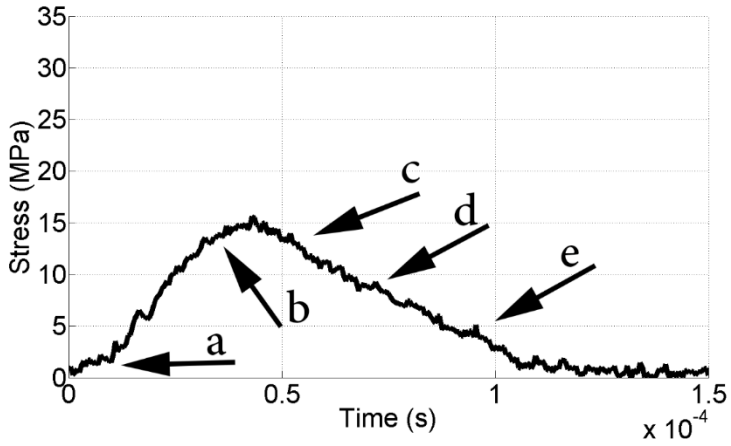

Figure 32 Dynamic tensile stress as a function of time in a Kuru Grey sample with a 10 second thermal shock.

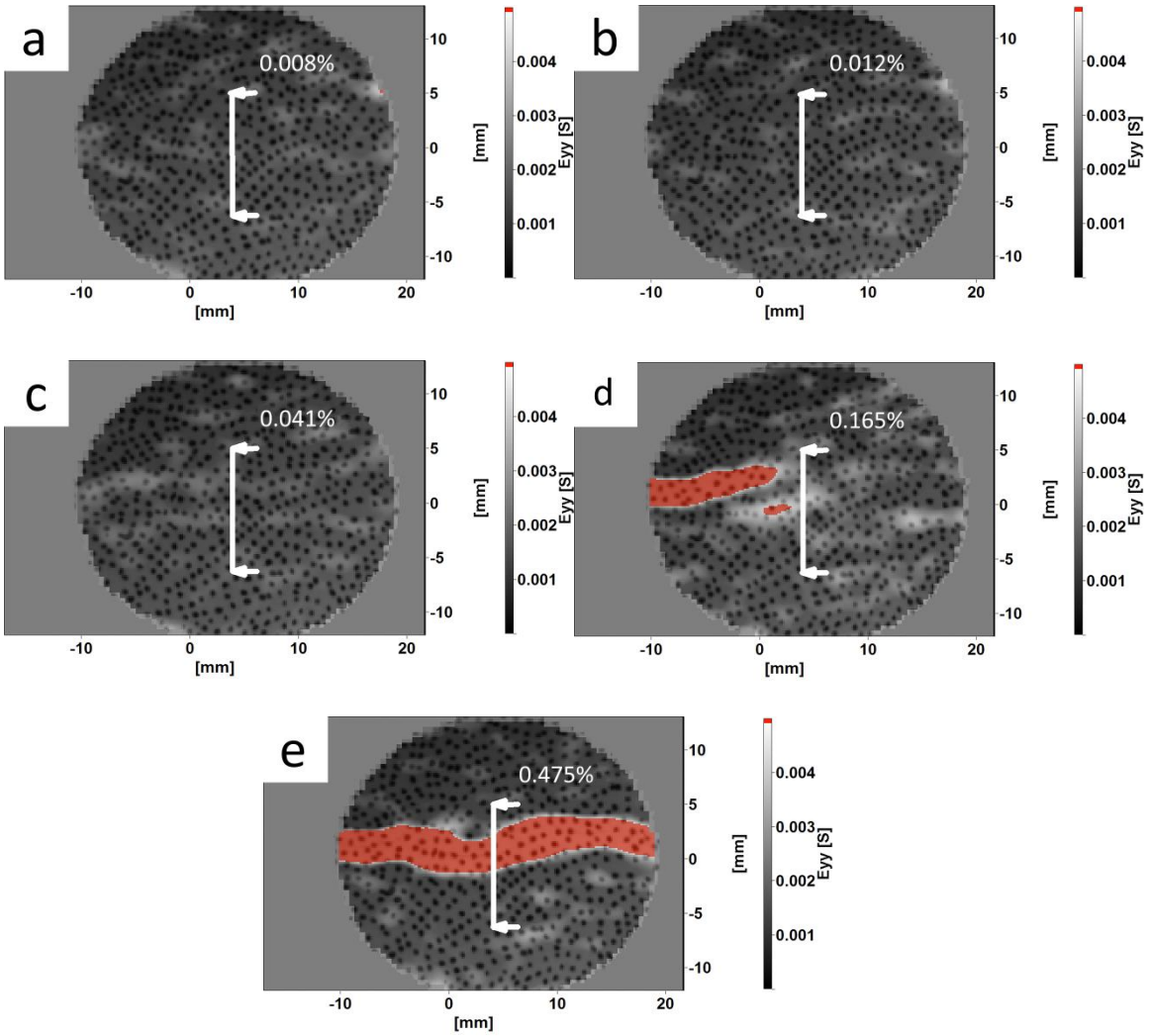

Figure 33 DIC images obtained during dynamic loading of the same Kuru Grey sample as shown in Figure 32. a) t=0µs, b) t=31.25µs, c) t=50µs, d) t=56,25µs, and e) t=62,5µs.

The engineering strain in the samples in the direction perpendicular to the loading direction prior to fracture was measured using LaVision StrainMaster (DaVis) 3D-DIC software. A virtual extensometer with a fixed gage length was placed at the center of the specimen, as shown in Figure 33. Figure 34 shows the average strain in the tested samples as a function of the normalized fractal dimension.

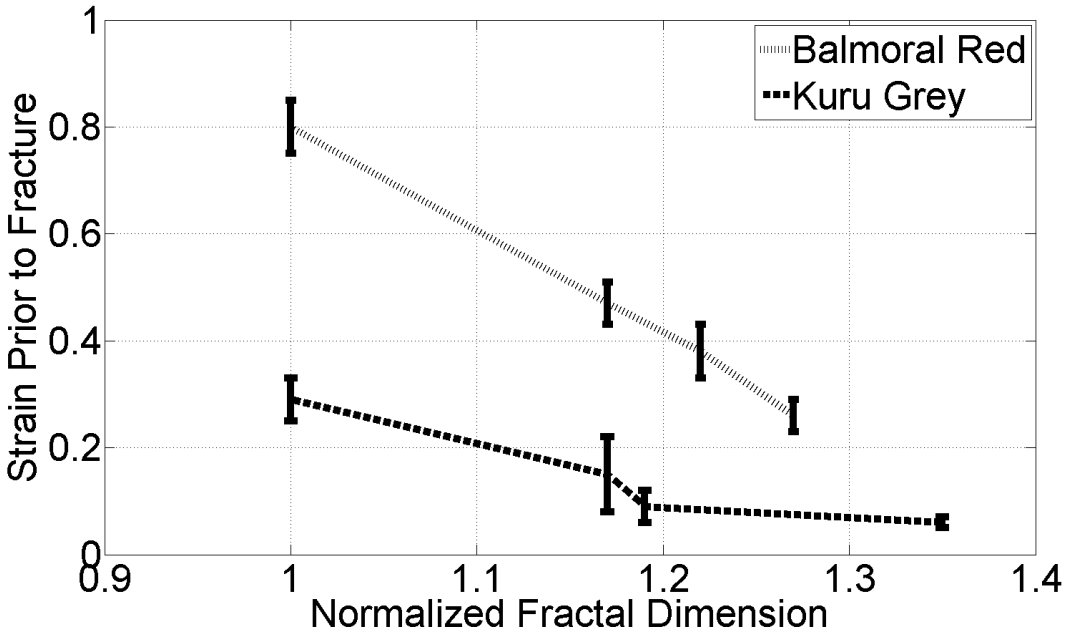

Figure 34 Surface strain prior to fracture as a function of the normalized fractal dimension.

Figure 34 shows a decreasing trend of the strain prior to fracture of the rocks, as the duration of the heat shock increases. In general, Balmoral Red shows a significantly higher surface strain compared to Kuru Grey. This observation can be explained by the smaller grain size of Kuru Grey, which leads to the more brittle behavior of this granite [161, 162]. On the other hand, the less pronounced decrease of the failure strain of Kuru Grey can be linked to the higher porosity of Kuru Grey compare to Balmoral Red. As discussed already before, the pores can act as barriers to the crack propagation, *i.e.*, when the crack reaches a pore, the pore increases the radius of the crack tip and thus blunts it, making it harder for the crack to propagate further. On the other hand, in the case of Balmoral Red, an increase in the duration of the thermal shock results in an increase in the crack density, which facilitates the macroscopic deformation of the rock and increases the surface strain prior to fracture.

7.8 Dynamic indentation tests

The results obtained from the single-button indentation tests for non-heat shocked and heat shocked samples of Kuru Grey are shown in Figure 35. It can be seen from the graphs that the depth of penetration remains almost the same with the same level of applied force for all samples. Another point which deserves attention is the appearance of the second maximum in the graphs. One explanation for the appearance of this second maximum is that the bit first damages the rock surface severely and then continues to move inwards. This movement leads to trapping of the produced powder between the crater surface and the bit. Therefore, further movement of the bit results in the compaction of the powder which appears as the second maximum. Consequently, a part of the applied force is spent on the compaction of the dust and powder beneath the bit instead of causing further damage to the rock sample. The force-displacement curves obtained from the tests are not similar to the typical experimental bit-rock interaction curves, where an elastic recovery is usually observed [156]. However, it has been shown that the bit-rock interaction behavior changes as the impact speed increases. At higher speeds, the elastic recovery is not anymore observed as the rock shatters into powder and dust in front of the indenter.

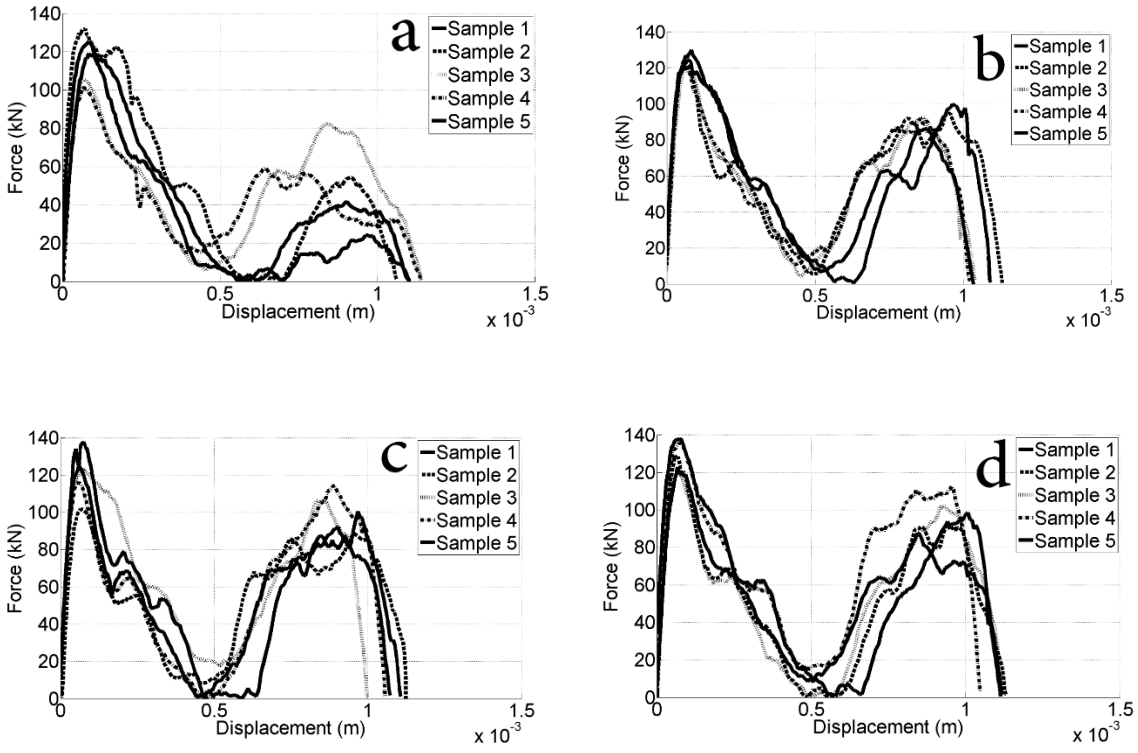

Figure 35 Force vs. displacement curves from single-button for a) non-heat shocked surface, b) 3 s heat shocked, c) 4 s heat shocked, and d) 6 s heat shocked surfaces of Kuru Grey.

The force-displacements curves of the triple-button tests are shown in Figure 36. The results show significant differences compared to the single-button curves, and clear second maxima are not observed in any of the plots. Nevertheless, the force-displacement curves

corresponding to 3 s and 4 s heat shocks (Figures 36b and 36c) have a similar shape with an intermediate drop in the applied force observed before the moderate increase towards the end of the test. The reason for the differences between the single-button and triple-button tests can be found from the geometry of the buttons. Firstly, in the triple-button tests the indenters are significantly smaller compared to the single-button test indenter. Accordingly, the amount of powder and dust produced in the triple-button tests is considerably smaller. In addition, as the area between the indenters is damaged and material is removed also from that area, it provides a space for the produced powder to escape from the crater. However, it should be noted that in the triple-button tests the bar is not moving the same distance as in the single-button tests. Therefore, it is not possible ascertain that the hypothesis above is definitely the reason for absence of the second maximum in the graphs.

The bit-rock interaction force for the samples without any heat shock is almost the same as for the samples with a 3 s heat shock. The results show rather low scatter, although, the indenter penetrates somewhat deeper into the rock with pre-existing damage caused by the heat shock. The degree of scatter increases as the duration of the heat shock increases to 4 s, although the level of the measured force remains almost the same. The scatter in the results further increases significantly when the duration of the thermal shock reaches 6 s. One hypothesis to explain the increased scatter is increase in the side chipping, which manifests itself as sharp drop in the force-displacement curves, as shown for example by Tkalich et al. [164], who performed static indentation tests on Kuru Grey granite. After such a drop, the force level increases and the loading process continues until the next drop caused by another side chipping event. It was mentioned before that a typical force-displacement curve tends to move backwards at the end of the test, although this behavior is not observed in this work. Instead, a sharp drop at the end of the tests is visible, but it simply indicates the end of the movement of incident bar, i.e., the end of the loading pulse. A typical force-displacement curve reaches to a maximum point and then turns back towards lower displacement values, which resembles the unloading of the sample. However, this behavior was not observed in any single-button nor in the triple-button test results. Nevertheless, Saksala et al. [156] reported that as the velocity of the impact increases, the curves tend to lose their typical shape and the unloading part starts to fade away.

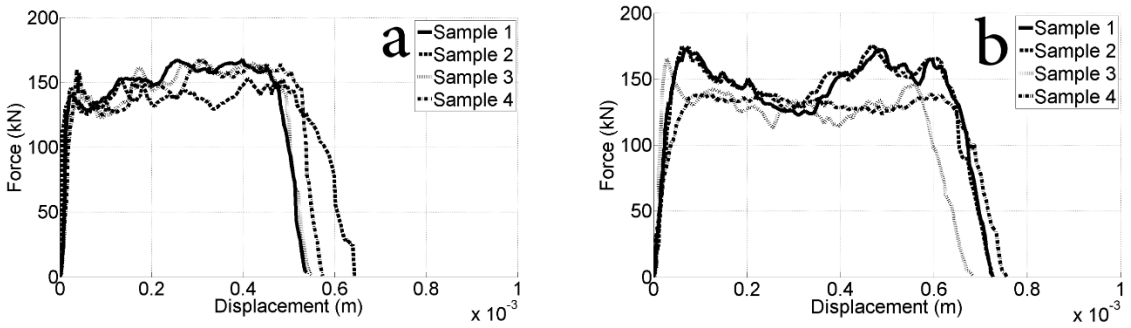

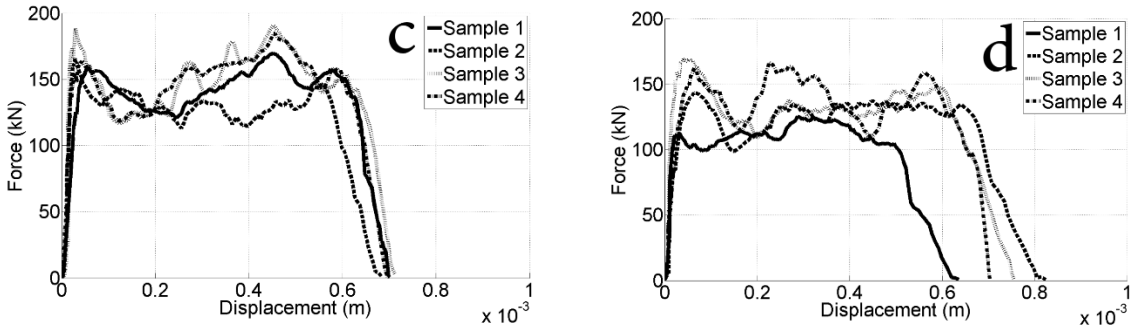

Figure 36 Force vs displacement data from the triple-button tests for a) non-heat shocked surface, b) 3 s heat shocked surface, c) 4 s heat shocked surface, and d) 6 s heat shocked surface of Kuru Grey.

Possible explanation for this observation is also that the increase of the impact speed leads to an increased damaged zone in front of the indenter(s), and the damaged material cannot push the bar elastically backward. Figure 37 shows the damaged area during the dynamic indentation test with a triple-button bit.

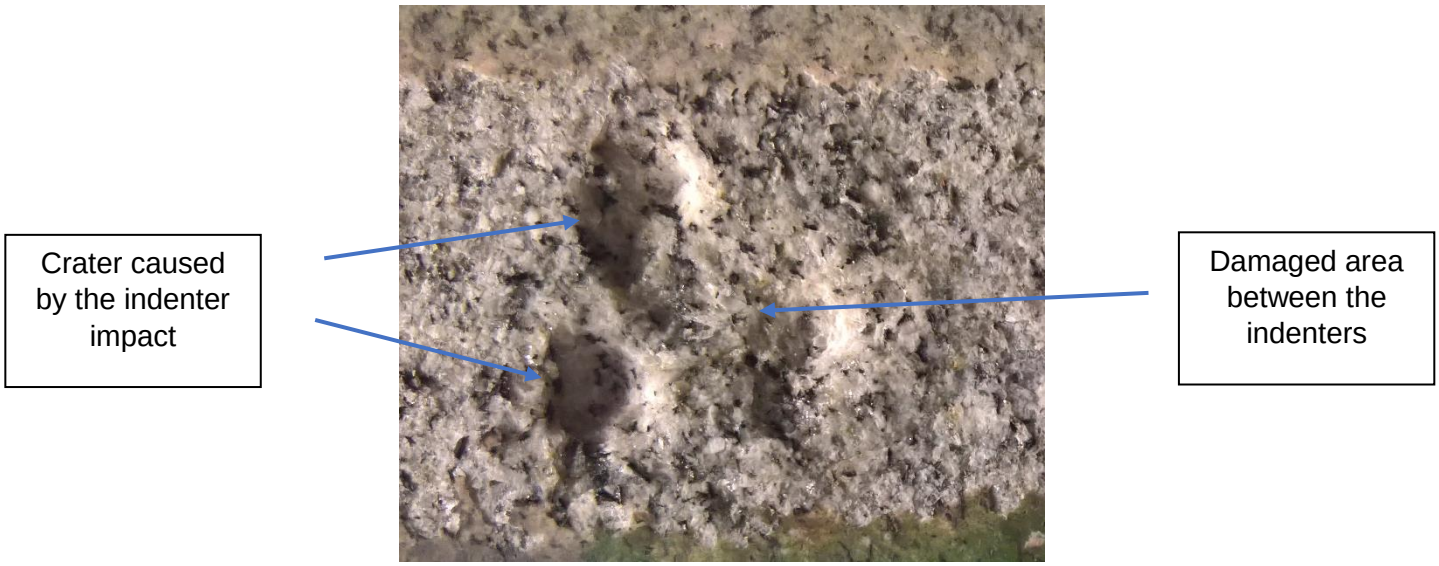

Figure 37 Damaged area on the surface of a 6 second heat shocked block sample of Kuru Grey.

7.9 Characterization of the dynamic indentation craters with optical profilometry

The presented force-displacement curves would suggest that the heat shocks do not have too much effects on the rock behavior. However, these curves do not provide much, of any, information about the volume of the crater and the true extent of the material removal. Since the rock has been already weakened by the heat shock, the indenters not only remove material in the direction of the applied force but also the side chipping increases remarkably, which is not evident in the force-displacement curves (apart from the 'serrated flow' discussed in previous paragraph). For this reason, profilometer analyses were carried out, clearly indicating that the volume of the craters increases with the duration of the thermal shock. As an example,

a crater formed during the dynamic indentation process on the sample with a heat shock of 6 second is shown in Figure 38.

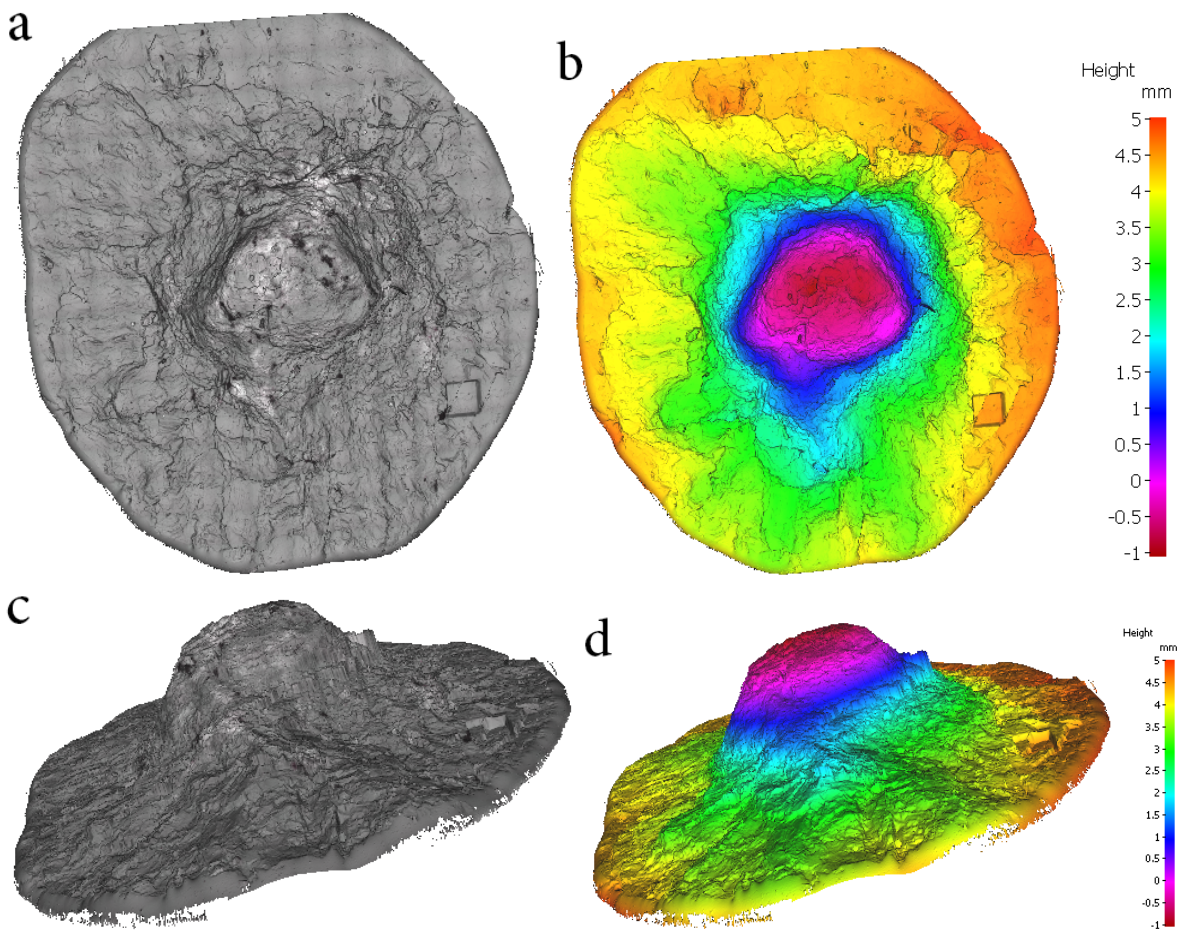

Figure 38 3D profilometry images of the crater formed during an indentation on a 6 s heat shocked surface of Kuru Grey. a) perpendicular view of the raw image, b) perpendicular view of the mapped raw image, c) a side view of the raw image, and d) a side view of the mapped raw image.

Table 6 summarizes the results obtained from the crater volume measurements showing that by increasing the duration of the heat shock, the volume of the crater increases as well. This increase is actually quite notable, i.e., 14%, 66%, and 77% for the 3 s, 4 s, and 6 s heat shocks, respectively. It should, however, be noted that the dynamic indentation process described in this work is actually not a single indentation test because the rock gets impacted several times by the pulse going back-and-forth in the incident bar. However, the force-displacement curves shown in Figure 38 only show the first impact while the volume of the crater is the results of all impacts. Nonetheless, the first impact causes the main damage and the rest of the impacts mainly compact the powder and the dust, which are produced from the first impact. The error in the crater volume determinations caused by the subsequent impacts is assumed to be relatively small and essentially similar for all the tests, so at least the relative differences observed in the crater volume are believed to be reliable.

Table 6 Volume of the craters caused by the dynamic indentation of non-heat shocked and heat shocked surfaces of Kuru Grey (in mm^3).

	0 s	3 s	4 s	6 s
	197.14	291.33	301.77	285.61
	202.63	261.56	305.1	329.69
	200.3	277.72	381.88	375.4
	188.35	227.15	399	449.52
	196.12	226.66	254.43	391.79
Average	**196.91**	**256.88**	**316.43**	**366.4**
STDEV	**5.435**	**29.32**	**47.39**	**62.27**

By knowing the work done by indenter, i.e. the area under the force-displacement curve and the volume of the crater, it is possible to calculate the specific destruction work. Thuro and Spaun [165] introduced the concept of destruction work in order to quantify the amount of mechanical work, which is need to remove a unit volume from the surface of the rock. Since in the single-button indentation tests the force-displacement curves show second maxima consistently, the destruction work was calculated separately for the first part of the curve covering the first peak and half of the following valley, and for the entire measured curve. The destruction work related to the first part of the curve is from here on called the primary specific destruction work, while the destruction work calculated for the whole measured curve will be called the total specific destruction work.

The specific destruction work calculated for the single-button tests is shown in Figure 39. The graph indicates that the destruction work decreases as the duration of the heat shock increases. This observation is of course expected even though it cannot be seen directly from the force-displacement curves. Also from Figure 39 it can be seen that the destruction work decreases at a faster rate when the duration of the heat shock reaches to four seconds. The reduction in the total destruction work compared to the non-heat shocked samples is about 6%, 20%, and 30% for 3 s, 4 s and 6 s heat shocks, respectively. It should be once again mentioned that the single-button tests do not simulate the real life situation, but these tests provide useful information for the numerical and modeling exercises of the bit-rock interactions. The decrease in the specific destruction work becomes less pronounced as the duration of the thermal shock increases further (from 4 s to 6 s). One possible explanation for this observation is that the damage on the sample's surface is already so severe that creating more damage does not facilitate additional material removal during the dynamic indentation. Another possible explanation is that heat shocks longer than four seconds does not add more cracks and damage to the surface as the excess damaged material is removed from the surface by the plasma spray.

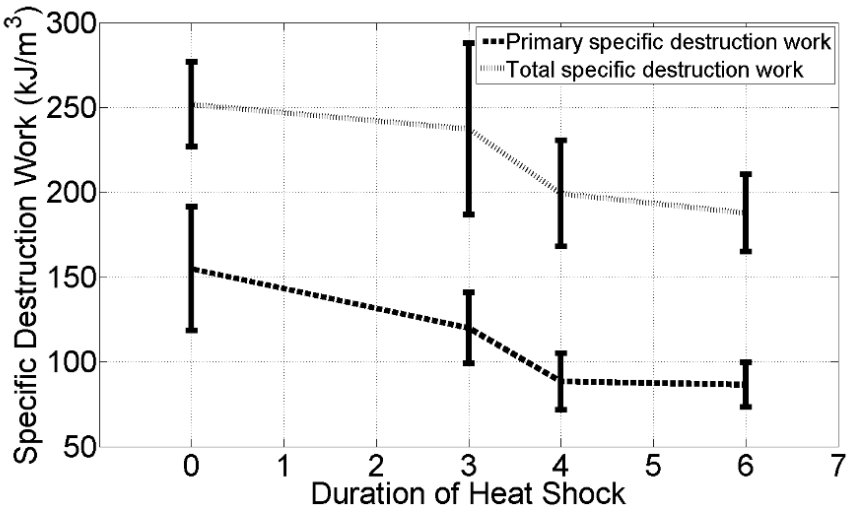

Figure 39 Specific destruction work for the first peak (primary) and for the complete force-displacement curve (total) obtained from the single-button indentation tests.

The destruction work was calculated also for the triple-button tests using the same procedure as for the single-button tests. Figure 40 shows a crater formed after the triple-button tests and Figure 41 the specific destruction work and the depth of craters caused by the impacts. The decrease in the specific destruction work for the thermally shocked samples compared to the non-heat-shocked samples is about 3%, 11%, and 30% for the 3 s, 4 s, and 6 s thermal shocks, respectively. The force-displacement curves obtained from the triple-button tests show a consistency in the shape for all the tests. Consequently, the mechanical energy used in the tests remains at the same level but the volume of the crater becomes bigger as the duration of the heat shock increases, which leads to the decrease of the destruction work. The decrease in the destruction work is not yet too significant for the 3 s heat shocked sample, but becomes more pronounced after a 4 s heat shock. Additionally, the depth of the crater increases as the heat shock damage increases. Nevertheless, the volume of the crater increases at a much faster rate compared to the depth of the crater due to increasing side chipping and material removal between the indenters. The amount of removed material outside the contact area of the button and the rock has a significant importance and a strong effect on the rate of penetration in drilling. From the energy point of view, it is better to remove bigger pieces and larger chips from the bulk of the rock rather than to grind the rock into dust and powder, which has a very high specific surface area. The removed volume outside the contact area is a function of the speed of the impact, and it has been shown [156] that at the low impact speeds of 10 m/s and 16 m/s there is almost no material removal between the indenters for intact Kuru Grey granite. On the other hand, increasing the impact velocity to 22 m/s leads to chipping of the rock between the buttons in 50% of the tests. In this work, the striker speed of 35 m/s (impact speed of 16 m/s) caused the material removal between the buttons in all tests. Moreover, according to the obtained results it is evident that the pre-existing damage has an impact on the side chipping and material removal from between the buttons. Based on the preliminary X-ray CT scan analysis on the heat shocked samples, the damage cause by the heat shock is limited to the depth of tens of microns from the surface of the samples. Consequently, it can be concluded that the side chipping will be significantly affected by a damaged layer as thin as 50-100 microns on the surface.

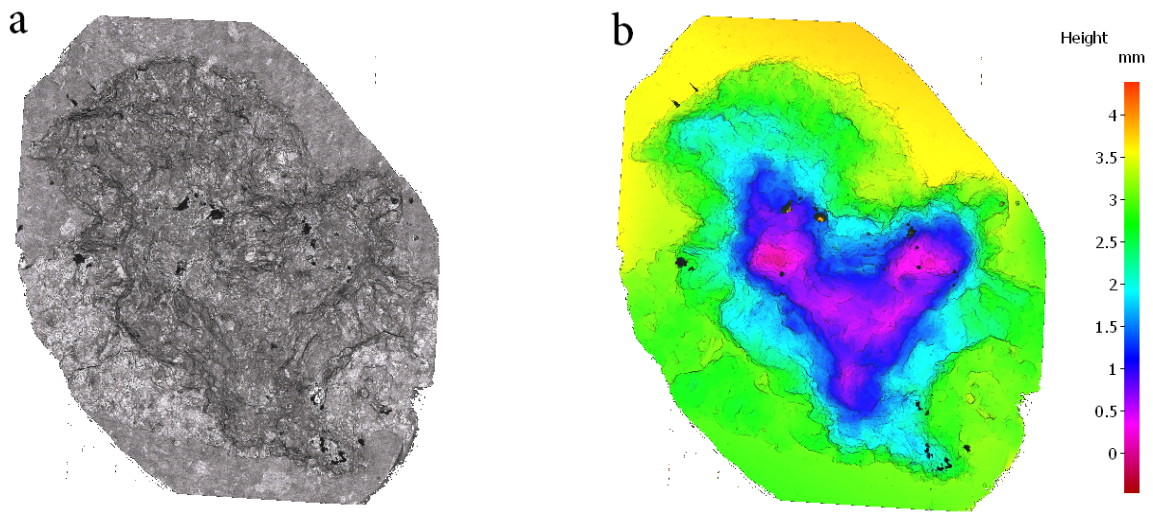

Figure 40 3D profilometry images of a crater formed during an indentation on a 6 s heat shocked surface. a) Perpendicular view of the raw image, b) perpendicular view of the mapped raw image

The triple-button tests can be considered as a simplified version of full-scale drilling, and therefore, they provide also an opportunity for the evaluation and assessment of the actual drilling events. In general, the engineers and scientist are more interested in the overall drilling rate and the rate of penetration, which can be extracted from the force-displacement curve. However, based on this work the bit-rock interaction forces are not very sensitive to small changes in the rock strength. On the other hand, the effects of pre-existing damage and the rock strength are clearly visible in the removed volume and especially in the side chipping and material removal from between the buttons.

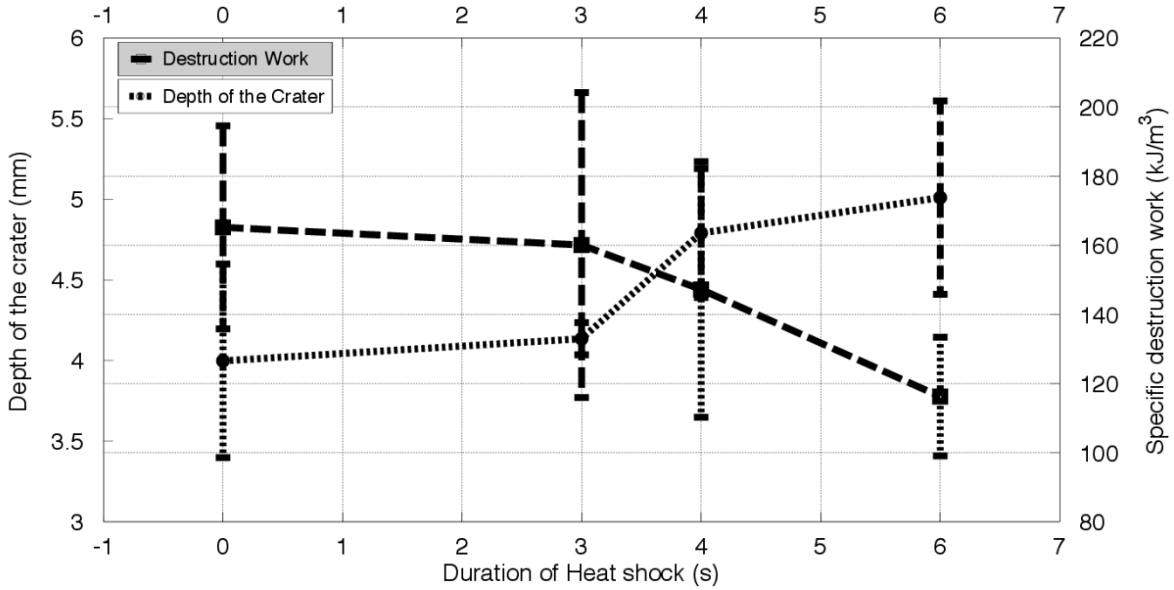

Figure 41 Specific destruction work and the depth of the crater as a function of the duration of the heat shock for triple-button indentation tests on Kuru Grey.

8. Concluding remarks and research questions revisited

The aim of this work was to modify the rock structure by heat treatments and to develop methodology for the evaluation of the effects of the heat shocks on the tensile strength of rocks based on surface cracks and surface damage and to provide reliable data for modeling purposes. One reason for the selected approach is that the characterization of surface cracks is much easier and faster than the full 3D characterization of the whole volume of the sample. Additionally, the full 3D characterization of the heat treated samples revealed that the damage caused by the heat shock is mostly limited to the very surface of the samples. Therefore, the surface characterization provides an adequate and fast evaluation of the damage caused by the thermal shock and to be used for the prediction the changes in the mechanical properties of the rocks.

The novel scientific contributions resulting from this work are as follows:

1. A methodology was developed to characterize and quantify the surface damage caused by a thermal shock to the rock material. Analyzing the change of the fractal dimension was proven an accurate and fast method to estimate the change in the strength of the material due to a heat shock.
2. The effects of the heat shocks on the microstructural features of the rocks were studied using optical images and scanning electron microscopy. The analysis revealed a difference between the different rocks' microstructures and how these microstructural features are affected by the heat shocks.
3. Quasi-static and dynamic mechanical testing was conducted on the rock material to study the effect of the testing conditions on the mechanical behavior of the rock. At a higher strain rate The strength of the rocks decreases faster by increasing the duration of the heat shock. Therefore, the strain rate sensitivity of the studied rocks decreases with increasing fractal dimension.
4. In addition to dynamic mechanical testing, digital image correlation was used to study the behavior of the rock during dynamic deformation. Of the two types of rocks tested in this work, the maximum surface strain of Balmoral Red prior to fracture was observed to decrease continuously with an increase of the fractal dimension. For Kuru Grey, the dynamic test results indicate that the maximum surface strain first decreases but then reaches a saturation point at higher values of the fractal dimension.
5. During dynamic indentation tests on large block samples lean to an increase in, increasing duration of the heat shock the size of the craters created by the impact. However, the level of the applied force remained almost at the same level irrespective of the sample condition. Although the force-displacement curves provide useful information about the rate of penetration into the rock, they do not correlate well with the mechanical properties of the rock nor do they describe the size of the craters and the extent of material removal.

Four research questions were introduced in Chapter 1. Those questions are revisited here and an answer to each question is provided based on the results obtained during the course of this work.

1. *What are the effects of heat shocks on the microstructural features and mechanical behavior of rock, and what are the effects of the testing condition on the rock's mechanical behavior?*

Two different rocks were studied in this work. Even though both rocks have a quite similar tensile strength before applying the heat shock, they clearly exhibit different tensile strengths after applying the thermal shocks. The reason for this can be found from the different microstructural response of the studied rocks to the heat shocks. In the case of Balmoral Red, after the thermal shock the existing cracks in the structure become longer and more cracks are introduced into the structure. However, the behavior of Kuru Grey is a bit different in a sense that in addition to introducing new cracks into the structure, the amount of porosity also increases. These pores can act as barriers to crack propagation by blunting the crack tips. Therefore, the tensile strength of Balmoral Red continues to decrease with increasing duration of the heat shock, while for Kuru Grey, the strength reaches a saturation point. Consequently, it is evident that the different rock microstructures exhibit different responses to heat shocks, which leads to different mechanical responses of the rock during the loading process.

Also changing of the testing environment leads to a different mechanical response of the rock materials. It was shown that changing the loading rate from quasi-static to dynamic has a significant impact on the mechanical behavior of the rock. In the quasi-static region, rocks without any thermal shock show quite consistent behavior. However, after applying a heat shock, significant scatter can be observed in the mechanical behavior of the rock. The situation is different in the dynamic loading conditions, as a significant part of the scatter in the mechanical behavior fades away and more consistent behavior is observed.

In conclusion, the mechanical behavior of the rocks is highly dependent on the microstructure and the testing conditions, and therefore, the rock features and testing condition variables have to be taken carefully into account before conducting the mechanical testing.

2. *How can one generate the desired cracks and crack patterns in the rock structure, and how can these crack patterns be characterized in an accurate, quantifiable, and efficient way?*

Two different methods were employed in this work to produce cracks and crack patterns; flame torch and plasma gun. Each methods generates different kind of patterns on the samples' surface. In the case of the flame torch, the number of cracks on the sample's surface and the complexity of the crack patterns increase, while use of the plasma plasma gun leads to the severe material removal from the surface of the samples.

A methodology was developed to characterize the surface damage caused by a heat shock. The fractal dimension of the surface crack patterns were obtained from optical images, which proved to be a fast, efficient, and accurate method to characterize the complex crack patterns on the surface of the rocks. Even though this method provides information only from the surface of the samples, it was shown to be sufficient for the fast estimation of the damage caused by the heat shock.

3. *Is there any correlation between the information obtained from the cracks and their patterns and the mechanical behavior of the rock?*

Due to the nature of the rock, the fractal dimension determined before the application of the fractal dimension to the thermal shock shows a high level of scatter, which complicates the

use of the absolute values to explain the mechanical behavior of the rock. However, there appears to be a correlation between the *relative* increase of the fractal dimension due to the heat shock and the mechanical response of the tested material. This correlation can be used to estimate and predict the mechanical behavior of the rock after different thermal shock treatments.

4. *How can sufficient, reliable, and reproducible data for numerical simulations and modeling proposes be generated?*

One of the challenges in the simulations of the mechanical behavior of the rock is to provide reliable and sufficient amount of data with appropriate laboratory tests experiments. Since the rock materials exhibit a great amount of natural scatter in their behavior, it is a rather challenging task to generate reproducible data for numerical simulations. The methodology developed and used in this work, however, seems to provide sufficiently adequate, reliable, and reproducible data for many simulating purposes.

References

[1] D. Lindroth, R. Morrell and J. Blair, "Microwave assisted hard rock cutting". United States of America Patent 5,033,144, 26 03 1991.

[2] K. Perry, I. Salehi and H. Abbasi, "Laser assisted drilling". United States of America Patent US 2010/0078414 A1, 01 04 2010.

[3] R. An, Y. Li, Y. Dou, D. Liu, H. Yang and Q. Gong, "Water-assisted drilling of microfluidic chambers inside silica glass with femtosecond laser pulses," *Applied Physics A,* vol. 83, no. 1, pp. 27-29, 2006.

[4] J. C. Fair, "Development of High-Pressure Abrasive-Jet Drilling," *J Petrol Technol,* vol. 33, no. 08, pp. 1-11, 1981.

[5] D. Miller and A. Ball, "Rock drilling with impregnated diamond microbits—An experimental study," *Int. J. Rock Mech. Min. Sci. Abstr.,* vol. 27, no. 5, pp. 363-371, 1990.

[6] J. J. Kolle, R. Otta and D. Stang, "Laboratory and Field Testing of an Ultra-High-Pressure, Jet-Assisted Drilling System," in *Society of Petroleum Engineers*, Amsterdam, 1991.

[7] S. Veenhuizen, T. O'Hanlon, D. Kelley and J. Aslakson, "Ultra-High Pressure Down Hole Pump for Jet-Assisted Drilling," in *Society of Petroleum Engineers*, New Orleans, 1996.

[8] J. Wilson, Minerals and Rocks, Telluride: J. Richard Wilson & Ventus Publishing, 2010.

[9] K. Cox, J. Bell and R. Pankhurst, The Interpretation of Igneous Rocks, London: Champan & Hall, 1993.

[10] U. D. o. Transportation, "Rock and Mineral Indentification for Engineers," Federal Highway Administration, New Jersey, 1991.

[11] J. Jaeger, N. Cook and R. Zimmerman, Fundamentals of rock mechanics, Malden, Blackwell, 2007.

[12] N. Cristescu, "Rock rheology," in *Mechanics of elastic and inelastic solids*, New York, Springer, 1989, pp. 5-16.

[13] E. Hoek and E. Brown, Underground excavations in rock, Abingdon, Taylor & Francis, 1980.

[14] Z. Bieniawski, Rock mechanics design in mining and tunnelling, Rotterdam, Balkema, 1984.

[15] Z. Bazant and E. Chen, "Scaling of structural failure," *Applied Mechanics Reviews ,* vol. 50, no. 10, pp. 593-627, 1997.

[16] Z. Bazant and J. Planas, Fracture and size effect in concrete and other quasi-brittle materials, Boca Raton, CRC Press, 1997.

[17] M. Aubertin, L. Li and R. Simon, "A multiaxial stress criterion for short- and long-term strength of isotropic rock media," *International Journal of Rock Mechanics and Mining Sciences,* vol. 37, no. 8, pp. 1169-1193, 2000.

[18] T. Y. Irfan and W. Dearman, "The engineering petrography of a weathered granite in Cornwall, England," *Quarterly Journal of Engineering Geology,* pp. 233-244, 1978.

[19] R. Williard and J. McWilliams, "Microstructural techniques in the study of physical properties of rocks," *International Journal of Rock Mechanics,* vol. 6, no. 1, pp. 1-12, 1969.

[20] F. Mendes, L. Aires-Barros and F. Rodrigues, "The Use of Modal Analysis in Mechanical Characterization of Rock Masses," in *1st international Congress of Rock Mechanics*, Lisbon, 1966.

[21] A. Marfunin, Advanced mineralogy: Volume 1, New York, Springer Science & Business Media, 2012.

[22] J. Hogan, R. Rogers, J. Spray and S. Boonsue, "Dynamic fragmentation of granite for impact energies of 6-28J," *Engineering Fracture Mechanics,* vol. 79, pp. 103-125, 2012.

[23] H. Wenk and J. Christie, "Comments on the interpretation of deformation textures in rocks," *Journal of Structural Geology,* vol. 13, no. 10, pp. 1091-1110, 1991.

[24] R. Wong, K. Chau and P. Wang, "Microcracking and grain size effect in Yuen Long marbles," *International Journal of Rock Mechanics and Mining Sciences & Geomechanics Abstracts,* vol. 33, no. 5, pp. 497-485, 1991.

[25] W. Olsson, "Grain size dependence of yield stress in marble," *Journal of Geophysical Research,* vol. 79, pp. 4859-4862, 1974.

[26] W. Brace, "Dependence of Fracture Strength of Rocks on Grain Size," in *The 4th U.S. Symposium on Rock Mechanics* , University Park, Pennsylvania, 1961.

[27] A. Tugrul and I. Zarif, "Correlation of mineralogical and textural characteristics with engineering properties of selected granitic rocks from Turkey," *Eng. Geol.,* vol. 51, no. 4, pp. 303-317, 1999.

[28] T. Onodera and H. A. Kumara, "Relation between texture and mechanical properties of crystalline rocks," *Engineering Geology,* pp. 173-177, 1980.

[29] R. Pirkryl, "Some microstructural aspects of strength variation in rocks," *International Journal of Rock Mechanics and Mining Sciences,* vol. 38, no. 5, pp. 671-682, 2001.

[30] A. Mardoukhi, Y. Mardoukhi, M. Hokka and V. Kuokkala, "Effects of heat shock on the dynamic tensile behavior of granitic rock," *Rock mechanics and rock engineering,* vol. 50, no. 5, pp. 1171-1182, 2017.

[31] R. Prikryl, "Assessment of rock geomechanical quality by quantitative rock fabric coefficients: Limitations and possible source of misinterpretations," *Engineering Geology,* vol. 87, no. 3-4, pp. 149-162, 2006.

[32] D. Howarth and J. Rowlands, "The effect of rock texture on drillability and mechanical rock properties," in *Proceedings of 6th Congress of the International Society of Rock Mechanics*, Montreal, 1987.

[33] W. Dreyer, "The Science of Rock Mechanics. Part I. The Strength Properties of Rocks," in *Series on Rock and Soil Mechanics*, Clausthal , Trans Tech Publications, 1973, p. 500.

[34] M. Haney and A. Shakoor, "The relationship between tensile and compressive strengths for selected sandstones as influenced by index properties and petrographic characteristics," in *Proceedings of 7th International IAEG Congress*, Lisbon, 1994.

[35] R. Goodman, Introduction to Rock Mechanics, New York, John Wiley and Sons, 1989.

[36] D. Dunn, L. LaFountain and R. Jackson, "Porosity dependence and mechanism of brittle fracture in sandstones," *Journal of Geophysical Research,* vol. 78, no. 14, pp. 2403-2417, 1973.

[37] K. Hoshino, "Effect of Porosity on the Strength of the Clastic Sedimentary Rocks," in *Proceedings of the 3rd International Congress on Rock Mechanics*, Denver, 1974.

[38] W. Zhu, P. Baud and T.-f. Wong, "Micromechanics of cataclastic pore collapse in limestone," *Journal of Geophysical Research,* vol. 115, no. B4, 2010.

[39] P. Baud, T. F. Wong and W. Zhu, "Effects of porosity and crack density on the compressive strength of rocks," *International Journal of Rock Mchanics & Mining,* vol. 67, pp. 202-211, 2014.

[40] R. Dwivedi, R. Goel, V. Prasad and A. Sinha, "Thermo-mechanical properties of Indian and other granites," *Int. J. Rock Mech. Min. Sci.,* vol. 45, no. 3, pp. 303-315, 2008.

[41] S. Liu and J. Xu, "Mechanical properties of Qinling biotite granite after high temperature treatment," *Int. J. Rock Mech. Min. Sci.,* vol. 71, pp. 188-193, 2014.

[42] S. Bauer and B. Johnson, "Effects Of Slow Uniform Heating On The Physical Properties Of The Westerly And Charcoal Granites," in *20th U.S. Symposium on Rock Mechanics*, Austin, 1979.

[43] D. Roy and T. Singh, "Effect of Heat Treatment and Layer Orientation on the Tensile Strength of a Crystalline Rock Under Brazilian Test Condition," *Rock Mechanics and Rock Engineering,* vol. 49, no. 5, pp. 1663-1677, 2016.

[44] N. Sengun, "Influence of thermal damage on the physical and mechanical properties of carbonate rocks," *Arabian J. Geosci.,* vol. 7, no. 12, pp. 5543-5551, 2014.

[45] B. Mahanta, T. Singh and P. Ranjoth, "Influence of thermal treatment on mode I fracture toughness of certain Indian rocks," *Eng. Geol.,* vol. 210, pp. 103-114, 2016.

[46] A. Verma, M. Jha, S. Maheshwar, T. Singh and R. Bajpai, "Temperature-dependent thermophysical properties of Ganurgarh shales from Bhander group, India," *Environ. Earth Sci.,* vol. 75, no. 4, pp. 1-11, 2016.

[47] V. Vishal, S. Pradhan and T. Singh, "Tensile Strength of Rock Under Elevated Temperatures," *Geotechnical and Geological Engineering,* vol. 29, pp. 1127-1133, 2011.

[48] Q. Rao, Z. Wang, H. Xie and Q. Xie, "Experimental study of mechanical properties of sandstone at high temperature," *Journal of Central South University of Technology,* vol. 14, no. 1, pp. 478-483, 2007.

[49] T. Yin, X. Li, W. Cao and K. Xia, "Effects of Thermal Treatment on Tensile Strength of Laurentian Granite Using Brazilian Test," *Rock Mechanics and Rock Engineering,* vol. 48, no. 6, pp. 2213-2223, 2015.

[50] N. Sirdesai, T. Singh, P. Ranjith and R. Singh, "Effect of Varied Durations of Thermal Treatment on the Tensile Strength of Red Sandstone," *Rock Mechanics and Rock Engineering,* pp. 1-9, 2016.

[51] S. Cho, Y. Ogata and K. Kaneko, "Strain–rate dependency of the dynamic tensile strength of rock," *International journal of rock mechanics and mining sciences,* vol. 40, no. 5, pp. 763-777, 2003.

[52] D. Singh, V. Sastry and P. Srinivas, "Effect of Strain Rate On Mechanical Behaviour of Rocks," in *International Society for Rock Mechanics*, Pau, 1989.

[53] T. Saksala, M. Hokka, V. Kuokkala and J. Mäkinen, "Numerical modeling and experimentation of dynamic Brazilian disc test on KURU granite," *International Journal of Rock Mechanics & Mining Sciences,* vol. 59, pp. 128-138, 2013.

[54] K. Xia, M. Nasseri, B. Mohanty, F. Lu, R. Chen and S. Luo, "Effects of microstructures on dynamic compression of Barre granite," *International journal of rock mechanics and mining sciences,* vol. 45, no. 6, pp. 879-887, 2008.

[55] S. Liu and J. Xu, "Effect of strain rate on the dynamic compressive mechanical behaviors of rock materials subjected to high temperatures," *Effect of strain rate on the dynamic compressive mechanical behaviors of rock materials subjected to high temperatures,* vol. 82, pp. 28-38, 2015.

[56] F. Dai and K. Xia, "Laboratory measurements of the rate dependence of the fracture toughness anisotropy of Barre granite," *International journal of rock mechanics and mining sciences,* vol. 60, pp. 57-65, 2013.

[57] F. Dai, K. Xia, H. Zheng and Y. Wang, "Determination of dynamic rock mode-I fracture parameters using cracked chevron notched semi-circular bend specimens," *Engineering Fracture Mechanics,* vol. 78, no. 15, pp. 2633-2644, 2011.

[58] C. Liang, S. Wu, X. Li and P. Xin, "Effect of strain rate on the fracture characteristics and mesoscopic failure mechanisms of granite," *International journal of rock mechanics and mining sciences,* vol. 76, pp. 146-154, 2015.

[59] W. Goldsmith, J. Sackman and C. Ewarts, "Static and dynamic fracture strength of Barre granite," *International Journal of Rock Mechanics and Mining Sciences & Geomechanics Abstracts,* vol. 13, no. 11, pp. 303-309, 1976.

[60] W. Brace and A. Jones, "Comparison of uniaxial deformation in shock and static loading of three rocks," *Journal of geophysical research,* vol. 76, no. 20, pp. 4913-4921, 1971.

[61] R. Perkins and S. Green, "Uniaxial stress behavior of porphyritic tonalite at strain rates to 10^3/second," *International Journal of Rock Mechanics and Mining Sciences & Geomechanics Abstracts,* vol. 7, no. 5, pp. 529-535, 1970.

[62] A. Kumar, "The effects of stress rate and temperature on the strength of Basalt and granite," *Geophysics,* vol. 33, no. 3, pp. 501-510, 1968.

[63] M. Hokka, J. Black, D. Tkalich, M. Fourmeau, A. Kane, N. Hoang, C. Li, W. Chen and V. Kuokkala, "Effects of strain rate and confining pressure on the compressive behavior of Kuru granite," *International Journal of Impact Engineering,* vol. 91, pp. 183-193, 2016.

[64] K. Hashiba, S. Okubo and K. Fukui, "A new testing method for investigating the loading rate dependency of peak and residual rock strength," *International Journal of Rock Mechanics and Mining Sciences,* vol. 43, no. 6, pp. 894-904, 2006.

[65] O. Sano, I. Ito and M. Terada, "Influence of strain rate on dilatancy and strength of Oshima granite under uniaxial compression," *Journal of geophysical research,* vol. 86, no. B10, pp. 9299-9311, 1981.

[66] K. Shin, S. Okubo, K. Fukui and K. Hashiba, "Variation in strength and creep life of six Japanese rocks," *International Journal of Rock Mechanics and Mining Sciences,* vol. 42, no. 2, pp. 251-260, 2005.

[67] K. Fukui, S. Okubo and A. Ogawa, "Some aspects of loading-rate dependency of Sanjome andesite strengths," *nternational journal of rock mechanics and mining sciences,* vol. 41, no. 7, pp. 1215-1219, 2004.

[68] B. Wilkins, "The long-term strength of plutonic rock," *International Journal of Rock Mechanics and Mining Sciences & Geomechanics Abstracts,* vol. 24, no. 6, pp. 379-380, 1987.

[69] E. Lajtai and L. Bielus, "Stress corrosion cracking of Lac du Bonnet granite in tension and compression," *Rock Mechanics and Rock Engineering,* vol. 19, no. 2, pp. 71-87, 1986.

[70] H. Kawakata, A. Cho, T. Kiyama, T. Yanagidani, K. Kusunose and M. Shimada, "Three-dimensional observations of faulting process in Westerly granite under uniaxial and triaxial conditions by X-ray CT scan," *Tectonophysics,* vol. 313, no. 3, pp. 293-305, 1999.

[71] H. Kawakata, A. Cho, T. Yanagidani and M. Shimada, "The observations of faulting in Westerly granite under triaxial compression by X-ray CT scan," *International journal of rock mechanics and mining sciences,* vol. 34, no. 3-4, pp. 151e1-151e12, 1997.

[72] H. Li, J. Zhao and T. Li, "Triaxial testing on a granite at different strain rates and confining pressures," *International journal of rock mechanics and mining sciences,* vol. 36, no. 8, pp. 1057-1063, 1999.

[73] M. Peterson and T. Wong, Experimental Rock Deformation - The Brittle Field, New York, Springer, 2005.

[74] J. Jaeger, Elasticity, Fracture and Flow with Engineering and Geological Applications, London, Chapman & Hall, 1969.

[75] E. Fjaer and H. Ruistuen, "Impact of the intermediate principal stress on the strength of heterogeneous rock," *Journal of geophysical research,* vol. 107, no. B2, pp. ECV3-1-ECV3-10, 2002.

[76] D. Trollope, "Effective stress criteria of failure of rock masses," in *Society of rock mechanics*, Lisbon, 1966.

[77] A. Griffith, "The phenomena of rupture and flow in solids," *Philosophical transactions of Royal Society,* vol. 221, pp. 163-198, 1920.

[78] J. Jaeger and N. Cook, Fundamentals of rock mechanics, London, Chapman & Hall, 1979.

[79] S. Murrell and P. Digby, "The thermodynamics of brittle fracture initiation under triaxial stress," *International journal of fracture mechanics,* vol. 8, no. 2, pp. 167-173, 1972.

[80] J. Walsh and W. Brace, "A fracture criterion for brittle anisotropic rock.," *Journal of geophysical research,* vol. 59, no. 16, pp. 3449-3456, 1964.

[81] E. Hoek, "Fracture of anisotropic rock," *Journal of the South African Institute of Mining and Metallurgy,* vol. 64, no. 10, pp. 201-523, 1964.

[82] A. Griffith, "The theory of rupture," in *International congress of applied mechanics*, Delft, 1924.

[83] S. Murrell, "The theory of the propagation of elliptical Griffith cracks under various conditions of plane strain or plane stress: Part I," *British Journal of Applied Physics,* vol. 15, no. 10, pp. 1195-1210, 1964.

[84] S. Murrell, "The theory of the propagation of elliptical Griffith cracks under various conditions of plane strain or plane stress: Parts II and III," *British Journal of Applied Physics,* vol. 15, no. 10, pp. 1211-1223, 1964.

[85] E. Orowan, "Fracture and strength of solids," *Reports on progress in physics,* vol. 12, no. 1, pp. 185-232, 1949.

[86] H. Elliot, "An analysis of the conditions for rupture due to Griffith cracks," *Proceedings of the Physical Society of London,* vol. 59, no. 2, pp. 208-223, 1947.

[87] G. Barenblatt, "Concerning equilibrium cracks forming during brittle fracture. The stability of isolated cracks. Relationships with energetic theories," *Journal of Applied Mathematics and Mechanics,* vol. 23, no. 5, pp. 1273-1282, 1959.

[88] G. Barenblatt, "The Mathematical Theory of Equilibrium Cracks in Brittle Fracture," *Advances in Applied Mechanics,* vol. 7, pp. 55-129, 1962.

[89] M. Blekherman and V. Indenbom, "The griffith criterion in the microscopic theory of cracks," *Physica status solidi A,* vol. 23, no. 2, pp. 729-738, 1974.

[90] B. Lawn, Fracture of brittle solids, vol. 44, Cambridge, Cambridge University Press, 1993.

[91] J. Gilman, "Direct Measurements of the Surface Energies of Crystals," *Journal of Applied Physics,* vol. 31, no. 12, pp. 2208-2218, 1960.

[92] S. Pugh, "The fracture of brittle materials," *British Journal of Applied Physics,* vol. 18, no. 2, pp. 129-162, 1967.

[93] M. Oglesby, P. Gutshall and M. P. J, "Cleavage surface energy of selenite," *American Mineralogist,* vol. 61, pp. 295-298, 1976.

[94] A. Santhanam and Y. Gupta, "Cleavage surface energy of calcite," *International Journal of Rock Mechanics and Mining Sciences & Geomechanics Abstracts,* vol. 5, no. 3, pp. 253-259, 1968.

[95] M. Swain and B. Lawn, "Indentation fracture in brittle rocks and glasses," *International Journal of Rock Mechanics and Mining Sciences & Geomechanics Abstracts,* vol. 13, no. 11, pp. 311-319, 1976.

[96] W. Krech, "The energy balance theory and rock fracture energy measurements for uniaxial tension," in *Advances in rock mechanics*, Washington D.C., 1974.

[97] M. Friedman, J. Handin and G. Alani, "Fracture-surface energy of rocks," *International Journal of Rock Mechanics and Mining Sciences & Geomechanics Abstracts,* vol. 9, no. 6, pp. 757-764, 1972.

[98] D. Lockner, "The role of acoustic emission in the study of rock fracture," *International journal of rock mechanics and mining sciences,* vol. 30, no. 7, pp. 883-899, 1993.

[99] W. Doll, "Kinetics of the crack tip craze zone before and during fracture," *Polymer engineering and science,* vol. 24, no. 10, pp. 798-808, 1984.

[100] L. Freund, Dynamic fracture mechanics, Cambridge, Cambridge University Press, 1990.

[101] B. Kostrov and S. Das, Principles of Earthquake Source Mechanics, Cambridge, Cambridge University Press, 1988.

[102] Z. Bieniawski, "Fracture dynamics of rock," *International Journal of Fracture Mechanics,* vol. 4, no. 4, pp. 415-430, 1968.

[103] E. Hoek and Z. Bieniawski, "Brittle fracture propagation in rock under compression," *International Journal of Fracture Mechanics,* vol. 1, no. 3, pp. 137-155, 1965.

[104] W. Brace and E. Bombolakis, "A note on brittle crack growth in compression," *Journal of geophysical research,* vol. 68, no. 12, pp. 3709-3713, 1963.

[105] S. Murrell, "The strength of coal under triaxial compression," in *Mechanical properties of non-metallic brittle materials*, London, Butterworths, 1958, pp. 123-153.

[106] F. McClintock and J. Walsh, "Friction on Griffith cracks in rocks under pressure," in *US national congress of applied mechanics*, New York, 1962.

[107] S. Murrell, "A criterion for brittle fracture of rocks and concrete under triaxial stress," in *5th symposium of rock mechanics*, Oxford, 1963.

[108] S. Murrell, "The Effect of Triaxial Stress Systems on the Strength of Rocks at Atmospheric Temperatures," *Geophysical Journal International,* vol. 10, no. 3, pp. 231-281, 1965.

[109] S. Murrell and P. Digby, "The Theory of Brittle Fracture Initiation under Triaxial Stress Conditions—I," *Geophysical Journal International,* vol. 19, no. 4, pp. 309-334, 1970.

[110] S. Murrell and P. Digby, "The theory of brittle fracture initiation under triaxial stress conditions—II," *Geophysical Journal International,* vol. 19, no. 5, pp. 499-512, 1970.

[111] C. Coulomb, "Test on the applications of the rules of maxima and minima to some problems of statics related to architecture," *Acad. Roy. Sci. Mem. Math. Phys,* vol. 7, pp. 343-382, 1773.

[112] J. Labuz and A. Zang, "Mohr–Coulomb Failure Criterion," in *The ISRM Suggested Methods for Rock Characterization, Testing and Monitoring*, Springer, 2012, pp. 227-231.

[113] J. Labuz and A. Zang, "Mohr–Coulomb Failure Criterion," in *The ISRM Suggested Methods for Rock Characterization, Testing and Monitoring*, Springer, 2012, pp. 227-231.

[114] E. Hoek and E. Brown, "Emprical Strengh criterion for rock masses," *Journal of Geotechnical and Geoenvironmental Engineering,* vol. 106, no. GT9, p. ASCE 15715, 1980.

[115] E. Eberhardt, "The Hoek–Brown Failure Criterion," in *The ISRM Suggested Methods for Rock Characterization, Testing and Monitoring*, Springer, 2012, pp. 981-988.

[116] E. Hoek and E. Brown, "The Hoek–Brown failure criterion a 1988 update," in *Proceedings of 15th Canadian rock mechanics symposium*, Toronto, 1988.

[117] E. Hoek, D. Wood and S. Shah, "A modified Hoek–Brown criterion for jointed rock masses," in *Eurock 92*, Chester, 1992.

[118] E. Hoek, P. Kaiser and W. Bawden, Support of underground excavations in hard rock, Rotterdam, A.A. Balkema, 1995.

[119] E. Hoek, C. Carranza-Torres and B. Corkum, " Hoek–Brown failure criterion a 2002 edition," in *Proceedings of the Fifth North American Rock Mechanics Symposium*, Toronto, 2002.

[120] T. Blenkinsop, Deformation Microstructures and Mechanisms in Minerals and Rocks, Dordrecht, Kluwer academic publishers, 2007.

[121] P. Tapponnier and W. Brace, "Development of stress-induced microcracks in Westerly Granite," *International Journal of Rock Mechanics and Mining Sciences & Geomechanics Abstracts,* vol. 13, no. 4, pp. 103-112, 1976.

[122] R. L. Kranz, "Microcracks in Rocks: A Review," *Tectonophysics,* vol. 100, no. 1-3, pp. 449-480, 1983.

[123] B. Atkinson, "Subcritical crack growth in geological materials," *Journal of geophysical research,* vol. 89, no. B6, pp. 4077-4114, 1984.

[124] H. Horii and S. Nemat-Nasser, "Compression-Induced Microcrack Growth in Brittle Solids: Axial Splitting and Shear Failure," *Journal of Geophysical Research,* vol. 90, no. B4, pp. 3105-3125, 1985.

[125] H. Horil and S. Nemat-Nasser, "Brittle Failure in Compression: Splitting, Faulting and Brittle-Ductile Transition," *Philosophical transactions of the royal society A,* vol. 319, no. 1549, pp. 337-374, 1986.

[126] P. Baud, T. Reuschle and P. Charlez, "An improved wing crack model for the deformation and failure of rock in compression," *International Journal of Rock Mechanics and Mining Sciences & Geomechanics Abstracts,* vol. 33, no. 5, pp. 539-542, 1996.

[127] T. Wong and R. Biegel, "Effects of pressure on the micromechanics of faulting in San Marcos gabbro," *Journal of Structural Geology,* vol. 7, no. 6, pp. 737-749, 1985.

[128] W. Olsson and S. Peng, "Microcrack nucleation in marble," *International Journal of Rock Mechanics and Mining Sciences & Geomechanics Abstracts,* vol. 13, no. 2, pp. 53-59, 1976.

[129] D. Evans and S. White, "Microstructural and fabric studies from the rocks of the Moine Nappe, Eriboll, NW Scotland," *Journal of Structural Geology,* vol. 6, no. 4, pp. 369-389, 1984.

[130] A. Vollbrecht, S. Rust and K. Weber, "Development of microcracks in granites during cooling and uplift: examples from the Variscan basement in NE Bavaria, Germany," *Journal of Structural Geology,* vol. 13, no. 7, pp. 787-799, 1991.

[131] C. Chopin, "Coesite and pure pyrope in high-grade blueschists of the Western Alps: a first record and some consequences," *Contributions to Mineralogy and Petrology,* vol. 86, no. 2, pp. 107-118, 1984.

[132] X. Wang, J. Liou and H. Mao, "Coesite-bearing eclogite from the Dabie Mountains in central China," *Geology,* vol. 17, no. 12, pp. 1085-1088, 1989.

[133] K. Xia and W. Yao, "Dynamic rock tests using split Hopkinson (Kolsky) bar system – A review," *Journal of Rock Mech Geotec Eng,* vol. 7, no. 1, pp. 27-59, 2015.

[134] Q. Zhang and J. Zhao, "Determination of mechanical properties and full-field strain measurements of rock material under dynamic loads," *International Journal of Rock Mechanics and Mining Sciences,* vol. 60, pp. 423-439, 2013.

[135] P. Shewmon and V. Zackay, Response of Metals to High Velocity Deformation, New York: Interscience Publishers Inc., 1961.

[136] J. Hudson, E. Brown and F. Rummel, "The controlled failure of rock discs and rings loaded in diametral compression," *Int. J. Rock Mech. Min. Sci.,* vol. 9, no. 2, pp. 241-248, 1972.

[137] F. Carneiro and A. Barcellos, "Concrete tensile strength," *RILEM Bulletin,* vol. 13, pp. 99-125, 1953.

[138] H. Hertz, Gesammelte Werke, Leipzig, Aufbau, 1895.

[139] L. Japaridze, "Stress-deformed state of cylindrical specimens during indirect tensile strength testing," *Journal of Rock Mechanics and Geotechnical Engineering,* vol. 7, no. 5, pp. 509-518, 2015.

[140] H. Luodes and N. Luodes, "Suomen Kiviteollisuus Oy," Finska, 21 09 2015. [Online]. Available: http://www.finskastone.fi/images/docs/Finska_Balmoral_Red_fine_grained_2007.pdf. [Accessed 11 01 2017].

[141] M. Fourmeau, D. Gomon, R. Vacher, M. Hokka, A. Kane and V. Kuokkala, "Application of DIC technique for studies of Kuru granite rock under static and dynamic loading," in *20th European Conference on Fracture*, Trondheim, 2014.

[142] W. Brown and I. Parsons, "Alkali feldspars: ordering rates, phase transformation and behaviour diagrams for igneous rocks," *Mineral Mag.,* vol. 53, pp. 25-42, 1989.

[143] T. Gasparik, Phase Diagrams for Geoscientists: An Atlas of the Earth's Interior, 1 ed., New York, Springer, 2003.

[144] F. Hausdorff, "Dimension und äußeres Maß," *Mathematische Annalen,* vol. 79, no. 1, pp. 157-179, 1918.

[145] B. Mandelbrot, The fractal geometry of the nature, New York, Henry Holt and Company, 1982.

[146] J. Feder, Fractals (Physics of Solids and Liquids), New York, Plenum Press, 1988.

[147] A. Kak and M. Slaney, Principles of Computerized Tomographic Imaging, Philadelphia: Society for Industrial and Applied Mathematics, 2001.

[148] A. Giuliani, V. Komlev and F. Rustichelli, "Three-Dimensional Imaging by Microtomography of X-ray Synchrotron Radiation and Neutrons," in *Innovative technological materials*, Heidelberg, Springer, 2010, pp. 123-128.

[149] M. Apostol, Strain rate and Temperature Dependence of the Compression Behavior of FCC and BCC Metals, Tampere, Tampere University of Technology, 2007.

[150] D. Gorham and X. Wu, "An Empirical Method of Dispersion Correction in the Compressive Hopkinson Bar Test," *J. Phys. IV,* vol. 07, no. C3, pp. 223-228, 1997.

[151] F. Dai, S. Huang, K. Xia and Z. Tan, "Some Fundamental Issues in Dynamic Compression and Tension Tests of Rocks Using Split Hopkinson Pressure Bar," *Rock Mechanics and Rock Engineering,* vol. 43, no. 6, pp. 657-666, 2010.

[152] M. Sutton, J. Orteu and H. Schreier, Image Correlation for Shape, Motion and Deformation Measurement: basic concepts, theory and applications, New York: Springer, 2009.

[153] N. McCormick and J. Lord, "Digital Image Correlation," *Materials Today,* vol. 13, no. 12, pp. 52-54, 2010.

[154] B. Pan, A. Asundi, H. Xie and J. Gao, "Digital image correlation using iterative least squares and pointwise least squares for displacement field and strain field measurements," *Optics and Lasers in Engineering,* vol. 47, no. 7-8, pp. 865-874, 2009.

[155] S. Yoeyama and G. Murasawa, "Digital image correlation," in *Experimental mechanics*, Paris, Eoiss Publishers, 2009.

[156] T. Saksala, D. Gomon, M. Hokka and V.T.Kuokkala, "Numerical and experimental study of percussive drilling with a triple-button bit on Kuru granite," *International Journal of Impact Engineering,* vol. 72, pp. 56-66, 2014.

[157] J. Ma, H. Wang, L. Weng and G. Tan, "Effect of porous interlayers on crack deflection in ceramic laminates," *J. Eur. Ceram. Soc,* vol. 24, no. 5, pp. 825-831, 2004.

[158] E. Eberhardt, B. Stimpson and D. Stead, "Effects of Grain Size on the Initiation and Propagation Thresholds of Stress-induced Brittle Fractures," *Rock Mech Rock Eng,* vol. 32, no. 2, pp. 81-99, 1999.

[159] A. Lasalmonie and J. L. Strudel, "Influence of grain size on the mechanical behaviour of some high strength materials," *Mater. Sci.,* vol. 21, no. 6, pp. 1837-1852, 1986.

[160] D. Tkalich, M. Fourmeau, A. kane and C. L. G. Cailletaud, "Experimental and numerical study of Kuru granite under confined compression and indentation," *International Journal of Rock Mechanics and Mining Sciences,* vol. 87, pp. 55-68, 2016.

[161] K. Thuro and G. Spaun, "Introducing the `destruction work´ as a new rock property of toughness," in *Prediction and performance in rock mechanics and rock engineering*, Turin, 1996.

I

Effects of surface cracks and strain rate on the tensile behavior of Balmoral Red granite

Ahmad Mardoukhi, Mikko Hokka, Veli-Tapani Kuokkala

EDP Sciences 94 (2015) 02007

EPJ Web of Conferences **94**, 02007 (2015)
DOI: 10.1051/epjconf/20159402007

Effects of surface cracks and strain rate on the tensile behavior of Balmoral Red granite

Ahmad Mardoukhi[a], Mikko Hokka, and Veli-Tapani Kuokkala

Tampere University of Technology, Department of Material Science, POB 589, 33101 Tampere, Finland

Abstract. This paper presents an experimental procedure for studying the effects of surface cracks on the mechanical behavior of Balmoral Red granite under dynamic and quasi-static loading. Three different thermal shocks were applied on the surface of the Brazilian Disc test samples by keeping a flame torch at a fixed distance from the sample surface for 10, 30, and 60 seconds. Microscopy clearly shows that the number of the surface cracks increases with the duration of the thermal shock. After the thermal shock, the Brazilian Disc tests were performed using a servohydraulic materials testing machine and a compression Split Hopkinson Pressure Bar (SHPB) device. The results show that the tensile strength of the rock decreases and the rate sensitivity of the rock increases as more cracks are introduced to the structure. The DIC analysis of the Brazilian disc tests shows that the fracture of the sample initiates at the center of the samples or slightly closer to the incident bar contact point. This is followed by crushing of the samples at both contact points with the stress bars.

1. Introduction

Geothermal energy has recently attracted a lot of attention among engineers and scientists. However, there are still significant technological and scientific challenges to deal with before the lucrative energy resources can be easily reached. One of the biggest challenges is the drilling of the wells as deep as five kilometers to reach the required temperature to produce electricity. This challenge becomes bolder in the areas far away from the tectonic plate boundaries and in regions where the bedrock consists of hard rocks such as granite typically found in the Nordic countries. The current drilling technologies are based on rotary and percussive drilling. To improve the current drilling technology, the engineers need to know the rock strength and other properties at the drilling conditions, which include high hydrostatic pressures and elevated temperatures. However, since the straightforward experimental testing at these conditions is scientifically and practically very difficult, various numerical simulations and constitutive modeling approaches are currently being used for predicting the fracture behavior and the rock-tool interactions such as tool wear. Saksala et al. [6] studied the fracture behavior of Kuru granite by analyzing the Brazilian Disc tests with numerical and experimental approaches. In a separate study, Saksala et al. [7] extended the modeling approach to 3D and studied the bit-rock interactions and rock fracture in percussive drilling. Tang et al. [8,9] carried out numerical simulations to study the influence of microstructure on rock failure in uniaxial compression. They analyzed the effect of the structure heterogeneity of the rock on the fracture behavior and reported that the macro-fracture occurs abruptly as soon as the specimen reaches the peak stress. They also reported observations of micro-cracks over the whole volume of the specimens prior to the macro-fracture, and that the splitting failure is the dominant mechanism in uniaxial loading. However, due to the heterogeneous nature of rocks, other kinds of failure mechanisms were also observed.

The construction of material models and validation of the simulation results, however, relies on good scientific understanding of the material behavior as well as experimental data for calibrating the material models. The dynamic testing of rocks, however, is challenging, especially with the bar methods, since the material fails at very low strains. Therefore, it is very difficult to achieve the stress equilibrium, and cracks tend to initiate on the incident loading side of the sample before the other parts of the sample are fully loaded. Luckily, non-contact full-field deformation analysis techniques, such as photoelasticity, Moire, coherent gradient sensor, and digital image correlation (DIC) can be used to analyze the fracture behavior during a dynamic impact [1–5].

From the scientific point of view, there are still various problems in the understanding of rock behavior. For instance, the crack initiation, propagation, and coalescence are not completely understood, and many observations cannot be explained by any solid theory. Therefore, a material model that takes into account these factors and predicts the material behavior is needed for high quality drilling simulations. For example, the simulations of several repeated impacts of the drill on the same location of the rock surface require understanding of the effects of microcracks formed during the first impact. However, producing reliable experimental data that accurately describes the rock behavior at the impact speeds is not an easy task. Percussive drilling occurs at impact speeds of around 5–20 m/s, and each impact causes dynamic loading on the rock. Therefore, understanding of the

[a] Corresponding author: ahmad.mardoukhi@tut.fi

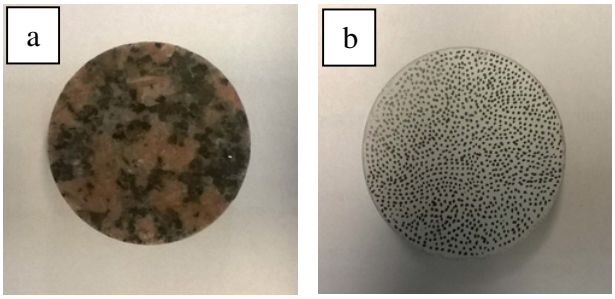

Figure 1. a) Natural surface of a Balmoral Red granite sample and b) DIC spackle pattern on the sample.

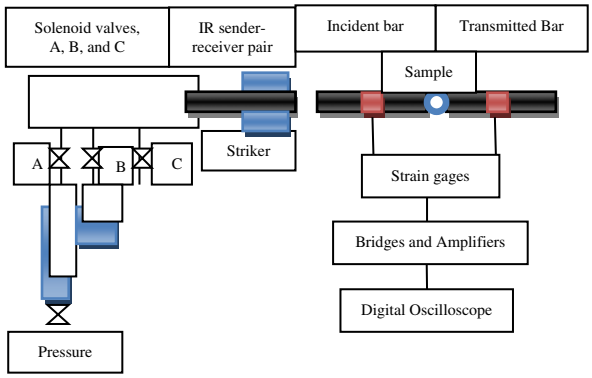

Figure 2. Schematic picture of the Split Hopkinson Pressure Bar device at Tampere University of Technology.

dynamic material behavior and obtaining numerical data are crucially important for the simulation purposes and material modeling, but also for the designing of new and more efficient drills and methods for faster and easier drilling. In this paper, the effects of microstructure, and especially the influence of surface cracks and the crack patterns on the mechanical behavior of the rock material were studied. The mechanical behavior of Balmoral Red granite was studied using Brazilian Disc (BD) tests at a wide range of strain rates. High speed photography and DIC were used to analyze the fracture behavior of the rock samples. The experimental setup, data acquisition, and interpretation of the results are presented in details.

2. Experimental

The material studied in this work was coarse grained Balmoral Red granite. This granite comprises Potash Feldspar, Quartz, Plagioclase, Biotite, and Hornblende. The mean value of the open porosity is 0.38% and the quasi-static compression strength is close to 180 MPa. The rock microstructure has no texture, the minerals are distributed homogeneously, and the mechanical properties are essentially isotropic. The Brazilian Disc samples with a diameter of 40.5 mm were cut from granite plates with a thickness of 21 mm. Figure 1a shows the natural surface of the BD sample, and Fig. 1b the sample with the DIC spackle pattern. The samples were tested at different strain rates, and the effect of surface cracks was studied by applying different heat shocks to the samples. Before the thermal shocks, liquid penetrant and optical microscopy were used to analyze the pattern of the surface cracks. Thermal shocks of 10, 30, and 60 seconds were applied on the BD samples by keeping the samples at a fixed distance from an oxygen-acetylene flame torch. After the heat shock, the samples were allowed to cool down to room temperature in air. After the cooling the liquid penetrant was re-applied on the surface to see the changes in the crack patterns caused by the thermal shock. The images were obtained using a stereomicroscope using UV light. Fractal dimensions of the surface crack patterns were calculated from the obtained images using a box counting method in Matlab.

The low strain tests were performed using an Instron 8800 servohydraulic materials testing machine with a displacement rate of 1 mm/s, and the high strain rate tests with a compression Split Hopkinson Pressure Bar (SHPB). The pressure bars were of Maraging steel with a diameter of 22 mm and a length of 1200 mm. The tests were performed using a 300 mm striker bar with an impact speed of 10 m/s. Each test was repeated five times. Two Photron SA-X2 high speed cameras were used to record the deformation and fracture of the samples during the high strain rate tests. As the rock surface itself does not provide a very strong contrast for the correlation algorithm, the surfaces of the samples were painted with white base coat and the black speckles were applied on it using a permanent ink marker, as shown in Fig. 1b. The images were recorded at 160 kfps, the size of the image at this rate being 256 *176 pixels. Two Decocool lights were used for illuminating the sample. The recorded images were analyzed using the LaVision StrainMaster (DaVis) 3D-DIC software. The displacements were calculated by comparing the deformed images to the first (reference) image using a step size of 9 pixels and a subset size of 25 pixels. The analyzed area was masked from the left reference image using a circular mask to cut out the outermost edges of the sample. The seed points were manually selected from areas that did not move much during the test. Figure 2 shows a schematic picture of the high strain rate testing setup.

The tensile stress in the center of the sample can be calculated when the force acting on the specimen is known. In this work, the forces on the sample surfaces were calculated from the incident and reflected pulses, and from the transmitted pulse. The forces on the incident and transmitted sides of the sample were compared with each other to verify stress equilibrium. However, the transmitted pulse typically contains fewer oscillations, and therefore it was used for calculating the tensile stress in the sample. The mathematical description for calculating the tensile stress from the contact forces is presented for example in ref. [6].

3. Results and discussion

Figure 3 shows an example of the optical analysis used to characterize the crack patterns on the sample surface. Figures 3a and 3c are the original grayscale optical images obtained from the sample before and after a 30 second heat shock, and Figs. 3b and 3d show the black and

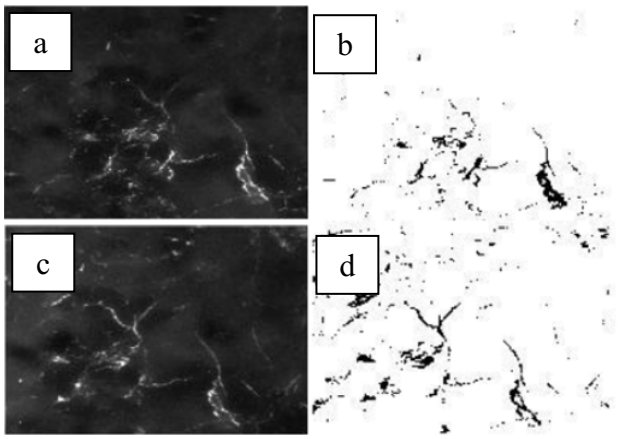

Figure 3. Optical images a) before and c) after the thermal shock, and identified cracks b) before and d) after the thermal shock.

Table 1. Fractal dimensions for the heat shocked samples.

	10 Seconds		30 Seconds		60 Seconds	
	Before	**After**	**Before**	**After**	**Before**	**After**
	1.3097	1.2583	1.1796	1.3631	1.4464	1.5132
	1.2779	1.349	1.2498	1.2783	0.9976	1.4426
	1.3254	1.3313	1.3819	1.4733	1.3375	1.4001
	1.3192	1.3094	1.3567	1.4296	1.4912	1.5821
	1.3239	1.324	1.4424	1.6094	1.518	1.5241
Average	**1.31122**	**1.3144**	**1.3406**	**1.406**	**1.390**	**1.405**
STD	**0.245**	**0.0345**	**0.106**	**0.124**	**0.213**	**0.0938**
Change		**0.3%**		**8%**		**8%**

white images after thresholding of the images shown in Figs. 3a and c. The fractal dimensions of the crack patterns were calculated from the black and white images. The fractal dimensions of the crack patterns increase during the thermal shock, indicating that the pattern of the cracks after the thermal shock is more complex and the network contains more interconnected surface cracks.

The fractal dimensions were obtained for a total of 15 samples, i.e., five samples for each heat shock of 10, 30, and 60 seconds. The average of the fractal dimensions prior to the heat shock for all 15 samples was 1.334 ± 0.13. The effect of the heat shock on the crack pattern can be estimated from the change in the fractal dimensions. After the 10 second heat shock, the fractal dimensions are essentially the same as before the heat shock. However, after the 30 and 60 second heat shocks the fractal dimensions increase by 8%. Unfortunately, there was a significant scatter in the fractal dimensions obtained prior to the heat shocks, and therefore the comparison of the effect of different heat shocks on the mechanical properties is somewhat limited. The relative change in the fractal dimensions, however, seems to correlate quite well with the change in the mechanical properties. Table 1 summarizes the fractal dimensions for the heat shocked samples before and after the heat shock.

The results of the low strain rate tests are shown in Fig. 4. The stress as a function of time for the granite specimens without any heat shocks are shown in Fig. 4a,

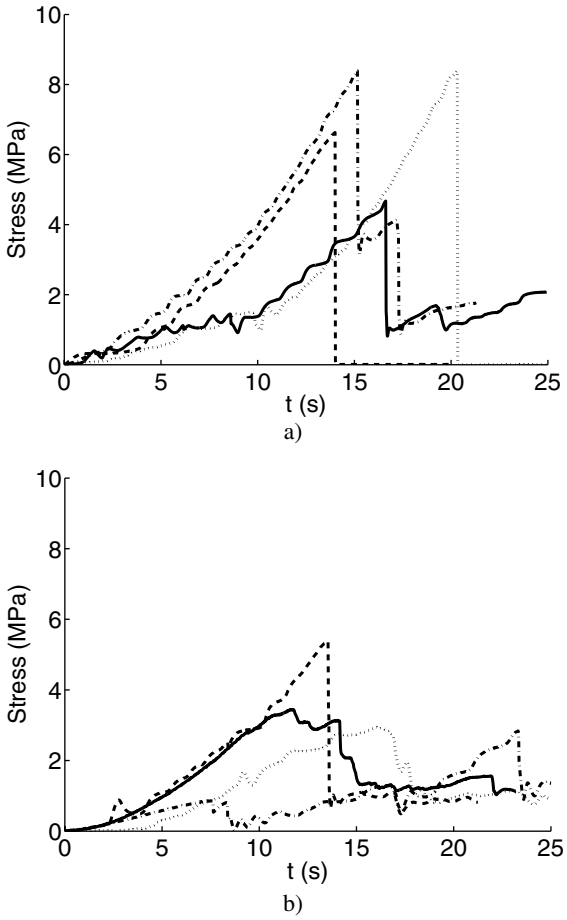

Figure 4. Low strain rate test results showing the tensile stress as a function of time for a) samples without a thermal shock and b) samples with a 60 second thermal shock.

while Fig. 4b shows the corresponding data for the samples with a 60 second heat shock. The tensile strength of the rock without a heat shock varies between 8 MPa and 4 MPa, and the fracture of the sample always occurs as a very clear and rapid drop of the stress to essentially zero. However, after the 60 second heat shock, siginificant scatter appears in the fracture behavior of the rock, as can be seen in Fig. 4b. The heat shocked samples do not fail by only one rapidly propagating fracture, as observed for the rock samples without a heat shock (Fig. 4a), but the failure occurs by several smaller consecutive drops in the tensile stress. The strength of the rock also drops by about 50%, with only one sample showing a significantly higher strenght. This behavior is evidently due to the increase in the number of cracks generated during the heat shocks, which facilitates the fracture and realease of the energy absorbed by the sample during the impact.

During the dynamic loading, the fracture behavior of the studied material is different and the scatter is significantly reduced. Figure 5 shows the tensile stress as a function of time for the samples without a heat shock (5a) and for the samples with a 60 second shock (5b). The average tensile strength obtained from the five dynamic tests on the non-shocked specimens is 28 MPa. The heat shock, however, decreases the dynamic strength significantly, as the average tensile strengths for the heat

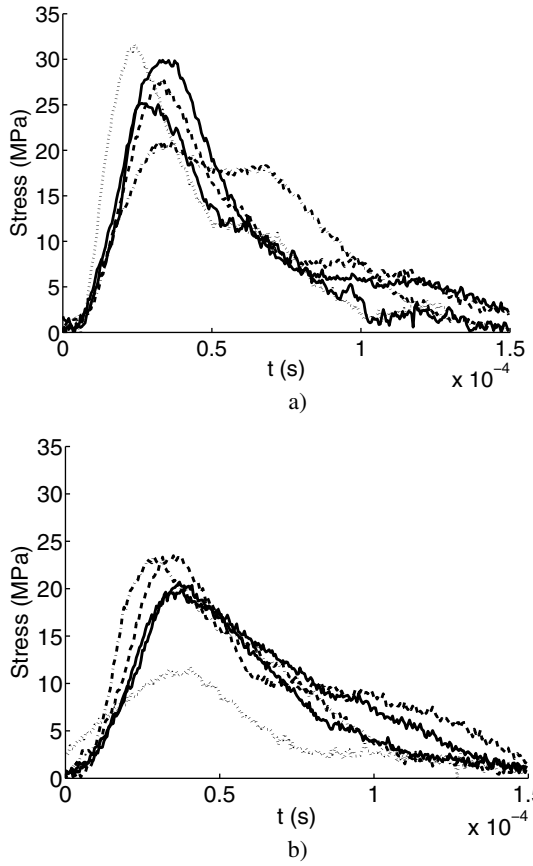

Figure 5. High strain rate test results showing the tensile stress as a function of time for samples a) without a heat shock and b) samples with a 60 second thermal shock.

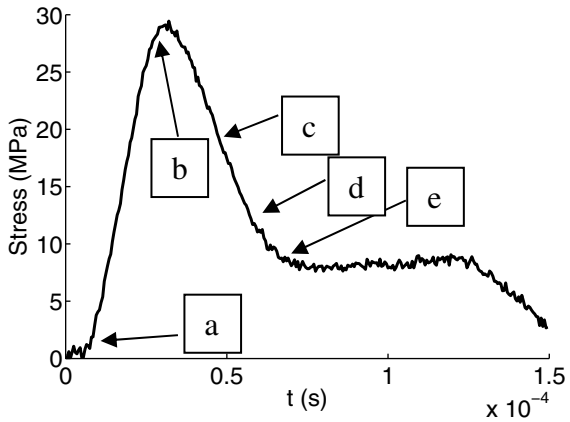

Figure 6. Tensile stress as a function of time for a sample with a 10 second thermal shock.

shocked samples are 23 MPa, 22 MPa, 19 MPa for the heat shocks of 10, 30, and 60 seconds. As described before, the fractal dimensions of the surface cracks increase with the duration of the heat shock. This can be interpreted as an increase in the number of cracks on the surface, and more importantly as an increase of the complexity and interconnectivity of the crack network. Based on the mechanical testing, the increase in the fractal dimensions correlates with the duration of the heat shock and also with the decrease in the strength of the tested samples.

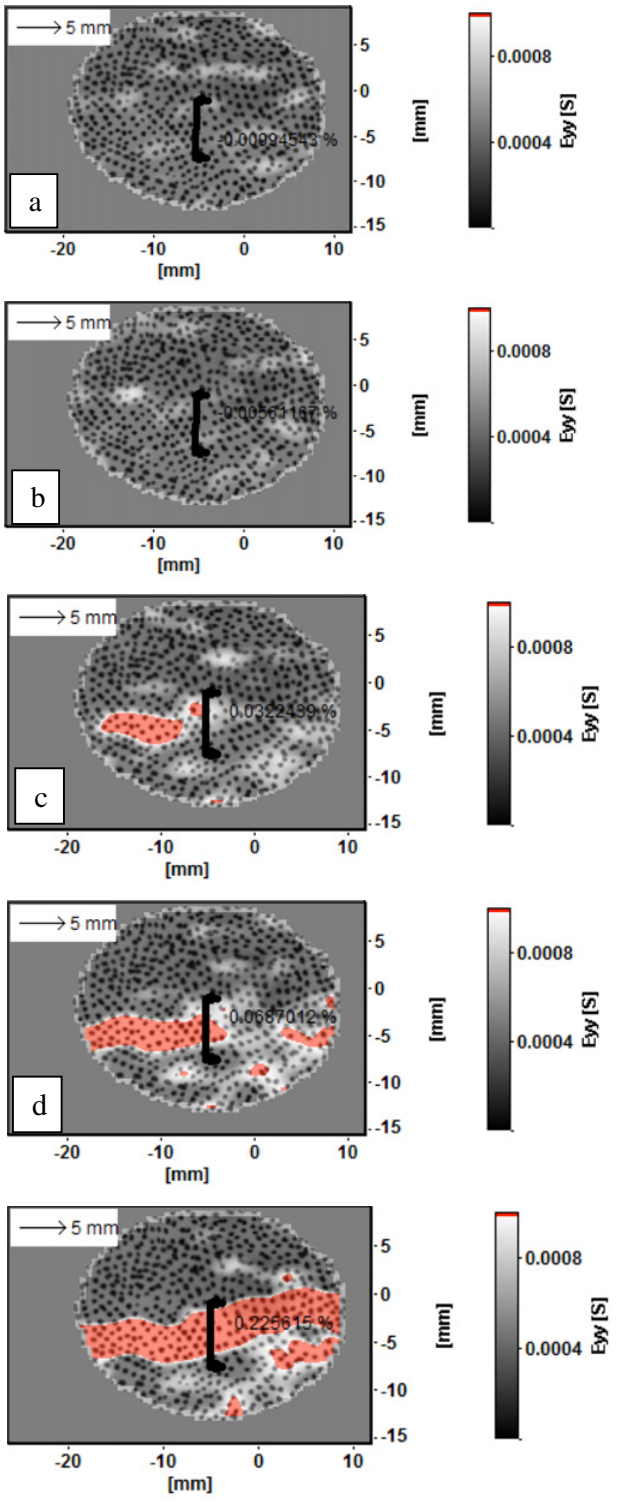

Figure 7. DIC images obtained during the dynamic loading of the sample for which the force-time plot is shown in Fig. 6. a) t = 0 μs, b) t = 31.25 μs, c) t = 50 μs, d) t = 56.25 μs, and e) t = 62.5 μs.

The 60 second heat shock decreases the low strain rate strength of the rock from 7 ± 0.43 MPa for the samples without a heat shock to 3.5 ± 2.5 MPa for the samples tested after the heat shock. The decrease of strength is therefore about 48%. When the loading rate is increased, the same 60 second heat shock decreases the rock strength

from 28 ± 3.35 MPa to 19 ± 0.53 MPa, i.e., by 32%. The increased loading rate therefore increases the rock strength by about 400% for the samples tested without a heat shock and by about 550% for the samples tested after a 60 second heat shock. Therefore, the relative increase in strength due to the rate effect seems to be stronger for the samples with a higher content of surface cracks.

The DIC analysis of the BD samples shows that the fracture of the specimens initiates at the center or slightly closer to the incident bar contact point. This observation and comparison of the forces on the incident and transmitted sides of the sample indicate adequate stress equilibrium. The engineering strain in the direction perpendicular to the loading direction prior to fracture was measured by placing a virtual strain gage at the center of the specimen using LaVision StrainMaster (DaVis) 3D-DIC software. The results reveal a decreasing trend of failure strain as the duration of the heat shock increases. For the non-heat treated samples the maximum strain prior to failure is 0.8%, while for the heat shocked samples the corresponding numbers are 0.6%, 0.6%, and 0.5% for the 10, 30, and 60 second heat shocks. The relative decrease in the maximum strain before fracture seems to be quite similar to that observed for the decrease in strength.

Figure 6 shows the tensile stress as a function of time for a sample tested after a 10 second heat shock. Point (a) in the Figure corresponds to the start of the loading and (b) indicates the moment just before the maximum stress. The high speed images corresponding to the time stamps indicated in Fig. 6 are shown in Fig. 7. Also the strain maps in the Y-direction (vertical direction, perpendicular to loading) are overlaid with the original high speed images. It can be seen from the images that the strains in the two first images (7a and b) are very low and essentially constant over the sample surface. The first strain localization does not yet show in the image obtained just microseconds before the strength of the rock starts to decrease. This indicates that the fracture initiates inside the sample and does not appear on the surface at this point. As the fracture propagates, it becomes visible also in the strain maps (Fig. 7c) as a strong concentration of deformation. The crack then propagates through the sample very quickly in Figs. 7d and e. This is followed by crushing of the contact points of the sample with the stress bars.

4. Conclusions

The mechanical behavior of Balmoral Red granite was studied using the Brazilian disc tests at quasi-static and dynamic strain rates. The effect of surface cracks on the mechanical properties was studied by generating Brazilian disc samples with different surface crack patterns by modifying the rock surface structure using thermal shock treatments. The optical images and fractal dimensions obtained from the surface of the samples before and after the heat shock clearly show an increase in the amount of surface cracks and in the complexity of the crack network.

At quasi-static strain rates the fracture of the rock samples without a heat shock occurs as a sharp drop of strength at maximum stress. The samples tested after the heat shock show significant scatter in the strength and the final fracture can occur in several short steps instead of one clear drop. However, at high strain rates the rock shows more consistent behavior and the scatter is significantly reduced. Based on the results, the strain rate effect is stronger for the samples with a 60 second heat shock than for the samples without any heat shock.

Digital image correlation was used to observe the crack initiation and propagation on the surface of the samples during the high rate tests. Time stamps from the test were recorded on the images, and the data from the HSPB was synchronized with the obtained images. The cracks initiate typically inside the sample and propagate to the surface only after the strength of the sample has already decreased significantly. The DIC can also be used to estimate the fracture strain of the material during a high strain rate test. This can be done, for example, with a virtual extensometer placed on the image. The obtained maximum strains prior to the fracture also decrease with the heat shock duration.

This work was supported by the Finnish Research Foundation for Natural Resources under the grant no. 1768/14.

References

[1] W.H. Peters, W.F. Ranson, Opt. Eng. **21**, 427 (1982)
[2] J.E. Field, S.M. Walley, W.G. Proud, H.T. 2. Goldrein, C.R. Siviour, Impact. Eng. **30**, 725 (2004)
[3] F. Hild, S. Roux, Exp. Mech. **42**, 69 (2006)
[4] V. Tiwari, M.A. Sutton, S.R. McNeill, Exp. Mech. **47**, 561 (2007)
[5] P.L. Reu, T.J. Miller, Strain Anal. Eng. Des. **43**, 673 (2008)
[6] T. Saksala, M. Hokka, V.T. Kuokkala, J. Mäkinen, Rock Mech. Mining Sci. **59**, 128 (2013)
[7] T. Saksala, Numer. Anal. Met. **37**, 309 (2012)
[8] C.A. Tang, H. Liu, P.K.K. Lee, Y. Tsui, L.G. 8. 8. Tham, Rock Mech. Mining Sci. **37**, 555 (2000)
[9] C.A. Tang, L.G. Tham, P.K.K. Lee, Y. Tsui, H. Liu, Rock Mech. Mining Sci. **37**, 571 (2000)

II

Effects of strain rate and surface crakcs on the mechanical behavior of Balmoral Red granite

Ahmad Mardoukhi, Yousof Mardoukhi, Mikko Hokka, and Veli-Tapani Kuokkala

Philosophical Transaction of the Royal Society 375 (2016) 20160179

PHILOSOPHICAL TRANSACTIONS A

Phil. Trans. R. Soc. A.
doi:10.1098/not yet assigned

Effects of strain rate and surface cracks on the mechanical behavior of Balmoral Red granite

Ahmad Mardoukhi *[1], Yousof Mardoukhi [2], Mikko Hokka [1], Veli-Tapani Kuokkala[1]

[1] *Tampere University of Technology, Department of Material Science, POB 589, FI-33101, Tampere, Finland*

[2] *University of Potsdam, Institute of Physics and Astronomy, D-14476, Potsdam, Golm, Germany*

Keywords: SHPB, Rock, Granite, Dynamic Loading, Fractal Dimension, Surface Cracks

Abstract

This work presents a systematic study on the effects of strain rate and surface cracks on the mechanical properties and behavior of Balmoral Red granite. The tensile behavior of the rock was studied at low and high strain rates using Brazilian Disc samples. Heat shocks were used to produce samples with different amounts of surface cracks, the surface crack patterns were analyzed using optical microscopy, and the complexity of the patterns was quantified by calculating the fractal dimensions of the patterns. The strength of the rock clearly drops as a function of increasing fractal dimensions in the studied strain rate range. However, the dynamic strength of the rock drops significantly faster than the quasi-static strength, and because of this, also the strain rate sensitivity of the rock decreases with increasing fractal dimensions. This can be explained by the fracture behavior and fragmentation during the dynamic loading, which is more strongly affected by the heat shock than the fragmentation at the low strain rates.

Introduction

The mechanical behavior of rocks has attracted a great deal of attention during the recent years, which has led to significant improvements in excavation and tunneling technologies. For this reason, new and more efficient rock drilling methods are being widely used in mines, quarries, construction sites, and more recently also with geothermal heat plants. To further improve the drilling technologies, both reliable quantitative data and better understanding of the rock behavior and fracture are needed. Using the experimental and numerical rock mechanics, one can design more efficient drill tools and methods that target drilling of specific rock types. This leads to efficient fragmentation of the rock without excess wear of the tools. Evidently, increasing the rate of penetration leads to high rate loading of the rock at high frequencies especially in percussive drilling. Therefore, the estimations of strength or fracture criteria calibrated based on the static values are not sufficient to describe the rock behavior in high rate drilling processes. Because of this, the effect of strain rate on the mechanical behavior of rock has been extensively studied in tension (1,2) and in compression (3,4). Based on the work of Liang et al. (5), in the quasi-static region the samples fracture into smaller pieces as the strain rate increases. In addition, the fracture mechanism changes from intergranular to transgranular by increasing the strain rate. At low strain rates, axial splitting was reported as the main macroscopic fracture mechanism. This mode changes slowly to shear fracture at higher strain rates. Previous research on the dynamic response of rocks shows significant differences when compared to the static response (6,7,8,9,10). For instance, the peak strength is highly dependent on the loading rate (11). Brace et al. (7) and Sano et al. (12) reported that the peak strength of most rocks is proportional to $\frac{1}{n+1}\mathrm{Log}\,\dot{\varepsilon}$, where n is a constant describing the time-dependency of the rock behavior. This relationship applies to uniaxial compressive loading, triaxial compression (13), and shear (14). It has

*Author for correspondence (ahmad.mardoukhi@tut.fi)
†Present address: Department of Material Science Tampere University of Technology, POB 589, FI-33101, Tampere, Finland

been reported that *n* can be used to estimate the loading-rate dependency of fracture toughness (14), stress dependency of creep life (15), and the relation between crack growth rate and the stress intensity factor (16,17). Unfortunately, the data and the information about rock strength and mechanical properties vary and the conclusions are valid only for that particular rock and only under the conditions where the tests were carried out. Therefore, modeling and simulations are often being used to gain more insight into the rock behavior on a more general level. Great amount of effort has been put into modeling and simulation of rock behavior. Saksala et al. (18) carried out experimentation and simulation on the percussive drilling with triple button bits. Tang et al. (19,20) studied the effect of microstructure on rock failure. From the works similar to this paper, Saksala et al. (21) and Cai and Kaiser (22) simulated the behavior of the Brazilian test in different conditions. The most recent research includes 3D modeling of the rock structure, where cracks are embedded in the model as discontinuities (23). As it was mentioned before, the modeling and simulations require detailed information about the effects of the cracks on the dynamic response and fragmentation of the material to verify and calibrate the material models. In the past some effort has been made to characterize the effect of cracks on rock behavior. For instance Walsh (24,25) studied the effect of cracks on the compressibility of rocks and uniaxial elastic compression of rocks. In another work Cooper and Simmons (26) investigated the effects of cracks on the thermal expansion of rock. Unfortunately, not enough attention has been paid to the effects of cracks on the characteristics of rock materials, and there are still numerous aspects which are not completely understood, such as the details of crack initiation, propagation, and coalescence. To overcome these shortcomings, this paper presents a systematic study to analyze the effects of surface cracks and strain rate on the mechanical behavior of Balmoral Red granite. With this information, the modeling and simulations of consecutive impacts of the percussive drill tool become possible when the effects of both the strain rate and the surface cracks can be quantified.

Experimental procedure

The material used in this study is coarse-grained Balmoral Red granite. The chemical composition of this granite is shown in Table 1. The microstructure of the rock shows no texture and the minerals are distributed homogenously. The mechanical properties are essentially isotropic. The quasi-static compression strength of Balmoral Red is about 180 MPa and the mean value of porosity is 0.38%.

Table 1 Mineral composition of Balmoral Red Granite (27).

Mineral composition	Wt.%
Potash Feldspar	40
Quartz	33
Plagioclase	19
Biotite & Hornblende	8

The Brazilian Disc (BD) samples with a diameter of 40.5 mm were core drilled from slabs with a thickness of 21 mm. The samples with different thermal shocks were tested at high and low strain rates to study the effects of strain rate and crack patterns on the mechanical response of the material. Before the thermal shocks, liquid penetrant was applied on the sample surface and the surface cracks and their patterns were observed using optical microscopy. Then thermal shocks of 10, 30 and 60 seconds were applied on the BD samples by keeping an oxygen-acetylene flame torch at a fixed distance from the center of the samples. The samples were cooled down to room temperature in air after the heat shocks, after which the liquid penetrant was reapplied on the surface to analyze the surface crack patterns after the heat shock. It is worth to mention that the amount of the liquid penetrant applied on the surface is only a few drops and the remaining of the liquid penetrant on the surface is wiped out to avoid permanent absorption. Before testing, the samples are left to dry in room temperature for a few days to eliminate the effect of retentive liquid inside the samples. The images were obtained using a stereomicroscope under ultraviolet light. To obtain the fractal dimension, the images were imported to Matlab as RGB images and converted to binary images (or black and white). As the dominant color in the liquid penetrant is red, the threshold is set on “Red” color so that if a pixel has a “Red” color higher than the threshold value, the pixel is considered as a crack pixel, which is represented by

digit “1”, otherwise the pixel is “0”. This creates a binary image, which shows the identified surface cracks. The fractal dimension of the surface crack pattern can then be calculated from the binary images using a box counting method in Matlab (28).

The low strain rate tests were carried out using an Instron 8800 servohydraulic materials testing machine with the displacement rate of 1 mm/min, and the high strain rate tests were performed using a Hopkinson Split Pressure Bar (SHPB) device. The pressure bars were made of AISI 4340 steel with the length of 1200 mm and a diameter of 22 mm. The striker with the length of 300 mm was made of the same material. The bars are resting on adjustable stanchions, making the alignment of the bars possible in z- and y-directions. The striker bar is impacted on the incident bar using an air gun. Three IR sender-receiver pairs are used to measure the impact speed. The signal from these sensors is used for triggering the recording system as well. Two active strain gages are attached in the middle of the incident and transmitted bars. The signal from strain gages is amplified by a Kyowa CDV 700 A series signal conditioner and recorded by a 12-bit 10MSample Yokogawa digital oscilloscope. All functions of the device from pressurizing of the gun until reading of the data from the oscilloscope are controlled by a computer. A detailed description of the instrument and the data acquisition is given in (29). A numerical dispersion correction adopted from the work of Gorham (30) was used to correct the unwanted changes in the stress waves caused by dispersion. A disc of soft and deformable copper with a thickness of 0.1 mm was used to increase the rise time of the incident pulse and to improve the dynamic equilibrium. The impact speed used in the dynamic tests was 10 m/s, and each test was repeated five times. Figure 1 shows a schematic picture of the SHPB device.

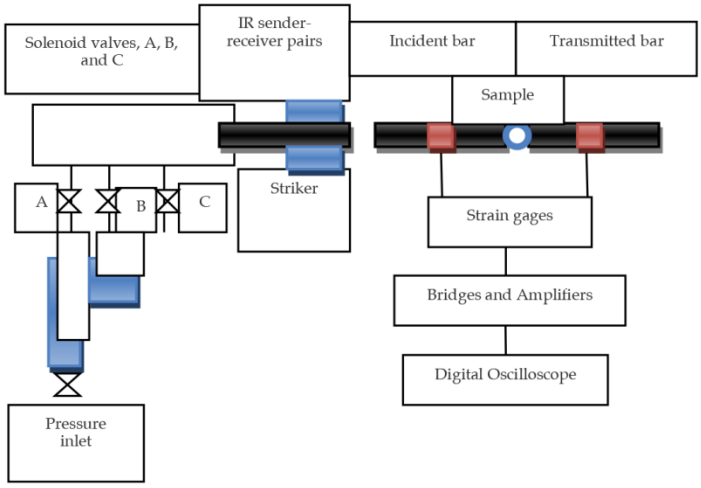

Figure 1 Schematic picture of the Split Hopkinson Pressure Bar device at Tampere University of Technology.

Results and Discussion

Figure 2 shows optical images obtained under UV light from a sample after a 60 second heat shock. Figures 2a and 2b show the original images, whereas Figures 2c and 2d show the processed images. It is evident from the images that after the thermal shock the existing cracks become longer and new cracks are introduced on the surface. Also the interconnectivity of the surface cracks becomes more complex. The absolute values of the fractal dimension do not show consistent relationship between the rock strength and the crack pattern, but it seems that there is a relationship between the mechanical behavior of the rock and the relative increase of the fractal dimension (normalized fractal dimensions), as will be shown later. Some small cracks that are identified on the sample surface before the heat shock are not identified in the image obtained after the thermal shock. This is simply because the large and high contrast cracks become more

visible during the heat shock, and the previously identified cracks give less contrast compared to the new cracks and cannot be identified by the thresholding of the images. Identifying the cracks is based on a threshold limit of the "Red" color (Primary color in the liquid penetrant). There simply is much more red color and contrast in the larger cracks formed during the heat shock compared to the small cracks that existed already prior the heat shock, and because of this, the smaller cracks are not always identified after the heat shock.

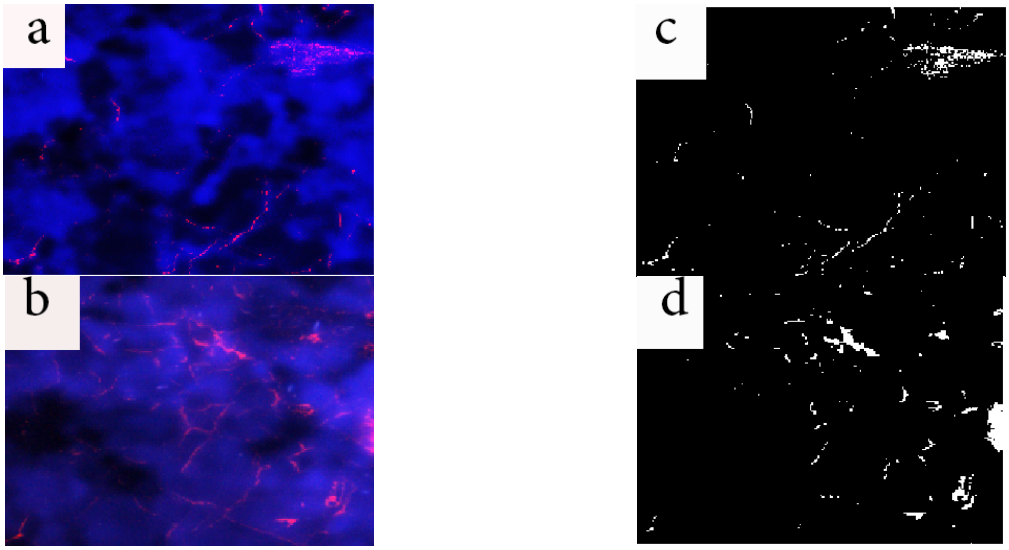

Figure 2 Optical images a) before and b) after a 60 s thermal shock and the identified cracks c) before and d) after the thermal shock.

Fractal dimensions of 30 samples were calculated before and after the heat shock. The average fractal dimension for all the samples without any heat shock was 1.065 ± 0.102. After the thermal shocks, normalized values of 1.17, 1.22 and 1.27 were obtained for the samples with 10, 30 and 60 second heat shocks, respectively. Table 2 and Table 3 summarize the fractal dimensions before and after the heat shocks for the low strain rate and the high strain rate test samples. The fractal dimension for the non-heat shocked samples are show in the Tables under the column "*Before*".

Table 2 Fractal dimensions of the heat shocked Balmoral Red samples for low strain rate tests.

	Quasi-Static Tests					
	10 seconds		30 seconds		60 seconds	
	Before	After	Before	After	Before	After
	1.016	1.070	1.005	1.089	1.071	1.387
	1.024	1.176	1.070	1.287	1.118	1.368
	1.071	1.325	1.056	1.064	1.032	1.142
	1.064	1.225	1.0590	1.554	1.100	1.492
	1.029	1.327	1.047	1.342	1.116	1.560
Average	1.0426	1.2246	1.0472	1.2670	1.0876	1.3887
STDEV	0.0284	0.1081	0.0252	0.2006	0.0362	0.1594
Normalized		1.17		1.21		1.28

Table 3 Fractal dimensions of the heat shocked Balmoral Red samples for high strain rate tests.

	Dynamic Tests					
	10 seconds		30 seconds		60 seconds	
	Before	After	Before	After	Before	After
	1.89	1.474	1.053	1.448	1.210	1.484
	0.661	0.986	1.057	1.223	1.0130	1.386
	1.082	1.174	1.065	1.354	1.113	1.331
	1.330	1.414	1.080	1.143	1.011	1.323
	1.008	1.1204	1.0669	1.3324	1.1345	1.4547
Average	1.054	1.2335	1.0642	1.3001	1.0949	1.3959
STDEV	0.251	0.205	0.011	0.119	0.083	0.072
Normalized		1.17		1.22		1.28

Figure 3 shows the results of the low strain rate tests. The average strength of the rock before the thermal shock was 8.2 ± 2.2 MPa. After the thermal shock, the strength drops to 5.8 ± 0.7 MPa, 4.3 ± 0.5 MPa, and 3.8 ± 1.1 MPa for 10 s, 30 s and 60 s heat shocks, respectively. As it can be seen from Figure 3, before the thermal shocks the rock shows quite consistent behavior. After reaching the maximum stress, the strength of the rock drops sharply to zero as the sample splits into two parts. However, after the heat shock this behavior changes. The sharp drop in the stress-time curve becomes less pronounced, and in some cases several local maxima can be observed instead of one clear maximum. This is especially clear for samples with the 60 s heat shock. This behavior is due to cracking also in other directions than the loading direction. The macroscopic fracture does not take place only by one dominant crack. As the load on the heat shocked samples increases, the main crack initiates similarly to the non-heat shocked samples, but the crack does not propagate through the entire sample. Instead, the crack stops at some point and another crack starts to propagate, possibly in a different direction. This behavior continues until the main dominant macro-crack parallel to the loading direction propagates through the sample. In the low strain rate tests this happens so slowly that the fragmentation of the sample can be observed simply by looking at the sample during the test. This behavior explains the several maxima observed in the stress-time curves obtained for the thermally shocked samples.

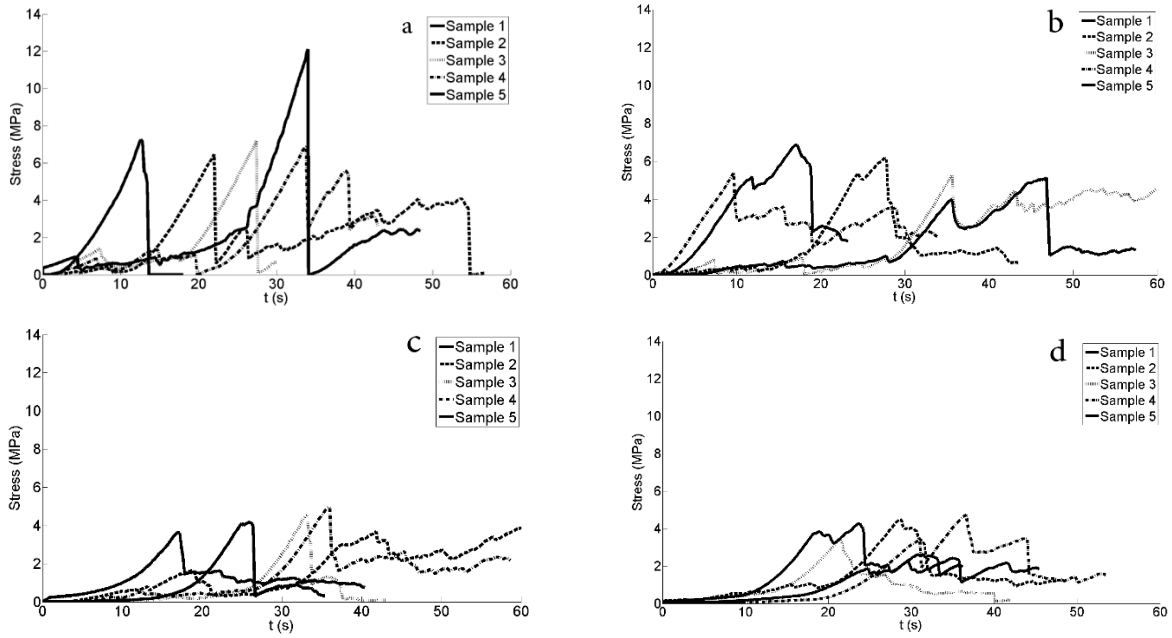

Figure 3 Low strain rate tensile stress as a function of time for a) samples without a thermal shock, b) samples with a 10 second thermal shock, c) samples with a 30 second thermal shock, and d) samples with a 60 second thermal shock.

The response of the rock is somewhat different as the strain rate is increased. Figure 4a shows the tensile stress as a function of time for the samples without any heat shock, and Figure 4b shows the response of the samples after a 30 second heat shock. The average tensile strength of the rock for the non-heat shocked samples was 29 ± 3 MPa. As the duration of the thermal shock increases, the strength deceases significantly to 23 ± 4 MPa, 16 ± 2 MPa, and 12 ± 2 MPa for 10, 30 and 60 second thermal shocks, respectively. After the heat shock, the strong peak in the stress-time curves again partly disappears, and the stress drops at a slower rate after the peak stress. When compared to the low rate tests, the scatter at the higher rate is reduced and the rock shows more consistent behavior.

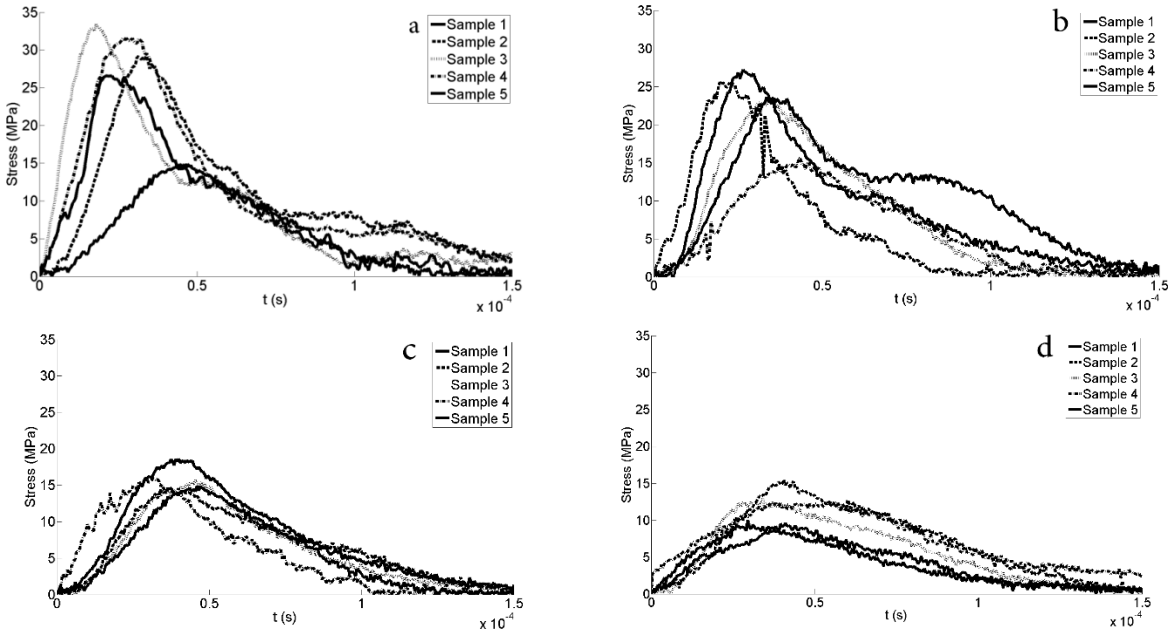

Figure 4 High strain rate tensile stress as a function of time for samples a) without a heat shock and b) with a 10 s heat shock, c) with a 30 s heat shock, and d) with a 30 s heat shock.

Figure 5a shows the strength of the rock at the dynamic and quasi-static loading conditions as a function of the normalized fractal dimension. The drop rate of the tensile strength, $\Delta\sigma/\Delta FD$, was used to estimate the effect of the heat shock. In this Equation, the $\Delta\sigma$ is the difference of the tensile strength of the rock between two consecutive heat shock conditions, e.g., between 10 s and 30 s heat shocks, and the ΔFD is the difference between the fractal dimension of the tested samples. The drop rate at the low strain rate is -13.78 MPa for a 10 second heat shock (between 0 s and 10 s), -52.57 MPa for a 30 second heat shock (between 10 s and 30 s), and -5.34 MPa for a 60 second heat shock (between 30 s and 60 s). The strength decreases at the high strain rate at the rates of -38.52 MPa, -141.32 MPa and -78.32 MPa for 10, 30 and 60 second thermal shocks, respectively. It is evident that the tensile strength of the rock decreases at a higher rate when the deformation rate is higher. The slopes of the curves in Figure 5a also support this observation. The reasons for this behavior are related to the fragmentation of the samples, which is affected strongly by the heat shock and strain rate, as will be discussed in the following paragraphs.

For the calculation of the strain rate sensitivity factor (Eq.1), the strain rate was obtained from the stress - time curves using a simple expression $\dot{\varepsilon} = \Delta\sigma/E\Delta t$, where $\Delta\sigma/\Delta t$ is the slope of the stress-time curve between zero and the maximum stress and E is the Young's modulus of the rock. In Equation 1, $\Delta\sigma$ is the difference in the maximum tensile strength of the rock at low strain rate and high strain rate loading, and the $\Delta Log(\dot{\varepsilon})$ is the difference in the strain rate between low and high rate loading.

$$M_{abs} = \frac{\Delta\sigma}{\Delta Log(\dot{\varepsilon})} \qquad (1)$$

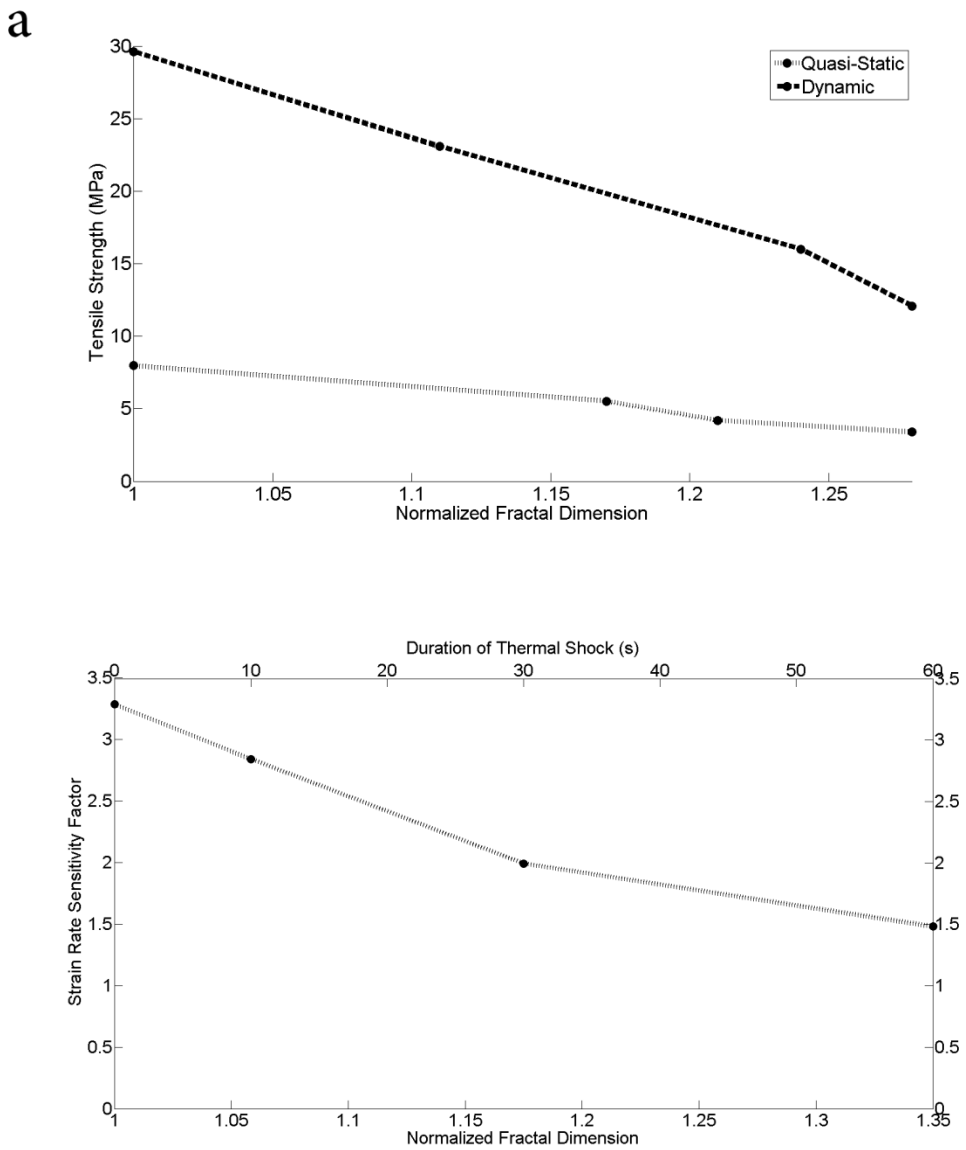

Figure 5 a) tensile strength of the rock and b) strain rate sensitivity as a function of the normalized fractal dimension (lower x-axis) and the duration of the thermal shock (upper x-axis).

For each test the M_{abs} was calculated using Equation 1, e.i., five M_{abs} values were obtained for each set of similarly shocked samples. The averages of the five values of M_{abs} are shown in Figure 5b as a function of normalized fractal dimension (lower x-axis) and duration of the heat shock (upper x-axis). The first point on the graph corresponds to the strain rate sensitivity factor calculated for non-heat shocked samples, whereas the consecutive data points corresponds to 10 s, 30 s, and 60 s heat shocked samples. As can be seen in Figure 5b, the strain rate sensitivity decreases with the increase of the fractal dimensions. This is caused by the faster decrease of the dynamic tensile strength compared to the decrease of the quasi-static strength, as shown in Figure 5a. Both the higher drop rate of strength at the dynamic conditions (Fig.5a) and the decrease in the strain rate sensitivity as a function of the normalized fractal dimensions (Fig.5b) could be explained by examining the fracture behavior of the rock at different conditions. In general, the fracture energy is consumed in large amounts in generating new surfaces, and in smaller amounts in the kinetic energy of the fragments, acoustic emission, and heating due to frictional sliding of the fracture surfaces. In the low rate tests the sample fractures into a few large fragments and the specific surface area of the fragments remains rather low. The drop of the strength due to the heat shock at the quasi-static tests can be explained simply by larger existing cracks. However, the situation is different at high strain rate deformation and the

fracturing of the sample consumes considerably more energy. The sample is partly pulverized, the fragments are ejected at high velocities, and some additional energy is consumed in frictional heating and acoustic emission. The pulverization of the sample in particular can be affected by the heat shock, which was observed in the high speed photographs. As the stress increases during the dynamic loading in a non-heat shocked sample, the tensile strength of the rock is exceeded at various locations simultaneously, and thousands of cracks initiate and propagate pulverizing parts of the sample. However, the heat shock reduces the local strength of the sample especially at the center area of the sample, where the maximum tensile load will occur during the Brazilian Disc test. When the stress increases during the dynamic loading of a heat shocked sample, the dynamic strength of the sample is first exceeded locally at the center only, while the majority of the regions outside this area still remain elastic. This leads to fewer microcraks being formed, lower degree of pulverization, and formation of larger fragments as the fractal dimension increases. Therefore, the dynamic strength of the rock is lowered by the larger surface cracks themselves, but also by the lower amount of new surface that is created during the fragmentation of the heat shocked samples. Because of this, the dynamic strength of the rock drops faster as a function of fractal dimensions than the quasi-static strength. However, confirming this hypothesis requires performing some more tests and carefully analyzing the size distribution of the fragments formed during the dynamic loading of samples with different heat shocks.

Concluding remarks

Mechanical behavior of Balmoral Red granite was studied at quasi-static and dynamic loading conditions using Brazilian Disk samples. The effects of surface cracks on the mechanical response of the rock were studied by generating different surface crack patterns on the surface of the samples. A methodology was developed to establish a relationship between the amount of surface cracks and the strain rate sensitivity of the rock using fractal dimensions.

The rock without any heat shocks shows consistent behavior at quasi static loading, but after the thermal shock, significant scatter can be observed in the rock behavior. The splitting failure and consequent sharp drop of the stress found for the non-heat shocked samples become less pronounced, and several maxima can be seen in the stress-time curves of the samples with significant heat shock damage. The response of the rock to dynamic loading is rather different. After the heat shock the rock still shows quite consistent behavior, but the sharp peak in the stress-time curve decreases with the increasing duration of the heat shock. The rock strength drops with the increasing fractal dimension. The strength decreases faster at the higher strain rate, and therefore the strain rate sensitivity decreases with the increasing fractal dimension. This observation can be explained by the effect of the surface cracks on the fracture behavior of the rock at quasi-static and dynamic conditions. The surface cracks reduce the pulverization of the sample at dynamic loading conditions, leading to a faster decrease of the strength as a function of fractal dimensions than at quasi-static conditions.

Acknowledgments

This work was supported by Suomen Luonnonvarain Tutkimussäätiö –Foundation under grant numbers 1768/14, 1779/15, and 1789/16.

References

1. Cho SH, Ogata Y, Kaneko K. Strain-rate dependency of the dynamic tensile strength of rock. International Journal of Rock Mechanics and Mining Sciences. 2003; 40(5): p. 763-777.
2. Grady DE, Hollenbach RE. Dynamic fracture strength of rock. Geophysical Research Letters. 1979; 6(2): p. 73-76.
3. Xia K, Nasseri MHB, Mohanty B, Lu F, Chen R, Luo SN. Effects of microstructures on dynamic compression of Barre granite. International Journal of Rock Mechanics and Mining Sciences. 2008; 45(6): p. 879-887.

4. Liu S, Xu J. Effect of strain rate on the dynamic compressive mechanical behaviors of rock material subjected to high temperatures. Mechanics of Materials. 2015; 82: p. 28-38.
5. liang C, Wu S, Xin P. Effect of strain rate on the fracture characteristics and mesoscopic failure mechanisms of granite. International Journal of Rock Mechanics and Mining Sciences. 1999; 3: p. 1057-1063.
6. Goldsmith W, Sackman JL, Ewerts C. Static and dynamic fracture strength of Barre granite. International Journal of Rock Mechanics and Mining Sciences & Geomechanics Abstracts. 1976; 13(11): p. 303-309.
7. Brace WF, Jones AH. Comparison of uniaxial deformation in shock and static loading of three rocks. Journal of Geophysical Research. 1971; 76(20): p. 4913-4921.
8. Perkins RD, Green SJ. Uniaxial stress behavior of porphyritic tonalite at strain rates to 10^3/second. International Journal of Rock Mechanics and Mining Sciences & Geomechanics Abstracts. 1970; 7(5): p. 529-535.
9. Kumar A. The Effect of Stress Rate and temperature on the strength of Basalt granite. Geophysics. 1968; 33(3): p. 501-510.
10. Hokka M, Black J, Tkalich D, Fourmeau M, Kane A, Hoang NH, et al. Effects of strain rate and confining pressure on the compressive behavior of Kuru granite. International Journal of Impact Engineering. 2016; 91: p. 183-193.
11. Okubo S, Fukui K, Q Q. Uniaxial compression and tension tests of anthracite and loading rate dependence of peak strength. International Journal of Coal Geology. 2006; 68(3-4): p. 196-204.
12. Sano O. Influence of strain rate on dilatancy and strength of Oshima granite under uniaxial compression. Journal of Geophysical Research. 1981; 86(B10): p. 9299-9311.
13. Shin K, Okubo S, Fukui K, K , Hashiba. Influence of strain rate on dilatancy and strength of Oshima granite under uniaxial compression. International Journal of Rock Mechanics and Mining Sciences. 2005; 42(2): p. 251-260.
14. Fukui K, Okubo S, Ogawa A. Some aspects of loading-rate dependency of Sanjome andesite strengths. International Journal of Rock Mechanics & Mining Sciences. 2004; 41(7): p. 1215-1219.
15. Wilkins BJS. The long-term strength of plutonic rock. International Journal of Rock Mechanics and Mining Sciences & Geomechanics Abstracts. 1987; 24(6): p. 379-380.
16. Hashiba K, S O, Fukui K. A new testing method for investigating the loading rate dependency of peak and residual rock strength. International Journal of Rock Mechanics and Mining Sciences & Geomechanics Abstracts. 2006; 43(6): p. 894-904.
17. Lajtai EZ, Bielus LP. Stress corrosion cracking of Lac du Bonnet granite in tension and compression. Rock Mechanics and Rock Engineering. 1986; 19(2): p. 71-78.
18. Saksala T, Gomon D, Hokka M, V.T.Kuokkala. Numerical and experimental study of percussive drilling with a triple-button bit on Kuru granite. International Journal of Impact Engineering. 2014; 72: p. 56-66.
19. Tang CA, Liu H, Lee PKK, Tsui Y, tham LG. Numerical studies of the influence of microstructure on rock failure in uniaxial compression — Part I: effect of heterogeneity. International Journal of Rock Mechanics and Mining Sciences. 2000; 37(4): p. 555-569.
20. Tang CA, Tham LG, Lee PKK, Tsui Y, Liu H. Numerical studies of the influence of microstructure on rock failure in uniaxial compression — Part II: constraint, slenderness and size effect. International Journal of Rock Mechanics and Mining Sciences. 2000; 37(4): p. 571-583.
21. Saksala T, Hokka M, Kuokkala VT, Mäkinen J. Numerical modeling and experimentation of dynamic Brazilian disc test on Kuru granite. International Journal of Rock Mechanics and Mining Sciences. 2013; 59: p. 128-138.
22. Cai M, Kaiser PK. Numerical Simulation Of The Brazilian Test And The Tensile Strength Of Anisotropic Rocks And Rocks With Pre-Existing Cracks. International Journal of Rock Mechanics and Mining Sciences. 2004; 41: p. 478-483.
23. Saksala T, Brancherie D, Ibrahimbegovic A. Numerical modeling of dynamic rock fracture with combined 3D continuum viscodamage-embedded discontinuity model. International journal for numerical and analytical methods in geomechanics. 2016.
24. Walsh JB. The effect of cracks on the uniaxial elastic compression of rocks. Journal of Geophysical Rsearch. 1965; 70(2): p. 381-389.
25. Walsh JB. The effect of cracks on the compressibility of rock. Journal of Geophysical Research. 1965; 70(2): p. 381-389.
26. Copper HW, Simmons G. The effect of cracks on the thermal expansion of rocks. Earth and Planetary Science Letters. 1977; 36(3): p. 404-412.

27. H L, Luodes N. Finska. [Online]. [cited 2016 01 16. Available from: http://www.finskastone.fi/en/2013-04-08-20-59-20/products/40-balmoral-red-fine-grained.
28. Feder J. Fractals (Physics of Solids and Liquids) New York: Plenum Press; 1988.
29. Apostol M. Strain rate and temperature dependence of the compression behavior of FCC and BCC metals Tampere: Tampere University of Technology; 2007.
30. Gorham DA, Wu X. An empirical method of dispersion correction in the compressive Hopkinson bar test. Journal de Physique. 1997; 07(C3): p. 223-228.

Authors' Contributions

All Authors contributed equally to this work. A. Mardoukhi, Y. Mardoukhi, M. Hokka, and V.T. Kuokkala were involved in designing the tests. Y. Mardoukhi conducted in writing the Matlab code for analyzing the fractal dimensions. A. Mardoukhi, M. Hokka, and V.T Kuokkala carried out the mechanical testing. A. Mardoukhi wrote the first draft. All authors discussed the results and implications and commented on the manuscript at all stages.

III

Effects of heat shock on the dynamic tensile behavior of granitic rocks

Ahmad Mardoukhi, Yousof Mardoukhi, Mikko Hokka, and Veli-Tapani Kuokkala

Rock Mechanics and Rock Engineering 50 (2017) 1171-1182

Rock Mech Rock Eng
DOI 10.1007/s00603-017-1168-4

ORIGINAL PAPER

Effects of Heat Shock on the Dynamic Tensile Behavior of Granitic Rocks

Ahmad Mardoukhi[1] · **Yousof Mardoukhi**[2] · **Mikko Hokka**[1] · **Veli-Tapani Kuokkala**[1]

Received: 13 June 2016 / Accepted: 4 January 2017

Abstract This paper presents a new experimental method for the characterization of the surface damage caused by a heat shock on a Brazilian disk test sample. Prior to mechanical testing with a Hopkinson Split Pressure bar device, the samples were subjected to heat shock by placing a flame torch at a fixed distance from the sample's surface for periods of 10, 30, and 60 s. The sample surfaces were studied before and after the heat shock using optical microscopy and profilometry, and the images were analyzed to quantify the damage caused by the heat shock. The complexity of the surface crack patterns was quantified using fractal dimension of the crack patterns, which were used to explain the results of the mechanical testing. Even though the heat shock also causes damage below the surface which cannot be quantified from the optical images, the presented surface crack pattern analysis can give a reasonable estimate on the drop rate of the tension strength of the rock.

Keywords SHPB · Rock · Granite · DIC · Dynamic loading · Fractal dimension

✉ Ahmad Mardoukhi
ahmad.mardoukhi@tut.fi

[1] Department of Material Science, Tampere University of Technology, POB 589, 33101 Tampere, Finland

[2] Institute of Physics and Astronomy, University of Potsdam, 14476 Potsdam, Golm, Germany

1 Introduction

Nowadays, percussive drilling is regarded as an effective procedure for excavation, tunneling, and shallow well boring in hard igneous rock such as granite. The efficiency of this method is closely related to the brittleness of the rock material. The more brittle the rock is, the longer radial cracks are formed by each impact of the drill. These cracks, in turn, facilitate the chipping occurs between the drill buttons, allowing the waste material to be removed faster. Even though percussive drilling is recognized as one of the most effective drilling techniques, it still lacks some efficiency in some specific environments. For instance, to extract geothermal energy the bores with the depth as deep as 5000 or 6000 m are needed. One can easily understand an attempt to drill a well that deep causes considerable difficulties.

Several attempts have made to develop new technology, such as microwave-assisted hard rock cutting (Lindroth et al. 1991), laser-assisted drilling (Perry et al. 2010), water-jet-assisted drilling (An et al. 2006), abrasive-jet drilling (Fair 1981), diamond drilling (Miller and Ball 1990), and ultra-high-pressure jet drilling (Kolle et al. 1991; Veenhuizen et al. 1996) to further increase the efficiency of percussive drilling. Although considerable research and development efforts have been put into developing these new techniques, none of them have yet become commercially viable. The reasons for this drawback can be found in the lack of technological readiness, but it may also be due to the nature of rock itself and in the ability to understand how to efficiently break the rock without causing excess wear and damage to the tools.

The mechanical behavior of rocks is influenced by many factors such as the mineral composition (Price 1996), the structure (Rippa and Vinale 1983), texture (Wenk and

Published online: 20 January 2017

Christie 1991), testing conditions (Hawkes and Mellor 1978), and etc. (Smorodinov et al. 1970; Chau and Wang 1996; Gorsevski et al. 2012; Dunn et al. 1973; Kranz 1983; Khair and Achanti 1996). Therefore, all of the above factors have to be considered in order to understand the rock behavior in different conditions and thus to choose the best drilling method and parameters, one should consider all the influencing factors on the behavior of rock material which is an extremely challenging process. Thus, a model which can take all the variables into account could be useful in designing new technology. Substantial amount of effort has been put into this matter. For instance, Tkalich et al. (2016) used a material model containing a piecewise yield function, hardening/softening laws, coupled damage, and non-associated plasticity and evaluated the influence of various material model features such as yield function and non-associativity. Saksala et al. (2014, 2016) simulated the percussive drilling with a triple-button indenter and also created a 3D model, in which the cracks were embedded as discontinuities. Following this paper, Cai and Kaiser (2004) studied the effects of preexisting cracks on the tensile behavior of rocks. Mardoukhi et al. (2015) developed a numerical model to analyze the effect of strain rate on the dynamic tensile behavior of granite. The modeling activities have also been supported by strong experimental work. For this paper in particular, the high-temperature behavior and the thermal crack formation are of great interest.

Luckily, the behavior of rock has been studied widely at high temperatures. Decrease in the tensile strength of rock by increasing the temperature has been reported by Dwivedi et al. (2008) and Liu and Xu (2014). Dwivedi et al. (2008) reported that the increase in temperature up to 150 °C reduces the tensile strength of the rock by 27%, while the compressive strength of the rock drops by 11.1%. Liu and Xu (2014) reported that not only the strength of rock decreases by increasing temperature, but also increasing the temperature affects the strain rate sensitivity of the tested material. Mahanta et al. (2016) studied the effect of heat treatment on mode I fracture toughness of three different Indian rocks. The study was carried out from ambient temperature up to 600 °C. The results indicate by increasing the temperature up to 100 °C, the fracture toughness of the all three rock increases significantly. Afterward, by increasing the temperature up to 600 °C, the fracture toughness decreases. The work done by Bauer and Johnson (1979) showed that the thermal expansion of feldspar and quartz plays an important role in the development of thermal cracks. The thermal cracks are the main reason for weakening the rock at higher temperatures. Sengun (2014) studied the influence of thermal damage on the physical and mechanical properties of carbonate rocks. He reported that up to 300 °C no significant changes are observed in the properties of carbonate but increasing the temperature from 300 to 600 °C causes the tensile strength of the rock decrease from 28 to 75%. Verma et al. (2016) reported that by increasing the temperature, the amount of porosity increases by 2.3% in Ganurgrah shales. They stated that these porosities act as a thermal barrier causing a decrease in thermal conductivity. On a similar work, Roy and Singh (2016) studied the effect of heat treatment and layer orientation on tensile properties of granitic gneiss under confined stress using Brazilian disk geometry. They also reported a decrease in the tensile strength of the rock by increasing the temperature of heat treatment. Sirdesai et al. (2016) reported that the main reason for the change in characteristic of rock upon heating is related to the minerals expansion. The change in the pores and micro-fracturing caused by the expansion alters the rock's tensile strength. There is a critical temperature zone (CTZ) for each rock which after this range, the decrease in the strength of the rock becomes more obvious (Rao et al. 2007; Vishal et al. 2011; Yin et al. 2015). For the case of red sandstone, this temperature zone is 200–250 °C.

Despite all the previous efforts for developing more efficient techniques, considerably less amount of attention has been put into altering the rock properties before drilling. This means applying some non-mechanical treatments of the rock, for instance, a heat shock, before the drilling. This work focuses on modifying the rock structure by a heat treatment and presents a method for the evaluation of the effects of a heat shock on the dynamic tensile strength of a rock material based on the characterization of surface cracks and damage. The quantification of the surface cracks is significantly easier than the full 3D characterization of the whole affected volume, and therefore, faster and easier to carry out. Although the method presented here does not give a perfect picture of the whole affected volume, it gives an adequate and fast evaluation of the damage caused by heat shock and it can be used for predicting changes in the mechanical properties of the rock.

2 Experimental Procedure

Two types of granite, the Balmoral Red and the Kuru Grey, were used in this study. Tables 1 and 2 show the chemical composition of these two rocks. The mean values of open

Table 1 Mineral composition of the Balmoral Red granite (Luodes and Luodes 2015)

Mineral composition	Wt%
Potash feldspar	40
Quartz	33
Plagioclase	19
Biotite and hornblende	8

Table 2 Mineral composition of the Kuru Grey granite (Fourmeau et al. 2014)

Mineral composition	Wt%
Quartz	35
Albite	31
Microcline maxi	28
Biotite	3
Diopside	2
Chlorite IIb	1

porosity were 0.38% and 0.44% and the quasi-static compression strengths were about 180 MPa and 220 MPa for the Balmoral Red and the Kuru Grey, respectively. The quasi-static tensile strength of the Balmoral Red is 8 ± 2 MPa, while that of the Kuru Grey is 11 ± 2 MPa. The microstructure of both rocks shows no remarkable texture, the minerals are distributed homogeneously, and the mechanical properties are essentially isotropic. However, the Kuru Grey has smaller grain size than the Balmoral Red.

There are four methods which are commonly used to determine the tensile strength of the rocks: the dynamic direct tension method, the semicircular band (SCB) method, the spalling method, and the Brazilian disk (BD) method (Xia and Yao 2015). For the purposes of this paper, the dynamic direct tension test may seem to be most fitting as the stress state is one dimensional. Nevertheless, difficulties arise when one considers the experimental setup of dynamic direct tension test. For example, the requirements for alignment are very strict, and the bending of the sample must be avoided. Preparing the test specimen is a difficult task due to its complex shape and restrictions on its machinability. In addition, high-strength epoxy glue would be required for fixing the sample to the bars (Xia and Yao 2015). The SCB method seems, in principle, to be easier compared to the dynamic direct tension test, yet one should note that the results obtained from SCB method define the flexural strength of the rock, which is different from the tensile strength obtained with the BD method (Zhang and Zhao 2014). The spalling method can also be used to measure the tensile strength of the rock, but this method also has its limitations: Firstly, achieving 1D stress state is difficult, secondly the compressive stress wave may influence the sample's properties before the tensile wave, and finally, the stress wave becomes attenuated in the rock materials (Xia and Yao 2015). In addition, applying heat shock to specimen with complex geometry is not an easy task, and there is always the risk of asymmetric crack patterns appearing. The BD method has been developed to overcome these difficulties, particularly the problems with direct tension test, and also to provide a convenient way for instrumentation. As any experimental method, the BD test has its own limitations as well. For a valid BD test, the sample should break first along the loading direction close to the center of the disk (Shewmon and Zackay 1961; Hudson et al. 1972). Also the stress state is two dimensional and the tensile strength is not measured directly, but it is calculated from the axial loading, assuming that the sample remains elastic and does not undergo any plastic deformation. Considering the above-mentioned points, the BD method was considered the best option for this work and was used to measure the tensile strength of rocks.

The Brazilian disk samples were prepared with a diameter of 40.5 mm and thickness of 21 mm for the Balmoral Red and with diameter of 41 mm and a thickness of 16 mm for the Kuru Grey. Figure 1 shows the natural surfaces of the BD samples. The samples were tested at the same strain rate but with different thermal shocks on the sample surface to study the effect of surface cracks on the mechanical properties of the materials. Before and after the thermal shocks, liquid penetrant and optical microscopy were used to analyze the patterns of the surface cracks. Thermal shocks of 10, 30, and 60 s were applied on the BD samples of both rocks by keeping the samples at a fixed distance from the tip of the acetylene and oxygen torch. After the thermal shocks, samples were cooled down to room temperature in air. As the both rocks are mostly composed of quartz, feldspar, and plagioclase, it is highly unlikely that the nature of the rock has been altered by the thermal shock, since the temperature required for quartz to go through phase transformation is about 600 °C and for feldspar is more than 1000 °C (Brown and Parsons 1989; Gasparik 2003). However, even though no phase transformations are expected, some mechanical damage such as cracking-induced by grain refinement most likely occurs during the heat shocks. Yet Dai and Xia (2010) reported that Barre granite, which shows strong tensile anisotropy under static loading, under high loading rates, the anisotropy can be ignored. The reason for this conclusion is that in the dynamic loading, the critical flaw is no longer dominant; rather thousands of preexisted cracks with wide range of sizes are activated simultaneously. Therefore, we believe that the anisotropy has no or a small effect of the tensile behavior of heat-shocked granite under dynamic loading.

After the heat shock, the liquid penetrant was re-applied on the samples to observe the change in the surface crack patterns caused by the thermal shock. The images were obtained with a LEICA CLS 150 XE stereomicroscope. The source of natural light in the microscope was replaced by an ultraviolet (UV) light source, and images were taken under UV light. The fractal dimension of the surface crack patterns was calculated from the obtained images using a box counting method in MATLAB. Box counting method is a common tool to estimate the fractal dimension of an object with complicated structure. This method is widely used when the fractal dimension of an object cannot be

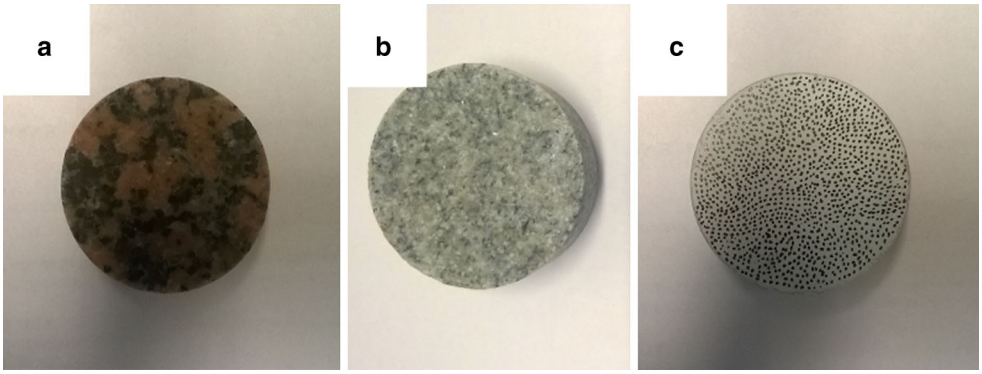

Fig. 1 Natural surface of **a** the Balmoral Red granite and **b** the Kuru Grey, and **c** a DIC speckle pattern on the sample

achieved by numerical or analytical procedures, e.g., cloud patterns or ocean waves or in this very particular case, the crack patterns on the surface of the rock samples. The accuracy of this method is mostly restricted by the image resolution. As the pixels are actually the grids used for box counting method, they may be altered by the background noise or nearby blurred pixels. The detailed description of box counting method, with detailed description of its possibilities and limitations, can be found in Feder (1988).

Additionally, surface roughness of the BD samples was measured using an Alicona Infinite Focus G5 optical profilometer. The images were taken at a contrast of 0.42 and the exposure time of 98 μs. The vertical resolution in the measurements was 14.3 nm and the horizontal resolution 13 nm.

The high strain rate tests were carried out using a compression Split Hopkinson Pressure Bar (SHPB) device. ISRM suggested that in Brazilian disk method, two steel loading jaws are used to transfer the load to the disk-shaped sample diametrically over an arc angle of roughly 10° at failure (Bieniawski and Bernede 1979). This design helps to reduce stress localization at the loading points, and thus, it prevents the premature failure. However, Dai et al. (2010) argued that even though this design works well for quasi-static condition, in SHPB tests the extra interferences between the jaw and the bar complicate the stress wave propagation and cause more difficulties in the experimentation. They also showed that in a dynamic BD tests without using jaws, no premature failure was observed, and they confirmed that for dynamic BD tests, the flat-ended bars provide essentially the same result as the curved jaws. Thus, for this work, the flat-ended pressure bars were made of AISI 4340 steel with a diameter of 22 mm and the length of 120 mm. The striker bar with the length of 300 mm was made of the same material. The bars are resting on adjustable stanchions and are supported by bearings, which makes the accurate alignment of the bars in z- and y-directions possible. The striker bar is impacted on the incident bar using an air gun. Three optical IR sender–receiver pairs are used to measure the impact velocity of the striker. These sensors also provide the trigger signal for the oscilloscope. There are two active strain gages attached to the center of the incident and the transmitted bars. The strain gage signals are amplified by a Kyowa CDV 700A series signal conditioner and recorded on a 12-bit 10MSample Yokogawa digital oscilloscope. All functions of this device, including loading the striker, pressurizing, shooting the striker bar, and reading the data from the oscilloscope, are controlled by a computer. More details of the instrument are given in Ref. (Apostol 2007). A numerical dispersion correction adopted from the work of Gorham and Wu (1997) was used to correct for any changes in the signals due to the dispersion of the waves as they travel in the steel bars. A disk of soft and deformable copper with a thickness of 0.5 mm was used to increase the rise time of the incident stress pulse and to improve the dynamic equilibrium. Using a pulse shaper has a great importance in the BD tests as the stress state over the disk sample is two dimensional and force balance on the boundaries does not necessarily ensure the dynamic equilibrium over the whole volume of the sample. Dai et al. (2010) showed that the dynamic force balance can be achieved by using a pulse shaper. Each test was repeated five times at the impact speed of 10 m/s. Figure 2 shows a schematic picture of the high strain rate testing setup.

Two Photron SA-X2 high-speed cameras were used to record the deformation, and DIC was used to study the fracture of the samples during the high strain rate tests. As the rock surface itself does not have a very strong contrast for the correlation algorithms, the surfaces of the samples were painted with white base coat and the black speckles were applied on the surface using a permanent marker, as shown in Fig. 1c. The images were recorded at 160 kfps, the size of the image at this rate being 256 × 176 pixels. Two Decocool lights were used for illuminating the sample. The recorded images were analyzed with the LaVision StrainMaster (DaVis) 3D-DIC software using a subset size of 25 pixels and step size of 9 pixels. For a good overview and description of the DIC method, its limitations, resolution, etc., the reader is

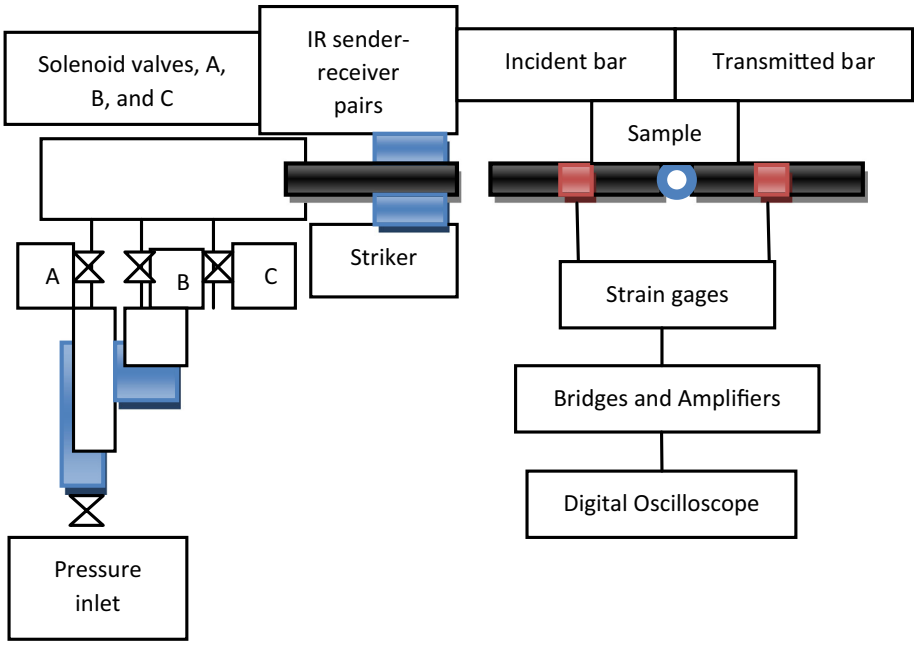

Fig. 2 Schematic picture of the Split Hopkinson Pressure Bar device at Tampere University of Technology

referred to Sutton et al. (2009). The DIC analysis of the BD samples shows that the fracture of the specimens initiates at the center or slightly closer to the incident bar contact point. This observation and the comparison of the forces on the incident and transmitted sides of the sample indicate adequate stress equilibrium.

3 Results and Discussion

3.1 Characterization of the Heat-Shocked Surfaces

Figures 3 and 4 show an example of the optical analysis used to characterize the crack patterns on the sample

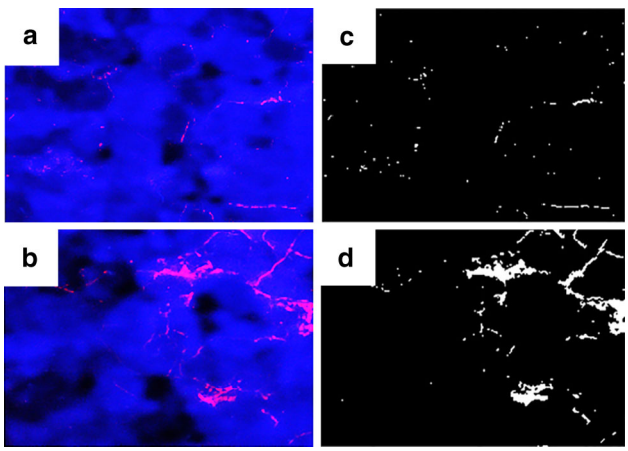

Fig. 3 Optical images **a** before and **b** after a 30-s thermal shock, and the identified cracks **c** before and **d** after the thermal shock for the Balmoral Red

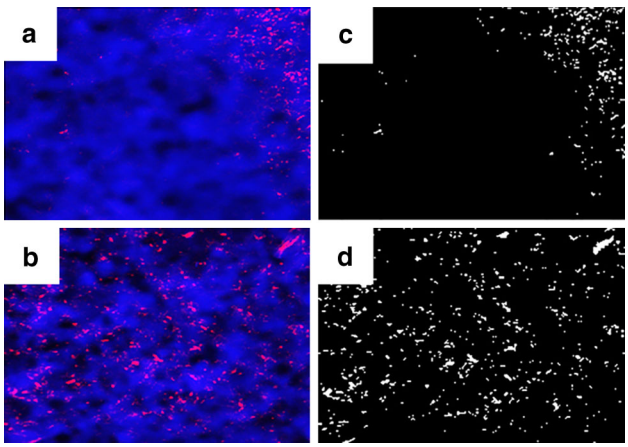

Fig. 4 Optical images **a** before and **b** after a 30-s thermal shock and the identified cracks **c** before and **d** after the thermal shock for the Kuru Grey

surface. Figure 3a, b is the original optical images obtained under UV light from a Balmoral Red BD sample before and after a 30-s thermal shock. Figure 4a, b shows the corresponding images for a Kuru Grey BD sample. Figure 3c, d show the processed images after thresholding of the UV images. The images taken under UV light are imported to MATLAB as RGB images, where the color of each pixel is represented by three numbers, i.e., Red, Green, and Blue. Since the dominant color in the liquid penetrant is "Red," the threshold is set on the "Red" color. If a pixel has a "Red" color higher than this threshold, the pixel is considered as a crack pixel represented by digit "1," otherwise the pixel is "0." This creates a binary matrix, the plot of which is a map of the identified surface

cracks. The obtained fractal dimension highly depends on the threshold value and the resolution of the image. The resolution of the image defines the spatial resolution of the crack detection method. The background noise is another important factor as it contributes to the RGB combination of the pixels. For these reasons, once the matrix is formed, the pattern of the cracks is evaluated by the naked eye to decide whether it represents the surface cracks of the real image or not.

The UV images in Figs. 3 and 4 reveal the difference between the surface crack patterns observed in the Balmoral Red and in the Kuru Grey. The pattern in the Balmoral Red prior to any heat shock consists of small surface cracks mainly located at the grain boundaries, while in the Kuru Grey the pattern is more composed of porosity inside the grains and at the grain boundaries. In the Balmoral Red, after the thermal shock the number of surface cracks increases and the interconnectivity of the cracks becomes more complex, while in the Kuru Grey the number of pores increases and short cracks connecting the pores become visible. The fractal dimension of the crack patterns increases during the thermal shock, indicating that the pattern of the cracks after thermal shocks is more complex and the network contains more interconnected surface cracks.

The fractal dimension was obtained for 15 samples of both granites, i.e., five samples for each thermal shock of 10, 30, and 60 s. The average fractal dimension before the thermal shock for the Balmoral Red was 1.07 ± 0.14, whereas for the Kuru Grey the fractal dimension was 1.22 ± 0.22. The effect of the heat shock on the crack patterns can be estimated from the change in the fractal dimension. After a 10-s heat shock, the average fractal dimension increases by 14% for the Balmoral Red and by 15% for the Kuru Grey. The 30- and 60-s heat shocks increased the fractal dimension for the Balmoral Red by 18 and 21% and for the Kuru Grey by 15 and 22%. Unfortunately, due to the nature of the rocks, the fractal dimension prior to the thermal shock shows significant scatter, which complicates the use of the absolute values of the fractal dimension for explaining the observed mechanical properties of the test materials. However, there seems to be a correlation between the fractal dimension after the thermal shocks and the mechanical properties, and especially the relative increase in the fractal dimension seems to be important, as will be shown later. Tables 3 and 4 summarize the fractal dimensions before and after the thermal shocks for the studied rock samples.

Figure 5 shows an example of the surface profiles obtained with the Alicona Infinite Focus G5 profilometer for the Balmoral Red granite. Figure 5a, c shows the raw images of the sample before and after the thermal shock, and Fig. 5b, d shows the corresponding processed images.

Table 3 Fractal dimension of the heat-shocked Balmoral Red samples

	10 s		30 s		60 s	
	Before	After	Before	After	Before	After
	1.19	1.47	1.05	1.45	1.21	1.48
	0.66	0.99	1.06	1.22	1.013	1.39
	1.08	1.17	1.07	1.35	1.11	1.33
	1.33	1.41	1.08	1.14	1.01	1.32
	1.01	1.12	1.07	1.33	1.13	1.45
Average	1.05	1.23	1.06	1.30	1.09	1.40
STDEV	0.25	0.20	0.01	0.11	0.08	0.07
Normalized		1.17		1.22		1.27

Table 4 Fractal dimension of the heat-shocked Kuru Grey samples

	10 s		30 s		60 s	
	Before	After	Before	After	Before	After
	1.38	1.76	1.17	1.16	1.16	1.29
	1.31	1.77	1.22	1.40	0.79	1.40
	1.46	1.57	1.21	1.48	0.99	1.38
	1.37	1.64	1.17	1.39	0.91	1.44
	1.71	1.72	1.27	1.37	1.11	1.21
Average	1.44	1.69	1.21	1.43	0.99	1.34
STDEV	0.16	0.08	0.04	0.05	0.15	0.09
Normalized		1.17		1.19		1.35

Similar images were obtained for all samples of the Balmoral Red and the Kuru Grey before and after the heat shocks. The areal roughness of the samples was measured using Alicona IF-MeasureSuite according to ASME B46.1-2002 (American National Standards Institute 2002) and Advanced Techniques for Assessment Surface Topography (Blunt and Jiang 2003). The average areal roughness for the 15 samples of the Balmoral Red before the heat shock was 9.46 ± 5.65 μm with the coefficient of variation of 60%. For the Kuru Grey samples, the roughness was 9.3 ± 4.4 μm and the coefficient of variation 47%.

Figure 6 shows the values of the fractal dimension after the heat shocks normalized by the fractal dimension before the heat shock. The normalized areal roughness was calculated for each test in the same way. The results are shown as a function of the duration of the heat shock for both test materials. Both properties increase as the duration of the thermal shock increases. This appears to be logical since the areal roughness is calculated based on the average surface height (S_a) (Blunt and Jiang 2003). As the duration of the heat shock increases, the number of surface cracks and thus the surface profile change as well. This leads to an increase in the areal roughness of the specimen. The results

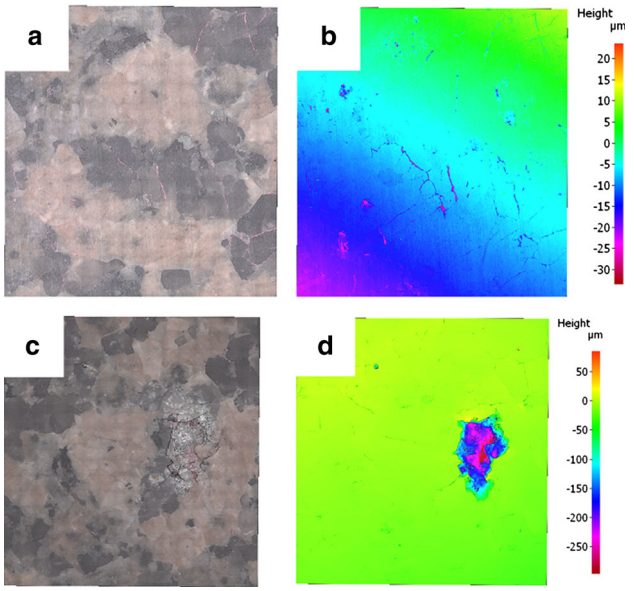

Fig. 5 Examples of images obtained using the Alicona Infinite Focus G5. **a** Raw image of the Balmoral Red sample before the heat shock, **b** height map of the image shown in **a**, **c** raw image after a 10-s heat shock, and **d** height map of image **c**

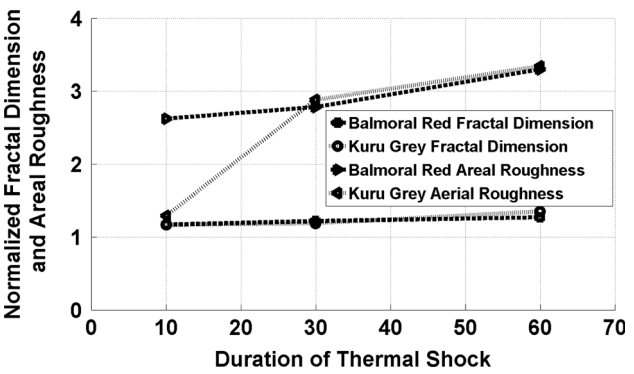

Fig. 6 Normalized fractal dimension and areal roughness as a function of the duration of the thermal shock for the Balmoral Red and the Kuru Grey

obtained for the areal roughness of the studied rocks are given in Tables 5 and 6. Profilometry analyses were carried out to confirm the results of the fractal dimension analysis, as more cracks essentially lead to an increase in the areal roughness. As both the fractal dimension and the areal roughness increase after applying thermal shocks, and an increase in the aerial roughness means an increase in surface cracks and porosity, the following discussion of the fractal dimension will be assumed to be valid for areal roughness as well.

3.2 Mechanical Testing

The results of the dynamic BD tests are shown in Fig. 7. The stress as a function of time for the Balmoral Red and the Kuru Grey specimens without any heat shock is shown in Fig. 7a, c, while Fig. 7b, d shows the corresponding data for samples with a 60-s thermal shock. The average tensile strength obtained for five non-heat-shocked Balmoral Red samples is 29 ± 3 MPa. However, when the duration of the thermal shock increases, the dynamic strength decreases significantly, as the average tensile strengths of the heat-shocked samples are 23, 16, and 12 MPa for the heat shocks of 10, 30, and 60 s. The behavior is very similar for the Kuru Grey; the average dynamic tensile strength for the non-heat-shocked specimens is 27 ± 3 MPa, while the strengths of the heat-shocked samples are 21, 16, and 15 MPa for the 10-, 30-, and 60-s heat shocks, respectively. After applying the thermal shocks, the strong peak in the stress versus time curves observed for the non-heat-treated samples fades away. Both the reduction in the maximum stress and the change in the shape of the curve can be explained by the increasing number, length, and interconnectivity of the cracks due to the heat shocks.

Table 5 Average areal roughness for the heat-shocked Balmoral Red samples

	10 s		30 s		60 s	
	Before	After	Before	After	Before	After
	3.87	33.15	6.37	34.39	9.55	30.74
	5.69	14.04	7.52	27.01	3.04	34.96
	10.58	25.85	12.05	20.03	11.08	55.20
	8.39	20.75	9.93	23.89	3.57	28.19
	13.35	14.66	10.61	23.74	26.32	27.56
Average	8.37	21.69	9.29	25.81	10.71	35.32
STDEV	3.77	8.02	2.31	5.39	9.42	11.48
Normalized		2.62		2.78		3.30

Table 6 Average areal roughness for the heat-shocked Kuru Grey samples

	10 s		30 s		60 s	
	Before	After	Before	After	Before	After
	5.46	8.01	4.49	21.21	8.17	25.27
	17.33	18.99	13.31	30.03	11.98	24.88
	7.45	10.07	9.95	23.58	14.53	32.89
	14.15	15.74	4.95	17.03	6.57	26.51
	12.43	23.81	5.77	22.48	2.87	37.58
Average	11.86	15.36	7.69	22.86	8.82	29.43
STDEV	4.86	6.46	3.81	4.71	4.57	5.59
Normalized		1.29		2.88		3.34

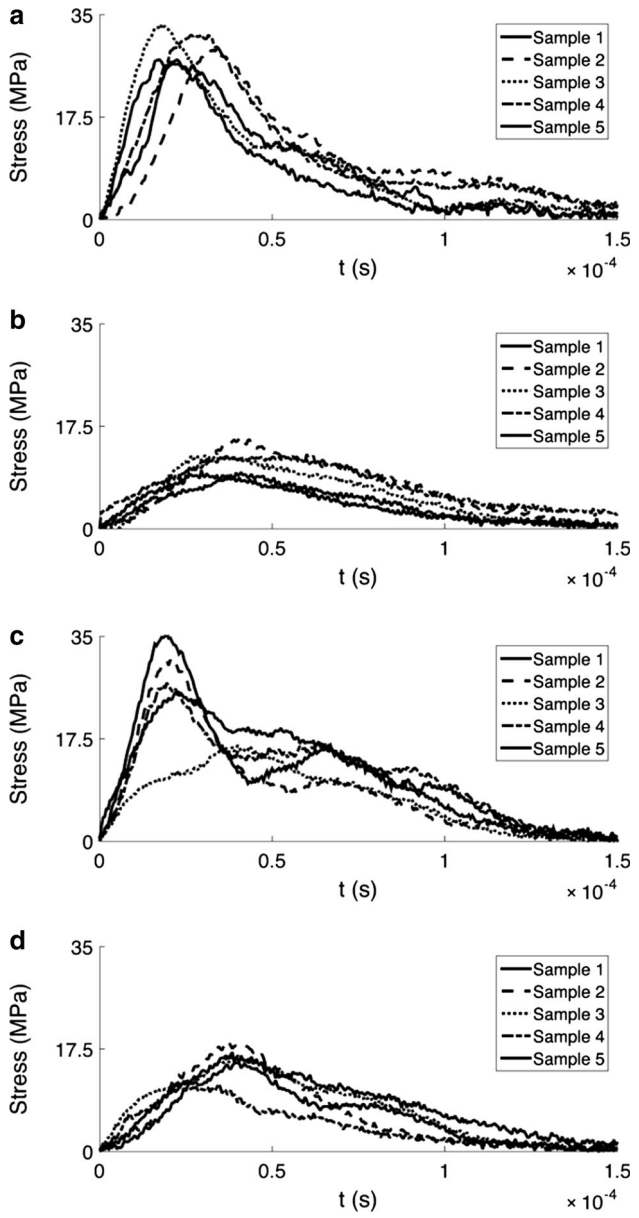

Fig. 7 High strain rate test results showing the tensile stress as a function of time for **a** the Balmoral Red samples without a heat shock, **b** the Balmoral Red samples with a 60-s heat shock, **c** the Kuru Grey samples without a heat shock, and **d** the Kuru Grey samples with a 60-s heat shock

Figure 8 shows the strength of the two studied rocks as a function of the normalized fractal dimension. The increase in the normalized fractal dimension up to 1.1 for both rocks leads to a rapid drop in the tensile strength. After this, while the strength of the Balmoral Red continues to decrease, the strength of the Kuru Grey also decreases but at a lower rate. As mentioned before, the porosity of the Kuru Grey increases during the heat shock. These pores can act as barriers for crack propagation (Ma et al. 2004). Therefore, it seems that after a certain point the increase in

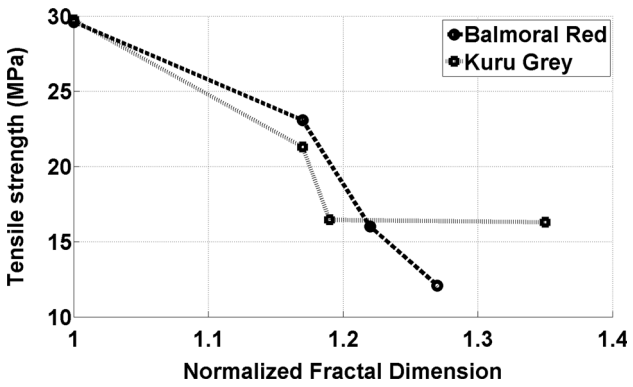

Fig. 8 Tensile strength of the rocks as a function of the normalized fractal dimension

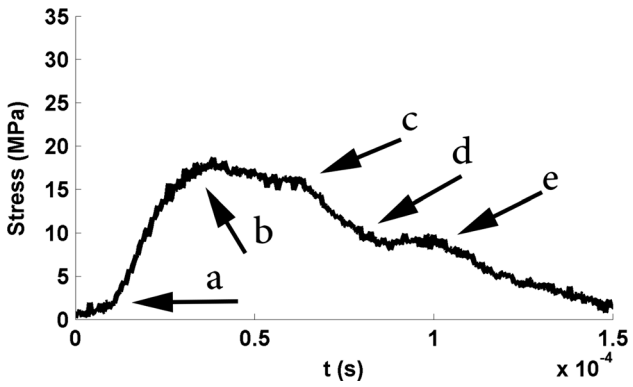

Fig. 9 Tensile stress as a function of time for a Kuru Grey sample with a 10-s thermal shock

the fractal dimension (due to microstructural changes) does not facilitate the fracture in the Kuru Grey, whereas the situation is different for the Balmoral Red. More cracks appear in the volume affected by the heat shock, more cracks become visible on the surface, and the existing cracks become longer, all of which facilitate the fracture of the rock at lower stress levels. This means that even though the fractal dimensions for both rocks show almost the same value, the response of the rocks is different due to the difference in their microstructural features.

It is quite obvious that the heat shock affects a certain volume of the rock rather than merely causing damage on the surface only. Furthermore, different heat shocks, e.g., a flame torch or a plasma gun, will cause different 3D crack patterns, which may seem similar on the surface. Also the tensile strength of the rock is a measure of the whole volume's ability to resist crack propagation. Therefore, any detailed description of the 3D crack distribution requires the use of advanced characterization methods, such as X-ray tomography, and is often restricted to small samples only. Mechanical testing of rocks, on the other hand, requires larger samples due to the heterogeneous nature of the rock microstructure. For these reasons, observing the

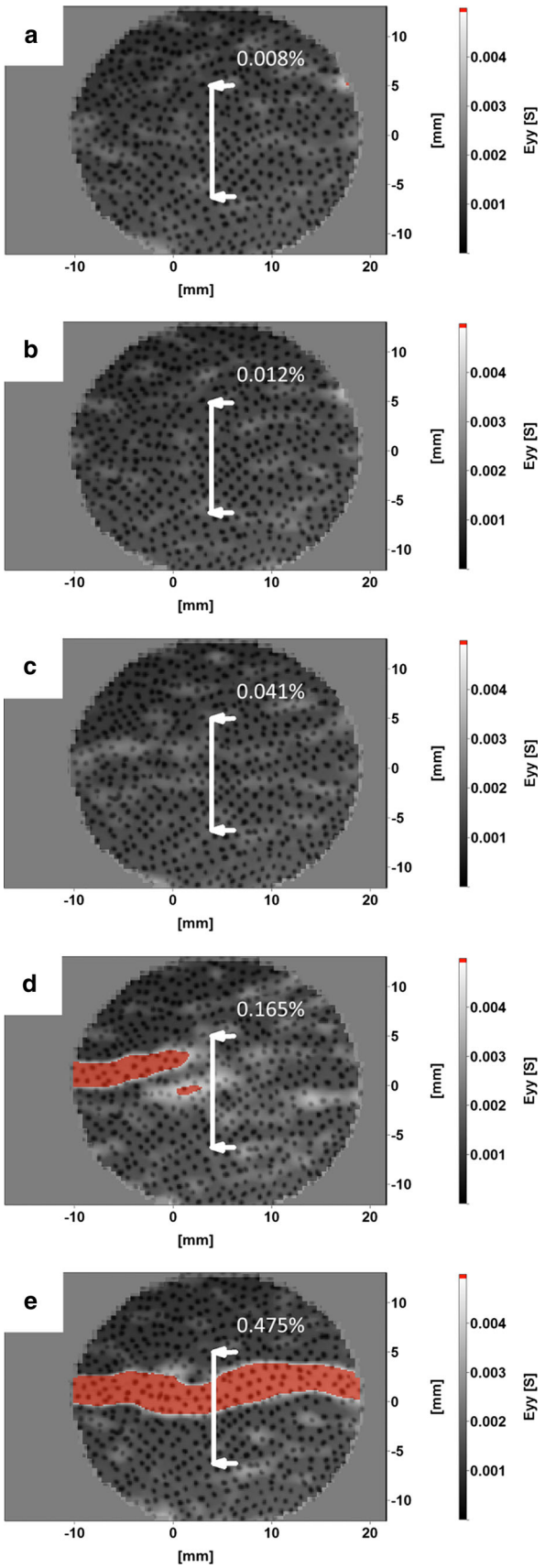

◀**Fig. 10** DIC images obtained during dynamic loading of a Kuru Grey sample for which the force–time plot is shown in Fig. 9. **a** $t = 0$ µs, **b** $t = 31.25$ µs, **c** t = 50 µs, **d** $t = 56{,}25$ µs, and **e** $t = 62{,}5$ µs

damage only on the surface is convenient, is fast, and can be done with simple optical microscopes that are easily available. The new methodology presented in this paper can be used to estimate the change in the rock's strength based on observations of the surface crack patterns. However, more work is needed to show the exact potential and accuracy of this method, and a comparison of samples with a known surface and volumetric crack and damage structures must be made in the near future.

Figure 9 shows the tensile stress as a function of time for a the Balmoral Red sample tested after a 10-s heat shock. Point (a) in the figure corresponds to the start of the loading and (b) indicates the moment just before the peak stress. The high-speed images corresponding to the times indicated in Fig. 9 are shown in Fig. 10. The strains in the *Y*-direction (vertical direction, perpendicular to loading) are also shown with the original images, indicating that the strains in the two first images (Fig. 10a, b) are very low and essentially constant over the sample surface. No strain localization appears in the images recorded just microseconds before the strength of the rock starts to decrease. Even Fig. 10c does not show very clear localization, nevertheless, the macroscopic strength of the rock has already started to decrease. This could be interpreted to indicate that the fracture initiates inside the sample and becomes visible on the surface only some microseconds after the peak stress. The crack then propagates through the sample very quickly in Fig. 10d, e. This is followed by crushing of the contact points of the sample and the stress bars. Unfortunately, due to the speckle pattern, the detailed characteristics of the crack propagation mechanism (transgranular or intergranular) in these two different granites could not be investigated.

The engineering strain in the direction perpendicular to the loading direction prior to the fracture was measured with LaVision StrainMaster (DaVis) 3D-DIC software by placing a virtual strain gage (see Fig. 10) with a fixed gage length at the center of the specimen. Tables 7 and 8 show the surface strain prior to fracture obtained with the DIC analysis for each thermal shock.

The results reveal a decreasing trend of the failure strain as the duration of the heat shock increases. In all tests, the Balmoral Red shows markedly higher maximum surface strains compared to those observed for the Kuru Grey. The reason for this can be found from the microstructure of the rocks, the smaller grain size of the Kuru Grey leading to a

Table 7 Strain on the surface prior to fracture for the Balmoral Red granite determined for the virtual gage length shown in Fig. 10

Duration of the heat shock (s)	Strain on surface prior to fracture (%)	Change (%)
0	0.8 ± 0.05	
10	0.47 ± 0.04	−41
30	0.38 ± 0.05	−52
60	0.26 ± 0.03	−67

Table 8 Strain on the surface prior to fracture for the Kuru Grey granite determined for the virtual gage length shown in Fig. 10

Duration of the heat shock (s)	Strain on surface prior to fracture (%)	Change (%)
0	0.29 ± 0.04	
10	0.15 ± 0.07	−48
30	0.09 ± 0.03	−69
60	0.06 ± 0.01	−79

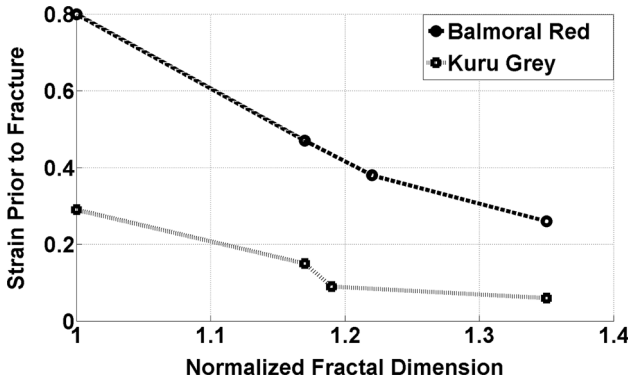

Fig. 11 Surface strain prior to fracture as a function of normalized fractal dimension

more brittle behavior (Eberhardt et al. 1999; Lasalmonie and Strudel 1986).

Figure 11 shows the strain prior to the fracture as a function of normalized fractal dimension. The decrease in the strain prior to fracture is more pronounced for the Balmoral Red. This behavior can be related to the fact that the defect structure of the Kuru Grey consists of more pores than of the Balmoral Red. One possible explanation could be that these pores act as barriers for crack propagation by increasing the radius of a crack tip that propagates into a pore. At the higher fractal dimension of 1.18, the strain prior to fracture for the Kuru Grey remains almost constant. The situation is different for the Balmoral Red; as the duration of the thermal shock increases, the crack density increases as well. This facilitates the deformation of the rock, and the surface strain prior to fracture decreases continuously with increasing fractal dimension.

4 Concluding Remarks

- A methodology was developed to characterize and quantify the surface damage caused by a heat shock on a Brazilian disk sample. Optical images were analyzed to obtain fractal dimension of the surface crack patterns, and the surface was further analyzed using an optical profilometer.
- Both the fractal dimension and the surface roughness obtained before and after the thermal shocks clearly show an increase in the amount of surface cracks and damage, as well as an increase in the complexity of the crack network. In the Balmoral Red, more cracks appear on the surface and the existing cracks become longer during the heat shock. However, in the Kuru Grey, in addition to introducing more cracks on the surface, the degree of porosity increases as well.
- The samples were tested with a Split Hopkinson Pressure Bar device, and the results were analyzed using digital image correlation. The tensile strength and the maximum surface strain prior to fracture of the Balmoral Red granite were observed to decrease continuously with the increase in the fractal dimension. However, for the Kuru Grey, both the strength and maximum strain on the surface first decrease and then become saturated at higher fractal dimensions. One possible explanation for the observed behavior is that the pores limit the crack propagation in the Kuru Grey at higher fractal dimensions.
- The surface damage, especially the fractal dimension of the crack pattern, can be used to predict the strength of the material. However, it is clear that the heat shock affects a larger volume than just the surface and there are also cracks under the surface that are not visible with visible or ultraviolet light. The presented surface characterization method, however, is faster, is easier to use, and can provide acceptable estimates for the effects of the heat shock on the tensile strength of the studied rocks. However, more thorough investigation is required to check the true accuracy of the technique.
- Digital image correlation was used to observe the crack initiation and propagation on the surface of the samples during the high rate tests. Time stamps from the tests were recorded on the images, and the data from the SHPB tests were synchronized with the obtained images. Typically, the cracks initiate inside the sample and propagate to the surface only after the strength of the sample has already decreased significantly. The DIC was used to estimate the fracture strain of the material during a high strain rate test by using a virtual extensometer placed on the image. The obtained maximum strains prior to the fracture also decrease with increasing heat shock duration.

Acknowledgements This work was supported by Suomen Luonnonvarain Tutkimussäätiö—Foundation under Grant Numbers 1768/14, 1779/15, and 1789/16.

References

American National Standards Institute (2002) Surface texture (surface roughness, waviness, and lay). The American Society of Mechanical Engineers, New York

An R, Li Y, Dou Y, Liu D, Yang H, Gong Q (2006) Water-assisted drilling of microfluidic chambers inside silica glass with femtosecond laser pulses. Appl Phys A 83(1):27–29

Apostol M (2007) Strain rate and Temperature Dependence of the Compression Behavior of FCC and BCC Metals. Tampere University of Technology, Tampere

Bauer S, Johnson B (1979) Effects of slow uniform heating on the physical properties of the westerly and charcoal granites. Austin, s.n.

Bieniawski ZT, Bernede M (1979) Suggested methods for determining the uniaxial compressive strength and deformability of rock materials: part 1. Suggested method for determining deformability of rock materials in uniaxial compression. Int J Rock Mech Min Sci Abstr 1(2):138–140

Blunt L, Jiang X (2003) Advanced techniques for assessment surface topography. Kogan Page Science, London

Brown W, Parsons I (1989) Alkali feldspars: ordering rates, phase transformation and behaviour diagrams for igneous rocks. Mineral Mag 53:25–42

Cai M, Kaiser P (2004) Numerical simulation of the Brazilian test and the tensile strength of anisotropic rock and rock with pre-existing cracks. Int J Rock Mech Min Sci 41:478–483

Chau K, Wang P (1996) Microcracking and grain size effect in Yuen long marbles. Int J Rock Mech Min Sci Abstr 33(5):479–485

Dai F, Xia K (2010) Loading rate dependence of tensile strength anisotropy of Barre granite. Pure appl Geophys 167(11):1419–1432

Dai F, Huang S, Xia K (2010) Some fundamental issues in dynamic compression and tensile tests of rock using Split Hopkinson Pressure Bar. Rock Mech Rock Eng 43(6):657–666

Dunn D, LaFountain L, Jackson R (1973) Porosity dependence and mechanism of brittle fracture in sandstones. J Geophys Res 78(14):2403–2417

Dwivedi R, Goel R, Prasad V, Sinha A (2008) Thermo-mechanical properties of Indian and other granites. Int J Rock Mech Min Sci 45(3):303–315

Eberhardt E, Stimpson B, Stead D (1999) Effects of grain size on the initiation and propagation thresholds of stress-induced brittle fractures. Rock Mech Rock Eng 32(2):81–99

Fair JC (1981) Development of high-pressure abrasive-jet drilling. J Petrol Technol 33(08):1–11

Feder J (1988) Fractals (physics of solids and liquids). Plenum Press, New York

Fourmeau M, Gomon D, Vacher R, Hokka M, kane A, Kuokkala VT, (2014) Application of DIC technique for studies of Kuru granite rock under static and dynamic loading. Trondheim Procedia Mater Sci 3:691–697

Gasparik T (2003) Phase diagrams for geoscientists: an atlas of the earth's interior, 1st edn. Springer, New York

Gorham DA, Wu X (1997) An empirical method of dispersion correction in the compressive Hopkinson bar test. J Phys IV 7:223–228

Gorsevski P, Onasch C, Farver J, Ye X (2012) Detecting grain boundaries in deformed rocks using a cellular automata approach. Comput Geosci 42:136–142

Hawkes M, Mellor M (1978) Experimental rock deformation—the brittle field. Springer, Berlin

Hudson J, Brown E, Rummel F (1972) The controlled failure of rock discs and rings loaded in diametral compression. Int J Rock Mech Min Sci Abstr 9(2):241–248

Khair A, Achanti A (1996) Effect of specimen size on compressive strength of coal. Golden, Colorado School of Mines

Kolle JJ, Otta R, Stang D (1991) Laboratory and field testing of an ultra-high-pressure, jet-assisted drilling system. Amsterdam, Society of Petroleum Engineers

Kranz R (1983) Microcracks in rocks: a review. Tectonophysics 100(1–3):449–480

Lasalmonie A, Strudel JL (1986) Influence of grain size on the mechanical behaviour of some high strength materials. Mater Sci 21(6):1837–1852

Lindroth D, Morrell R, Blair J (1991) Microwave assisted hard rock cutting. United States of America, Patent No. 5,033,144

Liu S, Xu J (2014) Mechanical properties of Qinling biotite granite after high temperature treatment. Int J Rock Mech Min Sci 71:188–193

Luodes H, Luodes N (20159 Mechanical and physical properties [Online]. http://www.finskastone.fi/images/docs/Finska_Balmoral_Red_fine_grained_2007.pdf

Ma J, Wang H, Weng L, Tan G (2004) Effect of porous interlayers on crack deflection in ceramic laminates. J Eur Ceram Soc 24(5):825–831

Mahanta B, Singh T, Ranjoth P (2016) Influence of thermal treatment on mode I fracture toughness of certain Indian rocks. Eng Geol 210:103–114

Mardoukhi A, Saksala T, Hokka M, Kuokkala VT (2015) An experimental and numerical study of the dynamic Brazilian disc test on Kuru granite. Tampere, Finnish association for structural mechanics

Miller D, Ball A (1990) Rock drilling with impregnated diamond microbits—an experimental study. Int J Rock Mech Min Sci Abstr 27(5):363–371

Perry K, Salehi I, Abbasi H (2010) Laser assisted drilling. United States of America, Patent No. US 2010/0078414 A1

Price N (1996) Fault and joint development in brittle and semi-brittle rocks. Pergamon Press, Oxford

Rao QH, Wang Z, Xie HF, Xie Q (2007) Experimental study of mechanical properties of sandstone at high temperatures. J Cent South Univ Technol 14:478–483

Rippa F, Vinale F (1983) Structure and mechanical behavior of a volcanic tuff. International Society for Rock Mechanics, Melbourne

Roy D, Singh T (2016) Effect of heat treatment and layer orientation on the tensile strength of a crystalline rock under Brazilian test condition. Rock Mech Rock Eng 49(5):1663–1677

Saksala T, Gomon D, Hokka M, Kuokkala VT (2014) Numerical and experimental study of percussive drilling with a triple-button on Kuru granite. Int J Impact Eng 72:56–66

Saksala T, Brancherie D, Ibrahimbegovic A (2016) Numerical modeling of dynamic rock fracture with a combined 3D continuum viscodamage-embedded discontinuity model. Int J Numer Anal Met 40(9):1339–1357

Sengun N (2014) Influence of thermal damage on the physical and mechanical properties of carbonate rocks. Arab J Geosci 7(12):5543–5551

Shewmon P, Zackay V (1961) Response of metals to high velocity deformation. Interscience Publishers Inc, New York

Sirdesai NN, Singh TN, Ranjith PG, Singh R (2016) Effect of varied durations of thermal treatment on the tensile strength of Red Sandstone. Rock Mech Rock Eng 50(1):205–213

Smorodinov M, Motovilov E, Volkov V (1970) Determinations of correlation relationships between strength and some physical

characteristics of rocks. International Society for Rock Mechanics, Belgrade
Sutton M, Orteu J, Schreier H (2009) Image correlation for shape, motion and deformation measurements. Springer, New York
Tkalich D, Fourmeau M, Kane A, Cailletaud CLG (2016) Experimental and numerical study of Kuru granite under confined compression and indentation. Int J Rock Mech Min Sci 87:55–68
Veenhuizen S, O'Hanlon T, Kelley D, Aslakson J (1996) Ultra-high pressure down hole pump for jet-assisted drilling. Society of Petroleum Engineers, New Orleans
Verma AK, Jha MK, Maheshwar S, Singh TN, Bajpai RK (2016) Temperature-dependent thermophysical properties of Ganurgarh shales from Bhander group, India. Environ Earth Sci 75(4):1–11
Vishal V, Pradhan SP, Singh TN (2011) Tensile strength of rock under elevated temperatures. Geotech Geol Eng 29:1127–1133
Wenk H, Christie J (1991) Comments on the interpretation of deformation textures in rocks. J Struct Geol 13(10):1091–1110
Xia K, Yao W (2015) Dynamic rock tests using split Hopkinson (Kolsky) bar system—a review. J Rock Mech Geotec Eng 7(1):27–59
Yin T, Li X, Cao W, Xia K (2015) Effects of thermal treatment on tensile strength of Laurentian granite using Brazilian test. Rock Mech Rock Eng 48(6):2213–2223
Zhang Q, Zhao J (2014) A review of dynamic experimental techniques and mechanical behaviour of rock materials. Rock Mech Rock Eng 47(4):1411–1478

IV

A numerical and experimental study on the tensile behavior of plasma shocked granite under dynamic loading

Ahmad Mardoukhi, Timo Saksala, Mikko Hokka, Veli-Tapani Kuokkala

Rakenteiden Mekaniikka 50 (2017) 41-62

Rakenteiden Mekaniikka (Journal of Structural Mechanics)
Vol. 50, No 2, 2017, pp. 41-62
http://rakenteidenmekaniikka.journal.fi/index
https:/doi.org/10.23998/rm.65301

VERTAISARVIOITU
KOLLEGIALT GRANSKAD
PEER-REVIEWED
www.tsv.fi/tunnus

A numerical and experimental study on the tensile behavior of plasma shocked granite under dynamic loading

Ahmad Mardoukhi[1], Timo Saksala, Mikko Hokka, Veli-Tapani Kuokkala

Summary. This paper presents a numerical and experimental study on the mechanical behavior of plasma shocked rock. The dynamic tensile behavior of plasma shock treated Balmoral Red granite was studied under dynamic loading using the Brazilian disc test and the Split Hopkinson Pressure Bar device. Different heat shocks were produced on the Brazilian disc samples by moving the plasma gun over the sample at different speeds. Microscopy clearly showed that as the duration of the thermal shock increases, the number of the surface cracks and their complexity increases (quantified here as the fractal dimension of the crack patterns) and the area of the damaged surface grows larger as well. At the highest thermal shock duration of 0.80 seconds the tensile strength of the Brazilian disc sample drops by approximately 20%. In the numerical simulations of the dynamic Brazilian disc test, this decrease in tensile strength was reproduced by modeling the plasma shock induced damage using the embedded discontinuity finite element method. The damage caused by the plasma shock was modeled by two methods, namely by pre-embedded discontinuity populations with zero strength and by assuming that the rock strength is lowered and conform to the Weibull distribution. This paper presents a quantitative assessment of the effects of the heat shock, the surface microstructure and mechanical behavior of the studied rock, and a promising numerical model to account for the pre-existing crack distributions in a rock material.

Key words: SHPB, dynamic rock fracture, continuum damage model, embedded discontinuities, strain rate sensitivity, fractal dimension, Weibull distribution

Received 19 March 2017. Accepted 2 June 2017. Published online 7 August 2017.

Introduction

Dynamic fracture behavior of rock materials is one of the most important concepts in rock engineering applications such as percussive drilling, rock burst, and rock blasts. Unfortunately, however, creating the exact environment of these applications in the laboratory is difficult due to the large scale of samples and equipment required to carry out the tests. The rock itself as a material further complicates the testing since its behavior depends on many factors, such as chemical composition [25], structure [26], texture [37], and grain size [34] alongside testing condition parameters such as temperature [7, 11, 35, 39, 41], confining pressure [14], specimen size, etc. [6, 9, 13, 18, 17, 32]. Studying the

[1]Corresponding author: ahmad.mardoukhi@tut.fi

dynamic behavior of rocks becomes even more challenging in environments such as deep drilling for geothermal energy, where the confining pressure and temperature change as the depth changes. Considering the amount of data needed for a complete description of the rock behavior, a model is required, which can take all these variables into account. A substantial amount of effort has already been put into this matter. For example, Saksala [27] simulated the percussive drilling with a triple-button indenter using a finite elements based approach, where the rock fracture was modeled with a continuum viscoelastic-damage model. Saksala et al. [29] continued their work and created a 3D model where the cracks are embedded as strong displacement discontinuities. From the works similar to this paper, Cai and Kaiser [5] studied the effects of pre-existing cracks on the tensile behavior of rocks.

Not only creating the exact condition for dynamic testing of rock is a difficult task to perform, numerical modeling of these conditions is challenging as well. The major problem is modeling the dynamic crack propagation [28]. In addition, Zhang and Zhao [43] stated that a strong loading rate sensitivity can be observed in the dynamic loading of rock materials. Many approaches have been used over the past years to simulate the rock behavior under dynamic loading condition. Most of these approaches were based on the finite element method (FEM) and discrete or distinct elements method (DEM). In FEM-based models the cracks are usually represented as inelastic localized deformation zones, see refs. [36, 38]. Zhu et al. [45] used a FEM-based numerical code of rock failure process analysis (RFPA) to simulate the behavior of Brazilian disc samples of rocks under combined static and dynamic loading conditions. The RFPA code was developed first by Tang [33]. In this code the rock fracture is modeled by a simple rate-independent isotropic damage model, and the Weibull distribution is used to describe the heterogeneity at a mesoscopic scale. Continuum models have the advantage of higher computational efficiency, but the results obtained from these models do not correspond perfectly to the experimental results. The reason for this can be found from the nature of these kind of models, which are rate-independent. On the other hand, DEM works quite well in the dynamic rock fragmentation and fracture because of the discontinuum assumption. The examples of using this method can be found, for example, in refs [16, 19, 44]. Combining FEM and DEM provides a unique opportunity to have the features of continuum and discontinuum techniques in one code. This approach was tested by Mahabadi et al. [21, 22], whose work shows promising results for fragmentation analysis under dynamic loading conditions.

In this work, we apply the modeling technique presented in refs. [27, 29] to the numerical simulation of the Brazilian disc test on plasma shocked granite. This method is based on a combination of isotropic rate-dependent damage model and an embedded discontinuity model. The thermal shock induced cracks are accounted for as randomly oriented displacement discontinuities, which are pre-embedded in the ordinary finite elements. In this method, the exposure time of the plasma shock is represented simply by assuming that a longer exposure time corresponds to a larger percentage of finite elements having a pre-embedded discontinuity.

In our previous papers [23, 24], we presented a systematic procedure for the evaluation of the effects of microstructure and testing conditions on the dynamic tensile behavior of granitic rocks, in which the properties of rock were modified using heat shocks. The heat shocks were applied using an oxygen-acetylene flame torch. Considering the fact that using a flame torch is not the best solution from the technical point of view, a plasma shock was used to deteriorate the rock microstructure and properties in this work.

Experimental procedure

The tested material in this study was coarse grain Balmoral Red granite with the mean porosity value of 0.44% and the quasi-static compression strength of about 180 MPa. Table 1 summarizes the chemical composition for this granite. The microstructure of the rock is homogenous and shows no texture. Evidently, the mechanical properties are isotropic and the distribution of minerals is homogenous as well.

Table 1 Mineral composition of Balmoral Red granite [20].

Mineral	Wt.%
Potash Feldspar	40
Quartz	33
Plagioclase	19
Biotite & Hornblende	8

There are four methods to determine the tensile strength of rock materials: dynamic direct tension test, spalling method, semi-circular bending test (SCB), and Brazilian disc method [40]. Dynamic direct tension test can be the most accurate test since the stress state is 1D, but this method has its downsides. The experimental setup of this method is complex. The requirement for aligning the system is strict to avoid bending of the sample during the test. Preparation of the sample is difficult as well because of the complex shape of the specimen and poor machinability of the granite material. Moreover, a proper high strength glue is needed for joining the sample and the pressure bars [40].

The SCB method is a simpler approach compared to the dynamic direct tension test, however, it should be noted that the result obtained with this method is the flexural strength which is different from tensile strength [43]. The spalling method is also used to measure the tensile strength of the rock materials, but the compressive stress wave may affect the sample properties before the tensile wave reaches the sample. Attenuation of the wave in this method is another drawback. To overcome these difficulties, the Brazilian disc (BD) method seems to be a good solution and yet, this method has its own downsides. The sample should break along the loading direction and close to the center of the sample for a valid BD test [15, 31]. However, the instrumentation and carrying out the BD test is easier compared to the above mentioned methods. For these reasons, in this work the BD method was employed to measure the tensile strength of the studied material.

The Brazilian Disc [3] samples with a diameter of 40.5mm were cut from a rock plate with a thickness of 21mm. Figure 1 shows the natural surface of the samples and the modified surface for Digital Image Correlation (DIC) analysis. Before and after applying the heat shocks, optical microscopy was used to analyze the surface structure of the rock. In addition, liquid penetrant was applied on the surface of the samples to characterize the surface cracks before applying the heat shock. The samples were tested at the same strain rate but with a different thermal shock. Three different thermal shocks were applied on the surface of the samples by moving the tip of the plasma gun at different speeds over the surface of the samples. The plasma gun with a power of 50 kW at the distance of 6.5 cm from the surface of the samples was passed with the speeds of 50, 75, and 100 mm/s, providing thermal shocks with durations of 0.80, 0.55, and 0.40 seconds. The temperature of the surface of the samples was measured using an infrared thermometer immediately after applying the plasma shock. The recorded temperatures were 100 °C, 88 °C, and 76 °C for 0.80, 0.55, and 0.40 second plasma shock, respectively. After the thermal shocks, the samples were cooled down in air to room temperature. Unfortunately, it was not possible to obtain the heating and cooling rate of the specimen during the thermal shock process.

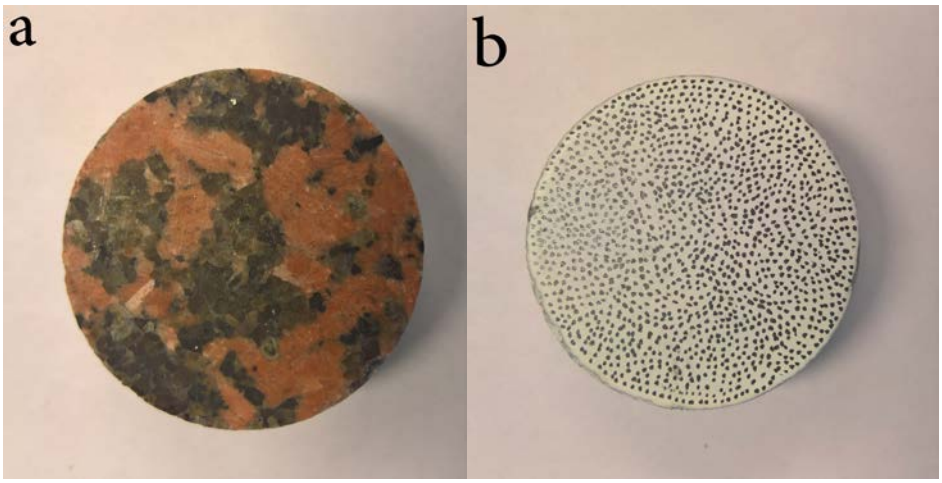

Figure 1 a) Natural surface of Balmoral Red granite and b) DIC speckle pattern on the sample.

After applying the heat shock, liquid penetrant was reapplied on the surface of the samples to observe the changes in the surface cracks caused by the thermal shocks. The samples were put under a LEICA CLS 150 XE microscope for microscopy analysis. The lights of the microscope were replaced by an ultraviolet (UV) light source. Later on these images were used to obtain the fractal dimension of the surface crack patterns by comparing the images taken before and after the heat shock. To obtain the fractal dimension, the box counting method was used. This method is commonly used when the fractal dimension of an object cannot be calculated by numerical or analytical methods. The accuracy of this method is highly dependent on image resolution, as the pixels are the grids used in the box counting method. For detailed description of this method, the reader is referred to [10].

High strain rate tests were conducted using a compression Split Hopkinson Pressure Bar (SHPB) device. As suggested by International Society of Rock Mechanics (ISRM), in a static BD test the bars should be modified by using special steel loading jaws to provide an arc contact angle of 10˚ at the failure of the disc sample [4]. Moreover, two adhesive papers should be used to wrap the sample on its periphery. However, this design causes some problems during dynamic testing, such as interferences in the wave propagation, which can result in errors in the measured data. Dai et al. [8] showed that if the SHPB system is properly aligned, the sample can be tested without the special jaws and adhesive papers.

The pressure bars were made of AISI 4340 steel with a diameter of 22 mm and the length of 1200 mm. The striker bar of the same material with the length of 120 mm and the impact speed of 10 m/s was used in the tests. Adjustable stanchions with supporting bearings were used to adjust the movement and alignment of the bars. An air gun was used to impact the striker on the incident bar. Three optical IR sender-receiver pairs were used to measure the impact velocity of the striker. These sensors were also used as the triggering signal for the oscilloscope. Two active strain gages were attached to the center of incident and transmitted bars. Kyowa CDV 700A series signal conditioner was used to amplify the signals of the strain gages, which were recorded on a 12-bit 10MSample Yokogawa digital oscilloscope. Detailed information about the instrument can be found for example in ref. [1]. A numerical dispersion correction based on the work of Gorham [12] was employed to correct the changes in the signals caused by the dispersion of the waves as they travel through the bars. A disc of soft deformable copper with the thickness of 0.5 mm was used to increase the rise time of the incident pulse and to improve the dynamic equilibrium. In this case, the striker bar impacts the pulse shaper before the incident bar, resulting in the generation of a nearly non-dispersive ramp pulse reaching the incident bar. This way the dynamic force balance on the specimen is facilitated [8]. Each

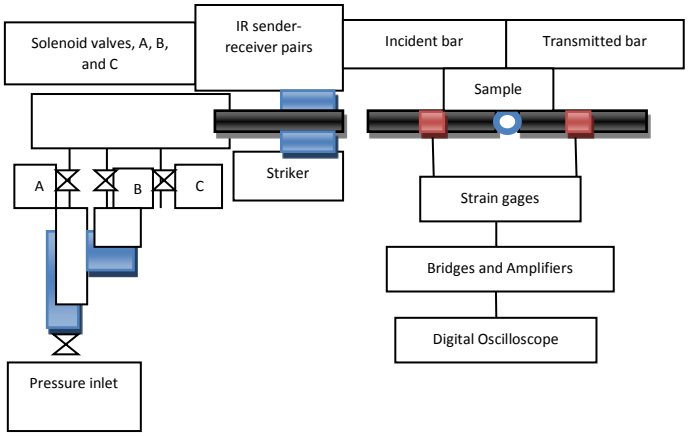

Figure 2 Schematic picture of the Split Hopkinson Pressure Bar device at Tampere University of Technology.

test was repeated five times with the impact speed of 10 m/s. Figure 2 demonstrates the schematic view of the high strain rate testing setup.

Digital image correlation was used to analyze the rock fracture during the high strain rate test. As the natural rock surface does not provide enough contrast for the correlation algorithm, the surfaces of the samples were coated by a thin layer of white paint, and black speckles were applied on the surface by a permanent marker. This modified surface is shown in Figure 1b. The images were recorded at 25 kfps with the size of 1024*812 pixels. Two Decocool lights were used for illuminating the surface of the samples. The obtained images were analyzed by StrainMaster (DaVis) 3D-DIC software using the subset of 17 pixels and the step size of 7 pixels.

Fractal dimension analysis

Figure 3 shows an example of the images taken by optical microscope to characterize the surface cracks and their pattern. Figures 3a and 3b are the images taken under UV light before and after applying a 0.80 s thermal shock. Figures 3c and 3d show the processed images after thresholding. The images taken by the microscope are imported to Matlab as RGB images. As the dominant color of the cracks seen in the microscope images is red and the background tends towards the blue color, the threshold was set for a specific amount of red color and a minimum amount of blue color to differentiate the affected area from the background. If a pixel meets the criteria for the thresholding, the pixel is considered as an affected point and is presented by digit “1”. Otherwise the pixel is set as “0”. This process produces a binary matrix, which in effect forms a map of the affected area. The obtained fractal dimensions are highly dependent on the threshold value, the resolution of the image, and the noise of the background. Considering these factors that affect the fractal dimension when the matrix is formed, the pattern will be checked by naked eye to decide if it represents the affected zone compared with the original image or not.

Figure 3 shows how the thermal shock applied by the plasma gun changes the surface of the sample. It is evident from Figure 3a that before applying the heat shock there are only few surface cracks and surface defects visible. After applying the heat shock, the surface of the sample becomes damaged and some parts of the sample surface are removed.

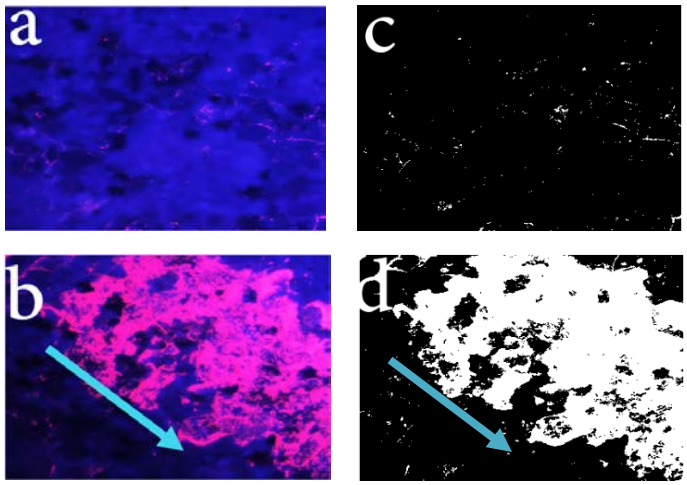

Figure 3 Microscope images a) before and b) after a 0.80 s plasma shock, and the damaged surface and identified cracks c) before and d) after the plasma shock. The arrow indicates the direction of the movement of the plasma gun.

The fractal dimension was obtained for 15 samples before and after applying the heat shock, i.e., five samples for each heat shock of 0.40, 0.55, and 0.80 seconds. The average fractal dimension for the 15 non-heat shocked samples is 1.04 ± 0.08. The average values for the heat shocked samples, in turn, are 1.39 ± 0.17, 1.60 ± 0.08, and 1.74 ± 0.05 for the 0.40, 0.55, and 0.80 second heat shocks, respectively. It should be noted that it is not possible to exactly correlate the mechanical properties of the rock material with the fractal dimension because the fractal dimension is obtained from the surface of the samples only. However, there seems to be a correlation between the relative change in the fractal dimension and the mechanical properties of the rock. Table 2 summarizes the calculated fractal dimension values for each test.

Table 2 Fractal dimension of the sample before and after applying a plasma shock.

	0.40s		0.55s		0.80s	
	Before	After	Before	After	Before	After
	1.1088	1.3978	1.0288	1.5251	1.1401	1.6888
	1.0544	1.4049	1.031	1.5807	0.7839	1.8155
	1.0548	1.5203	1.0985	1.6774	1.0609	1.7009
	1.0927	1.5471	1.0247	1.547	1.0825	1.7306
	1.0153	1.1173	1.0231	1.7074	1.0059	1.8066
Average	1.0652	1.3975	1.0412	1.6075	1.0146	1.7485
STDEV	0.0366	0.1703	0.0322	0.0806	0.1377	0.0591
Normalized		1.31		1.54		1.72

It is evident that as the duration of the thermal shock increases, the normalized fractal dimension increases as well. This is simply due to the fact that with lower speed the plasma gun stays for a longer time on the surface of the samples, thus more energy is applied on the surface of the samples and higher temperature is achieved. Since granitic rocks are composed of different minerals with different heat capacities and thermal expansion coefficients, increasing the temperature in a short

priod of time leads to the chipping of small particles from the surface of the samples and increases the amount of the damaged area, which leads to a higher value for the fractal dimension. As mentioned before, feldspar and quartz play the most important role in this phenomenon and they are the main cause for the thermal crack development [2].

Split Hopkinson Pressure Bar Results

The results of the dynamic BD tests are shown in Figure 4. Figure 4a shows the stress as a function of time for the specimens without any heat shock, while Figures 4b, 4c, and 4d show the results for the specimens' heat shocked for 0.80, 0.55, and 0.40 seconds, respectively. The average tensile strength for the five non-heat shocked samples is 29 ± 3 MPa. The corresponding value for 0.40s thermal shocked samples is 29 ± 3 as well, indicating that the thermal shock had almost no effect on the tensile strength of the tested material. However, as the duration of the thermal shock increases, the value of the tensile strength drops to 25 ± 4 MPa and 23 ± 3 MPa for the 0.55 and 0.80 second thermal shocks, respectively. The decreases of strength by 20% by applying the 0.8 heat shock shows the efficiency of using a plasma gun as the heat source. It has been shown [23] that applying the heat shock using flame torch leads to the decreases of strength by 58% in duration of 60 seconds. Therefore, the 20% decreases in strength of the rock only in duration of 0.8 second shows the effectiveness of this method. By increasing the duration of the heat shock, the strong peak in the stress vs time curves tends to get lower. This observation with the decrease in the tensile strength of the rock can be related to the fact that by increasing the duration of the thermal shock, the damaged volume under the surface increases.

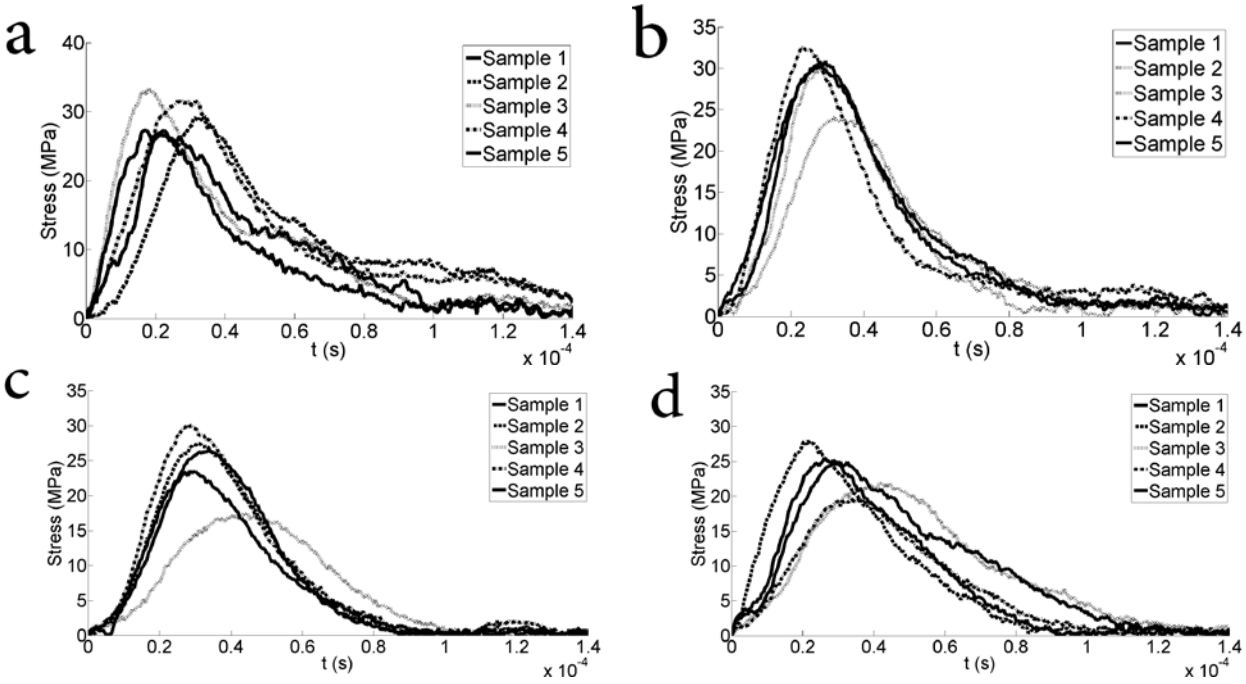

Figure 4. High strain rate test results showing the tensile stress as a function of time for a) samples without a heat shock, b) samples with a 0.40 s heat shock, c) samples with a 0.55 heat shock, and d) samples with a 0.80 s heat shock.

Figure 5 shows the strength of the rock as a function of the normalized fractal dimension. The strength of the rock shows no change up to the normalized fractal dimension of 1.3. This point correlates to the thermal shock with a duration of 0.40 s. This observation indicates that even though

the plasma gun is powerful (50 kW) and the plasma shock itself can provide a great amount of energy in a very short time, there is still a minimum amount of time needed for this energy to affect a reasonable thickness of the rock material. A thermal shock with a duration of 0.55 seconds decreases the strength of the rock from 29 ± 3 MPa to 25 ± 4 MPa (14% decrease). The decreasing trend of the tensile strength continues as the fractal dimension increases and for the point of 1.72 (0.80 s heat shock), the tensile strength reaches the average value of 23 ± 3 MPa (20% decrease).

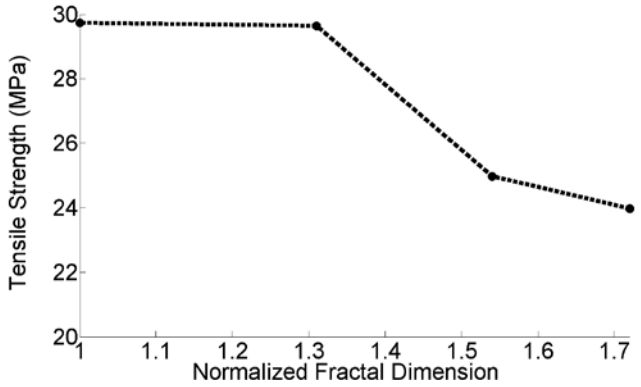

Figure 5. Tensile strength of the rock as a function of the normalized fractal dimension.

Numerical modeling

Material model for the rock

The material model for the rock fracture is based on a combination of isotropic rate-dependent damage model and an embedded discontinuity model. A detailed treatment, validation and mesh sensitivity studies of the model can be found in [28, 29]. Therefore, instead of pointless repetition of validation, parameter and mesh sensitivity simulations, only new simulations related to present application are presented here. However, the model is briefly described for the convenience of the reader.

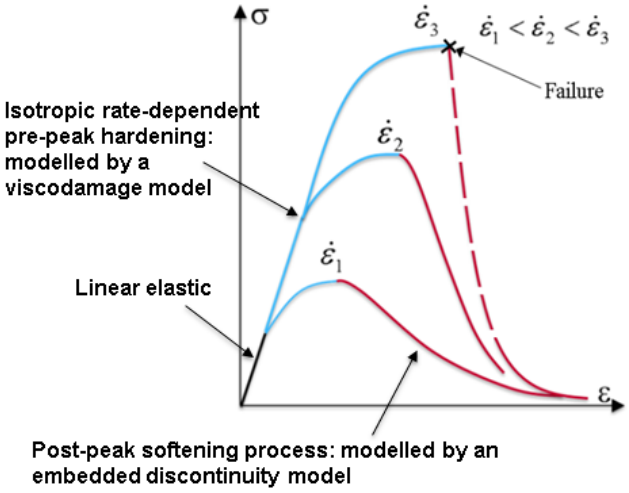

Figure 6. Schematic for the three-phase rock material model.

The behavior of rock materials under mechanical loading can be divided into three separate phases, as illustrated schematically in Figure 6. The first is the linear elastic phase followed, upon reaching the elastic limit, by a nonlinear pre-peak hardening involving micro-cracking. As the rate-dependent peak stress is reached, a macro-crack will develop triggering the third phase accompanied with non-linear softening. A distinctive feature of the present model is that the strain-rate dependency is included in the model component governing the pre-peak non-linear hardening part of the material response. By this choice, the post-peak softening process leading to the formation of a macrocrack is better captured. Physical justification for this approach is that the microcracking process takes a finite time to develop from micro-scale to macro-scale. Moreover, the classical viscoplasticity formulations with a single yield governing the whole material behavior with a single yield surface predict the final failure surface in a too blurred and messy manner, see [30].

An isotropic rate-dependent compliance damage model is chosen for the description of the nonlinear pre-peak hardening process (the first part is governed by linear elasticity). Here, the term "damage" is to be understood in the damage mechanics sense while in its other occurrences with a reference to the damage induced by the mechanical or thermal loading, it refers to the intuitive comprehension of the term, i.e. a material failure of any kind. For present purposes, such a model is characterised by

$$
\begin{aligned}
&\bar{\phi}(\boldsymbol{\sigma},\bar{\kappa},\dot{\bar{\kappa}}) = \| \boldsymbol{\sigma}_+ \|_{\mathbf{D}_\mathrm{e}} - \tfrac{1}{\sqrt{E}}(\sigma_\mathrm{t} + \bar{q}(\bar{\kappa},\dot{\bar{\kappa}})), \quad \| \boldsymbol{\sigma}_+ \|_{\mathbf{D}_\mathrm{e}} = \sqrt{\boldsymbol{\sigma}_+ : \mathbf{D}_\mathrm{e} : \boldsymbol{\sigma}_+}, \\
&\mathbf{D} = (1+\bar{\mu})\mathbf{D}_\mathrm{e}, \quad \dot{\bar{\mu}} = \frac{\dot{\bar{\lambda}}}{\| \boldsymbol{\sigma}_+ \|_{\mathbf{D}_\mathrm{e}}}, \\
&\dot{\bar{\kappa}} = -\dot{\bar{\lambda}} \frac{\partial \bar{\phi}}{\partial \bar{q}} = \dot{\bar{\lambda}} / \sqrt{E_0} \\
&\bar{q}(\bar{\kappa},\dot{\bar{\kappa}}) = \bar{h}\bar{\kappa} + \bar{s}\dot{\bar{\kappa}}, \quad \bar{h} = \bar{g}\sigma_\mathrm{t} \exp(-\bar{g}\bar{\kappa})
\end{aligned}
\tag{1}
$$

where $\bar{\phi}$ is the viscodamage loading function, $\boldsymbol{\sigma}_+ = \sum_{i=1}^{3} \max(0,\sigma_i)\mathbf{n}_i \otimes \mathbf{n}_i$ ($\otimes$ denotes the tensor or dyadic product) is the positive part of the stress tensor defined by the principal stresses σ_i, and directions $\mathbf{n}_i$, σ_t is the elastic limit stress, $\mathbf{D}$ is the compliance tensor being initially obtained from the initial compliance tensor $\mathbf{D}_\mathrm{e} = \mathbf{E}_0^{-1}$ ($\mathbf{E}_0$ being the undamaged stiffness tensor), while $\bar{\kappa}, \dot{\bar{\kappa}}$ are the internal variable and its rate, respectively, $\dot{\bar{\lambda}}$ is the viscodamage increment, and $\bar{q}$ is the hardening variable. Variable $\bar{\mu}$ ($\bar{\mu} \in [0,\infty]$) in (1) is related to the classical scalar damage variable as $\omega = \bar{\mu}/(1+\bar{\mu})$ which varies from 0 to 1. Moreover, $\bar{h}, \bar{s}$ are the hardening and viscosity moduli, respectively, and $\bar{g}$ is a parameter controlling the initial slope of the hardening curve. The inverse of the compliance tensor, $\mathbf{E}_d$, is the damaged stiffness modulus. Finally, operator: in (1) denotes the standard double contraction between tensors.

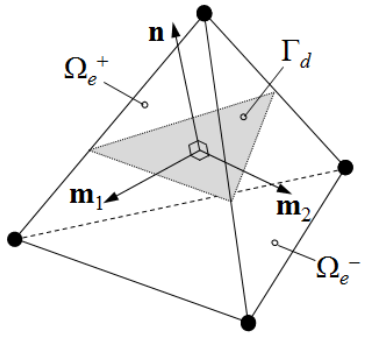

Figure 7. Four-node tetrahedral element with a discontinuity plane Γ_d.

The embedded discontinuity part of the model describes the post peak softening process leading to the final failure of the material. It is based on the decomposition of the displacement field into a regular part and the displacement jump due to a crack. When a body in $\mathbf{R}^3$ is discretized with 4-node tetrahedral elements (see Figure 7), the displacement and strain fields can be written as

$$\begin{aligned}\mathbf{u}(\mathbf{x}) &= N_i \mathbf{u}_i^e + (H_{\Gamma_d}(\mathbf{x}) - \varphi(\mathbf{x}))\,\boldsymbol{\alpha}_d \\ \boldsymbol{\varepsilon}(\mathbf{x}) &= (\nabla N_i \otimes \mathbf{u}_i^e)^{sym} - (\nabla \varphi(\mathbf{x}) \otimes \boldsymbol{\alpha}_d)^{sym} + \delta_{\Gamma_d}(\mathbf{n} \otimes \boldsymbol{\alpha}_d)^{sym}\end{aligned} \tag{2}$$

where the displacement jump is denoted by $\boldsymbol{\alpha}_d$, while N_i and $\mathbf{u}_i^e$ are the standard interpolation functions and nodal displacements (with summation on repeated indices), respectively. Moreover, H_Γ is the Heaviside function, and δ_Γ is the Dirac delta function. Function $\varphi(\mathbf{x})$ is defined for each element with an embedded discontinuity in order to obtain the nodal values in that finite element. The purpose of this function is to restrict the effect of the displacement jump within the corresponding finite element so that the essential boundary conditions remain unaffected. For more details of the finite element implementation of Eq. (2), see [29].

A bi-surface discontinuity model accounting for mode I and II fracture types developed in [28] reads:

$$\begin{aligned}&\phi_{\mathrm{t}}(\mathbf{t}_{\Gamma_d}, \kappa, \dot{\kappa}) = \mathbf{n} \cdot \mathbf{t}_{\Gamma_d} - (\sigma_{\mathrm{t}} + q(\kappa, \dot{\kappa})) \\ &\phi_{\mathrm{s}}(\mathbf{t}_{\Gamma_d}, \kappa, \dot{\kappa}) = \beta\left((\mathbf{m}_1 \cdot \mathbf{t}_{\Gamma_d})^2 + (\mathbf{m}_2 \cdot \mathbf{t}_{\Gamma_d})^2\right)^n - (\sigma_{\mathrm{s}} + \tfrac{\sigma_{\mathrm{s}}}{\sigma_{\mathrm{t}}} q(\kappa, \dot{\kappa})) \\ &\mathbf{t}_{\Gamma_d} = \mathbf{n} \cdot \mathbf{E}_d : \left(\nabla^s \mathbf{u} - (\nabla \varphi \otimes \boldsymbol{\alpha}_d)^{sym}\right) = \mathbf{n} \cdot \boldsymbol{\sigma} \\ &q = h\kappa + s\dot{\kappa}, \quad h = -g\sigma_{\mathrm{t}} \exp(-g\kappa) \\ &\dot{\boldsymbol{\alpha}}_d = \dot{\boldsymbol{\alpha}}_{\mathrm{I}} + \dot{\boldsymbol{\alpha}}_{\mathrm{II}} = \dot{\lambda}_{\mathrm{t}} \frac{\partial \phi_{\mathrm{t}}}{\partial \mathbf{t}_{\Gamma_d}} + \dot{\lambda}_{\mathrm{s}} \frac{\partial \phi_{\mathrm{s}}}{\partial \mathbf{t}_{\Gamma_d}} \\ &\dot{\kappa} = -\dot{\lambda}\left({}_{\mathrm{t}} \frac{\partial \phi_{\mathrm{t}}}{\partial q} + \dot{\lambda}_{\mathrm{s}} \frac{\partial \phi_{\mathrm{s}}}{\partial q} \right)\end{aligned} \tag{3}$$

where $\mathbf{n}$ and $\mathbf{m}_1, \mathbf{m}_2$ are the unit normal and two tangent vectors for the crack plane (see Figure 7), $\boldsymbol{\sigma}$ is the bulk stress, and σ_{t} and σ_{s} are the elastic limits in tension and shear, respectively. Furthermore, $\kappa, \dot{\kappa}$ are the internal variable and its rate related to the softening law for discontinuity. The softening slope parameter g is defined with the mode I fracture energy G_{Ic} as $g = \sigma_{\mathrm{t}} / G_{\mathrm{Ic}}$, and constant viscosity modulus s is assumed here. The third Equation in (3) shows equivalent expressions for the traction $\mathbf{t}_{\Gamma_d}$ in terms of the bulk stress or the discontinuity jump and the damaged stiffness $\mathbf{E}_d = \mathbf{D}^{-1}$. Finally, n and β are parameters that control the shape of the combined mode II and mode III (shear) surface.

A fixed crack concept is adopted here, i.e., $\mathbf{n}$ remains the same after introducing a discontinuity in an element. A crack is embedded perpendicular to the first principal direction into an element, when criterion $\varepsilon_{\mathrm{deqv}} \geq \varepsilon_{\mathrm{dlim}}$ is met. Here, equivalent damage strain $\varepsilon_{\mathrm{deqv}} = \sqrt{\boldsymbol{\varepsilon}_{\mathrm{d}}^{+} : \boldsymbol{\varepsilon}_{\mathrm{d}}^{+}}$ is defined with $\boldsymbol{\varepsilon}_{\mathrm{d}} = (\mathbf{D} - \mathbf{D}_{\mathrm{e}}) : \boldsymbol{\sigma}$ (damage strain), while $\boldsymbol{\varepsilon}_{\mathrm{d}}^{+}$ is the positive part of it (defined analogously as the positive part of the stress above), and $\varepsilon_{\mathrm{dlim}}$ is the limit damage strain.

In order to have a continuous response upon transition from the continuum model to the discontinuity model, the hardening variable q and the parameter controlling the post peak slope, g above, are set as $q(\kappa, \dot{\kappa}) = \bar{q}(\bar{\kappa}, \dot{\bar{\kappa}})$, $g = \sigma_{\mathrm{tdyn}} / G_{\mathrm{Icdyn}}$ where $\sigma_{\mathrm{tdyn}} = \sigma_{\mathrm{t}} + \bar{q}(\bar{\kappa}, \dot{\bar{\kappa}})$ is the dynamic tensile strength, and

G_{Icdyn} is the dynamic mode I fracture energy. This energy is needed to account for the correct dissipation of energy under high strain rates since.

The final component of the model is an isotropic damage model. It is introduced in order to alleviate the crack spreading and locking problems related to the embedded discontinuity kinematics implemented with the low order finite elements. In the present formulation, it is introduced into the post-peak softening process when almost all, say 80-90 %, of the load bearing ability of the element with a crack is used. Thereby, the final expression for the stress of an element with a crack reads

$$\boldsymbol{\sigma} = (1-\omega)\mathbf{E}_d : (\boldsymbol{\varepsilon}_{\text{tot}} - (\nabla\varphi \otimes \boldsymbol{\alpha}_d)^{sym}) \tag{4}$$

where ω is the isotropic damage parameter. For more details on this part of the model, see [28]. It should be emphasized that this component of the model is included only in order to deal with the poor performance of the low order finite element. As it becomes active at the very late stage of the post-peak softening process, it does not affect the overall material behavior description of the model.

In this model, embedded discontinuities (cracks) with any desired orientation **n** can be introduced into the elements of the mesh before the analysis. The pre-existing crack distributions can thus be easily modeled. However, it should be kept in mind that the model accounts only for failure types that meet the damage strain criterion presented above. Therefore, the model does not account for the failure in purely compressive stress states.

Split Hopkinson pressure bar simulation model

The SHPB test setup with the BD sample of rock is modeled as follows. The incident and transmitted bars are modeled with standard 2-node bar elements. The incident pulse is modeled as an external stress pulse, $\sigma_i(t)$, applied to the end of the incident bar. The contacts between the BD sample and the incident and transmitter bars are modeled in a standard manner by imposing contact constraints between the bar end nodes and the edge nodes of the discretized BD sample. The contact constraints are imposed with the forward increment Lagrange multiplier method, and the explicit modified Euler time integrator is employed in solving the response of the system in time [27]. The local element level solution, i.e., integration of Equations (1) and (3), is presented in [28].

Numerical simulations

The model described above is applied here in the simulation of the dynamic BD test on plasma shocked Balmoral red granite. The plasma shock itself and its effect on the rock microstructure are not modeled in this study. Instead, the plasma shock induced damage is accounted for by two different methods. In the first method this damage is assumed to be representable by the pre-embedded discontinuities with zero strength, and in the second method the damage is modeled as reduced and Weibull distributed mechanical properties. The material properties and model parameters used in the simulations here are given in Table 3.

The material property values for E, ν, ρ and GIc in Table 3 are valid for granite in general. Unfortunately, direct tensile test data on Balmoral red granite was not available for the authors. Therefore, the other model parameters, such as εdlim, $\overline{g}$, and σt, were calibrated by trial and error via single element model simulations to match the response of Balmoral granite under static and dynamic direct tension tests. The quasi-static indirect (i.e. measured in the Brazilian disc test) tensile strength of Balmoral granite is ≈ 8.2 MPa, which is matched with the values given in Table 3. As to the other parameter values in Table 3, they were chosen as follows. Continuum viscosity $\overline{s}$, dynamic fracture energy GIcdyn , and shear surface parameter β were calibrated by trial and error simulations so that the correct dynamic tensile strength, 29 ± 3 MPa, and the post-peak behavior of an intact BD sample made of Balmoral red granite in SHPB experiment was predicted. Viscosity for discontinuity

was chosen so that its value does not affect the post peak response significantly but still secures a stable and robust stress integration, for details see [28] and [29]. Elastic shear limit, σ_s, was simply set as two times the elastic tensile limit. Finally, shear surface parameter n value ½ provides the correct unit (MPa) for shear stress (with unitless β).

Table 3. Material properties and model parameter values for material point level simulations.

Quantity	Symbol	Value	Unit
Young's modulus	E	60	GPa
Elastic limit stress in tension	σ_t	5.5	MPa
Elastic limit stress in shear	σ_s	11	MPa
Poisson's ratio	ν	0.2	
Material density	ρ	2600	kg/m^3
Mode I fracture energy	G_{Ic}	100	N/m
Viscosity for continuum	$\bar{s}$	0.009	MPa·s/m
Viscosity for discontinuity	S	0.002	MPa·s/m
Limit damage strain	ε_{dlim}	5.5E-5	
Hardening slope parameter	$\bar{g}$	55	1/m
Shear surface parameter	n	1/2	
Shear surface parameter	β	10	
Strength ratio	q_{tr}/q_0	0.2	

The four-node tetrahedral mesh and an example of the crack normal distributions used in the simulations are shown in Figures 8a and c. The initial crack population was generated as follows: First, a zone where the plasma gun induced cracks are located was defined with a width of 15 mm. This area was divided into nine layers, as shown in Figure 8b. Then, the elements in these layers were searched. The number of cracks in each layer is dictated by two crack density percentages p_1 and p_2. In the first layer, which is the layer directly affected by the plasma gun, the number of elements having an initial crack is $N_{cr1} = p_1 N_{e1}$ (N_{e1} is the number (amount) of the elements in this layer). The number of cracks in the next layers up to layer 9 is simply $N_{crN} = p_2 N_{cr(N-1)}$ ($2 \le N \le 9$). The elements in each layer having a crack are randomly chosen in order to obtain a spatially random distribution of cracks. Finally, oriented embedded discontinuity was assigned for each element (in the mesh) designated as containing a crack. Figure 8c shows an example of the crack population with $p_1 = 0.8$ and $p_2 = 0.75$, resulting in 2471 cracks in total with layer 1 having 703 cracks and layer 9 only 72 cracks. The strength of a discontinuity representing an initial crack is set close to zero.

The orientation of the pre-embedded cracks is biased so that only the directions in the first quadrant are allowed. Namely, the crack normal vector for each pre-embedded discontinuity is generated by $\mathbf{n}_d = [r_1, r_2, r_3]^T$, where the components r_i are random numbers from a uniform distribution between 0 and 1. This orientation may not be the case in reality but serves for these preliminary modeling purposes. It is noted that an unbiased crack orientation scheme was also tested, but it did not provide the desired weakening effect within the present modeling approach that accounts presently only for tensile type of fracture.

The first set of simulations was carried out by varying the percentage p_1 while keeping p_2 fixed to 0.9. The results with $G_{Icdyn} = 5G_{Ic}$ for the final failure modes and tensile stresses (as a function of time) are shown in Figure 9. To facilitate the comparison, the tensile stress vs. time curves are calculated similarly as in the experimental procedure (i.e. by $\sigma_x(t) = P(t) / (\pi RH)$ where R and H are

the radius and thickness of the disc, and $P = (P_1 + P_2)/2$ is the average of the contact forces between the incident and transmitted bars and the disc).

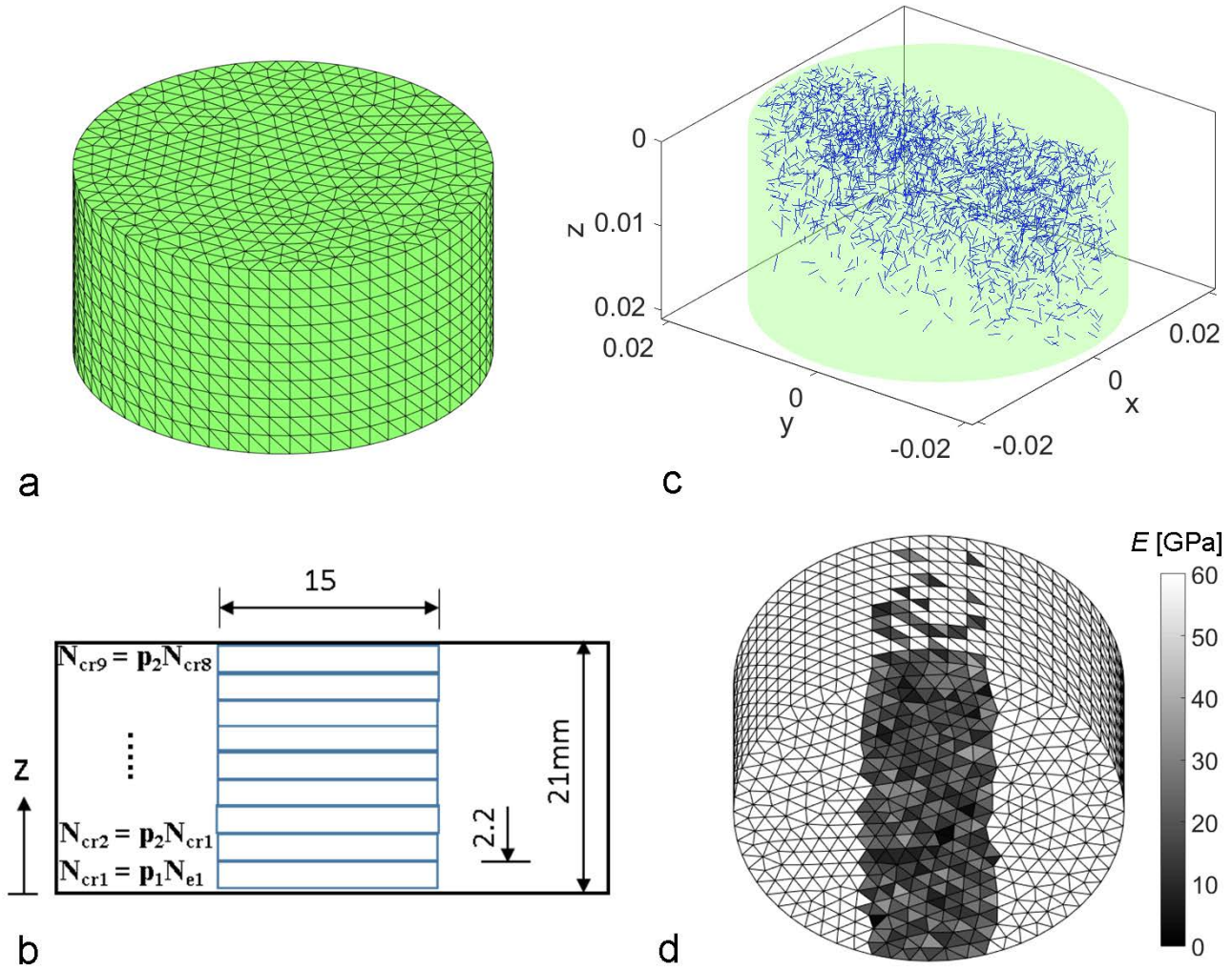

Figure 8. Finite element mesh with 22929 tetrahedrons a), initial crack/damage distribution scheme b), initial crack population (normals plotted) with 2471 cracks in the numerical BD (p_1 = 0.8, p_2 = 0.75), and Young's modulus distribution used in the simulations (p_1 = 1, p_2 = 0.75) d).

According to the results shown in Figure 9, all the failure modes display the major axial splitting crack but the details differ. The most notable difference is that the secondary radial cracks are less pronounced as the number of cracks increases. As for the tensile stresses shown in Figure 9f, a clear tendency of decreasing tensile strength can be observed upon increasing the crack number. With parameters p_1 = 0.8 and p_2 = 0.9, the tensile strength is 23 MPa, while without cracks it is 31.5 MPa. In this respect, the present approach seems to be able to capture the rock weakening effect of the microcrack populations. However, more experimental research is needed in order to decide whether this modeling approach correspond to the plasma shock induced damage and cracks.

One more simulation was carried out with crack density percentages p_1 = 0.8 and p_2 = 0.75. This scheme results in 2463 cracks in total with layer 1 having 703 cracks and layer 9 only 72 cracks. Thereby, this scheme presumably represents more realistically the plasma shock induced crack systems when only one side of the sample is treated with the plasma gun. The results with these parameter values are shown in Figure 10b.

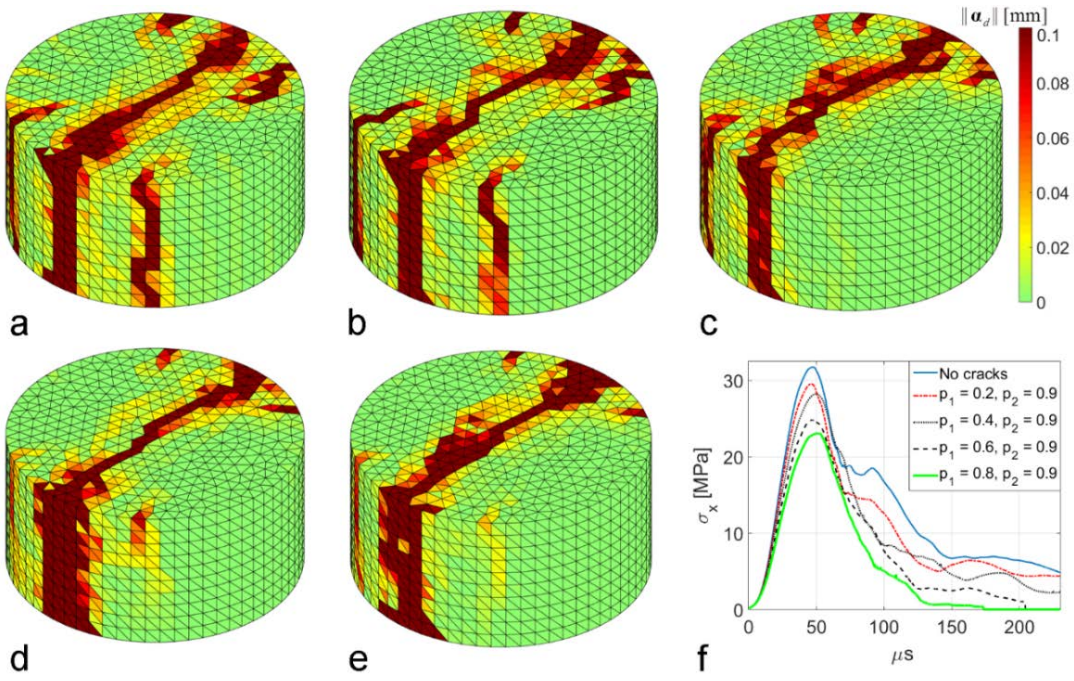

Figure 9. Simulation results showing the final failure mode in terms of the magnitude (norm) displacement jump with no cracks a), when $p_1 = 0.2$, $p_2 = 0.9$ (1054 cracks) b), $p_1 = 0.4$, $p_2 = 0.9$ (2057 cracks) c), $p_1 = 0.6$, $p_2 = 0.9$ (3020 cracks) d), $p_1 = 0.8$, $p_2 = 0.9$ (3856 cracks) e), and corresponding tensile stress vs time curves f).

Another simple approach to account for the plasma shock induced damage is to assume that the mechanical properties are deteriorated randomly. Here this approach is tested with the assumption that the tensile elastic limit and the Young's modulus conform to the Weibull distribution. The 3-parameter cumulative Weibull probability distribution function reads

$$\Pr(x) = 1 - \exp\left(-\left((x - x_u)/x_0\right)^{m_w}\right) \tag{5}$$

where m_w is the shape parameter, x_0 is the scale parameter corresponding to the mean value of x, and x_u is the location parameter. The parameter values used in this paper are $m_w = 3$, $x_u = 0$, for both σ_t and E and $x_0 = 0.37E_0$ for E and $x_0 = 0.2\sigma_{t0}$ for σ_t (where E_0 and σ_{t0} are values given in Table 3). These values for the mean value parameter x_0 are taken from Ref. [42]. Therein, experimental results for the mechanical properties of granite are reported after thermal treatment up to 600 °C. At his temperature, the Young's modulus and the tensile strength were reduced to 37 % and 20 %, respectively, from the values at room temperature. As for the elastic limit in shear, it is simply taken as two times the elastic limit in tension.

This distribution is used as follows. After generating a uniformly distributed random data between 0 and 1 ($Pr(x)$ in (5)), corresponding to the number of elements in the plasma shock affected zone of the mesh, and solving for x in (5) for each element, a spatially statistical distribution of a material property is obtained in the damaged zone. The zone of the plasma shock affected elements with this method is the same as with the pre-embedded discontinuities approach. Figure 8d shows the case for the Young's modulus with $p_1 = 1$, $p_2 = 0.75$. Moreover, the limit of the damage strain, ε_{dlim}, is also lowered to 20 % of the value given in Table 3. The simulation results with the Weibull approach are shown in Figure 10c-e for three different numerical specimens.

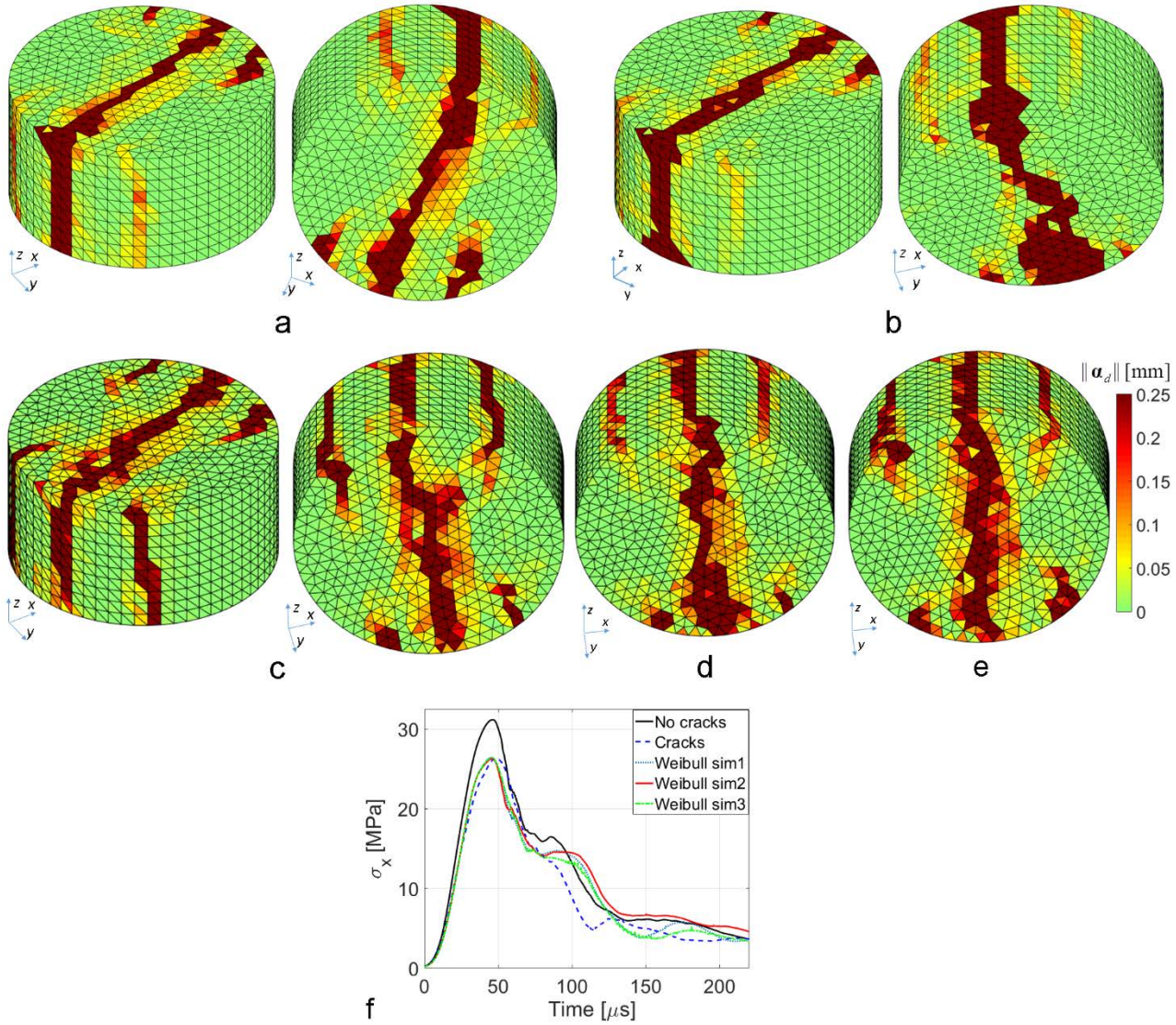

Figure 10. Simulation results showing the final failure mode in terms of the norm displacement jump with no cracks a), with initial cracks (p_1 = 0.8, p_2 = 0.75) b), with Weibull distribution approach for numerical specimen 1 c) (from different views), numerical specimen 2 d) (view from the treated side), numerical specimen 3 e) (view from the treated side), and corresponding tensile stress vs time curves f).

According to the results shown in Figure 10, the failure modes display similar overall features with deviations only in details. Most notably, the amount of damage with the initial crack population and Weibull approaches is larger at the bottom (z = 0) surface of the disc. Moreover, the deviations between the results for the different numerical specimen predicted with the Weibull method are negligible. This finding, which means that the brittle materials become more and more deterministic under increasing loading rate, is in line with the theoretical considerations and Monte Carlo simulations carried out with a probabilistic damage model based on Weibull distribution.

As for the tensile stresses shown in Figure 10f, the peak stress of the intact rock is 31.2 MPa, while the maximum stress with the initial crack and Weibull approaches are 26.3 MPa and 26.4 MPa, respectively. This means that the 15.7 % (initial cracks) and 15.4 % (Weibull distribution) weakening in the tensile strength with these methods are very close to the experimental value (14 %) with the longest tested exposure time. In this respect, both of the tested approaches are capable of capturing the rock weakening effect of plasma shock induced damage.

In passing, it is noted that mesh sensitivity study is not included here since it is already done with respect to the present application (albeit without the pre-embedded cracks or the weakened strengths) in [29] for 2D and [28] for 3D case. Therein, the present numerical is approach is shown to predict mesh objective results in uniaxial tension test as well as Brazilian disc test both in 2D and in 3D cases.

Discussion

The results obtained from the SHPB tests show a maximum tensile strength of 29 ± 3 MPa, which matches considerably well with the results of the first approach in the numerical simulation (31.75 MPa). After a 0.40 second heat shock, as mentioned before, the tensile strength does not essentially change and correlates to the situation in the simulation where p_1 = 0.2 and p_2 = 0.9. A 0.55 second heat shock decreases the strength of the rock to 25 ± 4 MPa. This value is a good match with the simulation condition where p_1 = 0.6 and p_2 = 0.9. When p_1 = 0.8 and p_2 = 0.9, the maximum tensile strength obtained from the numerical simulations (23 MPa) matches well with the SHPB result when the rock samples were heat shocked for 0.80 seconds. Comparison of the results of the SHPB tests with the second approach with an assumption that the mechanical properties are deteriorated leads to a different situation. The peak stress of the intact rock in the simulations is 31.2 MPa, while the maximum stress with the initial crack and Weibull approaches are 26.3 MPa and 26.4 MPa, respectively. This means that 15.7 % (initial cracks) and 15.4 % (Weibull distribution) weakening in the tensile strength with these methods are very close to the experimental value (14 %) with the longest used exposure time.

Even though the quantitative analysis provides an easier comparison to understand the behavior of the rock in different testing conditions, it does not provide a full description of the mechanical behavior. For this, one has to pay attention to many details such as the strain distribution during the loading, fragmentation, etc. DIC has proven to be a useful tool for the comparison of the simulation and experimental results. Figure 10 shows the high speed images of a sample during dynamic loading. The displacement in the direction perpendicular to the loading (Y-direction) between adjacent subsets, or $\Delta l = \varepsilon l_0$, are also shown in the original images. Figure 10a shows the displacement over the surface of the sample before the test starts. No displacement can be observed before the image of Figure 10c with the time stamp of 40 µs. This observation indicates that the fracture initiates inside the samples and then propagates to the surface only after the sample has already reached its maximum stress. After this point, the crack propagates with high speed, followed by crushing of the sample at contact points with the loading bars. Unfortunately, the speckle pattern applied on the surface of the samples for the DIC analysis prevents us from analyzing characterizing the actual initiation and propagation (intergranular or transgranular) of the cracks.

Finally, it is instructive to compare the numerically predicted failure mode development to the experimental one shown in Figure 11. Figure 12 shows the simulated development of the norm of displacement jump at different times in the case of the initial crack method.

When comparing the simulated results in Figure 12 to the experimental ones in Figure 11, it can be observed that there is a satisfactory agreement. Even though both sets of results are quantitative, the comparison is not trivial since the DIC images display displacements on the surface of the sample, while the simulation results are presented in terms of the displacement jump norm over the whole volume of the sample. However, qualitatively the experimental results in Figures 11 d and e seem to agree with the simulated ones presented in Figures 12 d and f.

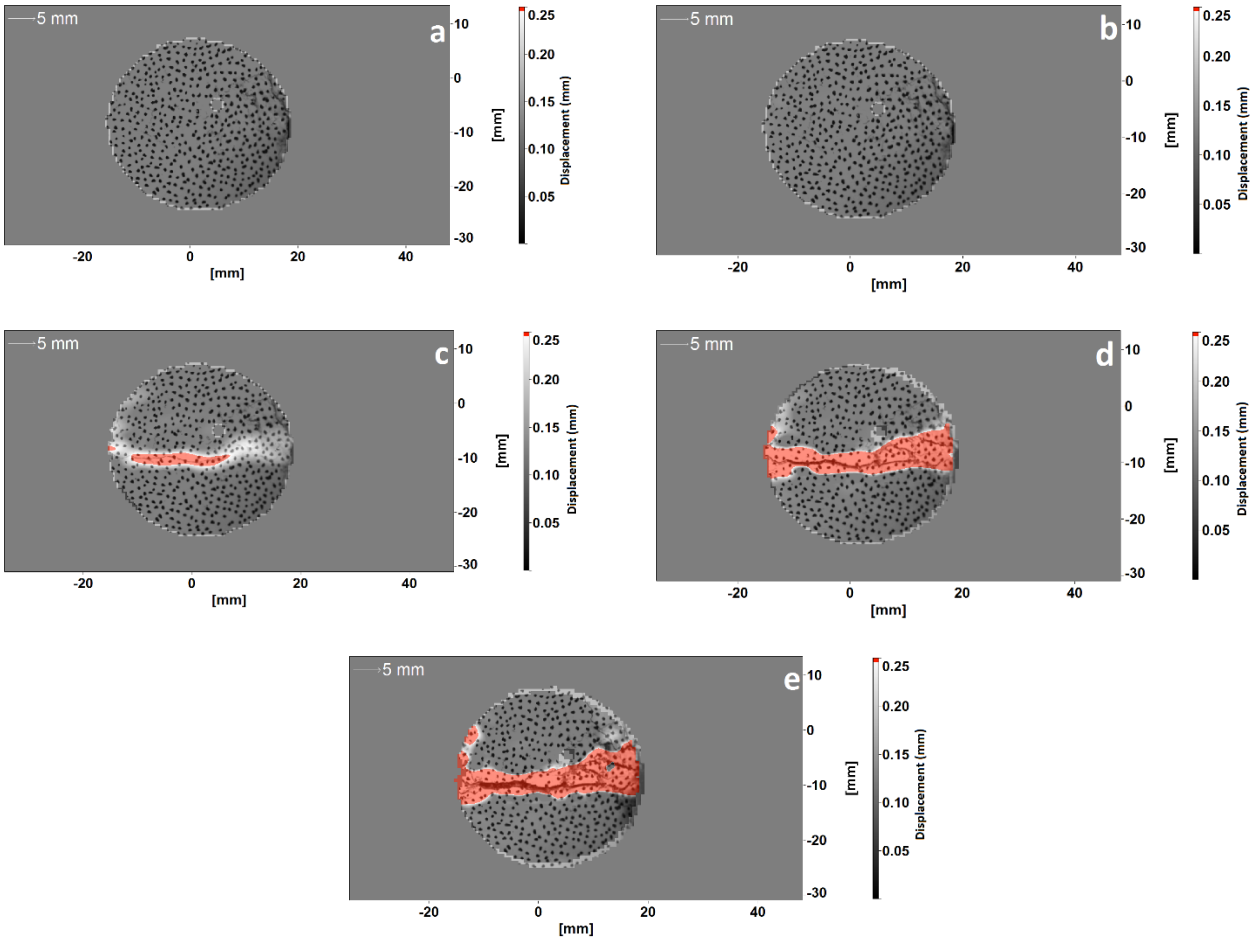

Figure 11. DIC images obtained during dynamic compression of a sample after 0.80 seconds heat shock for. a) t =-40 µs, b) t =0 µs, c) t = 40 µs, d) t = 80 µs, e) t = 120 µs.

Concluding Remarks

The surface of the rock material was modified by applying heat shocks on the surface of Brazilian disc samples using a plasma gun. Later on, Surface damage caused by the heat shocks was quantified using optical images to obtain the fractal dimension of the surface crack patterns. The fractal dimension results show the increase in the amount of surface damage as well as the increase in the complexity of the crack network. It is clear that the heat shock affects a larger volume than just the surface and that there are cracks also under the surface, which are not visible with visible or ultraviolet light. However, this method can provide reasonable estimates for the effects of the heat shock on the tensile strength of the studied rocks.

Afterwards, the samples were tested using the Split Hopkinson Pressure Bar device. The tensile strength of the tested material does not show any change for the 0.40 second heat shock, even though the fractal dimension results indicate surface damage also for this heat shock duration. This means that the affected volume was very small and the duration of heat shock was not long enough to transfer the energy deeper into the sample. However, when the duration of the heat shock increases to 0.5 seconds, the tensile strength of the material drops by 14% from its original value. Increasing the duration of the heat shock up to 0.80 second leads to a 20% decrease in the tensile strength of Balmoral Red.

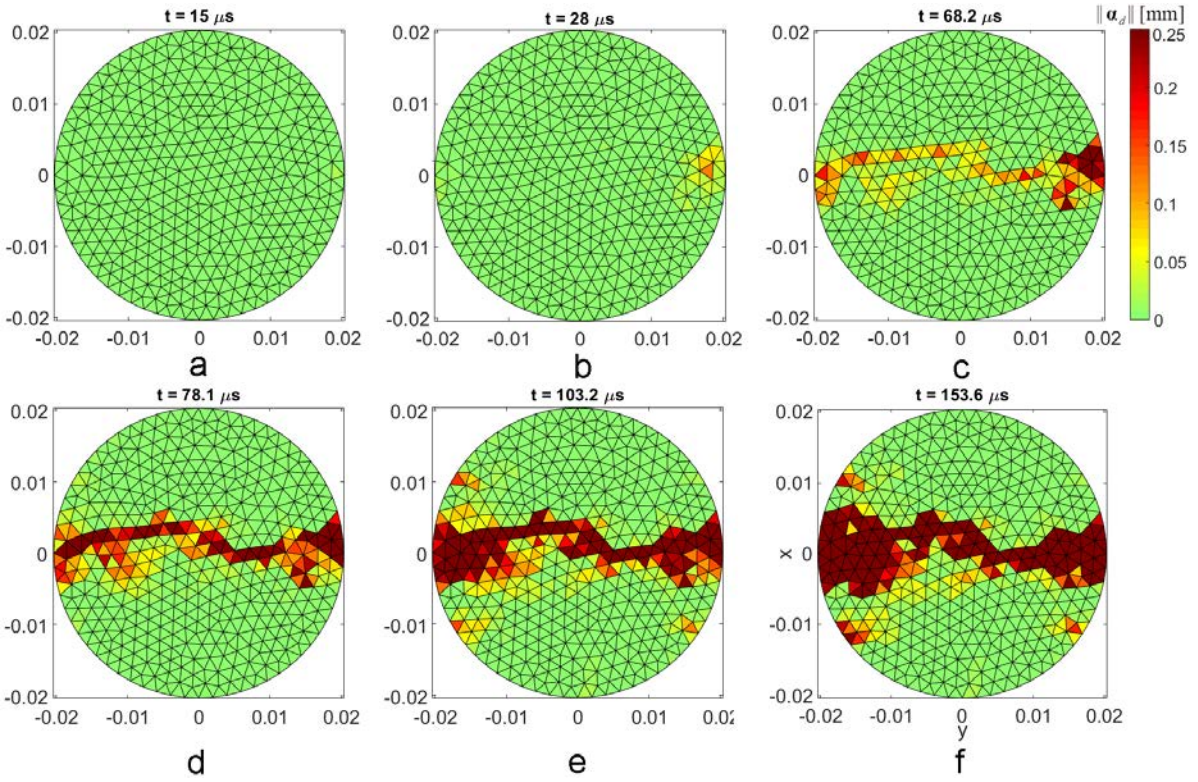

Figure 12. Example of the simulation results with the initial cracks method showing the development of the failure mode in terms of the displacement jump norm over time for the case $p_1 = 0.8$, $p_2 = 0.75$ at t = 15 μs a), t = 28 μs b), t = 68.2 μs c), t = 78.1 μs d), t = 103.2 μs e), and t = 153.6 μs f) .

Two different approaches were made to numerically simulate the dynamic behavior of the rock material. The first approach is based on the number of initial cracks. The results of the simulations based on this approach match with results obtained from the SHPB tests. The second approach is based on the assumption that the mechanical properties of the rock are degraded and conform to the Weibull distribution. The Weibull parameters can be adjusted with the data on thermally affected rock material properties. As for the tensile stresses, the peak stress of the intact rock is 31.2 MPa, while the maximum stress with the initial crack and Weibull approaches are 26.3 MPa and 26.8 MPa, respectively. This means a 15.7 % (initial cracks) and 14.1 % (Weibull distribution) weakening in the tensile strength, which are very close to the experimental value (14 %) with the longest tested exposure time. In this respect, both of the tested approaches are capable of reproducing the experimental weakening effect of the plasma shock induced damage.

Finally, digital image correlation was used to observe the crack initiation and propagation on the surface of the samples during the high rate tests. Time stamps from the tests were recorded on the images, and the data from the SHPB tests was synchronized with the obtained images. The obtained results from DIC correlate well with the numerical simulations showing the displacement values. However, it should be noted that the DIC results show the displacement on the surface of the samples, while the simulation results include the whole specimen volume.

Acknowledgment

The experimental part of this work was supported by Suomen Luonnonvarain Tutkimussäätiö – Foundation under grant numbers 1768/14, 1779/15 and 1789/16 and Finnish Cultural Foundation. The research related to simulations part was funded by Academy of Finland under grant number 298345.

References

[1] Apostol, M., 2007. *Strain Rate Dependence of the Compression Behavior of FCC and BCC Metals.* Tampere: Tampere University of Technology.

[2] Bauer, S. & Johnson, B., 1979. *Effects Of Slow Uniform Heating On The Physical Properties Of The Westerly And Charcoal Granites.* Austin, American Rock Mechanics Association.

[3] Berenbaum, R. & Brodie, I., 1959. Measurement of the tensile strength of brittle materials. *Brit. J. Appli. Phys.*, 10(6), pp. 281-287.

[4] Bieniawski, Z. & Bernede, M., 1979. Suggested methods for determining the uniaxial compressive strength and deformability of rock materials: Part 1. Suggested method for determining deformability of rock materials in uniaxial compression. *Int. J. Rock Mech. Min. Sci.*, 16(2), pp. 138-140. https://doi.org/10.1016/0148-9062(79)91451-7

[5] Cai, M. & Kaiser, P., 2004. Numerical simulation of the Brazilian test and the tensile strength of anisotropic rock and rock with pre-existing cracks. *Int. J. Rock Mech. Min. Sci.*, 41(0), pp. 478-483. https://doi.org/10.1016/j.ijrmms.2004.03.086

[6] Chau, K. & Wang, P., 1996. Microcracking and Grain Size Effect in Yuen Long Marbles. *Int. J. Rock Mech. Min. Sci.*, 33(5), pp. 479-485. https://doi.org/10.1016/0148-9062(96)00007-1

[7] Chen, Y., Ni, J., Shao, W. & Azzam, R., 2012. Experimental study on the influence of temperature on the mechanical properties of granite under uni-axial compression and fatigue loading. *Int. J. Rock Mech. Min. Sci.*, Volume 52, pp. 62-66. https://doi.org/10.1016/j.ijrmms.2012.07.026

[8] Dai, F., Huang, S., Xia, K. & Tan, Z., 2010. Some Fundamental Issues in Dynamic Compression and Tension Tests of Rocks Using Split Hopkinson Pressure Bar. *Rock. Mech. Rock. Eng.*, 43(6), pp. 657-666. https://doi.org/10.1007/s00603-010-0091-8

[9] Dunn, D., LaFountain, L. & jackson, R., 1973. Porosity Dependence and Mechanism of Brittle Fracture in Sandstones. *J. Geophys. Res.*, 78(14), pp. 2403-2417. https://doi.org/10.1007/s00603-010-0091-8

[10] Feder, J., 1988. *Fractals (Physics of Solids and Liquids).* new York: Plenum Press.

[11] Gautam, P. K., Verma, A. K., Maheshwar, S. & Singh, T. N., 2016. Thermomechanical Analysis of Different Types of Sandstone at Elevated Temperature. *Rock. Mech. Rock. Eng.*, 49(5), pp. 1985-1993. https://doi.org/ 10.1007/s00603-015-0797-8

[12] Gorham, D. & Wu, X., 1997. An Empirical Method of Dispersion Correction in the Compressive Hopkinson Bar Test. *J. Phys. IV*, 07(C3), pp. 223-228. https://doi.org/10.1051/jp4:1997340

[13] Gorsevski, P., Onasch, C., Farver, J. & Ye, X., 2012. Detecting grain boundaries in deformed rocks using a cellular automata approach. *Comput. Geosci.* , Volume 42, pp. 136-142. https://doi.org/10.1016/j.cageo.2011.09.008

[14] Hokka, M. et al., 2016. Effects of strain rate and confining pressure on the compressive behavior of Kuru granite. *Int. J. Impact. Eng.*, Volume 91, pp. 183-193. https://doi.org/10.1016/j.ijimpeng.2016.01.010

[15] Hudson, J., Brown, E. & Rummel, F., 1972. The controlled failure of rock discs and rings loaded in diametral compression. *Int. J. Rock Mech. Min. Sci.*, 9(2), pp. 241-248. https://doi.org/10.1016/0148-9062(72)90025-3

[16] Kazerani, T. & Zhao, J., 2011. Discontinuum-based numerical modeling of rock dynamic fracturing and failure. In: *Advances in rock dynamics and applications.* Boca Raton: CRC Press, pp. 291-320.

[17] Khair, A. & Achanti, A., 1996. *Effect of specimen size on compressive strength of coal.* Golden, Colorado School of Mines.

[18] Kranz, R., 1983. Microcracks in rocks: A review. *Tectonophysics,* 100(1-3), pp. 449-480. https://doi.org/10.1016/0040-1951(83)90198-1

[19] Lisjak, A. & Grasselli, G., 2014. A review of discrete modeling techniques for fracturing processes in discontinuous rock masses. *J. Rock. Mech. Geo. Eng.*, 6(4), pp. 301-314. https://doi.org/10.1016/j.jrmge.2013.12.007

[20] Luodes, H. & Luodes, N., 2007. *Suomen Kiviteollisuus Oy.* [Online] Available at: http://www.finskastone.fi/images/docs/Finska_Balmoral_Red_fine_grained_2007.pdf [Accessed 02 03 2016].

[21] Mahabadi, O., 2012. *Investigating the Influence of Micro-scale Heterogeneity and Microstructure on the Failure and Mechanical Behaviour of Geomaterials.* Toronto: University of Toronto. http://hdl.handle.net/1807/32789

[22] Mahabadi, O., Cottrell, B. & grasselli, G., 2010. An Example of Realistic Modelling of Rock Dynamics Problems: FEM/DEM Simulation of Dynamic Brazilian Test on Barre Granite. *Rock. Mech. Rock Eng.*, 43(6), pp. 707-716. https://doi.org/10.1007/s00603-010-0092-7

[23] Mardoukhi, A., Mardoukhi, Y., Hokka, M. & Kuokkala, V., 2016. Effects of strain rate and surface cracks on the mechnical behavior of Balmoral red granite. *Phil. Trans. R. Soc. A.*, 375(2085), p. 20160179. https://doi.org/10.1098/rsta.2016.0179

[24] Mardoukhi, A., Mardoukhi, Y., Hokka, M. & Kuokkala, V., 2017. Effects of heat shock on the dynamic tenisle behavior of granitic rocks. *Rock. Mech. Rock. Eng.*,50(5), pp. 1171-1182. https://doi.org/10.1007/s00603-017-1168-4

[25] Price, N., 1996. *Fault and Joint Development in Brittle and Semi-Brittle Rocks.* Oxford: Pergamon Press.

[26] Rippa, F. & Vinale, F., 1983. *Structure and mechanical behavior of a volcanic tuff.* Melbourne, International Society for Rock Mechanics.

[27] Saksala, T., 2009. Damage–viscoplastic consistency model with a parabolic cap for rocks with brittle and ductile behavior under low-velocity impact loading. *Int. J. Numer. Anal. Met.*, 34(13), pp. 1362-1386. https://doi.org/10.1002/nag.868

[28] Saksala, T., 2016. Modelling of Dynamic Rock Fracture Process with a Rate-Dependent Combined Continuum Damage-Embedded Discontinuity Model Incorporating Microstructure.

Rock mechanics and rock engineering, 49(10), pp. 3947-3962. https://doi.org/10.1007/s00603-016-0994-0

[29] Saksala, T., brancherie, D., Harari, I. & Ibrahimbegovic, A., 2014. Combined continuum damage-embedded discontinuity model for explicit dynamic fracture analyses of quasi-brittle materials. *Int. J. Numer. Meth. Eng.*, 101(3), pp. 230-250. https://doi.org/10.1002/nme.4814

[30] Saksala, T., Hokka, M., Kuokkala, V. & Makinen, J., 2013. Numerical modeling and experimentation of dynamic Brazilian disc test on Kuru granite. *International Journal of Rock Mechanics and Mining Sciences*, Volume 59, pp. 128-138. https://doi.org/10.1016/j.ijrmms.2012.12.018

[31] Shewmon, P. & Zackay, V., 1961. *Response of Metals to High Velocity Deformation.* New York: Interscience Publishers Inc..

[32] Smorodinov, M., Motovilov, E. & Volkov, V., 1970. *Determinations of Correlation Relationships Between Strength and Some Physical Characteristics of Rocks.* Belgrade, International Society of Rock Mechanics.

[33] Tang, C., 1997. Numerical simulation of progressive rock failure and associated seismicity. *Int. J. Rock Mech. Min. Sci.*, 34(2), pp. 249-261. https://doi.org/10.1016/S0148-9062(96)00039-3

[34] Tugrul, A. & Zarif, I., 1999. Correlation of mineralogical and textural characteristics with engineering properties of selected granitic rocks from Turkey. *Eng. Geol.*, 51(4), pp. 303-317. https://doi.org/10.1016/S0013-7952(98)00071-4

[35] Vishal, V. & S. P. Pradhan, Singh, T. N., 2011. Tensile Strength of Rock Under Elevated Temperatures. *Geotech. Geol.Eng.*, 29(6), pp. 1127-1133. https://doi.org/ 10.1007/s10706-011-9440-y

[36] Wang, W., 1997. Stationary and propagative instabilities in metals – a computational point of view. Delft: TU Delft.

[37] Wenk, H. & Christie, J., 1991. Comments on the interpretation of deformation textures in rocks. *J. Struct. Geol.*, 13(10), pp. 1091-1110. https://doi.org/10.1016/0191-8141(91)90071-P

[38] Winnicki, A., pearce, C. & Bicanic, N., 2011. Viscoplastic Hoffman consistency model for concrete. *Comput. Struct.*, 79(1), pp. 7-19. https://doi.org/10.1016/S0045-7949(00)00110-3

[39] Wisetsaen, S., Walsri, C. & Fuenkajorn, K., 2015. Effects of loading rate and temperature on tensile strength and deformation of rock salt. *Int. J. Rock Mech. Min. Sci.*, Volume 73, pp. 10-14. https://doi.org/10.1016/j.ijrmms.2014.10.005

[40] Xia, K. & Yao, W., 2015. Dynamic rock tests using split Hopkinson (Kolsky) bar system – A review. *J. Rock. Mech. Geo. Eng.*, 7(1), pp. 27-59. https://doi.org/10.1016/j.jrmge.2014.07.008

[41] Xu, X., F.Gao, Shen, X. & Xie, H., 2008. Mechanical characteristics and microcosmic mechanisms of granite under temperature loads. *J. Chi. Uni. Min.Tech.*, 18(3), pp. 413-417. https://doi.org/10.1016/S1006-1266(08)60086-3

[42] Yaseen, M., 2014. *Use of thermal heating/cooling process for rock fracturing: Numerical and experimental analysis.* Lille: Universite de Lille.

[43] Zhang, Q. & Zhao, J., 2014. A Review of Dynamic Experimental Techniques and Mechanical Behaviour of Rock Materials. *Rock Mechanics and Rock Engineering*, 47(4), pp. 1411-1478. https://doi.org/ 10.1007/s00603-013-0463-y

[44] Zhao, G. et al., 2015. Numerical study of the semi-circular bend dynamic fracture toughness test using discrete element models. *Sci. Chi. Tech. Sci.*, 58(9), pp. 1587-1595. https://doi.org/10.1007/s11431-015-5887-z

[45] Zhu, J., Liao, Z. & Tang, C., 2016. Numerical SHPB Tests of Rocks Under Combined Static and Dynamic Loading Conditions with Application to Dynamic Behavior of Rocks Under In Situ Stresses. *Rock. Mech. Rock. Eng.*, 49(10), pp. 3935-3946. https://doi.org/10.1007/s00603-016-0993-1

Ahmad Mardoukhi, Mikko Hokka, Veli-Tapani Kuokkala
Tampere University of Technology, Laboratory of Material Science
PO Box 589, FI-33101, Tampere, Finland
ahmad.mardoukhi@tut.fi, mikko.hokka@tut.fi, veli-tapani.kuokkala@tut.fi

Timo Saksala
Tampere University of Technology, Laboratory of Civil Engineering
PO Box 600, FI-33101, Tampere, Finland
timo.saksala@tut.fi

Unpublished manuscript

Experimental study of the dynamic indentation damage in thermally shocked granite

Ahmad Mardoukhi, Mikko Hokka, Veli-Tapani Kuokkala

Experimental study of the dynamic indentation damage in thermally shocked granite

Ahmad Mardoukhi*, Mikko Hokka, Veli-Tapani Kuokkala

Tampere University of Technology, Laboratory of Materials Science, POB 589, FI-33101, Tampere, Finland

Abstract This paper presents an experimental methodology to study the effects of pre-existing cracks and damage on the rock behavior under dynamic indentation. A modified Split Hopkinson Pressure Bar device was used to carry out dynamic indentation tests, where rock drill buttons were impacted on large rock samples. Before the mechanical testing, the samples were thermally shocked using a plasma spray gun for periods of 3, 4, and 6 seconds. The plasma gun produces very powerful heat shocks on the rock sample, and even very short exposures can change the surface structure of the samples and provide samples with different crack patterns and surface roughness for experimental testing. The effects of the heat shock damage on the dynamic indentation behavior of the rock were characterized with single- and triple-button indentation tests. Even though the force-displacement curves obtained from the indentation tests provide useful information about the bit-rock interactions, they provide only very little information about the volume of the craters, and especially the information about the side chipping and chipping between the indenters is missing. Therefore, the craters produced by the impacts were studied using optical profilometry to obtain the missing information. The specific destruction work was used to characterize the effects of heat shocks on the material removal during dynamic indentation. The results show that the force-displacement response of the rock does not change much even if the rock surface is severely damaged by the heat shock, however, the destruction work decreases significantly. This means that the same loading removes more volume if the material surface is pre-damaged, and that the efficiency of the indentation process cannot be evaluated from the bit-rock interaction forces alone. The presented experimental framework can be a useful tool for the verification of numerical models where the rock microstructure and especially the microcracks are essential.

Keywords: Granite, Heat shock, Dynamic indentation, Indentation damage, Destruction work

Introduction

Percussive drilling is widely used in tunnel excavation, shallow well boring, and mining industry. The method has applications also in oil and gas drilling in the areas where hard igneous rocks such as granite are found. The basic mechanism of percussive drilling is the repetition of impacts of the drill hammer on the rock mass. The efficiency of the method, however, depends on various properties of the rock including the brittleness and strength. The more brittle the rock is, the more favorable the creation of radial cracks and side chipping become during the process [1, 2]. The brittleness of the rock material can vary according to the drilling conditions. For instance, while drilling for geothermal energy, the depth of the wells can reach 5000 meters. At this depth, the confining pressure and temperature of the rock increase [3, 4, 5, 6]. Usually at these conditions, the rock shows less brittle or even somewhat ductile behavior while its strength increases significantly.

*Correponding author:
E-mail: ahmad.mardoukhi@tut.fi
Phone Number: +358-466278477

During percussive drilling, the rock is first deformed elastically, which is followed by the crushing of the surface asperities. In the third stage, the crushed zone begins to form under the indenter and finally the chips start to form along curved trajectories. The formation of the crushed volume and the side cracks are acknowledged as two essential phenomena of the fracturing process [7, 8, 9, 10] and therefore have a strong influence on the formation of the craters and the overall rate of penetration. The formation of the craters in the rocks has been studied extensively in the past [10, 8]. Maurer and Rinehart [10] studied the shape of the craters caused by an impact in sandstone and granite at different angles of impact. In sandstone, an impact at an angle of 90˚ makes the projectile penetrate into the sample crushing the material in front of it. The crushed material is forced aside by the penetrator, which leads to the creation of a cylindrical hole. This cylindrical hole is surrounded by a zone of compressed material. In the upper part of the crater, side chipping takes place and causes the formation of a cup-shaped crater. The situation is a bit different when the projectile impacts the surface of granite. In this case, the crater has a small sloping side and no cylindrical hole is observed. Instead, the craters in granite have a cup shape. The authors [10] also stated that as the projectile penetrates into the material, the fracture occurs in a stepwise manner propagating along a logarithmic spiral. Finally, the authors reported that the penetration of the projectile is directly proportional to its mass and the difference between the impact speed and the minimum speed at which cratering occurs. Swain and Lawn [8] categorized the evolution of the fracture caused by an indentation into four different stages. The first stage is the crack nucleation. In heterogeneous materials, flaws such as microstructural defects are the most favorable places for the cracks to nucleate, or the crack nuclei can be created by the deformation caused by the indentation. The second stage is the crack formation, during which the dominant flaw starts to extend into the material in a stable manner. At the beginning of this stage, the energy barrier plays an important role since it is the only factor, which restricts the full propagation of the crack. However, it should be noted that the depth to which the crack needs to grow to overcome the energy barriers is rather small compared to the dimensions of the contact area between the indenter and the target material. In the third stage, rapid propagation of the cracks takes place once the crack overcomes the energy barrier. Usually the depth of the crack extension in this stage is greater than the contact dimension between the indenter and the target material. At this depth, the tensile force drops below the value necessary to maintain the growth and the crack becomes stable once again. At this stage, the crack is called ‘well-developed [11, 12]. The best example of the well-developed fracture caused by an indentation is the Hertzian cone crack [13, 14, 15]. The fourth and final stage is called ‘unloading cracks’. The reverse load of the indentation causes the cone and the median cracks to close [16]. In addition, the residual stresses caused by the mismatch between the deformed part of the material and the surrounding elastic matrix can act in favor of the initiation and propagation of new cracks. These new cracks are called lateral cracks, which initiate from the deformation zone and propagate sideways or towards the specimen surface in a stable manner [17, 18]. Lateral cracking appears to be the most efficient indentation fracture mode as it causes surface material removal.

The complexity of chip formation and material removal during the indentation process makes the comprehensive experimental research of the rock behavior quite an overwhelming task, and therefore various modeling approaches are being developed. On the other hand, it is also quite difficult to establish a solid relationship between the existing cracks and their distributions and the strength and fragmentation of the rock, partly because rock samples with controlled crack sizes for mechanical testing are not easy to produce. Because of this, obtaining reliable experimental results to be used as input values for the numerical simulations and for model verifications can be quite challenging. Some preliminary work has been carried out by Saksala [19], who modeled the rock fracture under dynamic loading using a combined continuum damage embedded discontinuity model in the finite element method. Wang et al. [20] carried out simulations

of the rock fragmentation process with two drill bits subjected to impact loading. The authors stated that in this loading condition the results show the appearance of radial cracks, incipient chips, pulverized zones, and shell cracks. They also concluded that the dynamic pressure plays an important role in the failure of the sample when using two indenters. The authors showed that in a homogeneous rock, a smooth tensile crack from the loading face propagates through the sample. However, in a heterogeneous rock, the fracture usually propagates along a curvilinear path during the failure. Heterogeneous rocks absorb more energy due to the imperfections in their structure, which leads to the severe absorption of the compressive stress waves by the rock. Due to the severe attenuation of the compressive waves in heterogeneous rocks, the reflected tensile stress waves are also weaker. Liu et al. [21] simulated the fragmentation of rock using single and double indenters. The authors reported that the rock deforms elastically at the initial loading stage. Later on, the tensile cracks are initiated around the corners of the indenter and propagate in a conical Hertzian manner. Further loading of the rock leads to the appearance of the crushed zones. Due to the appearance of the crushed zones, new tensile cracks start to propagate towards the surface and cause side chipping. Use of two indenters leads to the side chipping of the rock between the indenters. The spacing between the indenters is an important factor and affects the fragmentation efficiency. Despite all the previous efforts, there is still a gap in the understanding of the rock behavior in dynamic indentation loading conditions, as the usual force-displacement curves do not explain the process fully. In addition, the role of pre-existing cracks has not been examined thoroughly. The pre-existing cracks are an important feature of the material removal process in percussive drilling, as every impact causes damage and cracks to the material, which facilitates the material removal during the next and consecutive impacts.

This paper presents a methodology to modify the surface properties of the rock material by applying heat shocks. The aim of the work is to develop an experimental methodology to facilitate future modeling efforts, and to quantify the effects of pre-existing cracks on the material removal during dynamic indentation. The heat shock method shows a good level of consistency in generating different crack patterns on a large piece of rock, which enables experimental testing of the same rock type with different amounts of pre-existing damage. Therefore, it becomes easier to study and analyze the effects and the role of the pre-existing cracks on the dynamic indentation behavior and especially on the material removal of rock materials. The effects of different surface crack patterns on the material removal are studied using a modified Hopkinson Pressure Bar device, where one or three drill buttons are embedded into the impact-end of the incident bar. The damage is characterized using optical profilometry, which provides useful information about the damaged volume caused by the indentation process.

Experimental Procedure

The material used in this work is Kuru Grey granite. Table 1 shows the chemical composition of the tested material. Kuru Grey has the mean value of open porosity of 0.44% and the quasi-static compression strength of about 220 MPa. The microstructure of the tested rock shows no evident texture. The minerals are also distributed homogenously and the mechanical properties are essentially isotropic.

Table 1 Mineral composition of Kuru Grey granite [22].

Mineral composition	Wt.%
Quartz	35
Albite	31
Microcline maxi	28

Biotite	3
Diopside	2
Chlorite IIb	1

Bulk samples of Kuru Grey with dimensions of 30cm × 30 cm × 30cm were used for the dynamic indentation tests. The heat shocks were applied by a 50kW plasma gun, which was moved over the sample surface at a fixed distance at the speeds of 100 mm/s, 75 mm/s, and 50 mm/s producing the shock duration of 3 seconds, 4 seconds, and 6 seconds, respectively. The temperature of the rock surface after the heat shock was 76˚C, 88˚C, and 100˚C for the 3 s, 4 s, and 6 s thermal shocks, respectively.

The indentation tests were carried out using single- and triple-button indenters with the hemispherical geometry shown in Figure 1. The experimental setup was basically a Split Hopkinson Pressure Bar (SHPB) without the transmitted bar. The drill buttons were embedded in the impact end of the incident bar. The experimental setup is shown in Figure 2. The readers are referred to refs. [23, 24, 25] for more technical details and examples of tests carried out at different speeds, etc.

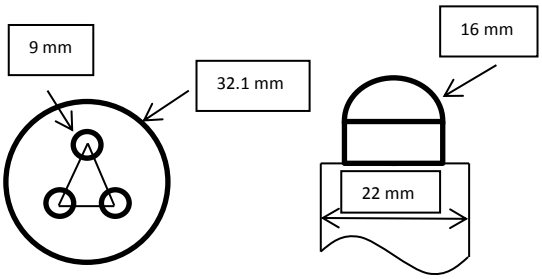

Figure 1 The triple-button and single button-bits

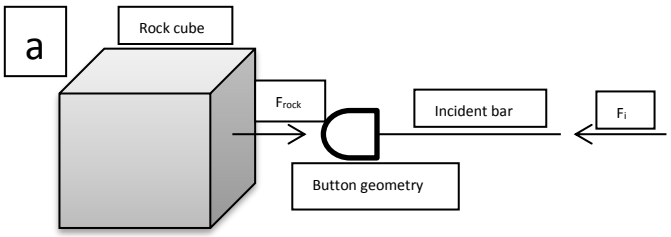

Figure 2 a) Schematic picture of the dynamic indentation test and b) the experimental setup.

The setup includes an air gun, a striker bar with the length of 20 cm, and an incident bar with the length of 120 cm and a diameter of 22mm made of AISI 4340 steel for the single-button tests. In the triple-button tests, the incident bar had a diameter of 32.1 mm. The stress pulses were measured using two strain gages bonded on the surface of the incident bar at the center of the bar. The force on the bar-rock interface was calculated using the following Equation:

$$F(t) = A_b E_b(\varepsilon_i(t) + \varepsilon_r(t)) \quad (1)$$

where A_b is the cross sectional area of the incident bar, E_b is the Young's modulus of the bar material, and ε_i and ε_r are the measured and dispersion corrected incident and reflected strains as a function of time. The numerical dispersion correction method used in this work was adopted from the original work of Gorham [26]. Two springs were used to apply a small force to push the incident bar towards the rock to secure a sufficient initial contact between the bits and the rock. In addition, the quality of the contact between the rock and the buttons was verified before each test with a sheet of white paper and a carbon paper between the rock and the indenters. If the contact was not even, the alignment of the rock and the bar was adjusted accordingly. Examples and more details of the alignment of the triple-button bit can be found in ref. [24].

The single-button tests were conducted at the impact speed of 19 m/s. In these tests the diameter of the striker and the incident bars were the same, and therefore the impact speed of the indenter on the rock is also close to the impact speed of the striker. However, the triple-button tests were carried out with an incident bar with a much larger diameter than the striker bar. Therefore, the triple-button tests needed a higher striker speed to compensate for the difference in the cross section. When the cross sectional areas of the incident bar and the striker are the same, the relationship between the striker speed and the stress in the incident bar can be evaluated using Equation (2):

$$V_s = \frac{2\sigma_{bar}}{\rho C} = \frac{2\sigma_{striker}}{\rho C} \quad (2)$$

where ρ is the density and C the speed of sound of the bar material. Equation (2) can also be used to evaluate the striker speed in the triple-button test that will result in the same indentation speed as in the single indentation test. Based on this, a striker speed of 41 m/s would be required in the triple-button tests, but due to the technical limitations of the device, the maximum striker speed of 35 m/s was used instead.

The craters produced by the indenter(s) were replicated using a commercial NDT quality resin. These replicas were analyzed using Alicona Infinite Focus G5 optical profilometer. The 3D images obtained from the profilometry were processed using IF-MeasureSuite software to measure the volume of the craters for the calculation of the destruction work.

Result and Discussion

Figures 3 a-d show the force vs. displacement curves for the single-button tests for the non-heat shocked surface as well as for the 3 s, 4 s, and 6 s heat shocked surfaces. As can be seen from these Figures, for all samples the depth of penetration is almost the same with the same level of applied force. Another important feature in these curves is the appearance of a second maximum. The most likely explanation for the shape of the force-displacement curve is that the bit first damages the rock surface severely and then continues to move inwards, trapping the produced powder between the crater surfaces and the bit. Further forward movement of the bit leads to the compaction of the powder, which manifests itself as the second maximum. Therefore, a part of the force applied on the rock is consumed on compacting the powder under the bit instead of causing further damage to the rock. The force-displacement curves do not resemble the typical experimental bit-rock interaction curves, where elastic recovery is often observed. However, it has been shown [24] that the behavior of the rock and the bit-rock interaction for this rock change at higher speeds, where elastic recovery is not observed as the material is shattered into dust in front of the indenter.

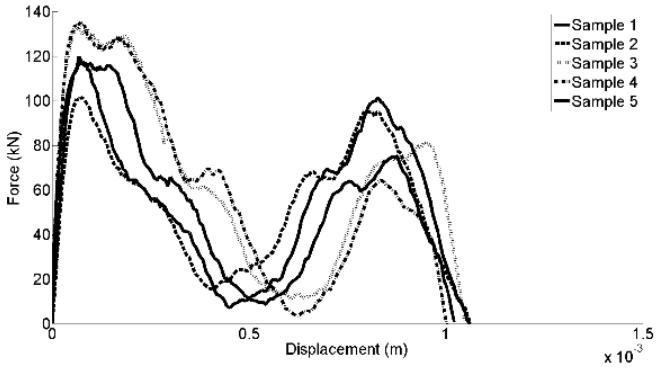

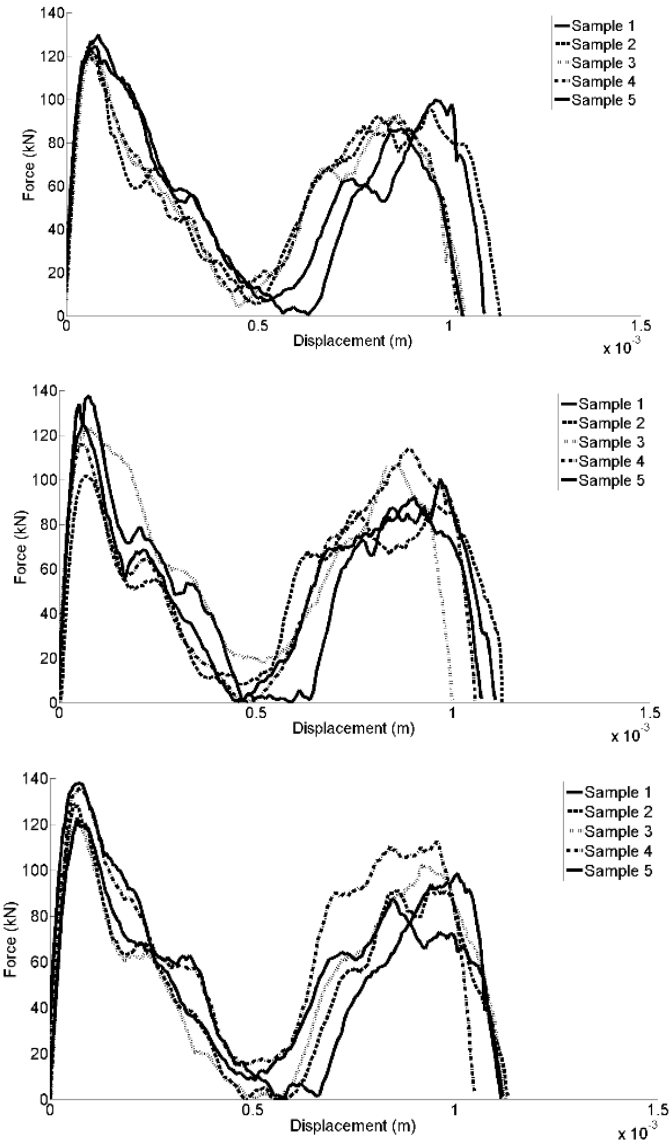

Figure 3 Force vs. displacement curves for a) non-heat shocked surface, b) 3 s heat shocked surface, c) 4 s heat shocked surface, and d) 6 s heat shocked surface.

The force-displacement curves give an impression that the heat shocks have no effect on the rock behavior. However, the force-displacement curves do not provide information about the volume of the crater. As the rock has been weakened by the heat shock, the indenter removes material in the direction of the applied force, but also the side chipping increases significantly, which is evidently not observable in the force-displacement data. The profilometry results indicate that the volume of the craters increases with the duration of the heat shock. As an example, Figure 4 shows the crater formed during the dynamic indentation process on the sample heat shocked for 6 seconds before the test.

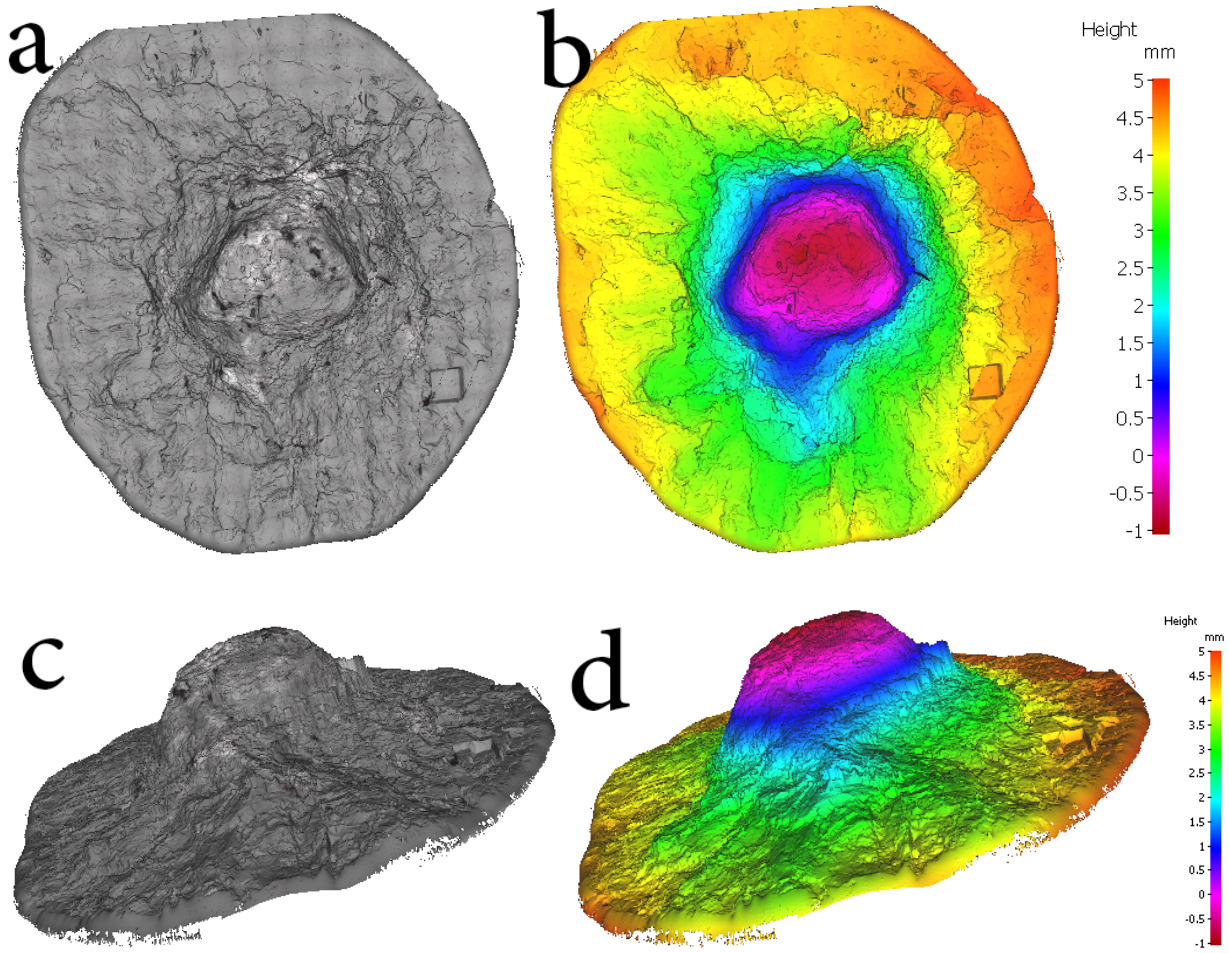

Figure 4 3D profilometry images of the crater formed during an indentation on a 6 s heat shocked surface. a) Perpendicular view of the raw image, b) perpendicular view of the mapped raw image, c) side view of the raw image, and d) side view of the mapped raw image.

Table 2 summarizes the data obtained from the crater volume measurements. It is evident that by increasing the duration of the thermal shock, the volume of the crater increases as well. This increase is 14%, 66%, and 77% for the 3 s, 4 s, and 6 s heat shocks, respectively. However, it is worth mentioning that the dynamic indentation tests described in this work are not single indentation tests, as the rock is impacted several times by the stress pulses reflecting back-and-forth in the incident bar. The force-displacement curves depicted in Figure 3 show only the first impact, whereas the volume of the crater is a result of all impacts. Nevertheless, the first impact causes the main damage and the rest of the impacts are mostly compacting the dust beneath the indenter, and therefore the error remains manageable.

Table 2 Volume of the craters caused by the dynamic indentation of non-heat shocked and heat shocked surfaces (mm^3).

	0 s	3 s	4 s	6 s
	197.14	291.33	301.77	285.61
	202.63	261.56	305.1	329.69
	200.3	277.72	381.88	375.4

	188.35	227.15	399	449.52
	196.12	226.66	254.43	391.79
Average	**196.91**	**256.88**	**316.43**	**366.4**
STDEV	5.435	29.32	47.39	62.27

Knowing both the volume of the crater and the work done by the indenter, i.e., the area under the force-displacement curve, allows the calculation of the destruction work (W_z) for each indentation. The concept of destruction work was first introduced by Thuro and Spaun [27], and it describes the amount of mechanical work that is needed to remove a unit volume from the surface of the rock. The force-displacement curves at this impact speed show consistently a second maximum, as described and explained earlier, and the destruction work was calculated separately for the first part of the force-displacement curve covering the first peak and half of the following valley, and for the entire measured force-displacement data. The former is from here on called the primary specific destruction work and the latter the total specific destruction work.

Figure 5 shows the specific destruction work obtained from the single-button tests. As can be seen from the graph, the destruction work decreases as the duration of the heat shock increases. This of course is expected, even though it is not evident from the force-displacement data. The destruction work decreases faster when the duration of the heat shock increases to four seconds. The reduction of the total destruction work compared to the non-heat shock tests is about 6%, 20%, and 30% for 3 s, 4 s and 6 s heat shocks, respectively. Even though the single-button tests do not resemble the real life situation of percussive drilling, it provides useful information for the future numerical research of the bit-rock interactions. The decrease in the specific destruction work becomes less pronounced after a certain duration of the heat shock (between 4 and 6 s heat shocks). One possible explanation for this observation is that the damage on the sample surface during a four-second heat shock is already so severe that adding more damage will not facilitate additional material removal. Another possible explanation is that heat shocks longer than four seconds do not add more cracks and damage to the surface, and that the more damaged material is always removed from the surface by the plasma spray.

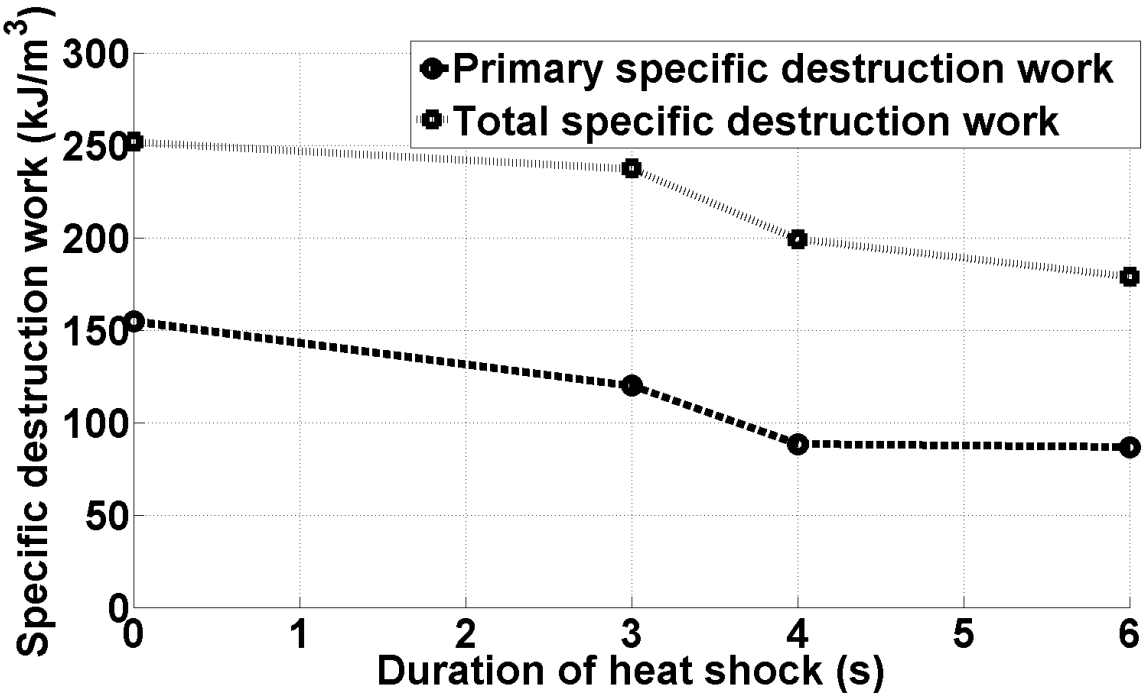

Figure 5 Specific destruction work for the first peak (primary) and for the full force-displacement curve (total) obtained from the single-button indentation test.

Figure 6 shows the force-displacement curves obtained from the triple-button indentation tests. The shapes of the curves are significantly different from those observed in the single-button tests, and a clear second maximum is not observed in any of the plots. However, the force-displacement curves for the 3 s and 4 s heat shocks (Figures 6b and 6c) have a somewhat similar shape where an intermediate drop in the bit-rock interaction force is observed before a gradual increase towards the end of the test. The reason for the difference between the single-button and triple-button bit-rock interaction forces is that the indenters used in the triple-button tests are considerably smaller than the button used in the single-button tests. Therefore, the amount of dust and powder, which is trapped under the indenter is smaller. Additionally, as the area between the indenters is damaged and material is removed also from that area, it provides the space for the produced dust and powder to leave the craters.

The bit-rock interaction force for the rock without a heat shock is essentially the same as for the rock with a 3 second heat shock. The data is consistent and the scatter is rather low. However, the indenter seems to penetrate slightly deeper into the rock with some pre-existing heat shock damage. When the duration of the heat shock increases to 4 seconds, the force levels remain unchanged and the scatter increases only slightly compared to the scatter in the tests with the intact rock. However, the scatter increases considerably in the results obtained for the rock with a 6 second heat shock. The increased scatter is most likely due to an increase in the side chipping, which typically manifests itself as sharp drops in the bit-rock interaction forces. Tkalich et al. [1] performed static indentation tests on rocks and concluded that the sharp drops after reaching the maximum are due to the chipping of the rock. Later on, the level of the force increases and the loading process continues until the next drop, which indicates another chipping event. As mentioned before, a typical force-displacement curve tends to move backward at the end of the test. However, this behavior is not observed in the force-displacement curves obtained in this work. Instead, a sharp drop at the end of the tests can be seen, indicating the end of the forward movement of the incident bar, i.e., the end of the test.

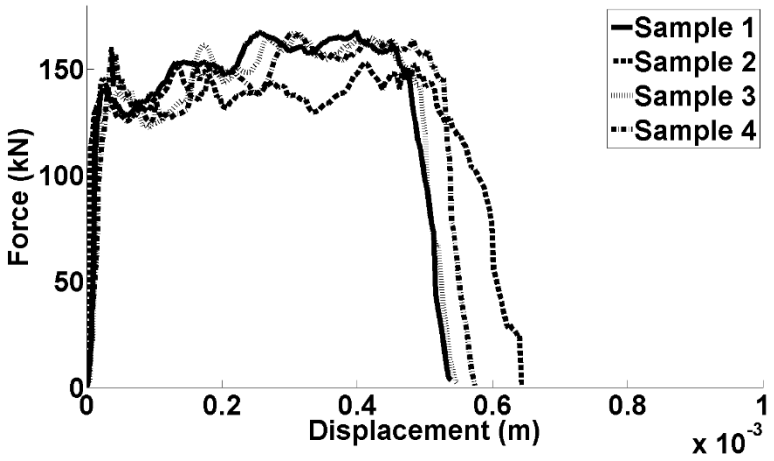
Sample 1
Sample 2
Sample 3
Sample 4
Force (kN)
150
100
50
0
0
0.2
0.4
0.6
0.8
1
Displacement (m)
x 10^-3

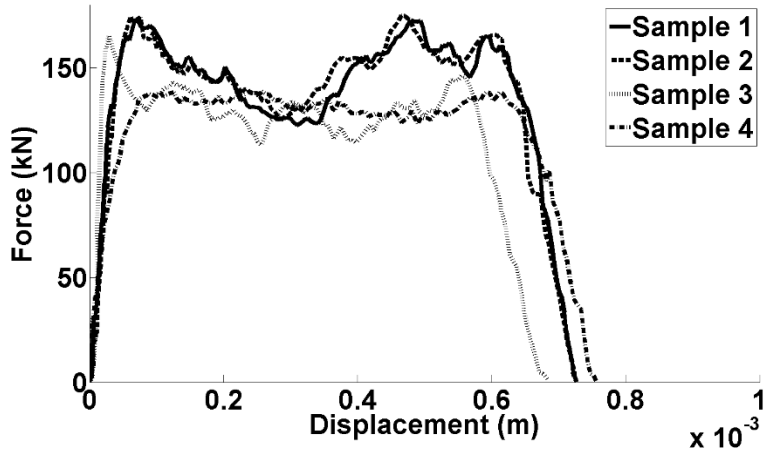
Sample 1
Sample 2
Sample 3
Sample 4
Force (kN)
150
100
50
0
0
0.2
0.4
0.6
0.8
1
Displacement (m)
x 10^-3

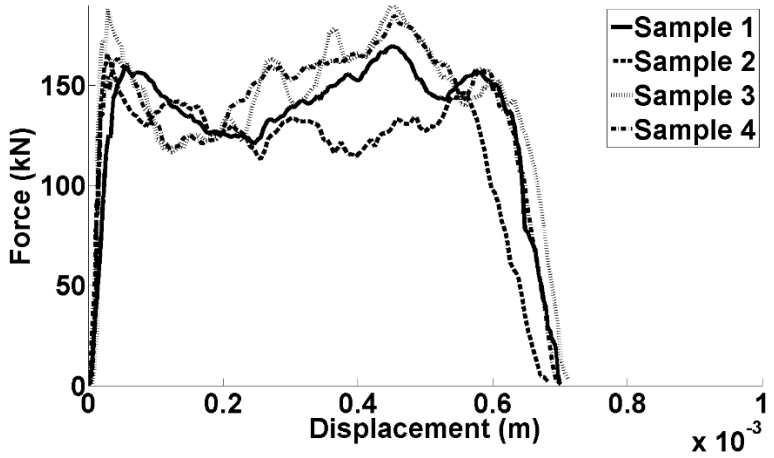
Sample 1
Sample 2
Sample 3
Sample 4
Force (kN)
150
100
50
0
0
0.2
0.4
0.6
0.8
1
Displacement (m)
x 10^-3

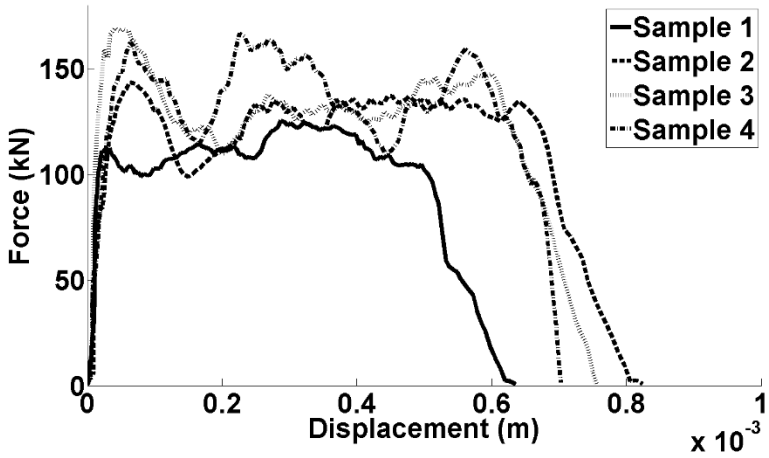

Figure 6 Force vs displacement data for a) non-heat shocked surface, b) 3 s heat shocked surface, c) 4 s heat shocked surface, and d) 6 s heat shocked surface.

A typical force-displacement curve reaches a maximum and then turns back towards smaller displacement values, indicating unloading of the sample. The unloading phase, however, is not observed in the single-button nor in the triple-button test results of this work. On the other hand, Saksala et al. [28] have observed that as the impact velocity increases, the curves start to lose their typical shape and the unloading part eventually starts to disappear. The most likely explanation for this observation is that the increase in the impact speed increases the damaged zone in front of the button(s), and the damaged material simply cannot push the bar backward. Figure 7 shows the damaged area during the dynamic indentation and Figure 8 the craters, which were analyzed using optical profilometry.

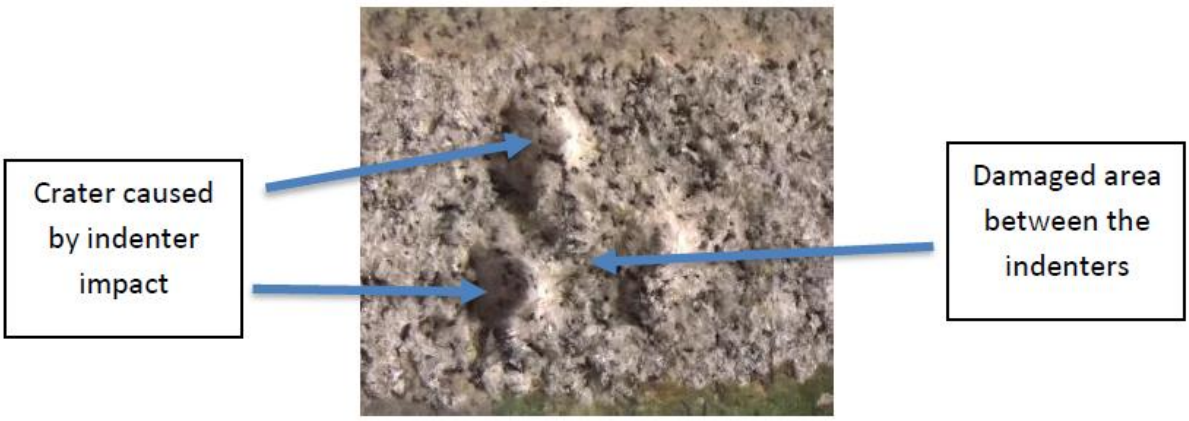

Figure 7 Damaged area on a 6-second heat shocked sample

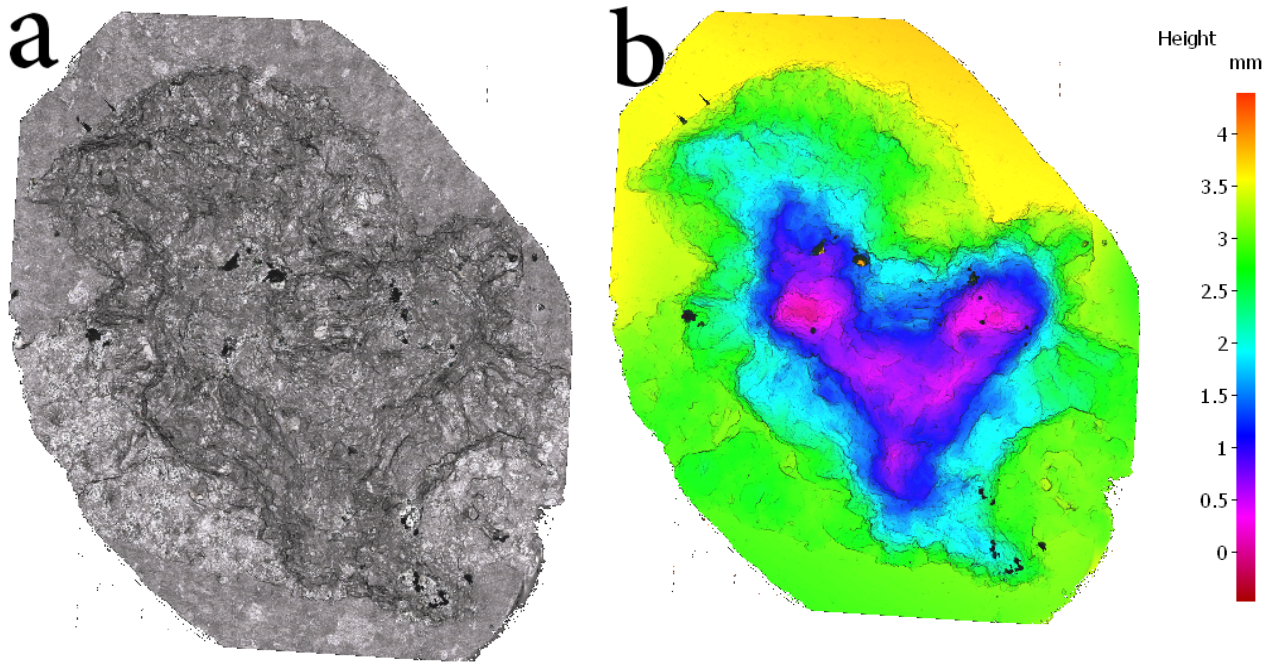

Figure 8 3D profilometry images of the crater formed during an indentation on a 6 s heat shocked surface. a) Perpendicular view of the raw image, b) perpendicular view of the mapped raw image

The destruction work was calculated in the same manner for the triple-button tests as described for the single-button tests. Figure 9 shows the specific destruction work for the triple-button tests and the depth of the crater caused by the impact. As it is evident, larger heat shock damage leads to lower specific destruction work. The decrease in the specific destruction work of the heat-shocked samples compared to the non-heat shock tests is about 3%, 11%, and 30% for 3 s, 4 s, and 6 s heat shock, respectively. The force-displacement curves for the triple-button tests are quite similar for all tests including the non-heat shocked and the heat-shocked surfaces. Therefore, the mechanical energy consumed in the tests varies only little. However, the volume of the craters becomes larger with increasing heat shock damage, which is seen as lower destruction work. The drop in the destruction work is not that high for the 3 s heat shock, but already at 4 s the drop becomes significant. Also the depth of the crater increases with increasing pre-existing heat shock damage. However, the total damaged volume increases much faster than the depth of the crater because of the increasing side chipping and the removal of the material in between the buttons. The amount of material removed outside the contact area between the buttons and the rock is actually very important, and it has a strong effect on the overall rate of penetration in drilling. From the energy consumption point of view, it is better to remove larger chips from the surface rather than grinding the rock into dust that has a very high specific surface area. The volume removed outside the button contact area, especially in between the buttons, is a function of the impact speed. It has been previously [28] reported that the lower striker speeds of 10 m/s and 16 m/s induce almost no material removal between the buttons for intact Kuru gray granite. However, increasing the striker speed up to 22 m/s causes the material to chip off between the buttons in 50% of the tests. In this study, the striker speed of 35 m/s caused material between the indenters to chip off even from the non-heat shocked samples. However, based on the results presented here it is evident that also the pre-existing damage has an effect on the side chipping and material removal from between the buttons. Larger craters are formed also in the center part of the drill bit at higher heat shock damages. Based on preliminary X-Ray CT analysis on the heat shocked rock samples, most of the damage actually occurs very near the sample surface. Therefore, it can be expected that the side chipping is strongly affected by the damage within a layer of 50-100 microns from the surface.

The triple-button indentation tests are a simplification of full-scale drilling, but the laboratory environment allows more careful evaluation of the results. In most cases, the scientists and engineers are interested in the overall drilling rate or the rate of penetration. Identification of different rock properties based on the bit-rock interaction forces would be very beneficial in drilling and mining, where the penetration through a rock layer could be detected from simple strain gage measurements. This could be used for example to identify the end of a pay layer. However, based on this work the bit-rock interaction forces are quite insensitive to small changes in the rock strength, and the effects of the pre-existing damage and rock strength are more clearly seen in the removed volume and especially in the side chipping and material removal from between the buttons. However, this is only a preliminary conclusion, and its verification will require more careful examination of the effects of heat shocks on the rock structure using, for example, X-Ray CT scans and electron microscopy. Future work will also include extensive numerical studies, but at the moment they are beyond the scope of this paper.

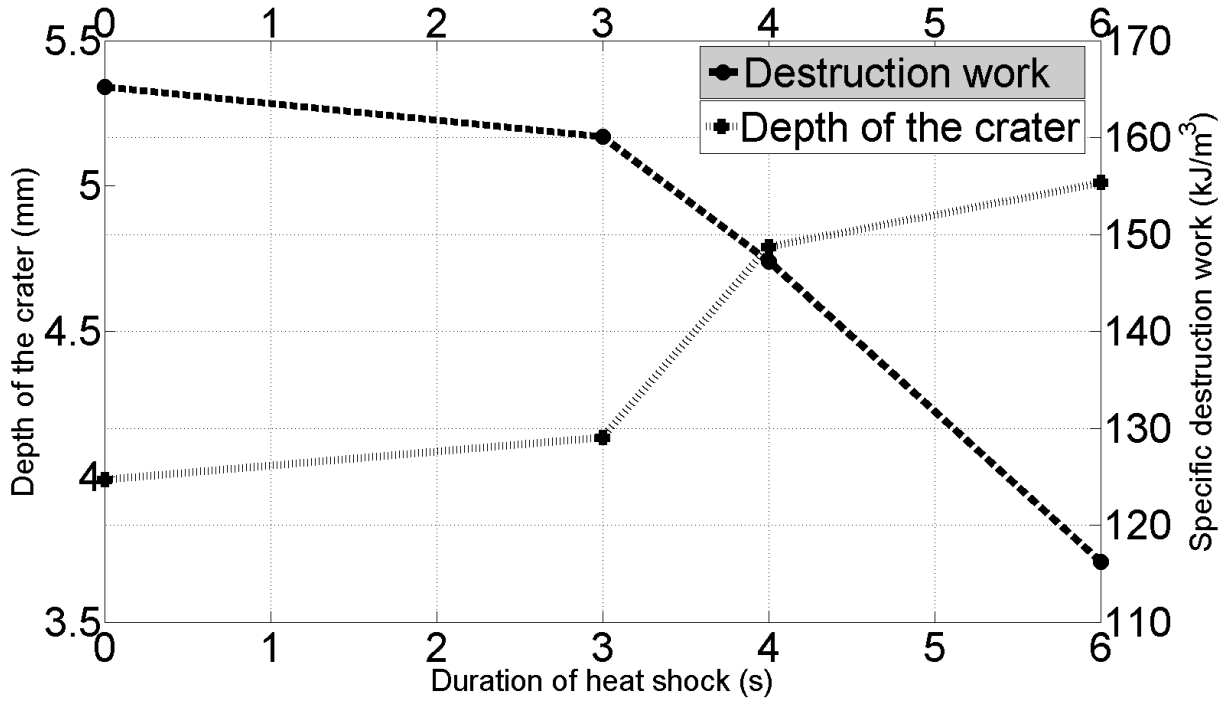

Figure 3 Specific destruction work and depth of the crater as a function of the duration of the heat shock for the triple-button indentation tests.

Concluding remarks:

- This works presents a methodology to alter the rock structure using heat shocks and to study the effect of this change on the mechanical behavior of rock under dynamic loading conditions. Based on the results obtained in this work, we believe that the presented methodology can provide useful information also for modeling and simulation purposes.
- At the high impact velocities used in this work, the force vs. displacement curves do not resemble typical experimental bit-rock interaction curves, where elastic recovery is usually observed. However,

it has been shown that the behavior of the rock and the bit-rock interaction change at higher speeds, where elastic recovery vanishes as the material is shattered into dust in front of the indenters.

- The force-displacement curves obtained from single-button indentation tests have two maxima. Most likely the second maximum is due to the further penetration of the indenter after crushing the rock surface. This further penetration compacts the dust and powder under the indenter and causes the appearance of the second maximum in the curves. However, the second maximum is not observed in the triple-button tests. The reason for this can be that the amount of powder and dust is considerably less since the geometry of the indenters in these tests is different from the single-button tests and the indenters have a smaller size. In addition, also the material between the indenters is damaged, providing enough room for the dust and powder to escape.
- Even though the force-displacement curves provide useful information about the rate of penetration inside the rock, they do not correlate well with the mechanical properties of the rock nor describe the size of the craters and extent of material removal. Therefore, optical profilometry was used to measure the volumes of the craters. The profilometry results indicate an increase in the size of the craters as the duration of the heat shock increases.
- The mechanical energy and the volume of the craters were used to calculate the destruction work. The destruction work decreases as the duration of the heat shock increases. However, in the single-button tests, after a certain duration of the heat shock, the decrease in the destruction work becomes less pronounced.
- In triple-button tests, the continuous decrease of the destruction work can be explain by increasing side chipping and material removal between the indenters with increasing thermal shock damage.

Acknowledgment

This study was supported by Suomen Luonnonvarain Tutkimussäätiö –Foundation under grant numbers 1768/14, 1779/15 and 1789/16 and Finland Cultural Foundation.

References

[1] D. Tkalich, M. Fourmeau, A. kane and C. L. G. Cailletaud, "Experimental and numerical study of Kuru granite under confined compression and indentation," *International Journal of Rock Mechanics and Mining Sciences,* vol. 87, pp. 55-68, 2016.

[2] O. Ajibose, M. Wiercigroch and A. Akisanya, "Experimental studies of the resultant contact forces in drillbit-rock interaction," *International Journal of Mechanical Sciences,* vol. 91, pp. 3-11, 2015.

[3] G. Han, M. Bruno and T. Grant, "Lab investigations of percussion drilling: from single impact to full scale fluid hammer," in *The 41st U.S. Symposium on Rock Mechanics (USRMS)*, Golden, 2006.

[4] R. Cunningham and J. Eenink, "Laboratory Study of Effect of Overburden, Formation and Mud Column Pressures on Drilling Rate of Permeable Formations," in *Society of Petroleum Engineers*, 1959.

[5] R. Wei and S. Zang, "Effects of Temperature and Strain Rate on Fracture Strength of Rocks and Their Influence on Rheological Structure of the Lithosphere," *Chinese journal of geophysics,* vol. 49, no. 6, pp. 1576-1584, 2006.

[6] C. Saiang, Influence of heat on the physical and mechanical properties of selected rock types, Lulea: Luleå tekniska universitet, 2011.

[7] P. Lindqvist and L. Hai-Hui, "Behaviour of the crushed zone in rock indentation," *Rock Mechanics and Rock Engineering,* vol. 16, no. 3, pp. 199-207, 1983.

[8] M. Swain and B. Lawn, "Indentation fracture in brittle rocks and glasses," *International Journal of Rock Mechanics and Mining Sciences & Geomechanics Abstracts,* vol. 13, no. 11, pp. 311-319, 1976.

[9] "Initiation of cracks in coal specimens by blunted wedges," *The engineer,* vol. 217, pp. 217-220, 1964.

[10] W. Maurer and J. Rinhart, "Impact crater from rock," *Journal of applied physics,* vol. 31, no. 7, pp. 1247-1252, 1960.

[11] B. Lawn, Fracture of Brittle Solids, Cambridge: Cambridge university press, 1993.

[12] B. Lawn and E. Fuller, "Equilibrium penny-like cracks in indentation fracture," *Journal of Materials Science,* vol. 10, no. 12, pp. 2016-2024, 1975.

[13] B. Lawn and R. Wilshaw, "Indentation fracture: principles and applications," *Journal of Materials Science,* vol. 10, no. 6, pp. 1049-1081, 1975.

[14] F. Langitan and B. Lawn, "Effect of a Reactive Environment on the Hertzian Strength of Brittle Solids," *Journal of Applied Physics,* vol. 41, no. 8, pp. 3357-3365, 1970.

[15] "On the theory of Hertzian fracture.," *Proceedings of the Royal Society of London A: Mathematical, Physical and Engineering Sciences,* vol. 299, no. 1458, pp. 291-306, 1967.

[16] J. Williams, B. Lawn and M. Swain, "Cone crack closure in brittle solids," *Physica status solidi a,* vol. 2, no. 1, pp. 7-29, 1970.

[17] B. Lawn and M. Swain, "Journal of Materials Science," *Microfracture beneath point indentations in brittle solids,* vol. 10, no. 1, pp. 113-122, 1974.

[18] B. Lawn and K. P. M.V. Swain, "On the mode of chipping fracture in brittle solids," *Journal of Materials Science,* vol. 10, no. 7, pp. 1236-1239, 1975.

[19] T. Saksala, "Modelling of Dynamic Rock Fracture Process with a Rate-Dependent Combined Continuum Damage-Embedded Discontinuity Model Incorporating Microstructure," *Rock Mechanics and Rock Engineering,* vol. 49, no. 10, pp. 3947-3962, 2016.

[20] S. Wang, S. Sloan, H. Liu and C. Tang, "Numerical simulation of the rock fragmentation process induced by two drill bits subjected to static and dynamic (impact) loading," *Rock mechanics and rock engineering,* vol. 44, no. 3, pp. 317-332, 2011.

[21] H. Liu, S. Kou, P. Lindqvist and C. Tang, "Numerical simulation of the rock fragmentation process induced by indenters," *International Journal of Rock Mechanics and Mining Sciences,* vol. 39, no. 4, pp. 491-505, 2002.

[22] M. Fourmeau, D. Gomon, R. Vacher, M. Hokka, A. kane and V. Kuokkala, "Application of DIC technique for studies of Kuru granite rock under static and dynamic loading," in *20Th European Conference on Fracture*, Trondheim, 2014.

[23] M. Apostol, Strain rate and Temperature Dependence of the Compression Behavior of FCC and BCC Metals, Tampere: Tampere University of Technology, 2007.

[24] T. Saksala, D. Gomon, M. Hokka and V. Kuokkala, "Numerical and experimental study of percussive drilling with a triple-button bit on Kuru granite," *International Journal of Impact Engineering,* vol. 72, pp. 56-66, 2014.

[25] A. Mardoukhi, Y. Mardoukhi, M. Hokka and V. Kuokkala, "Effects of heat shock on the dynamic tensile behavior of granitic rock," *Rock mechanics and rock engineering,* pp. 1-12, 2017.

[26] D. A. Gorham and X. Wu, "An Empirical Method of Dispersion Correction in the Compressive Hopkinson Bar Test," *Le Journal de Physique,* vol. 7, no. C3, pp. 223-228, 1997.

[27] K. Thuro and G. Spaun, "Introducing the `destruction work´ as a new rock property of toughness," in *Prediction and performance in rock mechanics and rock engineering*, Turin, 1996.

[28] T. Saksala, D. Gomon, M. Hokka and V.T.Kuokkala, "Numerical and experimental study of percussive drilling with a triple-button bit on Kuru granite," *International Journal of Impact Engineering,* vol. 72, pp. 56-66, 2014.

Tampereen teknillinen yliopisto
PL 527
33101 Tampere

Tampere University of Technology
P.O.B. 527
FI-33101 Tampere, Finland

ISBN 978-952-15-4003-5
ISSN 1459-2045